Development of a ceria-based catalyst prepared by the microemulsion method for highly selective CO_2 conversion via reverse water gas shift

by

Muhammad Waqas Iqbal

A thesis
presented to the University of Waterloo
in fulfillment of the
thesis requirement for the degree of
Doctor of Philosophy
in

Chemical Engineering

Waterloo, Ontario, Canada, 2021

Examining Committee Membership

The following served on the Examining Committee for this thesis. The decision of the Examining Committee is by majority vote.

External Examiner	NAME:	Hui Wang
	Title:	Professor
Supervisor(s)	NAME:	David Simakov
	Title:	Assistant Professor
Internal Member	NAME:	Eric Croiset
	Title:	Professor
Internal Member	NAME:	Peter Douglas
	Title:	Professor
Internal-external Member	NAME:	Yuri Leonenko
	Title:	Associate Professor

AUTHOR'S DECLARATION

I hereby declare that I am the sole author of this thesis.

This is a true copy of the thesis.

I understand that my thesis may be made electronically available to the public.

ABSTRACT

Reverse water gas shift (RWGS) is an emerging technology for CO_2 utilization. The RWGS process catalytically converts CO_2 to carbon monoxide (CO), producing syngas (a mixture of hydrogen (H_2) and CO) which can be further used to produce higher hydrocarbons. Economically this route is more promising than the carbon capture technology because RWGS converts CO_2 to valuable syngas that can offset the cost of CO_2 capturing. The main challenge is selecting a suitable catalyst that must be highly active, selective, stable, and durable in converting CO_2 to syngas.

In this study, cerium oxide (ceria) prepared through the reverse microemulsion (RME) process is used as a base catalytic material. An extensive investigation has been conducted to assess the potential of the RME-based bulk ceria and supported ceria on γ-alumina towards RWGS reaction, including reaction tests and several characterization techniques including X-ray diffraction (XRD), thermogravimetric analysis (TGA), Fourier transformed infrared spectroscopy (FTIR) to determine outlet gas composition, scanning electron microscopy-energy dispersive X-ray spectroscopy (SEM-EDX) to determine the surface elemental composition, gas adsorption to determine the specific surface area (BET-SSA) and inductively coupled plasma optical emission spectroscopy (ICP-OES) to determine the bulk composition, TEM (transmission electron microscope) to look for the particle shape and find the crystalline planes, TPR (temperature-programmed reduction) to check the reducing abilities of the catalyst, CO_2-TPD to find the relevant active site and *in-situ* FTIR studies to find the RWGS reaction mechanism.

First, RWGS reaction was studied over unsupported bulk ceria (CeO_2) prepared by reverse microemulsion (RME) method and direct precipitated method. Using a unique microemulsion ratio, highly porous ceria nanoparticles (RME-ceria) with targeted exposed (111) facets and

high specific surface area of 142 m^2 g_{cat}^{-1} were successfully synthesized compared to ceria nanoparticles prepare via direct precipitation method (DP-ceria) with specific surface area of 101 m^2 g_{cat}^{-1}. Long term stability tests (almost 100 h on stream) showed well stable activity of RME-ceria towards the RWGS. At lower GHSV of 10,000 ml g_{cat}^{-1} h^{-1}, nearly equilibrium conversion (~ 62%) was observed which stabilizes after 70 h on stream to around 52%. However, DP-ceria showed significant decline in conversion from 53% to 24% in similar time span of 70 h. Compared to DP-ceria, RME-ceria showed excellent activity and stability at all conditions towards the RWGS reaction.

Second, the RWGS reaction was studied for the first time in the field on catalysis over ceria-supported γ-alumina prepared via reverse microemulsion method. Three catalysts were prepared at three different loadings of ceria (20 wt%, 30 wt% and 40 wt%). All the catalyst were test for the application of RWGS reaction. Results confirm that 40% wt ceria-supported γ-alumina (40%Ce/Al) showed similar activity and stability as of unsupported RME-ceria. 40% Ce/Al showed very high specific surface area of 292.06 m^2 g_{cat}^{-1}, which is almost doubled compared to what we observe for the bulk RME-ceria. SEM results confirm the cluster like structure of the catalyst that leads to high porosity and high exposed surface area. Long term stability test at GHSV of 10,000 ml g_{cat}^{-1} h^{-1} showed stable 55% CO_2 conversion to CO with 100% selectivity. Finally, among all the Ce/Al catalyst formulations 40%Ce/Al catalyst appears as the optimum formulation for RWGS applications.

In the third part of this Ph.D. thesis, a thorough investigation was performed for the scope of stainless-steel reactors in the RWGS application. It was observed that at an operating temperature of above 550°C in a highly active carbonaceous environment of CO-H_2-H_2O stainless steel undergoes severe corrosion known as metal dusting. This disintegration leads to form nanometal particles that facilitate filamentous coke formation on the steel wall. Empty

reactor test (without catalyst) confirms the fact that in the absence of CO, stainless steel showed stable behavior (no reactivity for the incoming gas mixture of H_2-CO_2 below 550°C and only 4% CO_2 conversion to CO even after 90 h on stream).

Finally, suggestions for future work include the study of 40%Ce/Al using more advanced techniques like XPS, TME, and Raman spectroscopy for the in-depth surface analysis that would help to significantly enhance the activity at higher space velocities. It was also proposed that the effect of promoters like Cu, Co, and Fe should be studied. Literature showed that these promoters significantly enhance catalyst activity at a lower temperature. Conclusively, All the catalysts (unsupported and supported) showed 100%CO selectivity and stable conversion with excellent coking resistance.

ACKNOWLEDGMENT

First and foremost, I wish to thank my supervisor Professor David Simakov for his support, insight, and patience. I appreciate all his contributions, both time and ideas, to making my Ph.D. experience productive and inspiring. Thank you, Prof, for allowing me to grow as a research scientist. My sincere thanks go to my committee members, Prof. Eric Croiset, Prof. Peter Douglas, and Prof. Yuri Leonenko, for their time, interest, and helpful comments. I would also like to thank Professor Hui Wang for kindly serving as my external committee member.

I would like to acknowledge the financial support that I received through Prof. Simakov and the University of Engineering and Technology, Lahore, Pakistan.

My time at the University of Waterloo was made enjoyable in large part owing to lovely friends and lab mates: Zohaib Atiq Khan, Hiren Gagnani, Madhuja Chakraborty, Twara Patel, Nafiz Ahmed, Manas Kumar, Elnaz Halakoo, Sara Xu, Yichen Zhuang, Guanjie Sun, Yue Yu (Carol), Sogol Tabar, Robert Currie, Parabhjot Kaur, Alexandra McGowan, Faisal Khan, Edris Madadian, and Anastasiia Zakharova,

Finally, I must thank my family for their endless love and encouragement: my mother, Sabiha Iqbal, who support me in all my pursuits; my siblings, Muhammad Sheraz, Najia Iqbal, Mahroz Iqbal, Faraz Iqbal, Binish Iqbal, Aroosa Iqbal, and Erum Sheraz who always cheer me up; and most of all my beloved, encouraging, and patient Wife, Shafaq Zaheer, whose faithful support during the final stages of this thesis is highly cherished. I would like to thank my daughter Fatima Waqas for cheering me up during the stressful time. My special thanks to my mother-in-law, Raheela Rani, and my father-in-law, Zaheer Ahmed, for their love and prayers. Lastly, I would like to thank ALLAH almighty for his countless blessings. I am thankful to him for blessing me with a beautiful daughter Mirha Waqas just before the final exam.

Thank you all!

Table of Contents

List of Tables

List of Figures

List of Abbreviations

ADC	Analouge to digital converter
AMI	Altamira instruments
BET	Brunauer Emmett Teller
BP	British petroleum
BPR	Back pressure regulator
BZYZ	Zn- and Y-doped barium zirconate
CA	Complex method
CAF	Chemicals and fuels
CB	Carbon balance
CCS	Carbon capture and storage
CCU	Carbon capture and utilization
CDIAC	CO_2 information analysis center
CIS	Commonwealth of independent states
DD	Direct decomposition
DFT	Density functional theory
DP	Direct precipitation
DRIFT	Diffuse reflectance infrared Fourier transform spectroscopy
ECMB	Enhanced coal-bed methane

EDS	Energy Dispersive Spectroscopy
EGS	Enhance geothermal system
EOR	Enhance oil recovery
EPA	Environmental protection agency
EDS	Energy Dispersive Spectroscopy
FTIR	Fourier transformed infrared spectroscopy
GHG	Greenhouse gases
GHGRP	Facility greenhouse gas reporting program
GHSV	Gas hourly space velocity
HRTEM	High-resolution transmission electron microscopy
HT	Hard templet
ICP	Inductively Coupled Plasma
IPCC	Intergovernmental Panel on Climate Change
IR	Infrared analyser
LPG,	Liquefied petroleum gas
LSRP	localized surface plasmon resonance
MTPA	Million metric tons per annum
MWCNT	Multiwall carbon nanotubes
NASA	National Aeronautics and Space Administration
NC	Nanocubes

NIMC,	National Inst. of Materials and Chemical Research
NP	Nanoparticle
OBE	Oxygen binding energy
OES	Optical Emission Spectroscopy
ONRI,	Osaka National Research Institute
OSC	oxygen storage capacity
PC	Personal computer
PI	Pressure indicator
RH	Relative humidity
RITE,	Research Institute of Innovative Technology for the Earth
RME	Reverse microemulsion
RWGS	Reverse water gas shift
SEM	Scanning Electron Microscopy
SI	(Sol-immobilization method
SSA	Specific surface area
STP	Standard temperature and pressure
TC	Temperature controller
TEM	Transmission electron microscopy
TGA	Thermogravimetric analysis
TI	Temperature indicator

TMC	Transition metal carbides
TOT	Thousand metric tons
TPD	Temperature program desorption
TPR	Temperature program reduction
UK,	United Kingdom
US	United States
XRD	X-ray diffraction

List of Symbols

$C_{CO_2,b}$	Gas phase bulk CO_2 concentration, mol m^{-3}
$C_{CO_2,s}$	Surface CO_2 concentration, mol m^{-3}
D_m	Diffusion coefficient, m^2 s^{-1}
d_p	Particle size, m
f_1	CO_2 conversion to CO
f_2	CO_2 conversion to CH_4
$F_{C,out}$	Total outlet molar flow rate of carbon-containing species, mol s^{-1}
$F_{H_2,f}$	Feed molar flow rate of H_2, mol s^{-1}
$F_{CO_2,f}$	Feed molar flow rate of CO_2, mol s^{-1}
$F_{CO,out}$	Outlet molar flow rate of CO, mol s^{-1}
$F_{CH_4,out}$	Outlet molar flow rate of CH_4, mol s^{-1}
$F_{t,out}$	Total outlet molar flow rate, mol s^{-1}
GHSV	Gas hourly space velocity, ml g^{-1} h^{-1}
ΔH_{RWGS}	Enthalpy change, kJ mol^{-1}
K	Shape factor
k_c	Mass transfer coefficient
Pr	Prandtl number
Q_f	Volumetric feed flow rate, ml h^{-1}
R_g	Ideal gas constant, kJ mol^{-1} K^{-1}
R'_{obs}	Observed reaction rate, mol kg^{-1} s^{-1}
Re	Particle Reynolds number
r_p	Catalyst particle radius, m

S_{CO}	CO selectivity
S_{CH4}	Methane selectivity
Sc	Schmidt number
Sh	Sherwood number
T	Temperature
Ts	Surface temperature
W_c	Catalyst weight, g
X_{CO_2}	CO_2 conversion
y_i	Mole fraction (*i* stands for either CO_2, CO, or CH_4)
ΔH°_{298}	Standard reaction enthalpy, kJ mol^{-1}

Greek letters

α	H_2:CO_2 ratio in the feed
ε	Catalyst void fraction
λ	X-ray wavelength
λ_s	Solid thermal conductivity , kJ m^{-1} s^{-1} K^{-1}
λ_g	Gas thermal conductivity, kJ m^{-1} s^{-1} K^{-1}
θ	Diffraction angle
ρ_b	Catalyst bulk density, ml g^{-1}

Chapter 1

Introduction

1.1 Motivation

In recent decades due to rapid growth in modern civilization, the energy demand increased rapidly too. The only instant solution to fulfill this demand was the burning of traditional fuels like coal, coke, natural gas, and other fossils. This leads to polluting the environment with about 30 billion tons of CO_2 every year [1]. Anthropogenic CO_2 is one of the major greenhouse gases contributing to global warming and causing serious environmental damages due to its contribution to producing acidic rain and urban smog [2]. Mitigating the CO_2 emission to the atmosphere is a major challenge. Presently the CO_2 emission level is more than 60% than in the year 1990. According to IPCC (Intergovernmental Panel on Climate Change), in order to limit the upsurge of world average temperature to 2°C by 2050, there is a strong need to reduce CO_2 emission to at least a half of its present value [3]. Therefore, there is a strong demand to reduce CO_2 emissions.

There are three possible pathways available to date to reduce the atmospheric CO_2 emissions: first is to directly reduce CO_2 emission, second is CO_2 capture and storage (CCS), and the third is the CO_2 conversion to synthetic fuels and chemicals, which is also known as carbon capture and utilization (CCU). The first route needs technological advancements in utilizing fossil fuels or the use of carbon-free renewable energy resources. However, due to the rapid increase in the world population and high energy demand, it is difficult to follow this route. The second route is based on the direct capturing of CO_2 from flue gases and its storage in underground geological formations. This process is well established but highly energy-intensive, which leads to high capital and operating cost. In addition, the long-term

consequences of storing CO_2 underground are unknown. The third route is based on converting CO_2 directly to synthetic fuels or valuable chemicals with the help of renewable energy to create a closed carbon cycle [4-6]. To follow the third route, there are several approaches available for photo and electrochemical reduction, biological reduction, and thermo-catalytic reduction through renewable hydrogen conversion. Photo, electrochemical and biological reduction routes are viable but have major limitations such as the low CO_2 solubility and the cost of cultivating large biological systems [7]. The thermo-catalytic conversion of CO_2 to synthetic fuels using renewable energy sources is an alternative.

Conversion of CO_2 to synthetic fuels has a dual advantage as compared to other routes: the first advantage is direct CO_2 emission reduction, and the second one is creating a closed carbon cycle to store CO_2 in synthetic fuels and other valuable chemicals (excluding this carbon from the atmosphere). Importantly, this is subject to incorporating renewable H_2 generated using renewable (hydro, wind, solar) or low-carbon-footprint (nuclear) electricity into this artificial carbon cycle. Conceptually speaking, this approach is similar to carbon fixation by photosynthetic organisms that utilize solar light as a source of energy to drive the natural carbon cycle that has established a certain level of CO_2 in Earth's atmosphere. This cycle was recently disrupted by human activities via releasing the carbon stored in fossil fuels over millions of years.

The catalytic conversion of CO_2 to valuable chemicals and fuels is more viable than the sequestration process because it helps in mitigating CO_2 20-40 times higher (than sequestration) over a span of 20 years [8, 9]. However, thermo-catalytic conversion of CO_2 requires a cost-effective supply of H_2. Currently, H_2 is mainly produced via methane steam reforming, which is not a sustainable option. As an alternative, water could be used as a source of H_2. However, the reduction of water to H_2 itself requires energy. If this energy could be provided with a renewable source like wind, solar, tidal or hydro, then this will lead to a cost-

competitive pathway to reduce CO_2 emission by creating a closed carbon cycle [7]. Another issue related to this process is finding a suitable catalyst for the desired product. There are three main basic catalytic routes available for catalytic reduction of CO_2, including reduction of CO_2 to methanol, to CO, and to higher hydrocarbons using the Fisher-Tropsch process [10]. It is important to select a reducing pathway before selecting a highly suitable, active, and stable catalyst for that process.

Reduction of CO_2 to CO using renewable H_2 is of more importance because the syngas ($CO + H_2$) produced can be utilized for the production of either methanol or higher hydrocarbons. The process of reducing CO_2 to CO is known as the reverse water gas shift (RWGS) reaction that is an endothermic and equilibrium limited reaction. Therefore, there is a strong need to make an effort in developing a heterogeneous catalyst that can ensure fast kinetics and activity while having 100% selectivity towards the reduction of CO_2 to CO [10].

The main goal of this project is to develop a viable cerium oxide (CeO_2)-based heterogeneous catalyst prepared via a reverse micro-emulsion (RME) method for CO_2 reduction to CO via the RWGS reaction process with high activity, selectivity, and durability, as well as high resistance to deactivation and coking. To the best of the author's knowledge, no prior study reported in the literature investigated the deployment of the RME-based ceria for the application of the RWGS reaction.

1.2 Knowledge Gap

As mentioned earlier, the thermo-catalytic conversion of CO_2 to syngas is more advantageous because syngas is the basic building block for a variety of chemicals [7, 11, 12]. However, due to the lack of active, 100% CO selective, stable, and cost effective catalyst, the industrial applications of RWGS are hampered. One of the major drawbacks of this pathway is the thermodynamic stability of CO_2; without a catalyst, CO_2 molecule breaks at around 2400°C

[13]. Referring to industrial applications, it was revealed by the CAMERE process that there is a 20% higher obtained yield of methanol when CO_2 is first reduced to CO (via RWGS), rather than hydrogenating CO_2 directly to methanol [14]. Therefore, there is a strong need to find a catalyst that can help to overcome the thermodynamics barrier of CO_2 activation at relatively low temperatures, e.g., up to 600°C. The use of higher temperatures is unfavorable since it may cause fast catalyst deactivation via coking and sintering and reactor material (typically made from various kinds of stainless steel) degradation in a corrosive environment of the reaction mixture containing CO and H_2 [15-17].

For an industrial application of any catalyst, there are several parameters to be considered. The selection of an appropriate catalyst (for the selected reaction pathway) and the synthesis method are the first most essential parameters to be taken into consideration. After a comprehensive literature review conducted for this Ph.D. thesis, ceria (CeO_2) was selected as a candidate catalytic material because of its high reducibility and high selectivity towards the RWGS reaction. Only a few publications investigated the potential of the unsupported (bulk) ceria for the RWGS application [18-22]. These studies reported either low selectivity to CO generation or low CO_2 conversion to CO. Dai et al. reported the highest conversion (16% at 580°C) of CO_2 to CO (100% selectivity) over the bulk ceria produced via the hard template method [20]. With the aim to improve the catalytic performance of ceria, the reverse microemulsion method (RME) has been selected due to its ability to produce nano-sized catalysts with a high specific surface area [23-26]. To fill the knowledge gap of the application of CeO_2 for RWGS catalysis, the present work intended to investigate the properties and potential of the RME-synthesized ceria-based catalysts for the RWGS reaction application. The obtained results provide a new avenue for the application of ceria-based catalysts for the RWGS reaction.

1.3 Research Objectives

Main Goal:

The main goal of this project is to develop a highly active, selective, durable, and resistant (to deactivation and coking) ceria-based heterogeneous catalyst for the reduction of CO_2 to CO via the RWGS reaction at temperatures up to 600°C.

Catalysts synthesis and their application for RWGS were systematically studied and thoroughly discussed. A comprehensive characterization of the synthesized catalysts has been conducted using a variety of analytical techniques. The specific research objectives of the projects are outlined below.

Specific Objectives (RME stands for reverse micro-emulsion):

1) **Unsupported RME-ceria catalyst**

i) RME-based synthesis of a high surface area ceria (CeO_2) with higher reducibility to reduce CO_2 to CO via the RWGS reaction.

ii) Comprehensive characterization of the RME-ceria using analytical techniques and investigation of its application as a catalyst for the RWGS reaction.

2) **Alumina-supported ceria catalyst synthesized by the RME method**

i) RME-based synthesis of 20, 30, and 40 wt% $CeO_2/\gamma\text{-}Al_2O_3$

ii) Comprehensive characterization of the alumina-supported ceria catalysts using a variety of analytical techniques.

iii) Catalytic performance investigation to identify the optimal catalyst formulation (Ce loading)

RWGS is an endothermic, equilibrium-limited, and energy-intensive reaction. It requires the reduction of a highly stable CO_2 molecule to CO. Due to the high stability of CO_2, the

reaction is favorable at high temperatures only. Considering the socio-economical perspective, it is highly necessary to develop a catalyst that can help to conduct this highly energy intensive process at relatively low temperatures.

1.4 Thesis Layout

This thesis is a critical study towards a viable catalyst for the RWGS reaction. It is organized in eight chapters as follows:

Chapter 1 briefly introduces the thermo-catalytic RWGS reaction and related background and outlines specific objectives.

Chapter 2 is based on a critical literature review that gives a brief introduction to the global CO_2 emission data, different pathways for thermo-catalytic conversion of CO_2, complete review over RWGS reaction, possibly metallic, non-metallic catalyst, and supported catalysts utilized in the study of RWGS.

Chapter 3 describes the catalyst synthesis method, analytical techniques employed for catalyst characterization, and experimental system for catalytic performance evaluation. The catalytic performance experiments were performed in stainless steel reactors based on the initial blank experiments, confirming the non-catalytic behavior below 550°C. Chapter 7 outlined all the experiments in detail.

Chapter 4 provides an insight into the RWGS catalysis using the high specific surface area nano-ceria synthesized via the reverse micro-emulsion method (RME-ceria). This chapter also includes the investigation of a directly precipitated ceria (DP-ceria) for the purpose of a critical comparison of RME-ceria versus DP-ceria.

Chapter 5 deals with a detailed study on various ceria loadings in the γ-alumina supported ceria catalyst synthesized by the RME method for RWGS application, followed by a comprehensive characterization to identify the optimum loading.

Chapter 6 discusses the effect of the calcination temperature on the catalytic activity of the optimized RME-ceria supported on RME-alumina. This chapter also includes a mechanistic study using in-situ FTIR.

Chapter 7 investigates the coke formation in stainless steel reactors and metal degradation (metal dusting) of stainless steel at elevated temperatures (>550°C) under the conditions of the RWGS reaction.

Chapter 8 includes general conclusions, recommendations, and contributions to the research. Fig. 1.1 below shows the overview of this thesis as a block diagram.

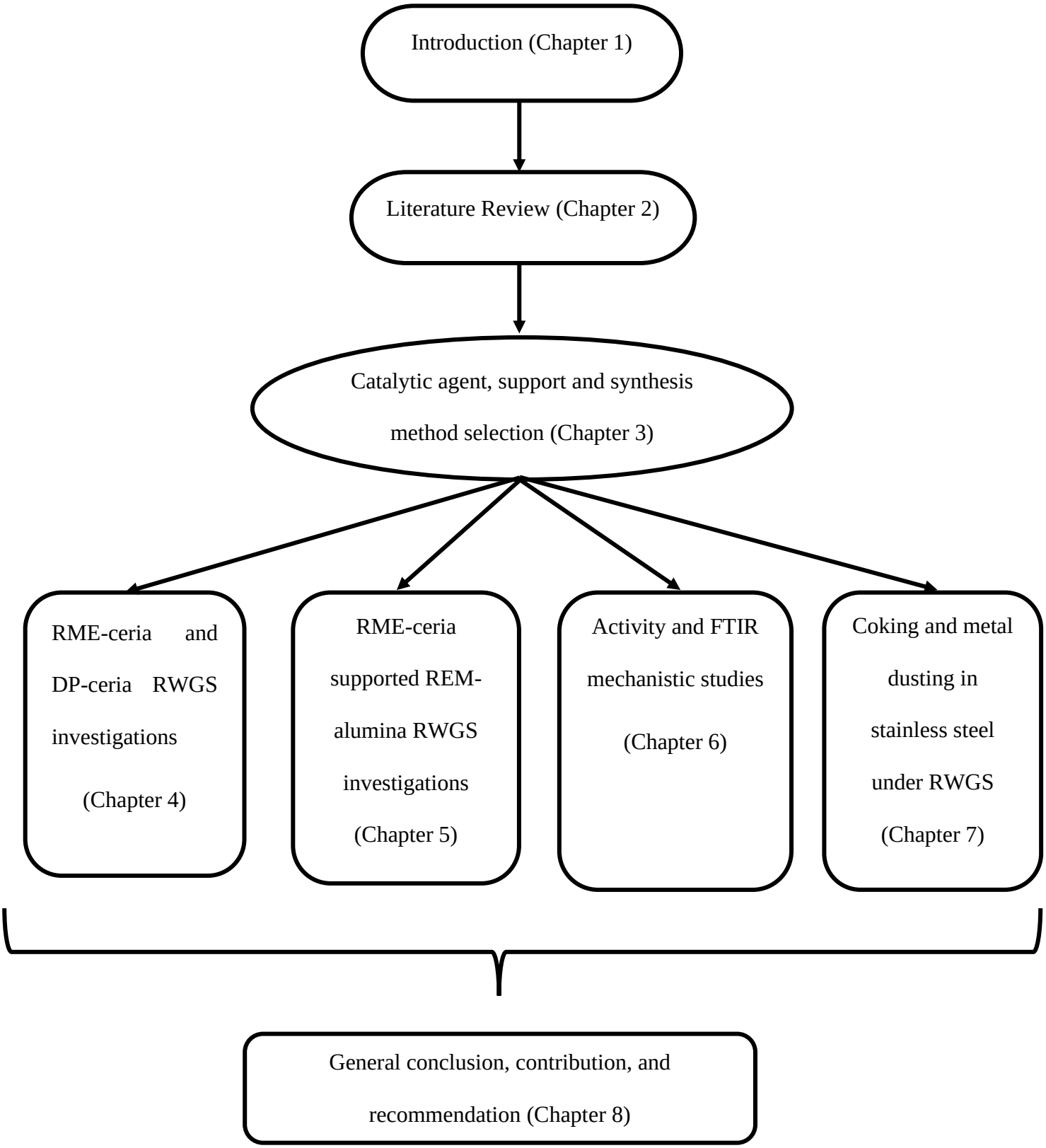

Figure 1.1: An overview of thesis structure.

Chapter 2

Literature Review

2.1 Global GHG's Emissions

Planet earth is getting warmer day by day because of the natural heat trapping ability of greenhouse gases. Carbon dioxide, methane, nitrous oxide, and fluorinated gases (F-gases) are the key greenhouse gases. According to the fifth assessment report of the Intergovernmental Panel on Climate Change (IPCC-AR5-2014), CO_2 is the major contributor towards total greenhouse emission globally with a leading percentage of 76%, while methane, nitrous oxide, and fluorinated gases contribution is 16%, 6.2%, and 2% respectively (Fig.2.1). It was reported that the global greenhouse gasses emission rate was +2.0%/year in 1970-80, +1.4% in 1980-90, +0.6% in 1990-2000, and +2.2% in the decade of 2000-10. The report also outlined that the global greenhouse gas emission raised from 27 Gt CO_2e (CO_2 equivalent) to 49 Gt CO_2e from 1970 to 2010, which is almost doubled [3].

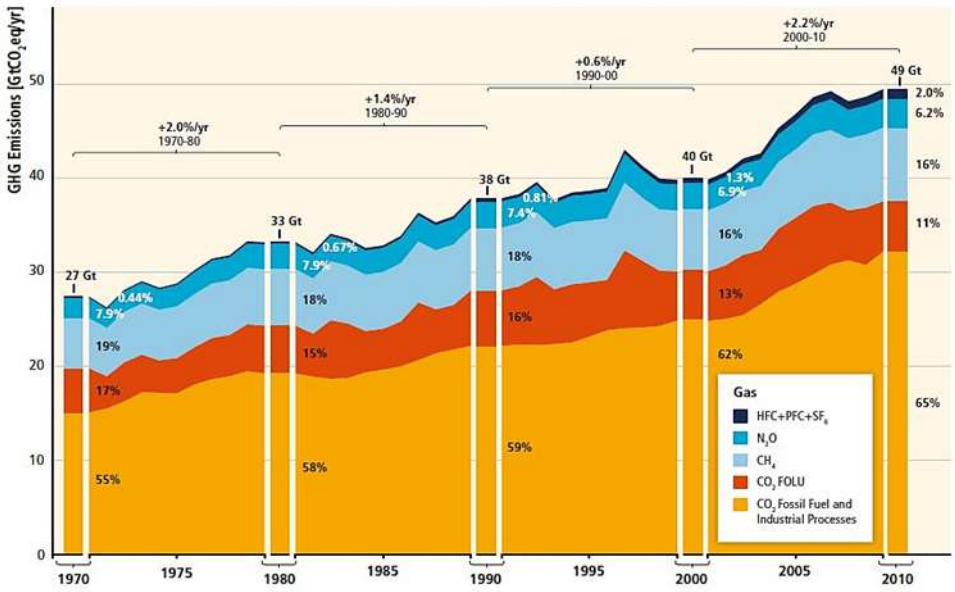

Figure 2.1: Total greenhouse gas emission presented in gigatons of CO_2 equivalent from 1970-2010 [3].

2.1.1 CO_2 Emission Sources

According to the report published by IPCC (climate change 2014: mitigation of climate change), anthropogenic CO_2 is the major greenhouse gas on the planet earth. CO_2 is accounted for 76% of all greenhouse gas emissions around the world through human activities [3]. Burning fossil fuels (oil, natural gas, and coal) for power generation and transportation is the major source of CO_2 emission worldwide. In 2017, CO_2 information analysis center (CDIAC) published the world's countries ranking based on the total CO_2 emission in 2014 by fossil fuels combustion, gas flaring, and cement production. In the list, China was placed on the top, while the United States and Canada were ranked second and tenth respectively [27]. Table (2.1) below is showing the list of the first 15 countries based on the 2014 data of total CO_2 emission expressed in thousand metric tons of carbon (TOT). Based on the total data available on the CDIAC website, a pie chart was made by the environmental protection agency (EPA) of the United States (Fig. 2.2) showing the contribution of countries towards CO_2 emission in terms of percentages [27, 28].

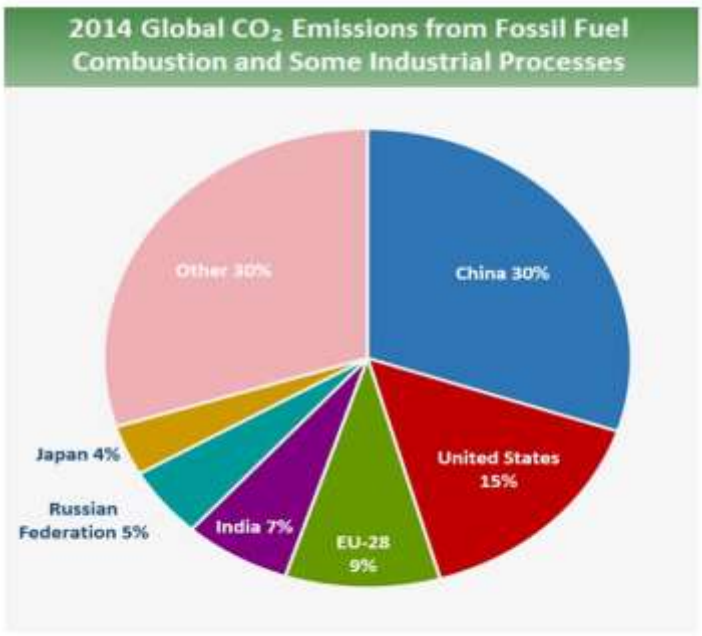

Figure 2.2: Global CO_2 emission from fossil fuels combustion and some industrial processes [28].

Table 2.1 World ranking based on total CO_2 emission measured in TOT (thousand metric tons) of carbon.

Rank	Nation	CO_2-TOT
1	China	2806634
2	United States	1432855
3	India	610411
4	Russian Federation	465052
5	Japan	331074
6	Germany	196314
7	Islamic Republic of Iran	177115
8	Saudi Arabia	163907
9	Republic of Korea	160119
10	Canada	146494
11	Brazil	144480
12	South Africa	133562
13	Mexico	130971
14	Indonesia	126582
15	United Kingdom	114486

Every year Environment and Climate Change Canada publishes its annual report titled "Facility greenhouse gas reporting program (GHGRP)" that maintains the data of GHG's emission since 2004 to date. Based on the recently published report in 2021, CO_2 accounted for 93% of the total GHG's emissions in Canada. Among all sources, stationary fuel combustion contributed to the 76% of the total emissions in Canada, as shown in Fig. 2.3.

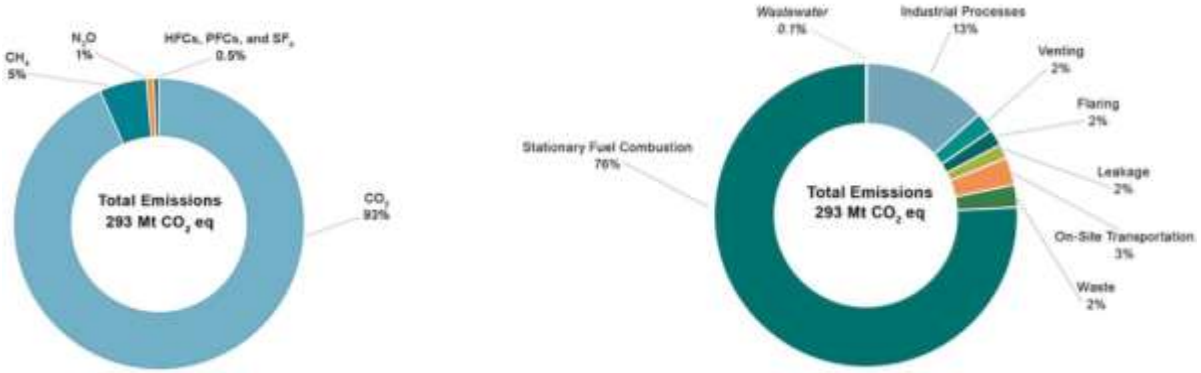

Figure 2.3: Total GHG's emission data for Canada in 2019 [29].

2.2 CO_2 Mitigation: Need and Technologies

CO_2 is present in the atmosphere since day one and is an essential part of Earth's carbon cycle. CO_2 produced from human activities (via food chain, industrial and power generation) and deforestation is disturbing the natural carbon cycle. Plants and natural forests are the main sources of atmospheric CO_2 removal via photosynthesis [7]. Due to the increasing demand for energy, the utilization of fossil fuels increased enormously. This enormous utilization of fossil fuels is disturbing the natural carbon cycle while adding extra CO_2 to the atmosphere. This extra CO_2 is acting as a heat trap, which leads to the rise in Earth's temperature. The global emission of CO_2 is increasing 2.2% per year, and now it's 81% above the 1970 level [3]. It was concluded in the fifth assessment of the intergovernmental panel on climate change (IPCC) published in 2017 that, to control the increase in global average temperature to 2°C by 2050, the CO_2 emission should be cut down to 50% of the present value [3]. Mitigation of this extra CO_2 is a major necessity of today's world. To mitigate climate change, anthropogenic CO_2 emissions can be controlled by the following three methods: (i) direct reduction in CO_2 emission, (ii) carbon capture and storage (CCS), and (iii) carbon capture and utilization (CCU).

2.2.1 Direct CO_2 Emission Reduction

The first route needs technological advancement in utilizing fossil fuels or the use of carbon free renewable energy resources. However, due to the rapid increase in the world population and high energy demand, it is difficult to follow this route. In 2019, world energy consumption demand increased by 1.3%. According to the BP statistical review of world energy, published in June 2020, oil and natural gas are the major sources to fulfill the world's energy demand. They accounted for about 70% of energy demand in America and Africa, about 64% in Europe & Eurasia, and about 98% in the Middle East. While in Asia, coal is the dominating fuel accounted for about 48% of regional energy consumption. The analysis clearly shows that none of the region (even the highly developed region like North America) is relying on renewable sources. For example, in North, South, and Central America, the renewable sources are not accounted for more than 10% of total need. Details are available in Fig. 2.4 [30].

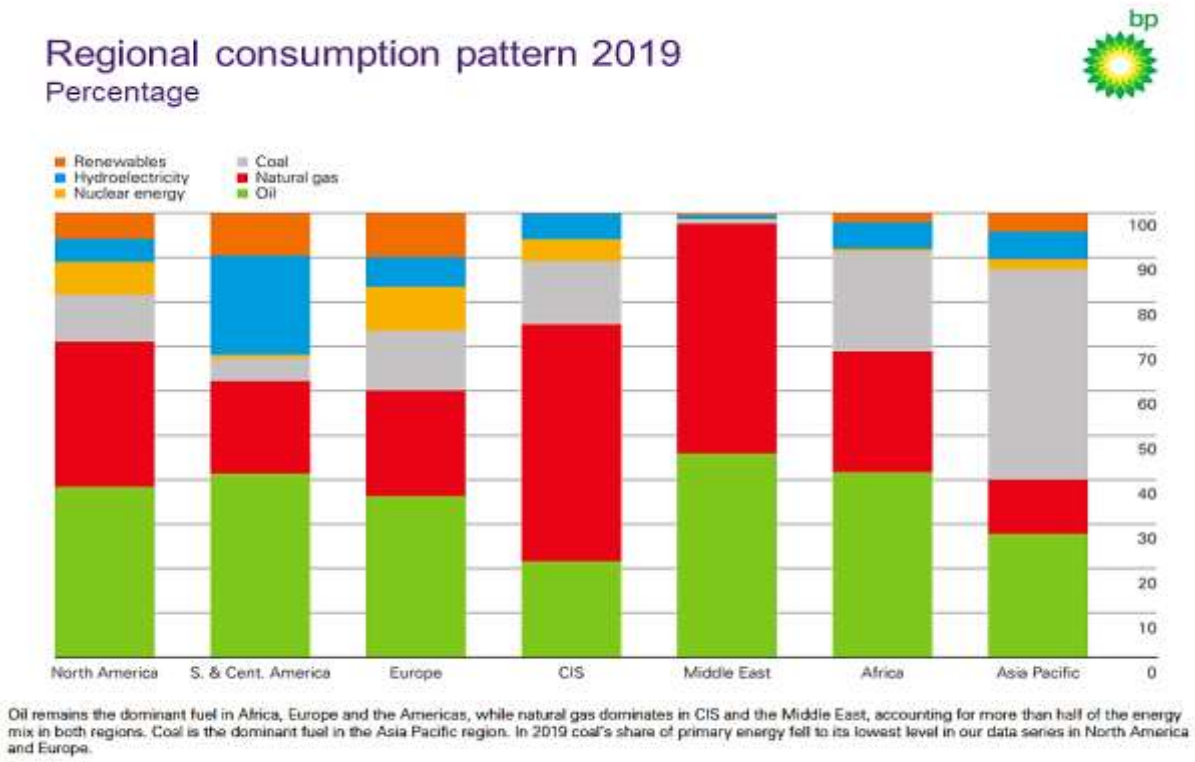

Figure 2.4: World's energy consumption by region [30].

2.2.2 Carbon Capture and Storage (CCS)

Another technology that could help to meet the climate change mitigation targets is carbon capture and storage (CCS). CCS is based on separating CO_2 from the flue gases and storing it in underground geological locations. CCS is a mature technology but still needs to overcome some technical and economic challenges for its large-scale arrangement. One of the main drawbacks of this technology is the requirement of large capital with zero profit [31]. On the other hand, CCS has some serious technical concerns, including CO_2 leakage rates (due to engineering factors or natural factors like earthquakes) and underground storage capacity. In some countries, the storage is only available offshore, which makes the process highly uneconomical due to extra transportation cost. UK, Norway, Singapore, Brazil, and India are facing this issue [31, 32].

2.2.3 Carbon Capture and Utilization (CCU)

The third route in this technological sequence is carbon capture and utilization (CCU). In the recent decade, CCU received enormous attention because it can convert extra atmospheric anthropogenic CO_2 to valuable chemicals and fuels, which could help in climate mitigation while creating an artificial carbon cycle. This gives CCU a major economic advantage over CCS because the product can be sold [31]. Instead of considering CO_2 as a pollutant and sequestering it to undergrounds, it can be considered as an abundant source of carbon to produce fuels and valuable chemicals (e.g., methanol, urea). Due to the thermodynamic properties (discussed below) of CO_2, its conversion to chemicals and fuels is energy-intensive, but on the other hand, it can be taken as a renewable source of carbon, non-toxic, and cheaply available in abundant amounts for low cost [33]. Therefore, energy-efficient implementation of CCU has a dual benefit over CCS (i.e., technical as well as economical). Technically, it will create an artificial carbon life cycle to help climate change, and on the other hand, the products

will be sold to generate revenue and can help to replace fossil fuels. Currently, urea, salicylic acid, methanol, and some cyclic organic carbonates are being produced on a large scale from CO_2, while the process of CO_2 conversion to other chemicals on a large scale still needs to be developed. The conversion of CO_2 to valuable chemicals will be helpful in offsetting the capturing cost [34].

A number of techniques have been developed for the utilization of CO_2 in recent decades, for example, direct make use of CO_2, increasing oil recovery from depleted oil wells, and used as an energy storage fluid in the geothermal process. All these technologies are still in their development phase. Norhasyima et al. [35] shortlisted 5 technologies for potential utilization of CO_2 for CCU application (Fig. 2.5). Considering the economic viability and materialization of CCU, they applied a minimum limit of 5 MTPA (million metric tons per annum) of CO_2 utilization.

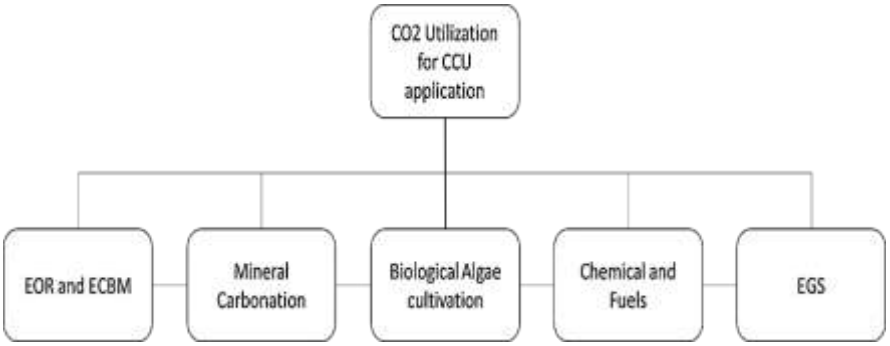

Figure 2.5: CO_2 utilization technologies for CCU application [35].

The advantages and the major challenges that should be dealt with before the deployment of the above mentioned technology are tabulated below (Table 2.2) [35]. CO_2 is a non-toxicinert gas, but a higher concentration could lead to severe environmental impacts and can cause death as well [35]. Environmental and health impacts of CCU technologies are not studied well yet due to the under-development phase of the technologies, but it needs severe attention. Among

all the above technologies, EOR (enhanced oil recovery) and ECBM (enhanced coal-bed methane) are mature technologies as many industries in the US have been inserting CO_2 into underground locations for many years [36]. Though, the environmental pollution created by the process itself and the chances of CO_2 leakage and its migration back to the atmosphere from underground locations need to be assessed from time to time [36]. There is a clear uncertainty related to long-term storage of CO_2 because of the possibility of CO_2 leakage from the injection well and cap rock failure [37, 38]. According to projection studies, it has been reported that there will be a 10% reversal of injected CO_2 back to the environment for the EOR current projects. Drilling during the construction of geothermal wells and leakage of CO_2 during storage are the potential environmental effects caused by EGS (enhanced geothermal system) process [39]. Finally, a measuring, monitoring, and verification study is necessary for EOR, ECBM, and EGS processes to make sure there will be no leakage of CO_2 from the underground geological locations in the long term.

Microalgae cultivation is an attractive source to recover various compounds from waste water like heavy metals, oil/grease, organic and aromatic compounds, and pharmaceuticals waste. However, they create severe environmental impacts because of the toxic by-products produced during the biological actions [40]. Furthermore, large-scale uncontrolled cultivation could lead to blooms, disease, or pests leading to population crashes and spills of cultured algae into natural ecosystems [41, 42]. Mineral carbonation has the advantage over EOR, ECBM, EGS, and microalgae processes because there are no harmful by-products produce, and there is no CO_2 emission because of leakage. However, there several other effects that may lead to soil, air, and water pollution, like mining of rocks, ore preparations, and waste disposal [43, 44]. Finally, chemical and fuels (CAF) manufacturing technology have clear advantage over all CCU techniques because CAF directly converts CO_2 to valuable chemicals and fuels [45, 46].

Table 2.2: CCU technologies advantages and challenges [35].

CO_2 Utilization Technology	**Advantages**	**Challenges**
EOR and ECBM	▪ Developed technology ▪ Imperishable storage ▪ Large CO_2 sequestration potential plus recovered oil and gas can offset the cost of CO_2 capture	• More CO_2 addition to the atmosphere because of more fossil fuels utilization • Long commercialization time • Low CH_4 cost • CO_2 transportation cost • Location specific
Mineral Carbonation	• Raw material abundance (Mineral or waste) • Free chemicals • No prior CO_2 separation required • No requirement for CO_2 feed quality	• High energy-intensive • Large amount of chemicals required • High mineral and processing cost
Biological algae cultivation	• Competitive biofuel source • Permanent CO_2 storage • Efficient in low CO_2 concentration • Not location specific	• pH and Impurities sensitive Drying and growth controlling cost • Permanent sun light and large area required • High energy cost to construct photobioreactors • Slow and inefficient process
Chemicals and Fuels	• can replace conventional fossil fuels for transportation and other uses	• Inefficient process • Requires renewable source of energy
EGS	• Good thermodynamic properties ensuring larger flow rates, reduction in circulating pumping power requirements, higher power output, and efficiency increase • Offsetting cost of drilling deep wells for EGS by CO_2 storage • Reduce water use	• Location Specific • CO_2 leakage from the reservoir • High cost for access to CO_2, the proximity of the EGS relative to the electricity grid, and access to cooling water supply

Conversion of CO_2 to synthetic fuels has dual advantages as compared to other routes: one is direct CO_2 emission reduction, and the second is creating an artificial carbon cycle to store CO_2 in terms of synthetic fuels and other valuable chemicals. This route seems to be more attractive because it can reduce GHGs along with the production of some valuable synthetic fuel, which will eventually lead to reducing the consumption of natural fossil fuels by creating an artificial carbon cycle. There are several approaches available to convert CO_2 to chemicals and fuels through photo and electrochemical reduction, biological reduction, and thermo-catalytic reduction using renewable hydrogen (Fig.2.6) [11].

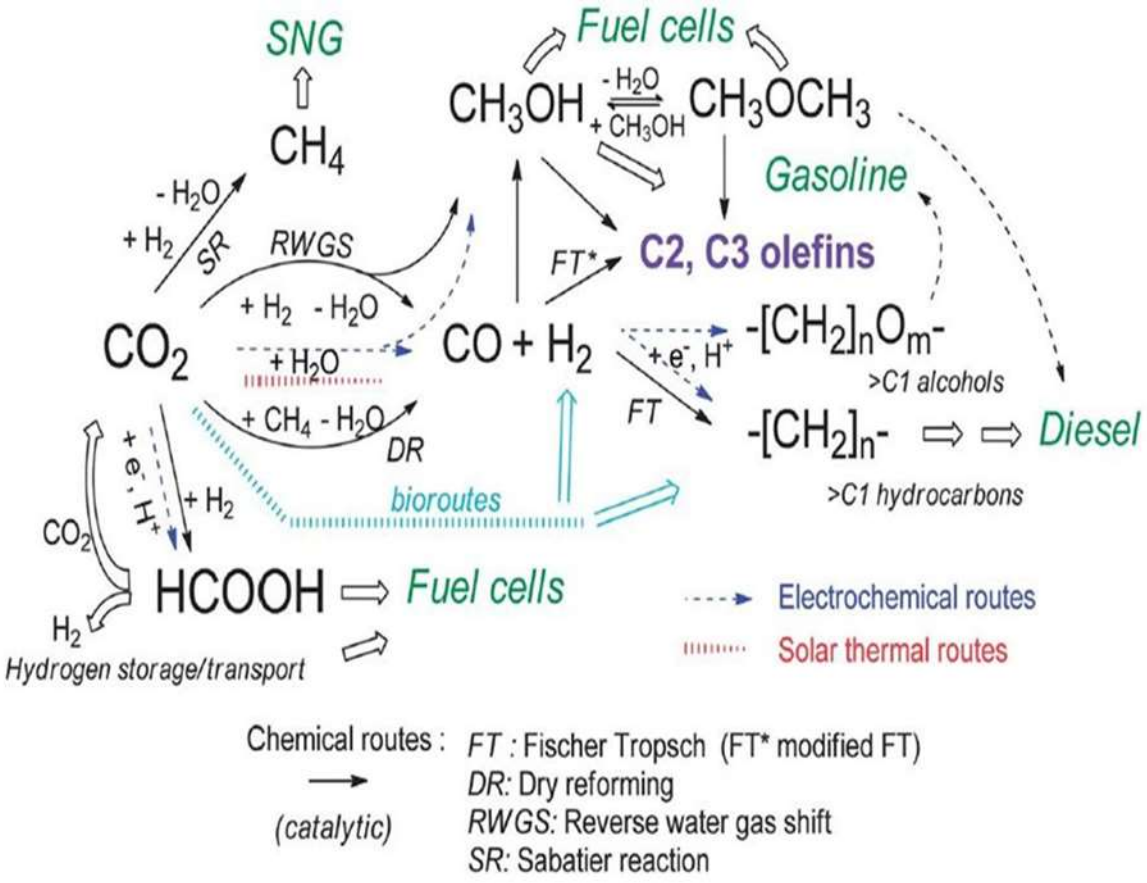

Figure 2.6: Pathways to convert CO_2 to chemicals and fuels [11].

Photo-electrochemical and biological reduction routes are viable but have major limitations like low CO_2 solubility and cost of cultivating a large biological system, respectively [7]. Therefore, thermo-catalytic conversion of CO_2 to synthetic fuels using renewable energy sources could be a better viable option. The catalytic conversion of CO_2 to valuable chemicals and fuel is more viable because it helps in mitigating CO_2 20-40 times higher than the sequestration process over a span of 20 years [8, 9]. This route seems to be more attractive because it can reduce GHGs along with the production of some valuable synthetic fuels that will eventually lead to reducing the consumption of natural fossil fuels by creating an artificial carbon cycle.

2.3 Thermo-Catalytic Conversion of CO_2

CO_2 is a non-polar stable molecule ($\Delta_f G_{298k} = -396\ kJ\ mol^{-1}$) at standard conditions and requires high activation energy to utilize it as a raw material in any industrial process [47, 48]. Therefore, large energy input is required for the CO_2 molecule activation and transformation. This barrier of high activation energy could be reduced by using homogeneous or heterogeneous catalysts [49-51]. Lewis's structure of CO_2 shows that the central carbon is electrophilic, and oxygen atoms show weak Lewis basicity. The reaction of CO_2 could be dominated by electron-donating reagents (nucleophiles). Carbamic and carbonic acids can easily be produced by the reaction of CO_2 with alkoxide, water, and amine. On the other hand, CO_2 molecules can also be activated with the help of nucleophilic centers on solid surfaces [8]. Therefore, there is a strong need to find out a catalyst that can help in overcoming the thermodynamic barrier of CO_2 activation.

2.3.1 Reaction Pathways for Catalytic Conversion of CO_2

CO_2 conversion processes can be divided into two groups: the first one is non-reductive conversion (A+B) to higher carbon organic chemicals in which carbon have an oxidation state

of +3 or +4; the second one is the reductive conversion to low-carbon chemicals and fuels in which carbon retain oxidation state of +2 or lower [52]. Fig. 2.7 shows the possible routes below [52-54]. The most important step in these routes is the catalytic conversion path. Only certain reaction pathways that contribute to the development of high demand chemicals should be followed, e.g., organic chemicals account for about 4% of emissions, while fossil fuel combustion in power plants accounts for about 90% of emissions [55]. Therefore, reductive conversion of CO_2 via hydrogen is selected for further studies.

Several pathways available for the thermo-catalytic reduction of CO_2 to valuable chemicals and fuels using renewable hydrogen are shown in Fig. 2.8 [12]. The most important factor in the implementation of these routes is the availability of cheap renewable hydrogen (r-H_2). It can be obtained via coal and biomass gasification or through water electrolysis using hydroelectricity in off-peak hours. CO_2 is a low energy molecule while H_2 is a high energy molecule; hence the conversion of CO_2 to fuels and chemicals via H_2 reduction will be a viable option for renewable energy storage into chemicals for long-term use. Therefore, much attention has n given to CO_2 hydrogenation [12].

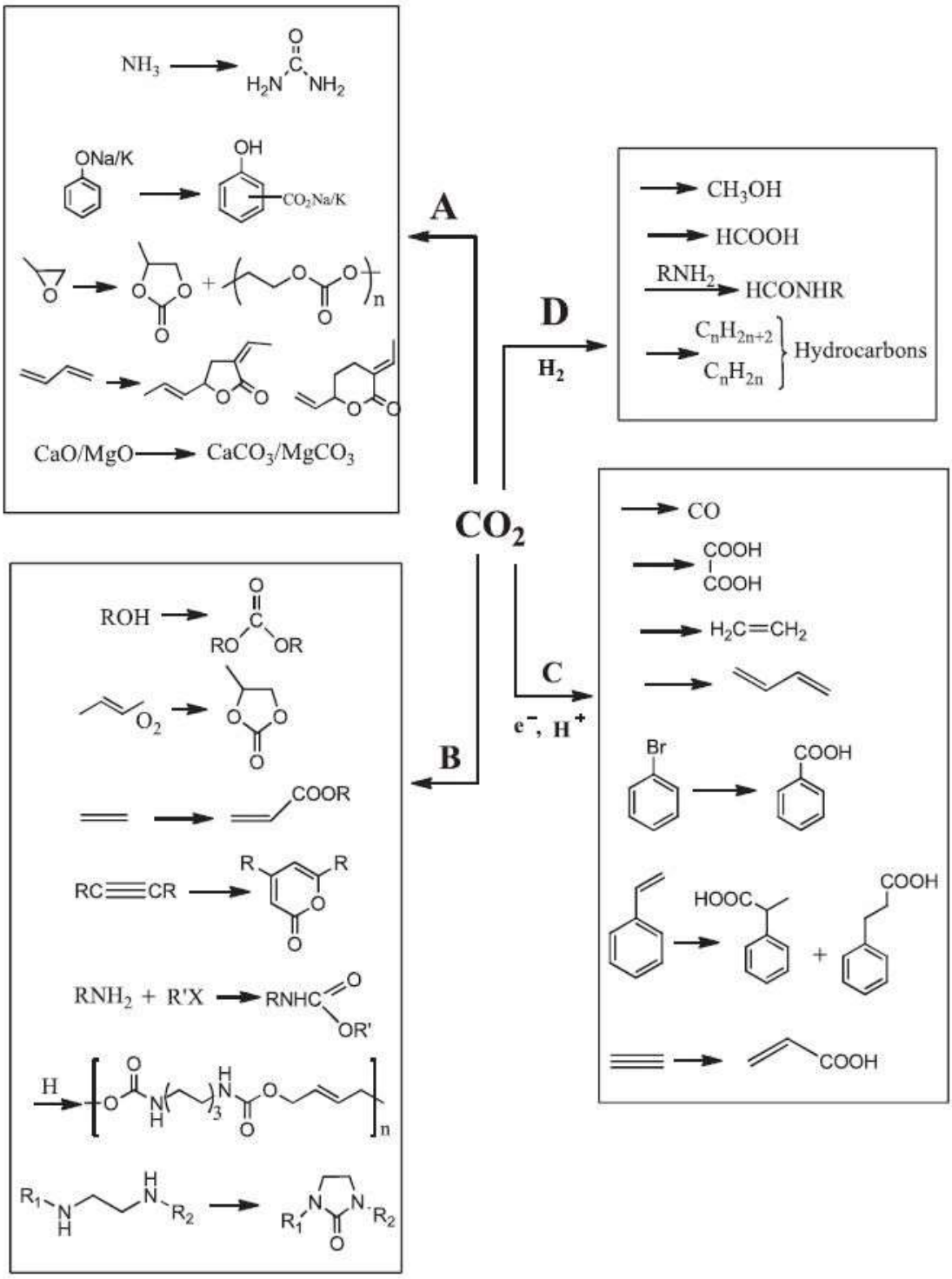

Figure 2.7: Chemical products that can be obtain from CO_2 via non-reductive routes (A+B); and reductive routes (electro-reduction(C) and hydrogenation (D)) [52].

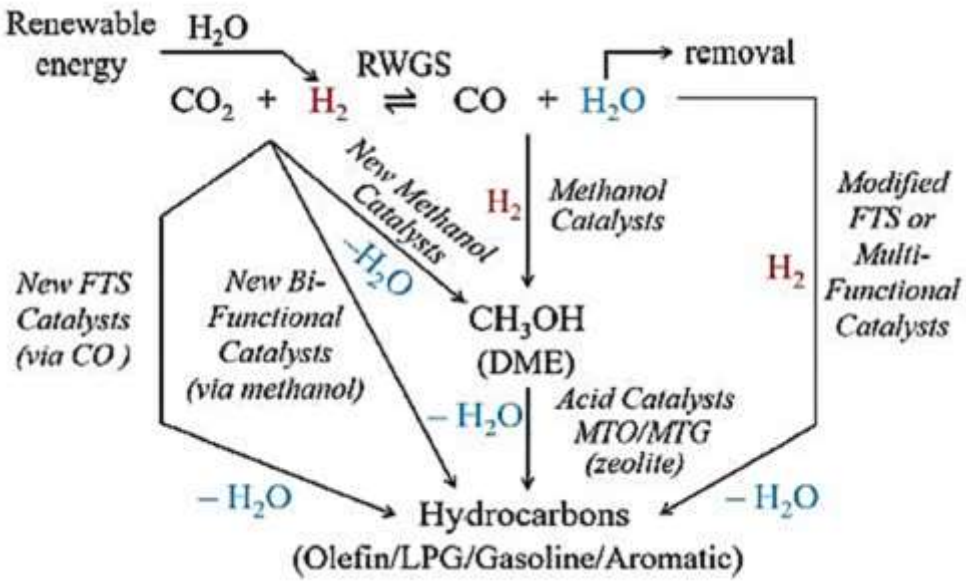

Figure 2.8: Different possible routes to produce different hydrocarbons through CO_2 hydrogenation [12].

Fig. 2.8 shows the ultimate products that can be obtained through thermo-catalytic hydrogenation of CO_2 are CO, methanol, and higher hydrocarbons via Fischer-Tropsch (olefins, LPG, gasoline, and aromatics). Therefore, it is important to select a reducing pathway before finding a highly suitable, active, and stable catalyst for that process. Reduction of CO_2 to CO using renewable H_2 is of more importance because the CO produced can be utilized in either way that is to produce methanol or higher hydrocarbons. The process of reducing CO_2 to CO is known as the reverse water gas shift reaction (RWGS). Thermodynamically direct conversion of CO_2 to methanol is more favorable. However, it was revealed by the CAMERE process that there is 20% higher yield of methanol obtained when CO_2 is first reduced to CO (via RWGS) and then CO to methanol, rather than hydrogenating CO_2 directly to methanol [14]. The RWGS reaction is an endothermic equilibrium limited reaction favorable at high temperatures (<700°C) [55, 56]. Therefore, there is a strong need to puteffort into developing

a heterogeneous catalyst that can ensure fast kinetic activity with almost 100% selectivity towards the reduction of CO_2 to CO.

2.4 Reverse Water Gas Shift (RWGS)

The RWGS is a reverse reaction to water gas shift (WGS). The water gas shift reaction (eq.1) was originally developed to increase the production of H_2 during the synthesis process of ammonia production.

$$CO + H_2O \rightleftharpoons CO_2 + H_2 \qquad (1)$$

For the catalytic hydrogenation of CO_2, the RWGS is considered as the key reaction because the CO produced can be utilized in either way to produce methanol or higher hydrocarbons. It's an endothermic process with a free-energy change and enthalpy change of $\Delta G_{298\,K} = 28.6\ kJ/mol$ and $\Delta H_{298\,K} = 41.2\ kJ/mol$ (STP):

$$CO_2 + H_2 \rightleftharpoons CO + H_2O \qquad (2)$$

This reaction is recognized over a century, but still there is a need to find out or to prepare an improved catalyst that can help to overcome the thermodynamic barriers. Due to the endothermic nature of the reaction, it requires high temperature, and also the reaction is equilibrium limited [10]. Equilibrium can be shifted towards the right by following two methods: (i) increase the input concentration of either reactant (CO_2 or H_2) to completely consume the other one (while recycling of the excess) (ii) continuous removal of the water vapor from the reactor. The latter can be implemented with the help of a desiccator bed or by using hydrophilic membranes that should be only selective towards water. There are a number of publications available on membrane application in the Fischer-Tropsch (FT) process [57, 58]. Kazumasa et al. [59] reported that at 1000 K, equilibrium conversion increased up to 30% when H_2:CO_2 is increased from 1 to 1.8. Another study showed that the activation energy of the RWGS reaction decrease from 75 to 51 kcal/mol at high temperature and pressure [60].

As mentioned above, the RWGS reaction is the first step in producing fuels by CO_2 hydrogenation. In Japan, RITE, in collaboration with NIMC, ONRI, and NIRE, has proposed a process concept for CO_2 recycle composed of four key technologies: CO_2 separation and liquefaction process, methanol synthesis process, water electrolysis for hydrogen production and supply process, and transportation process [61, 62]. The key technologies are those for membrane separation of CO_2 emitted from stationary sources, for H_2 production by water electrolysis using electric power derived from non-fossil energy, and for methanol synthesis by the catalytic hydrogenation of CO_2. A similar project is also running in the UK [63].

2.4.1 RWGS Side Reactions and Thermodynamics

Thermodynamics studies show that there are two possible side reactions that can occur along with the RWGS at low temperatures. These are methanation reaction ($\Delta H_{298\,K} = -206.5\ kJ/mol$; eq.3),

$$CO + 3H_2 \rightleftharpoons CH_4 + H_2O \qquad (3)$$

and Sabatier reaction ($\Delta H_{298\,K} = -165.0\ kJ/mol$; eq.4),

$$CO_2 + 4H_2 \rightleftharpoons CH_4 + 2H_2O \qquad (4)$$

Thermodynamic studies revealed that at atmospheric pressure, the conversion of CO_2 increases by increasing the H_2:CO_2 ratio and temperature [59, 64] as shown in Fig 2.9 [55]. Fig. 2.9 is representing the equilibrium composition of the reactant and product gases for the temperature range of 100-1000°C at a H_2:CO_2 ratio of 3. It can be easily seen that at low temperature (below 600°C), the Sabatier reaction is favorable, while above 700°C, the RWGS reaction is favorable as the only product above this temperature is CO. However, keeping the capital cost and energy losses in mind the reaction temperature should be kept as low as possible.

Apart from temperature control, continuous removal of the products can also shift the equilibrium towards the right. The Researcher from NASA and the Florida Institute of Technology has achieved 100% CO_2 conversion in a membrane based reactor without a catalyst, which is 5 times higher than the equilibrium conversion. The operating conditions were 35 to 60 bar pressure and 378-380°C temperature [65, 66]. The semipermeable membrane helps the continuous removal of the product. Vander Wiel et al. showed that to attain higher CO selectivity for the RWGS, the reaction should run at low residence times (5 to 64 ms) [65].

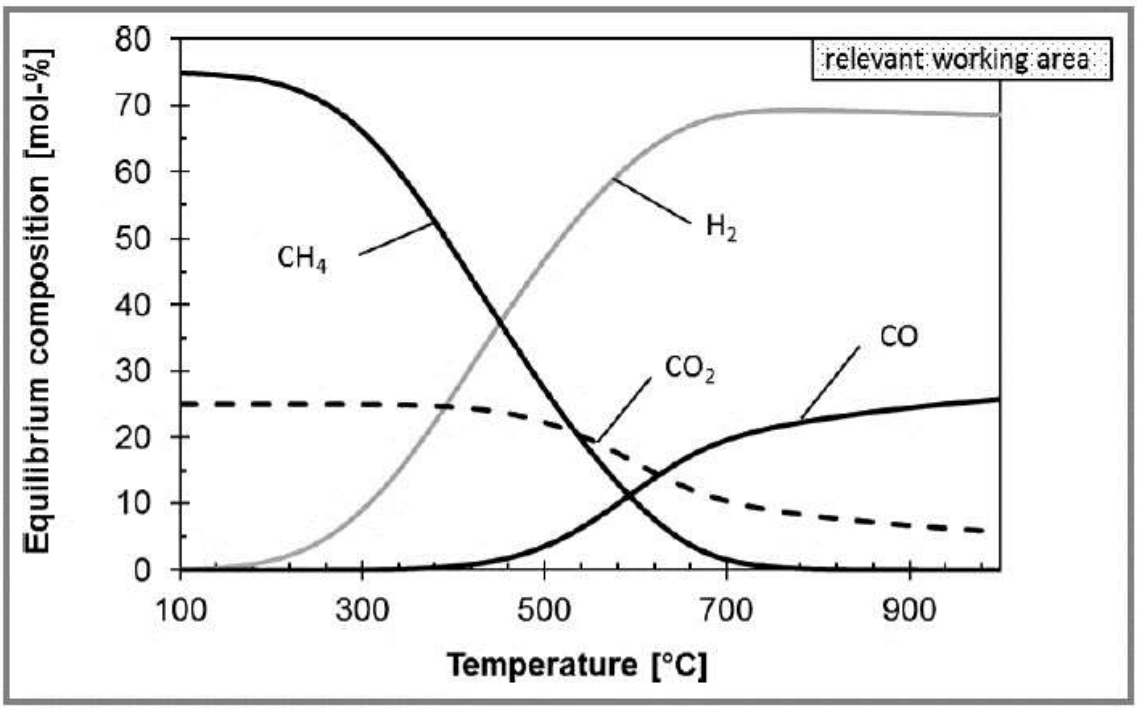

Figure 2.9: Thermodynamic equilibrium composition of RWGS reaction product gas at 1 bar and H_2:CO_2 ratio of 3 [55].

2.4.2 Rationale for RWGS Catalysis and Advantages

RWGS reaction was first observed in 1914 when two researchers Bosch and Wild were attempting to produce H_2 over an iron oxide catalyst using steam and CO [67]. Presently, the

RWGS reaction is the key step in producing a variety of chemicals, especially methanol. According to the investigative studies of Mallapragada et al. [68], the production of fuels with the FTS processes, using CO and H_2 as raw materials, can be deployed with greater efficiency when the CO is produced via RWGS from the CO_2 captured from flue gas or atmosphere. The RWGS reaction also has a great potential for space exploration because more than 95% of Mars's atmosphere contains CO_2. Consequently, the RWGS is an important reaction with potential end-user products [65, 66].

Any process that generates CO still needs 2 mole H_2 to convert CO to chemicals and fuels. Additional 1 mole H_2 for converting CO_2 to CO just increases the amount required from H_2 generation processes by 50%, not substantiating their existence in the overall process. In the future, the RWGS may be useful in space exploration because, in space technology, the synthetic air is produced by water electrolysis that generates pure hydrogen [56].

Considering the versatility of the RWGS reaction, it is necessary to develop highly active, selective, and stable catalysts that can help to run this reaction at low temperatures (up to 600°C) with 100% CO selectivity. Before reviewing already deployed catalyst for reverse water gas shift, it is necessary to look into the thermodynamic properties of CO_2.

2.5 Carbon Dioxide Thermodynamics

CO_2 is a well-known stable molecule ($\Delta_f G_{298k} = -394.4\ kJ\ mol^{-1}$). From the thermodynamic viewpoint, conversion of CO_2 will need energy that depends upon the reduction of the oxidation state of carbon from +4 in CO_2 to the targeted chemical substance. A plot of ΔG_f° of CO_2 versus oxidation state of carbon shown below. Fig. 2.10 can be taken as a key step in understanding the thermodynamics of possible conversion of CO_2 [54].

The thermodynamic data in Fig. 2.10 clearly shows that any conversion of CO_2 to a chemical substance that leads to reduce the O/C ratio or increase the H/C ratio (from zero)

needs energy, and the process will be endergonic. On the other hand, the reaction will be exergonic if CO_2 remains in its +4-oxidation state with varying O/C ratio in the derived product, for example, urea, carbamates, carbonates [53]. Thermodynamically the conversion of CO_2 is not favorable because of the existence of carbon in its most oxidized state +4 [69]. Consequently, this stability of CO_2 is a major resistance towards the establishment of industrial processes for its conversion to valuable chemicals and fuels. Thermodynamically any chemical reaction requires a difference in Gibbs free energy of reactant and products to happen (depending upon the conditions). This difference is well explained by the Gibbs-Helmholtz relationship (eq. 5).

$$\Delta G^{\circ} = \Delta H^{\circ} - T\Delta S^{\circ} \quad (5)$$

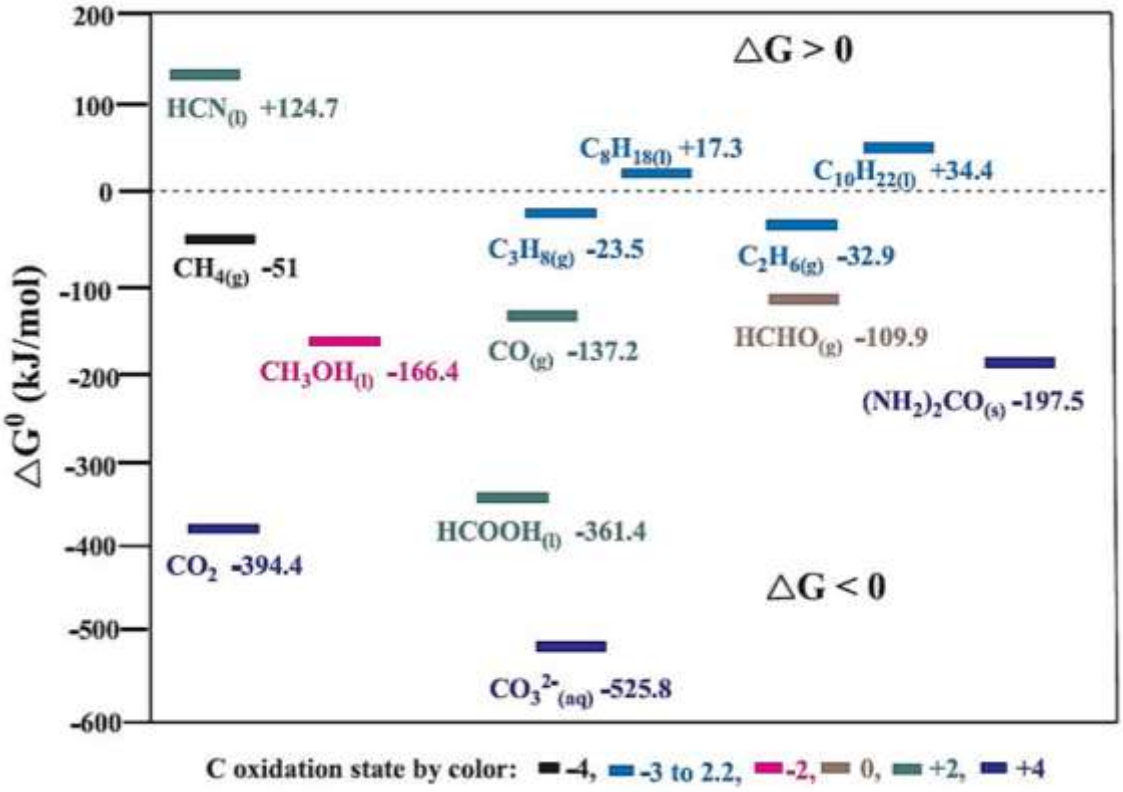

Figure 2.10: Gibbs free energy of some carbon species [54].

Most CO_2 conversion processes are non-spontaneous, having positive Gibbs free energy change at standard conditions ($\Delta G^\circ > 0$). Therefore, the final stability of the product produced while using CO_2 as a feedstock should be considered. In most cases, both terms (ΔH° and ΔS°) of Gibbs energy are not in favor of CO_2 conversion to other chemicals. The $C - O$ bond energy in CO_2 (a triatomic molecule) is 803 kJ/mol, which is almost doubled the bond energy of $O - H$ in a similar molecule like H_2O [70]. This shows that there is a significant amount of energy needed for the reduction of CO_2. Furthermore, to calculate the equilibrium constant at the reaction temperature, a relationship between Gibbs energy and temperature is required (eq. 6). This relationship can also be given by Van't Hoff equation (eq. 7), while p is showing constant pressure [54].

$$\Delta G^\circ = -RT ln K_f^\circ \qquad (6)$$

$$\left(\frac{d \ln K_f^\circ}{dT}\right)_p = \frac{\Delta H^\circ}{RT^2} \qquad (7)$$

For CO_2 conversion, the equilibrium constant as well as reaction heat can be calculated, while equilibrium conversion can be increased by increasing pressure [71]. However, change in temperature sometimes increase or decrease the rate of equilibrium conversion; for example, for the conversion of CO_2 to methane, ethylene, methanol, and ethanol, the increasing temperature can slow down equilibrium conversion while for HCHO and HCOOH the effect is opposite, i.e., speed up [71]. Consequently, a higher temperature is not always favorable. Regrettably, many CO_2 conversions have slow kinetics. Hence, to utilize CO_2 as a feedstock to produce valuable chemicals or fuels at favorable conditions, there is a strong need to develop an active catalysts.

2.6 Reverse Water Gas Shift Catalysts

In recent decades, several research studies have been published mainly focus on the conversion of CO_2 to CO over heterogeneous catalysts. Researchers are struggling hard to develop a highly active and selective catalyst that can help to derive this high energy-intensive endergonic reaction (RWGS) at a lower temperature with a higher conversion rate of CO_2 to CO and with maximum selectivity. A catalytic reaction requires the simultaneous occurrence of adsorption and desorption of reactant and product over the catalyst surface. Therefore, the selection of support material or metal promoter needs to be addressed keenly. Initially, precious metal catalysts were deployed for RWGS and showed promising results, but in recent decades transition metal catalysts have been found to show high activities towards H_2 and CO_2 dissociation, which makes them of considerable interest for researchers because of their low cost as compared to precious metals like (Pt and Pd).

To overcome the side reaction and enhance the RWGS selectivity towards CO, different mixed metal oxides along with precious metals and transition metal carbides (TMCs) have been utilized. The following table (2.3) is giving a comprehensive review (to the best of author's knowledge and research) of the catalysts that have been deployed specifically for the thermo-catalytic RWGS reaction application since 1989 till date. Table (2.3) is divided into 7 columns showing reported year, catalysts, reaction temperature, pressure, H_2/CO_2 ratio in the inlet feed, CO_2 conversion, and CO selectivity of the catalyst.

2.6.1 Supported Metal Catalysts

A solid catalyst mainly consist of three components: 1) catalytic agent, 2) support (usually porous), and 3) promoter and inhibitor [72]. In catalysis, the active ingredient of catalytic material plays the most important role towards the final product. As discussed before, there are several pathways available for the catalytic conversion of CO_2 depending upon the targeted

final product. The RWGS reaction is under study since 1914 [67]. Many different supported or unsupported catalysts based on noble metals, non-noble metals, and transition metal carbides have been deployed to study their potential towards the RWGS reaction. A comprehensive overview of the above-mentioned categories of catalysts is provided below.

2.6.1.1 Noble Metal Catalysts

In chemistry, the metallic elements that show high resistance towards corrosion and oxidation in moist air are known as noble metals. They are mainly comprising of platinum (Pt), palladium (Pd), ruthenium (Ru), rhodium (Rh), osmium (Os), iridium (Ir), gold (Au), and silver (Ag). It has been found that the partially filled outermost D-shell of noble metals allows them to easily adsorb reactants and lead them to form active intermediate compounds [73]. These special abilities of noble metals made them become a major class of catalysts for CO_2 reduction.

Chen et al. [74] studied the performance of Pt/TiO_2 catalyst towards the RWGS reaction. They found that the Pt particle size and reaction conditions highly affect the selectivity of the catalyst towards CO or CH_4. In-situ FTIR studies showed that in the presence of reactant gases (CO_2, H_2), TiO_2 reduces and forms an active site at the interface with Pt as Pt-Ov-Ti^{3+} and this active site is responsible for the reduction of CO_2 to CO. On the other hand, large Pt particles at high temperatures facilitate the further hydrogenation of CO to form CH_4, as shown in Fig. 2.11. Kattle et al. [75] also showed that the bonding energy of CO at the interface site of Pt/TiO_2 catalyst facilitates the further hydrogenation of CO to form CH_4. Porosoff et al. [76] studied the effect of secondary metal (Ni, Co, etc.) along with Pt over CeO_2 and γ-Al_2O_3 supports. They identified that there was a significant amount of CH_4 formed over $PtNi/CeO_2$ and PtNi/γ-Al_2O_3 bimetallic catalyst while $PtCo/CeO_2$ and PtCo/γ-Al_2O_3 were highly selective towards CO with a CO/CH_4 ratio of 259.4 and 245.8 respectively. Apart from reducible supports (CeO_2, TiO_2, etc.), irreducible supports (such as SiO_2, Al_2O_3, zeolites, etc.) along with Pt shows promising results for RWGS [76, 77]. Zhang et al. [78] and Ro et al. [79] showed that the

addition of second reducible support, i.e., Fe_2O_3 and MoO_x, considerably increases the reaction activity while decreasing the activation energy. Yang et al. [80] also studied the promoting effect of K (potassium) for RWGS reaction pathways and activity over Pt-supported L-zeolite catalyst. They found that both activity and selectivity of RWGS increases by the controlled addition of potassium to Pt/L catalyst, as shown in Fig. 2.12. With the help of *in-situ* DRIFT and micro-calorimetry techniques, Pt-O(OH)-K was found to be the leading active site. The electronic density of this active site facilitates the formation of CO through the formate intermediate.

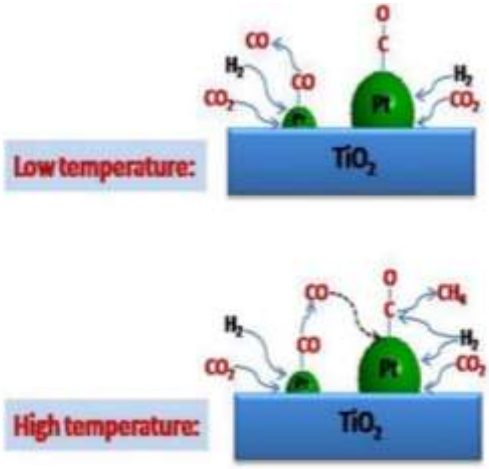

Figure 2.11: CO_2 hydrogenation over Pt/TiO_2 catalyst at low and high temperature.

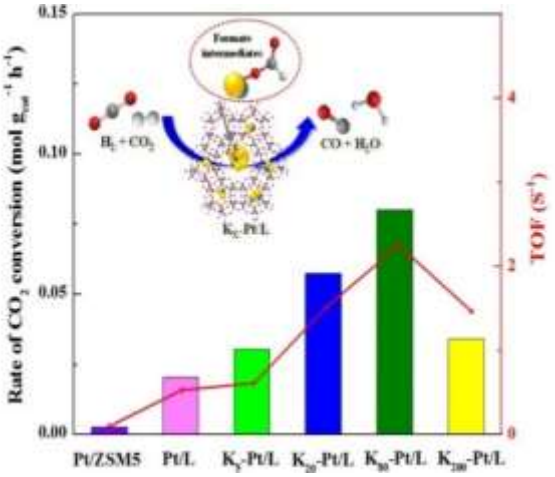

Figure 2.12: Reaction rates and proposed mechanism over K_x-Pt/L catalyst [74].

Rh supported catalyst has also been studied in the hydrogenation of CO_2 to alcohols, methane, and CO. Bando et al. [81] studied the promoting effect of Li on the catalytic activity of RhY catalysts. They found out that the selectivity of the catalyst towards the final product changes from CH_4 to CO by increasing the amount of Li. To investigate the promoting of Li they utilize *in-situ* FTIR and TPR characterization techniques. Heyl et al. [82] also studied CO_2 hydrogenation over K and Ni modified Rh/Al_2O_3 catalyst by in-situ and operando DRIFT

spectroscopy. Studies showed that K-promotion significantly enhances the selectivity of the process towards CO. Rh-K-Ni/Al_2O_3 showed the highest CO formation, while unprompted catalysts showed preference towards CH_4, as shown in Fig. 2.13. It was found that CO_2 adsorbed on the support as hydrogen carbonate rather than on the metal surface dissociative, shown in Fig 2.14. K also enhances CO desorption and resists further CO hydrogenation to CH_4.

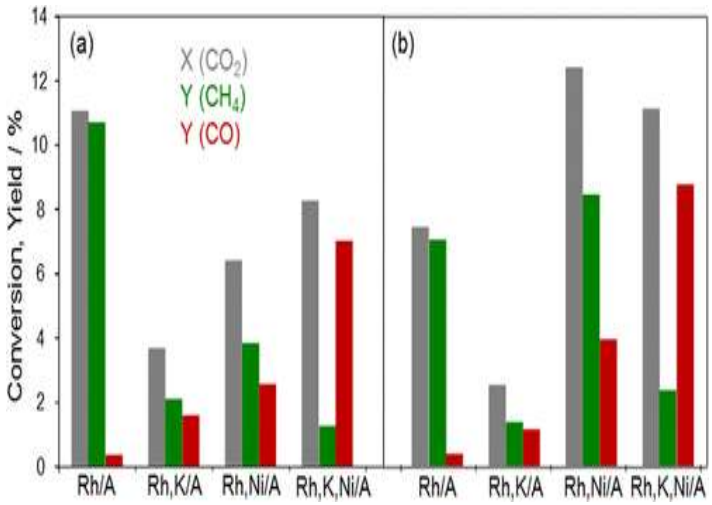

Figure 2.13: CO_2 conversion over K and Ni promoted Rh/Al_2O_3 catalyst [82].

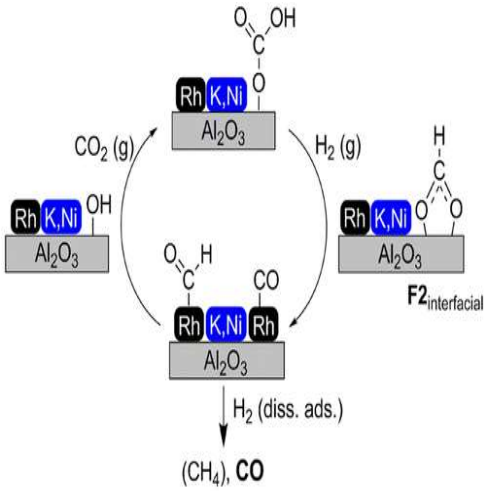

Figure 2.14: CO_2 hydrogenation mechanism over K and Ni promoted Rh/Al_2O_3 catalyst [82].

Highly dispersed supported Au nanoparticles have received great attention in catalytic hydrogenation of CO_2 to valuable chemicals [83-85]. Upadhye et al. [86] studied the activity of various oxide-supported (TiO_2, CeO_2, Al_2O_3) Au catalysts towards RWGS reaction in the absence and presence of visible light. They showed that under visible light, the catalytic activity of Au supported catalyst for RWGS is 30-1300 times higher than dark conditions. TiO_2 and CeO_2 supported Au catalysts showed the maximum CO_2 conversion rate (in visible light) of

2663 and 1417 µmol g_{cat}^{-1} $min^{-1,}$ respectively. There was a significant decrease in the apparent activation energy, from 47 kJ/mol in the dark to 35 kJ/mol in light, was observed due to the LSRP (localized surface plasmon resonance). Fig. 2.15 shows the effect of LSRP on the activity of plasmonic photo-catalysis, and Fig. 2.16 shows the proposed mechanism for LSRP enhanced RWGS reaction over Au/TiO_2 catalyst.

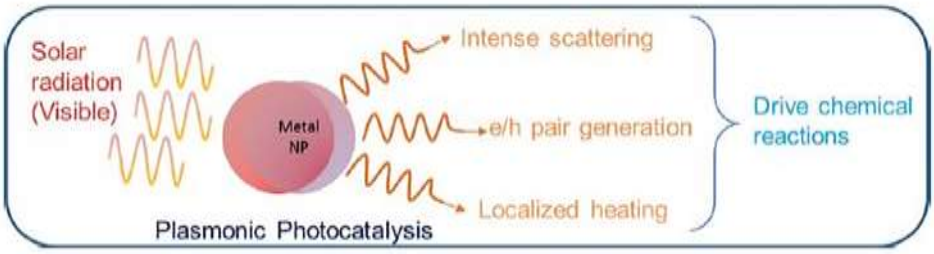

Figure 2.15: Effect of LSRP on the activity of plasmonic photo-catalysis [86].

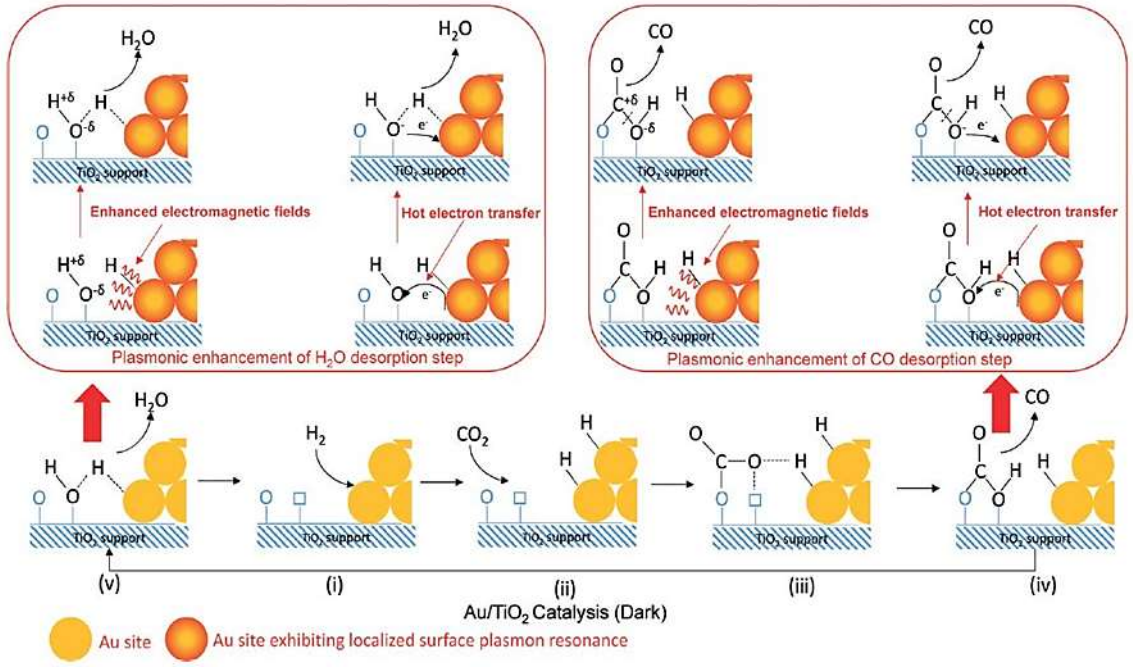

Figure 2.16: proposed mechanism for LSRP enhanced RWGS reaction over Au/TiO_2 catalyst [86].

2.6.1.2 Non-Noble Metal Catalysts

Despite the high activities of noble metal catalyst towards RWGS reaction, their large-scale application is still questioned due to high cost and rareness [10]. Cu received significant attention as an alternative due to its corrosion resistance. There are various commercial Cu based catalysts that are available for WGS [87-89] and methanol synthesis [90, 91]. Jurković et al. [92] investigated different oxide-supported (Al_2O_3, CeO_2, SiO_2,TiO_2, and ZrO_2) Cu catalysts and demonstrated the effect of support on the activity of RWGS and reaction pathway. TPR studies identified alumina and ceria as the most promising supports. However, zirconia shows the worst activity and had the worst Cu dispersion as well. Stone et al. [93] presented a comparative study of Cu-ZnO and Cu-ZnO/Al_2O_3 catalyst for RWGS reaction. They prepared different catalysts by varying concentrations of Cu and Zn from Cu rich to Zn rich. The result shows that Cu rich catalyst holds the highest activity because at high Cu/Zn ratio, dispersion of Cu increased in the final catalyst. Chen et al. [94-96] showed that alumina-supported Cu nanoparticles enhanced the adsorption of formates. They also find out that for Cu nanoparticles and SiO_2 supported Cu; the RWGS reaction undergoes through formate formation. Also, the forward and reverse mechanism is independent of CO_2 and CO adsorption sites.

Nickel has excellent hydrogenation catalytic activities, which leads its catalyst to be more selective for methane production rather than CO. However, oxide-supported Ni nanoparticles with high oxygen capacities are still considered for the RWGS [73]. On the other hand, iron-based catalyst shows significant activities towards the RWGS due to their stability. Kim et al. [97] investigated the catalytic activities of Fe-oxide nanoparticles for the RWGS reaction at 600˚C. Characterization studies revealed that atomic C and O formed during the reaction over Fe-oxide surface, which then penetrates into the bulk of iron oxide and forms iron carbide. Consequently, the surface Fe structure remains unchanged, which leads to long term stability of the catalyst. Loiland et al. [98] studied the RWGS reaction over alumina supported Fe and

K promoted alumina supported Fe catalysts at 723 K and 753 K and atmospheric pressure. Both catalysts show high CO selectivity (>99%). It was found out that the addition of K increases the reaction rate 3 times. *In-situ* DRIFT studies show stable intermediate formation over K supported catalyst while no stable intermediates were observed on the non-prompted catalyst. Promoter helps better Fe dispersion along with the formation of stable intermediates that leads to the formation of CO.

2.6.1.3 Atomically Dispersed Supported Metal Catalysts

As discussed before, metal particle size plays an important role in CO_2 hydrogenation reaction catalyst stability and selectivity [74]. Currently, single-atom dispersed catalysts are of much interest because of the high catalytic performance and well defined structure [99, 100]. Matsubu et al. [101] prepared TiO_2 supported Rh catalysts containing atomically dispersed Rh isolated sites (Rh_{iso}) and Rh-nanoparticles (Rh_{Np}). They observed a very strong correlation between turnover frequency of the RWGS and isolated Rh sites. During the reaction, induced disintegration of Rh_{Np} to Rh_{iso} was observed, which leads to control of the change in reactivity with time. Furthermore, they demonstrated that the nanoparticles and isolated single atoms of the same material show different selectivity (shown in Fig. 2.17).

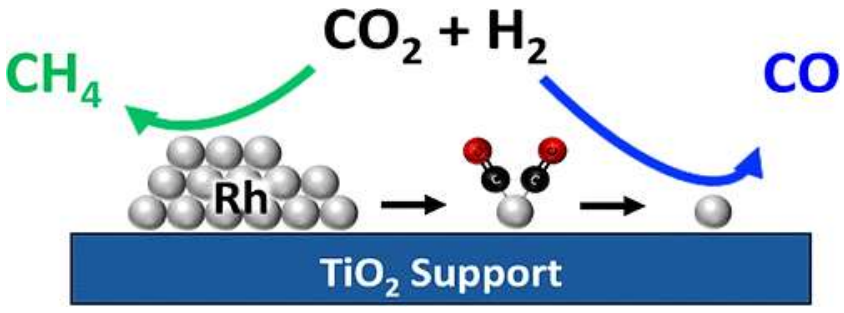

Figure 2.17: Rh particles size effect on CO_2 hydrogenation [101].

Similarly, Kwak et al. [102] synthesized atomically dispersed alumina and MWCNT(multiwall carbon nanotubes) supported Pd catalyst. Alumina supported Pd shows efficient conversion of CO_2 to CO, while MWCNT supported Pd catalyst shows poor selectivity (Fig. 2.18). However, the addition of La_2O_3 made Pd/MWCNT active for RWGS. This clearly shows that a dual functionality of the catalyst is needed for CO_2 hydrogenation. It requires an active site of catalyst that can activate CO_2 and a metallic component that can dissociate H_2.

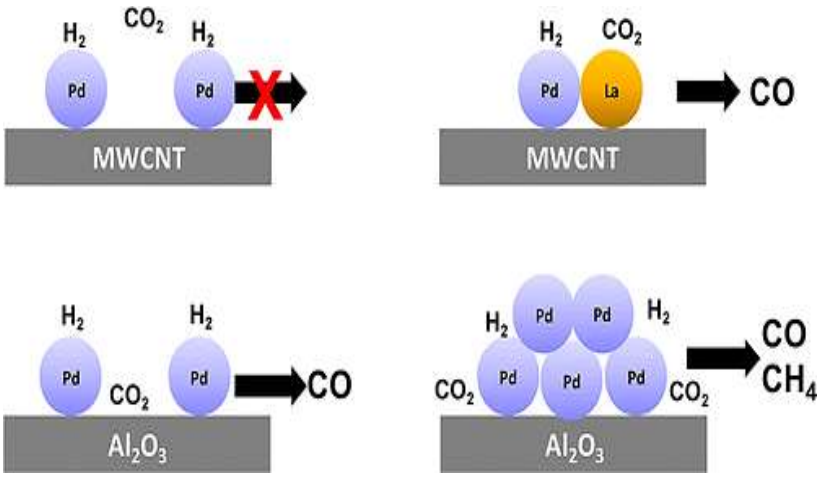

Figure 2.18: RWGS reaction over single atom Pd on different supports and the effect of La dopant [102].

2.6.2 Transition Metal Carbide Catalysts

In 1973 Levy and Boudart first show the platinum like behavior of tungsten carbide [103]. After this revolutionary work, transition metal carbides (TMCs) received tremendous attention in utilizing them for CO_2 hydrogenation. TMCs behave like noble metals and are less expensive. Porosoff et al. [104] studied the CO_2 conversion to CO over six different TMCs (TiC, ZrC, NbC, TaC, Mo_2C, WC). They showed that the activity of carbides for CO_2 hydrogenation could be easily predicted by OBE (oxygen binding energy) because the

formation of the oxy-carbide and the subsequent removal of O is the main crucial steps in the CO_2 conversion catalytic cycle. DFT studies show that for TMCs with high OBE, like TiC, it is not easy to remove surface oxygen to complete CO_2 reduction catalytic cycle, whereas TMCs with low OBE, such as Mo_2C are highly active in adsorbing and dissociation of CO_2. Liu et al. [105] also show that polycrystalline α-Mo_2C is a highly efficient catalyst towards RWGS. It gives about 16% CO_2 conversion at 400°C and CO selectivity of >99%. Xu et al. [106] also studied β-Mo_2C supported metal (Cu, Ni, Co) catalyst for the hydrogenation of CO_2. All the catalysts (Cu/β-Mo_2C, Ni/β-Mo_2C, Co/β-Mo_2C) show high activity in CO_2 hydrogenation with different selectivity towards CO, CH_4, and hydrocarbons shown in Fig. 2.19. Cu/β-Mo_2C show high selectivity for CO and methanol formation, while Ni/β-Mo_2C and Co/β-Mo_2C show very high activity in decomposing CO_2 and leads to form CH_4 and C_nH_{2n+n} hydrocarbons, respectively.

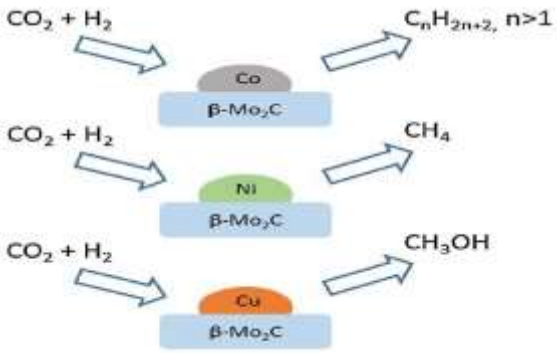

Figure 2.19: Reaction selectivity of Cu/β-Mo_2C, Ni/β-Mo_2C, Co/β-Mo_2C catalysts [106].

Zhang et al. [107] have synthesized a series of Cu/β-Mo_2C catalysts via a temperature-programmed carburization method by using Cu-MoO_3 as the precursor. These catalysts exhibit extraordinary RWGS reaction activity (showing a mass specific conversion rate of 47.7×10^{-5} mol CO_2 g-cat^{-1} s^{-1}) and stability (maintaining 85% of initial activity after 40 h time on stream).

The excellent performance of Cu/β-Mo_2C in the high temperature RWGS reaction (600°C) is due to the strong interaction between Cu and the hexagonal β-Mo_2C support, which greatly enhances the copper dispersion and prevents the agglomeration of Cu particles under real working condition. The stabilized Cu nanoparticles show great advantages over traditional Cu-based catalysts.

2.6.3 Mixed Metal and Metal Oxide Catalysts

In the CAMARE process, ZnO is used as the RWGS catalyzing agent. However, ZnO starts losing its activity gradually when it is exposed to high flow rates and high reaction temperature. Joo and Jung [108] and Park et al. [109] synthesized several ZnO and ZnO/Al_2O_3 catalysts by varying the Zn/Al ratio to improve the high temperature stability. Park et al. showed that in the presence of large ZnO particles, the stability of ZnO/Al_2O_3 catalyst highly improved. Therefore, the ZnO/Al_2O_3 having Zn/Al ratio of 4 was more stable than ZnO/Al_2O_3 catalyst with Zn/Al ratio of 1. Joo and Jung found out that ZnO/Al_2O_3, calcined at 850°C before reaction, shows constant stability for 240 h at a reaction temperature of 600°C and is 100% CO selective. They also showed that this high stability of the ZnO/Al_2O_3 (calcined at 850°C) was due to the formation of $ZnAl_2O_4$ spinel structure that prevents the reduction of ZnO.

Mixed oxides, such as $Zn_xZr_{1-x}O_{2-y}$[110], $Ni_xCe_{0.75}Zr_{0.25-x}O_2$[111], and 80 wt% Fe_2O_3–$Ce_{0.5}Zr_{0.5}O_2$ [112], show promising results in RWGS due to their high oxygen mobility and high temperature reducibility. Kim et al. [113] doped Y, Zn, and Ce into barium zirconate-based perovskite-type catalysts to catalyze the RWGS reaction. The Zn- and Y-doped barium zirconate (BZYZ) catalyst showed an outstanding activity for the RWGS reaction even at an intermediate temperature of 600°C. In contrast, the insertion of additional Ce into the BZYZ structure did not have any positive effect on catalytic activity for the RWGS reaction because of the appearance of a Zn- deficient surface structure and chemical instability of the catalyst.

Wang et al. [114] showed that incorporation of CeO_2 with In_2O_3 increases the surface area of catalyst. CeO_2 helps to adsorb dissociative H_2 and intermediate carbonates while creating more oxygen vacancies. The interaction of In_2O_3-CeO_2 catalyst creates a synergistic effect, which leads to outstanding activity for the RWGS.

2.6.3.1 Ceria Based Catalysis for RWGS

Recently, apart from the highly active noble metals (Pt, Pd, Rh etc.) and transition metals (like Cu and Ni) the rare earth metal Ce received significant attention due to its highly active behavior. CeO_2 (Ceria) based catalysts show promising results in RWGS because of their high oxygen capacity. CeO_2 can lose O^{2-} atom at high temperature and reduce cerium from Ce^{4+} to $Ce^{3+,}$ creating an oxygen vacancy in the crystal lattice while keeping the crystalline structure. This oxygen vacancy acts as the leading active site for catalytic reactions [23, 115]. Table 2.3 outlined all the potential catalysts that have been deployed so far for the thermo-catalytic RWGS application. It can easily be seen that only a few studies have been reported over unsupported ceria for the application of the RWGS reaction [18-22]. These studies reported either low selectivity to CO generation or low CO_2 conversion to CO.

Dai et al. [20] reported the RWGS studies over unsupported (bulk) ceria prepared using three different synthesis methods, including hard templet (Ce-HT), complex (Ce-CA), and precipitation method (Ce-PC). 50mg of each catalyst was tested for a temperature range of 300°C-580°C in a quartz tube reactor at atmospheric pressure. Feed gas comprising of CO_2 (10.0% vol), H_2 (40% vol), and Ar (50% vol) was flown over the packed bed at the GHSV of 60,000 ml g_{cat}^{-1} h^{-1}. All three catalysts at all temperatures showed 100% CO selectivity and maximum CO_2 conversion of 15.9%, 9.3%, and 12.7% for Ce-HT, Ce-CA, and Ce-PC, respectively, at 580°C. Kovacevic et al. [22] reported the RWGS reaction activity over three different morphological shapes (cubes, roads, and particles) of bulk ceria. Activity tests were performed in a quartz tube reactor at the atmospheric pressure and at a constant temperature of

580°C using a feed gas (30 ml min^{-1}) mixture of 3% H_2, 37% CO_2, and 60% N_2. In each run, the amount of catalyst was adjusted to maintain the CO_2 conversion less than 5% to ensure no discrepancy in the experiments. Nanocubes shows the maximum rate of approximately 78 µmol g_{cat}^{-1} min^{-1} CO produced. A minor deactivation was also observed in all the experiments. Similarly, Liu et al. [21] also studied the RWGS phenomena over bulk ceria (cubes, rods, and octahedra) and Ni supported ceria (nano-cubes) prepared via hydrothermal and wet impregnation method, respectively. Catalysts were tested at atmospheric pressure for the temperature range of 400°C-800°C. A reaction gas mixture of H_2:CO (1:1) was flown over the fixed bed at the rate of 100 ml min^{-1}. All bulk ceria catalysts showed 100% CO selectivity above 500°C, while the ceria nanocubes showed the highest CO_2 conversion at all temperatures. Maximum, Less than 50% CO_2 conversion was observed for ceria nanocubes at 800°C. On the other hand, Ni-supported nanoceria showed better CO_2 conversion and CO selectivity at all temperatures. Maximum approximately 50% CO_2 conversion was recorded at 800°C. These studies show minor deactivation, low surface area, or low CO_2 conversion rates even at a temperature as high as 800°C. Therefore, considering the potential of ceria for RWGS, there is a strong need to investigate the RWGS over ceria (at Temperature up to 600°C) prepared via a method other than already been taken, like reverse microemulsion (RME). To the best of the author's knowledge, this study has not been reported in the catalysis field before.

Table 2.3: RWGS process performance of different heterogeneous catalysts

year	Catalyst	T(°C)	Pressure (bar)	Feed H_2:CO_2	CO_2 Conversion (%)	CO Selectivity (%)	Reference
1989	Rh/TiO_2	300	10.13	1:1	-	-	[116]
	$Rh\text{-}Na/TiO_2$	260			-	-	
	Rh/Nb_2O_5	220			-	-	
	$Rh\text{-}Na/\ Nb_2O_5$	200			-	-	
	Rh/MgO	200			-	-	
	$Rh/\ Nb_2O_5$	200		3:1	-	-	
	Rh/ZrO_2	200			-	-	
	Rh/TiO_2	300			-	-	
1991	5% wt Au/ZrO_2	260	17	3:1	~12	80	[85]
1992	Cu/ZnO	165	1	9:1	-	-	[117]
1994	Pd/Al_2O_3	260	1	1:1	-	78	[118]
	$Pd/La_2O_3/Al_2O_3$				-	70	
	$Pd/PrO_2/Al_2O_3$				-	76	
	Pd/CeO_2 (5)$/Al_2O_3$				-	87	
	Pd/CeO_2 (10)$/Al_2O_3$				-	81	
1997	$CuO/ZnO/Al_2O_3$	250	1	6:1	17	-	[119]
1998	Li/RhY(Li:Rh = 0)	250	30	3:1	24.1	0.3	[81]
	Li/RhY(Li:Rh = 3)				12.0	3.7	
	Li/RhY(Li:Rh = 7)				11.1	27.6	
	Li/RhY(Li:Rh = 10)				13.1	86.6	
1999	Cu-Ni/γAl_2O_3	600	1	1:1	28.7	79.7	[120]
2000	10 wt.% Cu/Al_2O_3	500	1	1:9	60	-	[94]
2001	10% Cu-0.3%Fe/SiO_2	600	1	1:1	12	-	[64]
2001	1 wt.% Rh/SiO_2	200	50	3:1	52	88.1	[121]
2003	9% Cu/SiO_2	600	1	1:1	1	-	[122]
	9% Cu-1.9% K/SiO_2				12.8	-	
2003	Cu-ZnO	240	1	CO_2:H_2:He ; 1:1:8	7-12	-	[93]
	Cu-Zno/Al_2O_3				4-15	-	
2003	ZnO (calcined 500 °C)	650	1	3:1	62.7	-	[108]
	Al_2O_3 (calcined 500 °C)				20	-	
	ZnO/Al_2O_3 (Zn: Al= 1:2) (calcined 500°C)				54	-	
	ZnO (calcined 850 °C)				49.4	-	
	Al_2O_3(calcined 850 °C)				22	-	
	ZnO/Al_2O_3 (calcined 850 °C)				41.7	100	

Table 2.3(Contd)

Year	Catalyst	T(°C)	Pressure (bar)	Feed H_2:CO_2	CO_2 Conversion (%)	CO Selectivity (%)	Reference
2004	0.3% Fe/SiO_2	600	1	1:1	1	-	[123]
	10% Cu/SiO_2				2	-	
	Cu-Fe/SiO_2(Cu/Fe = 10:0.3)				15	-	
	Cu-Fe/SiO_2(Cu/Fe = 10:0.8)				16	-	
2004	2% Pt/CeO_2	225		4:1	13.7	-	[124]
2008	2%Ni/CeO_2	400	1	1:1	7	77	[125]
	CeO_2				~0.1	100	
2010	Mn 12% /Fe 17% /Al_2O_3 (wt.%)	290	13.8	3:1	37.7	10.7 (%CO Yield)	[126]
	Ce 2% / Mn 12% / Fe 17% /Al_2O_3 (wt.%)				38.6	11.5(%CO Yield)	
	Ce 10 % / Mn12 % / Fe 17% /Al_2O_3 (wt.%)				35.8	17.5(%CO Yield)	
2010	2% Rh/TiO_2	270	20.26	1:1	7.89	14.5	[127]
	2% Rh-2.5% Fe/TiO_2				9.16	28.4	
	2.5% Fe/TiO_2				2.65	73.0	
2010	Pt/Fe_2O_3@SiO_2(Photo-deposition)	500		H_2 , CO_2, Ar ; 2.5, 5, 2.5 mL/min	-	100 (14%CO Yield)	[78]
	Pt/Fe_2O_3@SiO_2(Hydrothermal)				>Photodeposition	100	
2011	Pt-Co/MCF-17	300	5.5	3:1	5	99	[128]
	Pd/Al_2O_3	260	1	1:1	-	78	
	$Pd/CeO_2/Al_2O_3$	260	1	1:1	-	87	
	$Pd/La_2O_3/Al_2O_3$	260	1	1:1	-	70	
	Pd/La-ZrO_2	150	-	1:1	30	98.2	
2012	1% Pt/Al_2O_3	875	-	10:7	42	-	[77]
	1% Pt/TiO_2		-		48	-	
2012	Pt/TiO_2	300	-	-	15	-	[129]
2012	CeO2-Ga_2O_3	500	1	1:1	11	-	[130]
2013	Fe/Al_2O_3	600	10	1:1	-	35(%CO Yield)	[131]
	Mo/Al_2O_3				-	33(%CO yield)	
	Fe-Mo/Al_2O_3				-	37(%CO Yield)	
2013	NiO/SBA-15	400	1	1:1	5	100	[132]
		900			55		
2013	Ni-CeO_2	750	1	1:1	40	100	[133]
2013	Au/TiC	227-327	0.5 CO_2, 4.5 H_2	-	-	<Cu/TiC	[84]
	Cu/TiC			-	-	>Au/TiC	
	Ni/TiC			-	-	>Cu/TiC	

Table 3(Contd)

Year	Catalyst	T(°C)	Pressure (bar)	Feed H_2:CO_2	CO_2 Conversion (%)	CO Selectivity (%)	Reference
2013	$PtNi/CeO_2$	300	0.04(30Torr)	3:1	10(fixed)	60.7(CO/CH_4 ratio)	[76]
	Pt/CeO_2					150.7	
	Ni/CeO_2					27.5	
	$PdNi/CeO_2$					31.9	
	$PtCo/CeO_2$					259.4	
	Co/CeO_2					43.0	
	$PtNi/\gamma\text{-}Al_2O_3$					62.1	
	$Pt/\gamma\text{-}Al_2O_3$					200.5	
	$Ni/\gamma\text{-}Al_2O_3$					40.1	
	$PdNi/\gamma\text{-}Al_2O_3$					46.5	
	$PtCo/\gamma\text{-}Al_2O_3$					245.8	
	$Co/\gamma\text{-}Al_2O_3$					73.9	
2014	(1 wt% NiO/CeO_2)/ 50% wt SBA-15	750	1	1:1	40	100	[134]
	(3 wt% NiO/CeO_2)/ 50% wt SBA-15				45		
2014	$BaZr_{0.8}Y_{0.2}O_3$	600	-	1:1	26.7	93	[113]
	$BaZr_{0.8}Y_{0.16}Zn_{0.04}O_3$		-	1:1	37.5	97	
	$BaCe_{0.2}Zr_{0.6}Y_{0.16}Zn_{0.04}O_3$		-	1:1	36.3	94	
	$BaCe_{0.3}Zr_{0.3}Y_{0.16}Zn_{0.04}O_3$		-	1:1	22.3	92	
	$BaCe_{0.7}Zr_{0.1}Y_{0.16}Zn_{0.04}O_3$		-	1:1	10.8	74	
2014	10% mol La-ZrO_2	150	-	1:1	18	100	[59]
	1% wt Pt/10% mol La-ZrO_2		-		40	99.5	
	1% wt Pd/10% mol La-ZrO_2		-		30	98.2	
	1% wt Ni/10% mol La-ZrO_2		-		28	96.5	
	1% wt Fe/10% mol La-ZrO_2		-		28	100	
	1% wt Cu/10% mol La-ZrO_2		-		28	100	
2014	$PtCo/CeO_2$	300.85	1	2:1	6.6	4.5(CO:CH4)	[135]
	$PdNi/CeO_2$				2.5	0.6	
	Mo_2C				8.7	14.5	
	7.5 wt% Co/Mo_2C				9.5	51.3	
2014	Ni	550	1	3:1	47.4	74.4	[111]
	Ni+NiCeZr (physical Mix)				48	87.5	
2014	Rh/Al_2O_3	403	1	4:1	-	40	[136]
	Rh/Al-K	444			-	52	
	Rh/Al-Ba	444			-	100	
2014	$Mo/\gamma Al_2O_3$	600	1	1:1	13	97	[137]
	Ni-$Mo/\gamma Al_2O_3$				35		

Table 2.3(Contd)

Year	Catalyst	T(°C)	Pressure (bar)	Feed H_2:CO_2	CO_2 Conversion (%)	CO Selectivity (%)	Reference
2015	Au/SiO_2	300	8.1	2:1	-	-	[83]
	Au-MoOx/SiO_2				-	-	
2015	Au-TiO_2 (Deposition-Precipitation)	400	7.5	2:1	-	100	[86]
	Au-CeO_2	400			-		
	Au-Al_2O_3	400			-		
	Cu-TiO_2 (Impregnation)	400			-		
2015	Fe-Oxide NPs	600	-	1:1	38	>85	[97]
2015	β -Mo_2C	200	20	5:1	6	39	[106]
	Cu/ β-Mo_2C				4	44	
	Ni/ β-Mo_2C				8	37	
	Co/ β-Mo_2C				9	31	
	β-Mo_2C	250			17	34	
	Cu/ β-Mo_2C				13	40	
	Ni/ β-Mo_2C				21	29	
	Co/ β-Mo_2C				23	24	
2015	0.5% w/w Rh/TiO_2	200	-	1:10	-	-	[101]
	2% w/w Rh/TiO_2		-		-	-	
	4% w/w Rh/TiO_2		-		-	-	
	6% w/w Rh/TiO_2		-		-	-	
2015	Ni/Ce-Zr-O	700	1	1:1	-	93	[138]
2015	TiC	300		2:1		0.0($CO:CH_4$)	[104]
	ZrC					0.0	
	NbC					17.1	
	TaC					0.0	
	Mo_2C					154.3	
	WC					20.1	
2016	$La_{0.75}Sr_{0.25}FeO_3$	550	1	1:1	15.5	95	[56]
2016	Pt/SiO_2	200	7.1	2:1	-	-	[79]
	$PtMo_{0.15}/SiO_2$				-	-	
	$PtMo_{0.3}/SiO_2$				-	-	
	$PtMo_{0.45}/SiO_2$				-	-	
2016	Fe/ɣAl_2O_3	450, 480	1	1:1	-	>99	[98]
	Fe-K/ɣAl_2O_3				-	>99	

Table 2.3(Contd)

Year	Catalyst	T(°C)	Pressure (bar)	Feed H_2:CO_2	CO_2 Conversion (%)	CO Selectivity (%)	Reference
2016	Rh/A (A = ɣAl_2O_3) No High Temp. Treatment	350	1	H_2:CO_2:N_2 ; 1:1:3	~11	~0.2(%CO Yield)	[82]
	Rh,K/A	350			~4	~1.8(%CO Yield)	
	Rh,Ni/A	350			~6.8	~2.2(%CO Yield)	
	Rh,K,Ni/A	350			~8.8	~7.6(%CO Yield)	
	Rh/A (A = ɣAl_2O_3) High Temp. Treated at750 °C	350			~7.8	~0.2(%CO Yield)	
	Rh,K/A	350			~2.2	~1(%CO Yield)	
	Rh,Ni/A	350			~12	~4(%CO Yield)	
	Rh,K,Ni/A	350			~11	~9(%CO Yield)	
2016	In_2O_3	500	-	1:1	16	-	[114]
	In_2O_3:CeO_2 = 3:1 w/w				17	-	
	In_2O_3:CeO_2 = 1:1 w/w				20	-	
	In_2O_3:CeO_2 = 1:3 w/w				11	-	
	In_2O_3:CeO_2 = 1:9 w/w				9	-	
	CeO_2				2.5	-	
2016	CeO_2-Cubes (Hydrothermal method)	560	1	H_2, CO_2, N_2	<5%	71 µmol . g_{cat}^{-1} min^{-1}	[22]
	CeO_2-Rods			3%, 37%, 60		61 µmol . g_{cat}^{-1} min^{-1}	
	CeO_2-Particles (Decomposition of $Ce(OH)_4$)					24 µmol . g_{cat}^{-1} min^{-1}	
2016	CeO_2-nanocube	800	1	1:1	~46	100	[21]
	CeO_2-nanorod				~43		
	CeO_2-nanooctahera				~37		
	Ni/CeO_2-nanocube				~48		
2017	Cu/β-Mo_2C	300	1	2:1	~6	96.5	[107]
		400			~17	97.6	
		500			~30	99.0	
		600			~38	99.2	
2017	Ni-CeO_2	400	1	4:1	69.21	28	[139]
	Co-CeO_2				34.91	63	
	Fe-CeO_2				8.69	100	
	Mn-CeO_2				8.12		
	Cu-CeO_2				31.34		
2017	Pt/TiO_2	400	1	1:1	14.9	100	[74]
2017	Co/CeO_2	550	1	1:1	24.8	100	[140]
2017	Fe/Al_2O_3	600	1	4:1	~58	>99	[141]
	Fe-Cu/ Al_2O_3				~60	>99	
	Fe-Cs/ Al_2O_3				~62	>99	
	Fe-Cu-Cs/ Al_2O_3				~64	>99	

Table2.3 (Contd)

Year	Catalyst	T(°C)	Pressure (bar)	Feed H_2:CO_2	CO_2 Conversion (%)	CO Selectivity (%)	Reference
2017	Cu/Al_2O_3	360	3	1:1	~7(%CO by Vol)	-	[92]
	Cu/CeO_2				~8.5(%CO by Vol)	-	
	Cu/TiO_2				~4(%CO by Vol)	-	
	Cu/ZrO_2				~1.5(%CO by Vol)	-	
	Cu/SiO_2				~1.5(%CO by Vol)	-	
2017	0.1%Ir/TiO_2 (atomic Ir)	350	1	45%H_2,45%CO_2,10%He	2.1	~100	[142]
	0.5%Ir/TiO_2 (atomic Ir)				2.1	~95	
	1%Ir/TiO_2 (atomic Ir)				2.1	~85	
	2%Ir/TiO_2 (atomic Ir)				2.1	~30	
	5%Ir/TiO_2 (atomic Ir)				2.1	21.8	
	1%Ir/TiO_2(nanoparticle Ir)				2.1	~70	
	1%Pt/TiO_2(nanoparticle Pt)				~14	~90	
	1%Au/TiO_2(nanoparticle Au)				~9	~100	
2017	Pt/L	500	1	1:1	13.1	100	[80]
	K_{80}-Pt/L				27.4		
2017	Pt/mullite	550	1	1:1	22.9	83.9	[143]
	K-Pt/mullite				30.9	99.2	
2017	$Ce_{1.2}Cu_1$	400	1	40%H_2,10%CO_2,50%Ar	-	100	[144]
	$Ce_{1.1}Cu_1$				-		
	$Ce_1Cu_{1.1}$				-		
	$Ce_1Cu_{1.2}$				-		
2017	α-Mo_2C	400	1	H2:CO_2:N_2 ; 1:1:3	~16	>99	[105]
2018	CeO_2 (Hard Templet method)	580	1	H_2:CO_2:Ar ; 40:10:50	16	100	[20]
	CeO_2(Complex Method)				9	100	
	CeO_2(Precipitation Method)				13	100	
2018	Co NCs	250	1	CO_2:H_2:Ar ; 50:1:19	5.9	96.1	[145]
	Co@CoO NCs				14.1	>99	
	Co@CoO-N NCs				19.2	>99	
2018	$CuFe/Al_2O_3$	700		1:1	42	-	[146]
2018	C/CeO_2-NR(Nano-Rod) (Calcined 900 °C)	450	1	5:1	52	-	[147]
	Cu/CeO_2-NS(Nano-Sphere)				42		
2018	Au/TiO_2	450	-	4:1	~42	100	[148]
	Au/Al_2O_3				~20		

Table2.3(Contd)

Year	Catalyst	T(°C)	Pressure (bar)	Feed H_2:CO_2	CO_2 Conversion (%)	CO Selectivity (%)	Reference
2018	Ni/Al	750	1	4:1	~59	~95	[149]
	Ni/CeAl				~60	~95	
	NiCr/CeAl				~70	~85	
	NiFe/CeAl				`72	~95	
2018	Ru/CeO_2 (5wt.%)	750	1	1:1	-	40(%CO Yield)	[150]
	Ru/SDC(5wt.%)					40(%CO Yield)	
	Fe/SDC(5wt.%)					~42(%CO Yield)	
	$Ru_{20}Fe_{80}$/SDC(5wt.%)					~40(%CO Yield)	
	$Ru_{45}Fe_{55}$/SDC(0.5wt.%)					~41(%CO Yield)	
	$Ru_{45}Fe_{55}$/SDC(1wt.%)					~40(%CO Yield)	
	$Ru_{45}Fe_{55}$/SDC(2wt.%)					~47.5(%CO Yield)	
	$Ru_{45}Fe_{55}$/SDC(3wt.%)					~51(%CO Yield)	
	$Ru_{45}Fe_{55}$/SDC(5wt.%)					~50(%CO Yield)	
2018	$P_{20\ 80}$ ($Cu_{20}Ce_{80}$; N_2 1bar ;Pyrolysis)	400	1	15%H_2,15%CO_2,70%Ar	~4	100	[151]
	$P_{40\ 60}$ ($Cu_{40}Ce_{60}$; N_2 1bar; Pyrolysis)				~0		
	$Pf_{20\ 80}$ ($Cu_{20}Ce_{80}$; N_2 1bar: Flash Pyrolysis)				~9		
	$Pf_{40\ 60}$ ($Cu_{40}Ce_{60}$; N_2 1bar; Flash Pyrolysis)				~1		
	$Pf_{20\ 80}$($Cu_{20}Ce_{80}$; Air 1bar; Flash Pyrolysis)				~17		
2018	2%Ni/M1 (M1 is surfactant assisted MgO)	400	1	1:1	~4	>99.5	[152]
	5%Ni/M1				~6	>94	
	7%Ni/M1				~14	>79.2	
	7%Ni/M2 (M2 is ultrasonic assisted MgO)				~17	>71	
	10%Ni/M1				~17	>62	
	15%Ni/M1				~17	>53	
2018	U-Cr/ZrO_2	600	1	1:1	~36	100	[153]
	C-Cr/ZrO_2				38.34		
	R-Cr/ZrO_2				~30		
	C-Cr/ZrO_2				38.34		
	I-Cr/ZrO_2				~30		
	ZrO_2				~7		
	Cr_2O_3				~12		
	17%Cr/Al_2O_3				~22		

Table2.3(Contd)

Year	Catalyst	T(°C)	Pressure (bar)	Feed H_2:CO_2	CO_2 Conversion (%)	CO Selectivity (%)	Reference
2018	0.5%Ru/CeO_2	250	1	4:1	5	<98	[154]
	0.5%Ru/Al_2O_3				5	60	
	0.5%Ru/TiO_2				5	80	
2018	CeO_2-M	600	1	1:1	~2.5	100	[155]
	1% Co-CeO_2-M				~17	<99	
	2%Co- CeO_2-M				~25	<99	
	5%Co- CeO_2-M				~34	<99	
	10%Co- CeO_2-M				~36	<98	
	5%Co- CeO_2-CP				~35	<99	
	5%Co- CeO_2-IM				~28	<99	
2018	Fe/Al_2O_3	600	1	4:1	55 (12,000GHSV)	~95	[156]
	1% CsFe/Al_2O_3				60	~85	
	2.5% CsFe/Al_2O_3				65	~90	
	5% CsFe/Al_2O_3				68	~99	
2018	CuSBA-0.2g	300	1	3:1	~5	<98	[157]
	SCuCe-0.2g				~18	100	
	SCuCe-0.05g				~6	100	
2019	β-Mo_2C	450	1	3:1	58 (20,000GHSV)	62	[158]
2019	5%Cu/CeO_2	600		H_2:CO_2:Ar ; 3:3:4	~22.5	-	[159]
	5%Fe/CeO_2				~16		
	40% CuZn/Al_2O_3-commercial				~11		
	5%Cu0.8Fe/CeO_2-DP				~24		
	5%Cu1.6Fe/CeO_2-DP				~27		
	5%Cu3.2Fe/CeO_2-DP				~26		
	1.6Fe/CeO_2				~21		
2019	Pt/TiO_2	600	1	-	~34	100	[160]
	Pt/20%CeO_2-TiO_2				~38		
	Pt/10%CeO_2-TiO_2				~38		
	Pt/5%CeO_2-TiO2				~38		
	Pt/1%CeO_2-TiO_2				~36		
2019	CuSiO/CuO_x	500	1	H_2, CO_2, Ar	17.8	100	[161]
	TiO_2/CuO			72%, 24%, 4%	6.6		
	SiO_2/CuO_x				6.2		

Table2.3(Contd)

Year	Catalyst	T(°C)	Pressure (bar)	Feed H_2:CO_2	CO_2 Conversion (%)	CO Selectivity (%)	Reference
2019	MOF-74	400	2	3:1	11.2 (24,000GHSV)	99.1	[162]
	Au@Pd@MOF-74-5				7.8	99.8	
	Au@Pd@MOF-74-20				8.2	99.3	
	Au@Pd@MOF-74-40				10.7	100	
	Au@Pd@MOF-74-100				10.1	100	
	Pt/MOF-74-12				18.1	100	
	Pt/MOF-74-24	350			1.9	100	
	Pt/MOF-74-24	375			22.4	100	
	Pt/MOF-74-24	400			33.8	99.7	
	Pt/MOF-74-24		1		19.5	99.7	
	Pt/MOF-74-24		4		40.6	99.4	
	Pt/MOF-74-24		2	1:1	25.5	99.8	
	Pt/MOF-74-24			5:1	33.4	99.5	
	Pt/MOF-74-36			3:1	27.3	99.7	
	Pt/Au@Pd@ MOF-74				27.4	99.6	
	Pt/ZnO				33.2	99.7	
2019	Fe/ Al_2O_3	650	1	1:1	-	~27 (%COYield)	[163]
	Ni-Fe/ Al_2O_3				-	~29 (%COYield)	
	Co-Fe/ Al_2O_3				-	~30 (%COYield)	
	Fe/ Al_2O_3			3:1	-	~27 (%COYield)	
	Ni-Fe/ Al_2O_3				-	~37 (%COYield)	
	Co-Fe/ Al_2O_3				54.9	42.8 (%COYield)	
	Fe/ Al_2O_3			5:1	-	~38 (%COYield)	
	Ni-Fe/ Al_2O_3				-	~51 (%COYield)	
	Co-Fe/ Al_2O_3				-	~54.9 (%COYield)	
2019	Co-400R (reduced at 400 °C)	400	1	1:1	12.3	71.6	[164]
	Co-400R	500			29.4	80.9	
	Co-600R (reduced at 600 °C)	400			45.8	97.2	
	Co-600R	500			54.2	99.9	
2019	5 wt.% Ti_4O_7-doped SCY (SCY-b)	1000	1	1:1	52	47 (% CO yield)	[165]
	Quartz Particles				13	12 (% CO yield)	
2019	Co-C-700 (pyrolyzed at 700 °C)	450	1	2:1	~29	89	[166]
	Co-C-N-700				~32	90	

Table2.3(Contd)

Year	Catalyst	T(°C)	Pressure (bar)	Feed H_2:CO_2	CO_2 Conversion (%)	CO Selectivity (%)	Reference
2019	$Cu/ZnO/Al_2O_3$ (40/50/10 wt.%)	500	3	4:1	17	100	[167]
	Cu/Al_2O_3				40		
	Cu/ZnO				58		
	$Ru-Cu/ZnO/Al_2O_3$ (0.5/39.8/49.75/9.95 wt.%)				46		
	$Ru/ZnO/Al_2O_3$ (0.5/82.92/16.58 wt.%)				30		
	Ru/Al_2O_3 (0.5/0.95 wt.%)				64		
2019	Commercial Mo_2C	550	1	4:1	~42 (12,000 GHSV)	~85	[168]
	β-Mo_2C				~59	~85	
	Cu- Mo_2C				~57	~95	
	Cs- Mo_2C				~52	~99	
	Cu-Cs- Mo_2C				~59	~80	
2019	Fe_3O_4	480	1	H_2:CO_2:He ; 1:1:4.6	12.5	100	[169]
				1:4:1.6	4.4	100	
				4:1:1.6	33.7	98.6	
2019	α- MnO_2 nanowires	890	1	H_2:CO_2:Ar ; 1:1:3	43	100	[170]
	δ- MnO_2 nanosheets	850			50	100	
	ε-MnO_2 nanoflowers	900			20	100	
2019	$2\%Ni/Al_2O_3$	600		1:1	~27(15,000GHSV)	~95	[171]
	5% Ni/Al_2O_3				~31	~94	
	7% Ni/Al_2O_3				~32	~93	
	10% Ni/Al_2O_3				~32.5	~92	
	5% $Ni-1Mg/Al_2O_3$				~32.5	~90	
	5% $Ni-1K/Al_2O_3$				~33	~89	
	5% $Ni-2K/Al_2O_3$				~34	~90	
	5% $Ni-1Ce/Al_2O_3$				~32.5		
	5% $Ni-1La/Al_2O_3$				~34		
	5% $Ni-2La/Al_2O_3$				~33		
2019	$Ni-Co-Mo/Al_2O_3$	400	7	-	60	100	[172]

Table2.3(Contd)

Year	Catalyst	T(°C)	Pressure (bar)	Feed H_2:CO_2	CO_2 Conversion (%)	CO Selectivity (%)	Reference
2019	CeO_2-NR (Nano-Rod)	400	1	9:1	21.1 (20,000GHSV)	88.5	[19]
	CeO_2-NC (Nano-Cube)				19.3	89.8	
	Cu/ CeO_2-NR				55	97	
	Cu/CeO_2-NC				50.1	97.5	
	Co/ CeO_2-NR				84.9	5.5	
	Co/CeO_2-NC				87.7	3.7	
2019	NP-Cu-R	400	1	20%H_2, 5%CO_2, 75%Ar	2	100	[173]
	NP-Cr_2O_3/Cu-R				20	100	
2020	Ni-ZnO/MCM-41	600	1	1:3			[174]
	1%Ni ; 9%Zn (wt.%)				~2	98.5	
	2.5%Ni ; 7.5%Zn				~2	85.9	
	5%Ni ; 5%Zn				~30	98.9	
	7.5%Ni ; 2.5%Zn				~37	98.4	
	9%Ni ; 1%Zn				~58	96.2	
2020	Co@SiO_2	600	1	4:1	~56	~61	[175]
	1%NiCo@SiO_2				~60	~70	
	2%NiCo@SiO_2				~58	~70	
2020	15%Ni/Zno-Al_2O_3 (Calcined at 400 °C)	600	1	1:1	~33	~88	[176]
	15%Ni/Zno-Al_2O_3 (Calcined at 500 °C)						
	15%Ni/Zno-Al_2O_3 (Calcined at 600 °C)						
	15%Ni/Zno-Al_2O_3 (Calcined at 700 °C)				~34		
2020	Unpromoted-WC/γ-Al_2O_3	350	20	3:1	14.0	96.4	[177]
	K-WC/γ-Al_2O_3				5.3	100	
	Na-WC/γ-Al_2O_3				3.7	100	
	Unpromoted-WC "H_2 Treated"				24.3	88.0	
	K-WC/γ-Al_2O_3 "H_2 Treated"				20.3	98.1	
	Na-WC/γ-Al_2O_3 "H_2 Treated"				13.6	100	
2020	CeO_2	700	1	1:1	~21	-	[18]
	$Ce_{0.93}Ti_{0.07}O_2$				~14	-	
	$Ce_{0.88}Ti_{0.12}O_2$				~22	-	
	$Ce_{0.9}Ti_{0.05}Ca_{0.05}O_{1.95}$				~10	-	
	$Ce_{0.85}Ti_{0.1}Ca_{0.05}O_{1.95}$				~14	-	
	$Ce_{0.9}Ca_{0.1}O_{1.9}$				~9	-	

Table2.3(Contd)

Year	Catalyst	T(°C)	Pressure (bar)	Feed H_2:CO_2	CO_2 Conversion (%)	CO Selectivity (%)	Reference
2020	H@Z/S-Calcined	400	30	3:1	31.4(3000 GHSV)	100	[178]
	Z/H@S-Calcined				~16		
	Cu/ZnO/SiO_2				~10		
2020	Ni/CeZr	700		4:1	72(24000 GHSV)	91	[179]
	FeNi/CeZr				71		
	RuNi/CeZr				72		
	RuFeNi/CeZr						
2020	Fe/CeAl (CeO_2-Al_2O_3)	500	1	4:1	~39 (30,000GHSV)	~99	[180]
	FeMo/CeAl				~26	100	
	FeNi/CeAl				~55	~51	
	FeCu/CeAl				~45	100	
2020	Mo(1)/FAU	500	1	1:1	14.3 (7500 GHSV)	99	[181]
	Cu(1)/FAU				6.8	98	
	Fe(1)/FAU				5.9		
	Ni(1)/FAU				17.2	45	
2020	Micro-emuslsion method	400	1	1:1			[182]
	1%.wt CuO-ZnO/γ-Al_2O_3 (AM-1%)				8.8 (36,000 GHSV)	100	
	3%.wt CuO-ZnO/γ-Al_2O_3 (AM-2%)				6.83		
	Incipient-wetness impregnation method						
	1%.wt CuO-ZnO/γ-Al_2O_3 (IM-1%)				5.07		
	3%.wt CuO-ZnO/γ-Al_2O_3 (IM-2%)				2.67		
2020	Cu	400	1	H_2:CO_2:Ar ; 4:1:5	0.14 mmol . g_{cat}^{-1} min^{-1}	100	[183]
	$CeO_{2-\delta}$				0.40 mmol . g_{cat}^{-1} min^{-1}		
	1Cu/$CeO_{2-\delta}$				1.15 mmol . g_{cat}^{-1} min^{-1}		
	3Cu/$CeO_{2-\delta}$				1.27 mmol . g_{cat}^{-1} min^{-1}		
	5Cu/$CeO_{2-\delta}$				1.62 mmol . g_{cat}^{-1} min^{-1}		
	8Cu/$CeO_{2-\delta}$				1.77 mmol . g_{cat}^{-1} min^{-1}		
	10Cu/$CeO_{2-\delta}$				1.51 mmol . g_{cat}^{-1} min^{-1}		
	12Cu/$CeO_{2-\delta}$				1.40 mmol . g_{cat}^{-1} min^{-1}		
	15Cu/$CeO_{2-\delta}$				1.29 mmol . g_{cat}^{-1} min^{-1}		
2020	Cu/CeO_2-hs	600	1	3:1	~50	100	[184]
	Cu/CeO2-np				~39		
	Cu/CeO2-nc				~10		

Table2.3(Contd)

Year	Catalyst	T(°C)	Pressure (bar)	Feed H_2:CO_2	CO_2 Conversion (%)	CO Selectivity (%)	Reference
2020	ZnO:0.5Cu	600	1	3:1	38	-	[185]
	ZnO:1Cu				39	-	
	ZnO:1.5Cu				41	-	
	ZnO:3.5Cu				45	-	
	ZnO:6.5Cu				42.5	-	
	1Cu:ZnO				32.5	-	
2020	β-Mo_2C	600	1	3:1	58	>98	[186]
	Mo_2C@N-C(100)				59		
	Mo_2C@N-C(5)				32		
	Mo_2C@N-C(10)				45	>99.5	
	Mo_2C@N-C(20)				52	>98	
2020	Mo_xC-A	375	1	3:1	16.7	>91	[187]
	Mo_xC-B				21.0	>97	
	Mo_xC-C				18.5	>91	
	Mo_xC-D				18.3		
	Mo_xC-D1				17.5	>97	
	Mo_xC-E				15.5		
2020	sCu/CeO_2 (s = Cu metal loading per g of CeO_2)	400	1	H_2:CO_2:Ar			[188]
	1CuCe(rod)			4: 1 : 95 (vol%)	~27	100	
	5CuCe(rod)				~35		
	10CuCe(rod)				~36		
	20CuCe(rod)				~42		
	40CuCe(rod)						
	80CuCe(rod)						
2020	Ni_1 DD (Direct Decomposition method)	650	1	1:1	45	>99.99	[189]
	Ni_5Pd_5 DD				50		
	Ni_1Pd_9				42		
	Pd_1 DD				34		
	Ni1 SI (Sol-immobilization method)				37		
	Ni5Pd5 SI				38		
	Ni1Pd9 SI				38		
	Pd1 SI				11		

Table2.3(Contd)

Year	Catalyst	T(°C)	Pressure (bar)	Feed H_2:CO_2	CO_2 Conversion (%)	CO Selectivity (%)	Reference
2020	Cu/CeO2/ZSM-5 Catalysts	600	1	5:1			[190]
	48CeZ				~17	100	
	3CuZ				~5		
	3Cu48CeZ				~55(continuous decline)		
	5Cu48CeZ				~61(continuous decline)		
	10Cu48CeZ				~50(continuous decline)		
	3Cu20CeZ				~34(continuous decline)		
	5Cu20CeZ				~39(continuous decline)		
	10Cu20CeZ				~45(continuous decline)		
	3Cu10CeZ				~20(continuous decline)		
	5Cu10CeZ				~32(continuous decline)		
	10Cu10CeZ						
2020	L-K-Mo_2C/γ-Al_2O_3 (Lab Scale Reactor)	450	21	3:1	22.1 (36.7 L Kg^{-1} S^{-1})	97.3	[191]
	P-K-Mo_2C/γ-Al_2O_3				26.8 (36.7 L Kg^{-1} S^{-1})	99.3	
	LC-P-Mo_2C/γ-Al_2O_3				42.7 (36.7 L Kg^{-1} S^{-1})	99.1	
	P-K-Mo_2C/γ-Al_2O_3				33.1 (18.3 L Kg^{-1} S^{-1})	99.88	
	P-K-Mo_2C/γ-Al_2O_3				42.1 (1.80 L Kg^{-1} S^{-1})	99.1	
	P-K-Mo_2C/γ-Al_2O_3 (Pilot Scale Reactor)				48.0 (1.70 L Kg^{-1} S^{-1})	98.9	
	P-K-Mo_2C/γ-Al_2O_3(Lab Scale Reactor)		1		21.2 (1.80 L Kg^{-1} S^{-1})	93.3	
	P-K-Mo_2C/γ-Al_2O_3	600	21		59.0 (3.70 L Kg^{-1} S^{-1})	98.1	
	Revitalized P-K-Mo_2C/γ-Al_2O_3				58.7 (3.70 L Kg^{-1} S^{-1})	43.2	
	P-K-Mo_2C/γ-Al_2O_3	300			1.20 (36.7 L Kg^{-1} S^{-1})	99.2	
	Cu-ZnO/Al_2O_3	300			23.3 (36.7 L Kg^{-1} S^{-1})	92.6	
	$FeCrO_x$	450			47.5 (36.7 L Kg^{-1} S^{-1})	48.6	
2020	VC-1 (Vanadium Carbide)	600	1	H_2:CO_2:N_2 ; 3:1:1	~33	>99.95	[192]
	VC-2				~44	>99.95	
2020	Cu-Al	400	1	H_2:CO_2:Ar ; 2:1:10	~2	100	[193]
	Co-Al				~9.5		
	Co-Al-AT (Alkaline Treated)				~5		
2021	ZnMnCoCa 1441	700	1		~49	High	[194]
	MnCoCa 122				~55		
	ZnMnCoCa 111				~39		
	ZnMnCo 118				~55		

Table2.3(Contd)

Year	Catalyst	T(°C)	Pressure (bar)	Feed H_2:CO_2	CO_2 Conversion (%)	CO Selectivity (%)	Reference
2021	Pd@UiO-66	400	20	3:1	~16(24,000 GHSV)	52.3	[195]
	Pd@Pt_{NPs}@UiO-66				~17	85.9	
	Pd@Pt_{NCs}@UiO-66				~19	72.3	
	Pd@Pt_{NCs}@UiO-66		10		~9	69.5	
	Pd@Pt_{NCs}@UiO-66		30		~22	86.2	
	Pd@Pt_{NCs}@UiO-66		20		~23(12,0000 GHSV)	78.4	
	Pd@Pt_{NCs}@UiO-66				~15(36,0000 GHSV)	83.9	
2021	0Cs-CuCe	450	1	9:1	~60	77	[196]
	1Cs-CuCe					89	
	2Cs-CuCe					95	
	3Cs-CuCe					96	
	4Cs-CuCe					98	

Chapter 3

Selection of catalytic agent, support, synthesis method, catalysts preparation and experimental techniques

3.1 Introduction

The history of catalysis (making cheeses, bread, and wine) is 2000 years long [197], but it was J.J. Berzelius who first defined a catalyst scientifically in 1836 [198]. However, the definition presented by Ostwald in 1895 is considered as the most accurate until now [199]: “A catalyst is a substance that accelerates the chemical reaction without influencing equilibrium location and reaction thermodynamics."

In industrial processes, the application of heterogeneous catalysis is more common than homogeneous catalysis because it is easier to separate the catalyst from products and unconverted reactants [200]. Heterogeneous catalysis is a surface phenomenon that requires the adsorption of the reactants on the solid surface preceded by the products desorption. Therefore, the catalytic properties are determined collectively by the solid particle's surface composition and electronic or geometric surface configurations [201]. For the following overall reaction (eq. 8), two types of catalytic reaction mechanisms are proposed in the literature [72]. Fig.3.1 shows the simple schematic of the mechanisms. According to reaction mechanism (a), one reactant needs to be chemisorbed on the solid surface to make an intermediate that will eventually react with the other reactant in the fluid phase to produce products. Similarly, according to the mechanism (b), both reactants must be chemisorbed on the surface and react to produce products. Where X, X_1, and X_2 represent the corresponding active catalytic sites.

$$A + B \leftrightarrow C + D \qquad (8)$$

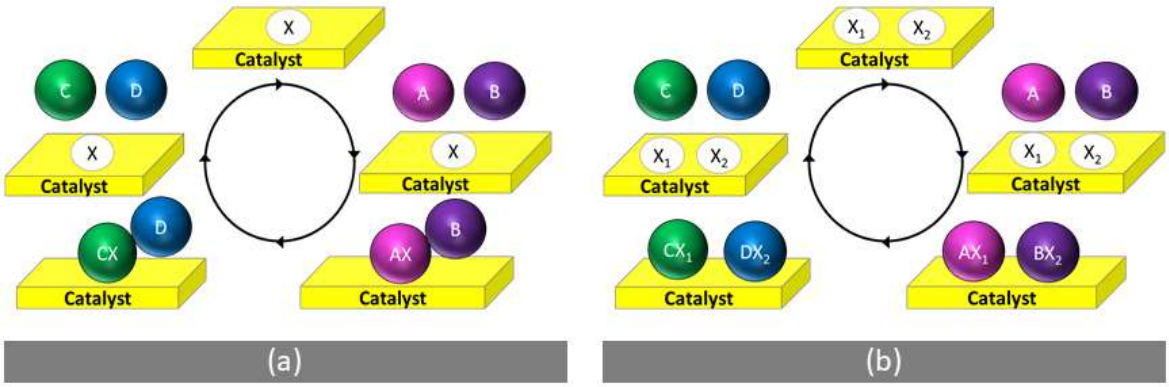

Figure 3.1: Catalytic reaction mechanism (a) one reactant chemisorption (b) both reactant chemisorption.

A catalytic reaction occurs at the solid-fluid interface and is directly proportional to the concentration of active sites X. This strongly emphasizes that to attain the desired reaction rate, a catalyst with a larger interfacial area is essential. In addition to the specific surface area, catalyst stability, reaction selectivity, and resistance to deactivation (due to coking, poisoning, and sintering) need to be considered while selecting a potential catalyst candidate for this study. Generally, a catalyst consists of a catalytic agent, support, and in some instances, the promoter. Therefore, for targeting the desired reaction, i.e., RWGS, it is essential to select a catalytic agent, support, and synthesis method that could help synthesize a catalyst with the smallest particle size (with larger surface area and active sites X), high selectivity towards CO, high stability in retaining the crystal structure and resistance to deactivation and coking.

After a comprehensive literature review, CeO_2 was selected as the potential catalytic agent, γ-Al_2O_3 was selected as the support, and the reverse-microemulsion method (RME) was chosen as the catalyst synthesis method. The following sections will give a deep insight into each selection individually.

3.2 Catalytic Agent (CeO_2) Selection

Considering the primary goal of this study, CeO_2 (ceria) was selected as the potential catalytic agent because of its high reducing abilities [202-204], 100% CO selectivity towards RWGS [20-22], and its ability to retain fluorite crystal structure after reduction [115, 205, 206].

Cerium is the amplest rare earth metal on the earth's crust and is more common than lithium, cobalt, and copper [207]. Cerium oxide (ceria) has been the subject of several scientific studies in the field of heterogeneous catalysis for decades. It can lose O^{2-} atom at high temperatures and reduce cerium from Ce^{4+} to Ce^{3+}, creating an oxygen vacancy in the crystal lattice while keeping the crystalline structure. This oxygen vacancy acts as the leading active site for catalytic reactions [23, 115]. Fig. 3.2 shows a simple schematic of ceria having Ce^{4+}, $Ce^{3+,}$ and oxygen vacancy [208]. Commercially, ceria is used as a catalyst support in three-way catalyst [209] and fuel cells as solid electrolyte [210, 211]. A three-way catalyst simultaneously oxidizes hydrocarbon, CO, and NO_x in exhaust gases, turning them into innocuous elements such as water, nitrogen, and CO_2. In addition to commercial uses, ceria has been reported as an alternate material for CO oxidation [212-214], NO oxidation [215], hydrocarbons oxidation [216], steam reforming of bio-oil [217], and for low-temperature water-gas shift reaction [218-220].

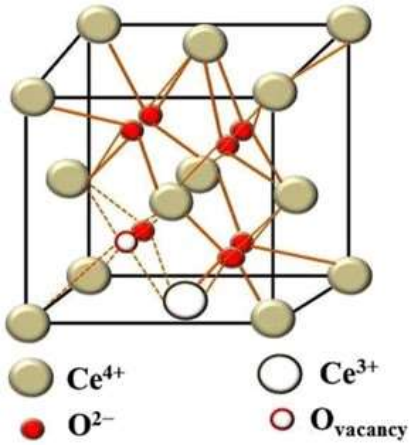

Figure 3.2: Schematic of CeO_2 showing Ce^{4+}, Ce^{3+} and Oxygen vacancy [208].

High performance, selectivity, and long life are the backbone of many scientific pursuits in the synthesis and design of a catalyst. A catalyst surface morphology plays a vital role in the activity and the selectivity for a specific reaction [221]. Ceria could be synthesized in different morphological shapes, including cube, rod, wires, tubes, and octahedra with different exposed crystallographic plane facets (111), (100), (110), or (200) [205]. Fluorite structured ceria expose stable (111) planes [222, 223]. Désaunay et al. [222] studied the H_2 oxidation on three different morphological shapes of ceria: cubes (100), rods (110), and octahedra (111) and found that the H_2 oxidation activity was highest on the (100) facets while the least on the (111) facets. Other studies reported the similar behavior of ceria rods to have the highest CO oxidation activity with activity trend of rods > cubes > octahedra [212-214]. It has been reported that ceria nanoparticles generally have octahedral shapes with exposed (111) crystallographic planes [224, 225]. It has also been reported that pre-treatment of the ceria surface effectively changes the product selectivity. Mullins et al. showed that over fully oxidized ceria (111), methanol adsorption is preceded by formaldehyde and water desorption, while when ceria (111) was pre-reduced, desorption of CO and H_2 took place [226].

This concludes that cubes and rod-shaped ceria particles, having (100) and (110) exposed facets, are more active towards oxidation reactions, while ceria with (111) facet is the least active towards oxidation reaction. Table 2.3 outlined all the potential catalysts that have been deployed so far for the thermo-catalytic RWGS application. It can easily be seen that only a few studies have been reported over unsupported ceria (cubes, rods, particles) for the application of the RWGS reaction [18-22]. These studies said ceria cubes being the highest active with either low selectivity to CO or low CO_2 conversion to CO. Dai et al. reported the highest conversion (16% at 580°C) of CO_2 to CO (with 100% selectivity) over the bulk ceria produced via the hard template method [20].

In the light of the above facts, it was necessary to study and explore the potential of RWGS over unsupported and supported high specific surface area octahedral shaped nano-ceria particles with

exposed (111) facets. To control the morphological structure of ceria in addition to higher surface area, a careful review was required for the selection of catalytic support and synthesis method.

3.3 Catalyst Support Selection

Although the catalytic activity of a catalyst is essential, even more critical is the selectivity. Selectivity could be enhanced by supporting a catalytic agent over a porous metallic oxide that could significantly increase the specific surface area leading to an increase in active sites concentration on the exposed surface [72]. Porous materials provide specific surface areas up to several hundred m^2 g^{-1}. For example, α-alumina has areas ranging from 1-10 m^2 g^{-1}, while γ-alumina provides areas ranging from 100-300 m^2 g^{-1}. The high surface area supports also help in better dispersion of the catalytic agent that reduces the chance of sintering or agglomeration [72].

Table 2.3 shows that the conversion and selectivity were significantly enhanced when the same catalytic agent was incorporated for the different supports. For example, Pettigrew et al. [118] incorporated various lanthanide oxides as support with Pd for RWGS studies and found the order of activity as CeO_2> PrO_2 > La_2O_3. Wang et al. [227] also reported that CeO_2 supported Au shows higher activity than Au/TiO_2 due to the higher oxygen mobility of CeO_2. Kim et al. [77] showed that Pt/TiO_2 catalyst produces more CO_2 conversion than Pt/Al_2O_3 because of the strong metal-support interaction and high reducibility of support. Similarly, Jurković et al. [92] also investigated the potential of Cu-supported catalysts for the RWGS reaction and found out the order of activity as CeO_2>Al_2O_3>TiO_2>ZrO_2=SiO_2. Therefore, the selection of catalyst support is an essential step towards developing a highly active and selective supported catalyst for RWGS.

After a careful literature review, γ-Al_2O_3 was selected as the potential porous support because of its higher specific surface area and CO selectivity.

3.4 Synthesis Method Selection

After selecting the catalytic agent and support candidates for the study, the next significant and crucial step was selecting the synthesis method.

In conjunction with regulated shaped particles, the synthesis of nano-scale size with different atomic configurations or facets is an effective method to boost the selectivity, durability, and operation of heterogeneous catalysis [228-233]. It has been reported that limiting the size to nanoscale could introduce quantum effects [234-238]. Zhou and Huebner studied particle size's impact on the CeO_2 lattice and reported that a decrease in particle size from 60 nm to 4 nm results in doubling the amount of oxygen vacancies [239]. Soykal et al. reported that during steam reforming of ethanol, the smaller size ceria particles undergo higher reduction, leading to higher conversion at 450°C [240]. Zhang et al. also reported that for the controlled synthesis of nanocrystalline ceria (up to ~ 6 nm), the oxygen storage capacity (OSC) raised significantly [225]. Therefore, the synthesis of nano-sized ceria is essential for better activity and selectivity.

Considering the uniqueness of the work, the following points were considered for the method selection:

1) The synthesis method should be able to produce nano-size ceria with high specific surface area.
2) The synthesis method should be able to produce ceria with exposed (111) facets.
3) The synthesis method should be able to produce highly porous $CeO_2/\gamma\text{-}Al_2O_3$.
4) The most important objective is to deploy a synthesis method that has not been used for bulk CeO_2 and supported $CeO_2/\gamma\text{-}Al_2O_3$ applications specifically for reverse water gas shift (RWGS).

After a comprehensive literature review, it was found that the reverse microemulsion method (RME) is the only synthesis method that fulfills all the above-mentioned requirements. There is literature available on the synthesis of CeO_2 via reverse microemulsion method [23-26, 241, 242],

but these studies focus on different applications (especially oxidation). The corresponding maximum specific surface area and smallest particle size reported in these studies is 125 m^2 g^{-1} and 6 nm [23], ~53 nm [24], 185 m^2 g^{-1} and 2.6 nm [25], 65 m^2 g^{-1} and 15 nm [26], 2-3 nm [241], 250 m^2 g^{-1} (with low thermal stability) and 6 nm [242]. Considering the potential of RME method to produce high specific surface area, smaller particle size, and controlled morphology (targeted (111) facets), it is selected as the primary catalysts synthesis process for this Ph.D. studies.

3.4.1 Reverse Microemulsion (RME) Method

The microemulsion is a system that consists of water, oil, and surfactant. Though the appearance indicates homogeneity, in fact, the microemulsion comprises two distinct phases. In reverse microemulsions, oil is present as a continuous phase, while water, surrounded by surfactant molecules, is suspended in the oil phase. This water-in-oil mechanism is known as a reverse emulsion . Owing to the hydrophilic heads of surfactant molecules being drawn by the water, the tail stretches out of the water droplet. An additive is applied to the system to improve the reliability of both systems and is known as a co-surfactant. When various RMEs are added together, they behave as nano-reactors, restricting the number of reactants to prevent particle growth. As surfactant shell and micelles interact, the surfactant shell may accumulate, and the reactant may react [243]. Fig. 3.2 shows the simple schematic of the process [244].

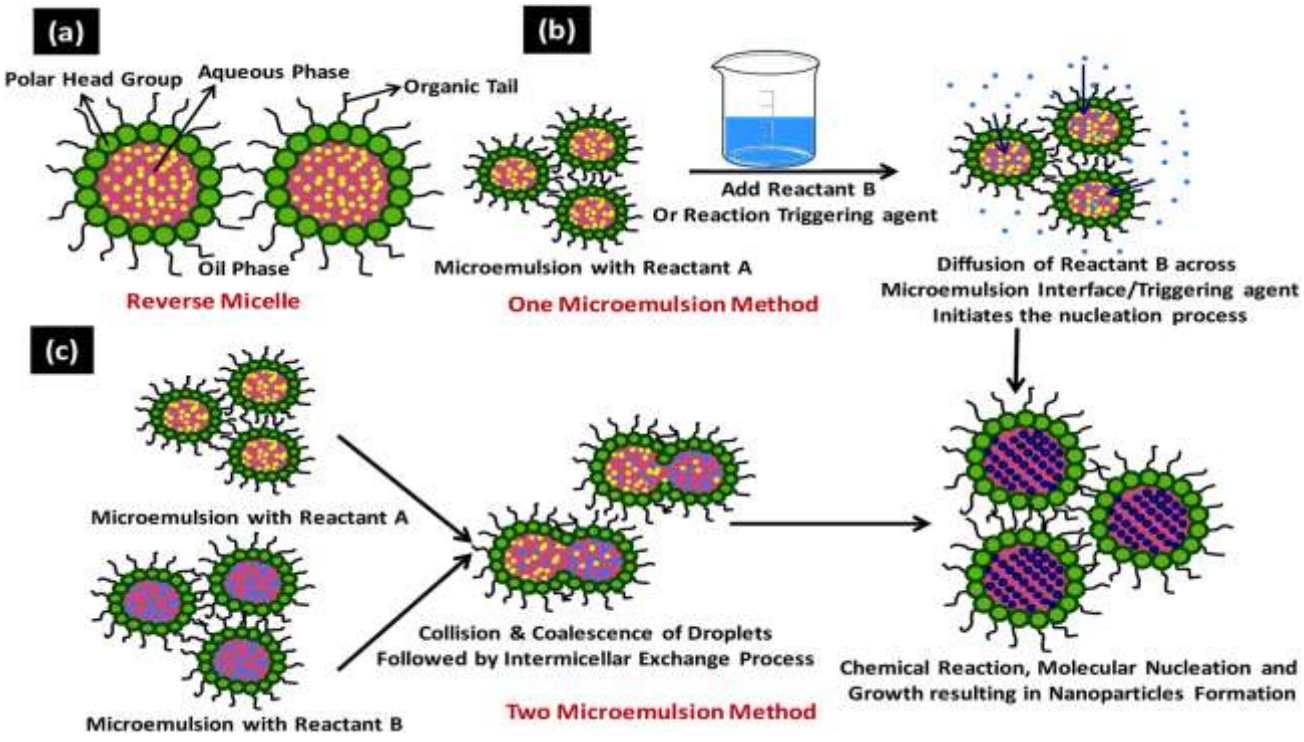

Figure 3.3: (a) typical reverse micelle system, (b) various steps involved in one microemulsion process, and (c) reaction sequence involved in the two microemulsion nanoparticles synthesis [244].

3.4.2 RME Composition Selection

Schulman et al. [245] were the first who introduces reverse microemulsion (RME) as a new synthesis method in 1959. They demonstrated that to obtain a transparent system, all the four components (surfactant, co-surfactant, oil, and aqueous phase) need to be present in a perfect ratio. They also reported that sometimes an extra amount of co-surfactant might add to get a completely transparent solution. Later, it was reported that the R_w (molar ratio of water/surfactant) and strength of the aqueous phase in the final solution directly affects the mean particle size [25, 246, 247]. Therefore, to control the crystal growth and crystallite size, the catalyst synthesis's first necessary step was selecting the RME solution's final ratio and strength of the aqueous phase.

As an initial guess, the RME composition (15, 10, 40, and 35% Vol. ; Aqueous phase, surfactant, co-surfactant, and Oil phase, respectively) was selected from our group's ongoing work on Mo_2C at that time, published earlier this year, 2021 [248]. However, this formulation does not work to develop bulk RME-ceria, and several experiments were conducted to finalize the RME composition and aqueous phase strength. Considering the initial guess, for the aqueous phase to surfactant ratio of 1.5, the Rw appeared to be ~50, which was relatively high, leading towards bigger water droplets and eventually will be providing more space for reaction and crystal growth within the reverse micelles [25, 246, 247]. Thus, the ratio was decreased to 1, which significantly reduced the Rw to roughly 35. The next step was to find out the co-surfactant, oil phase ratios, and aqueous phase strength in the final mixture.

Four different cerium nitrate solutions were prepared to determine the final ratio and strength, i.e., 25, 50, 100, and 200 g/L. Targeting the total RME volume of 10 ml, surfactant, co-surfactant, and oil phase was mixed in a ratio of 1:4:3.5, respectively. Next, 2 ml of cerium nitrate solution of each strength was added to make the final solution composition of 1:1:4:3.5. All the final solutions appeared translucent under constant stirring, as shown in Fig. 3.4. When these RME's were placed away from the stirrer plate for 5 minutes, the solutions separated into two transparent immiscible layers, as shown in Fig 3.5.

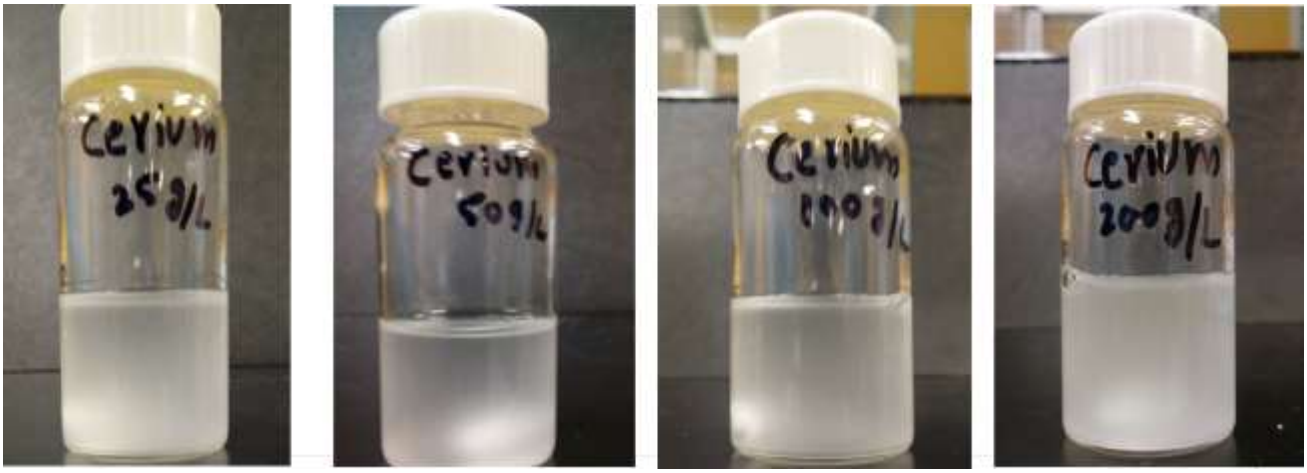

Figure 3.4: Translucent RMEs containing 25, 50, 100 and 200 g/L cerium nitrate.

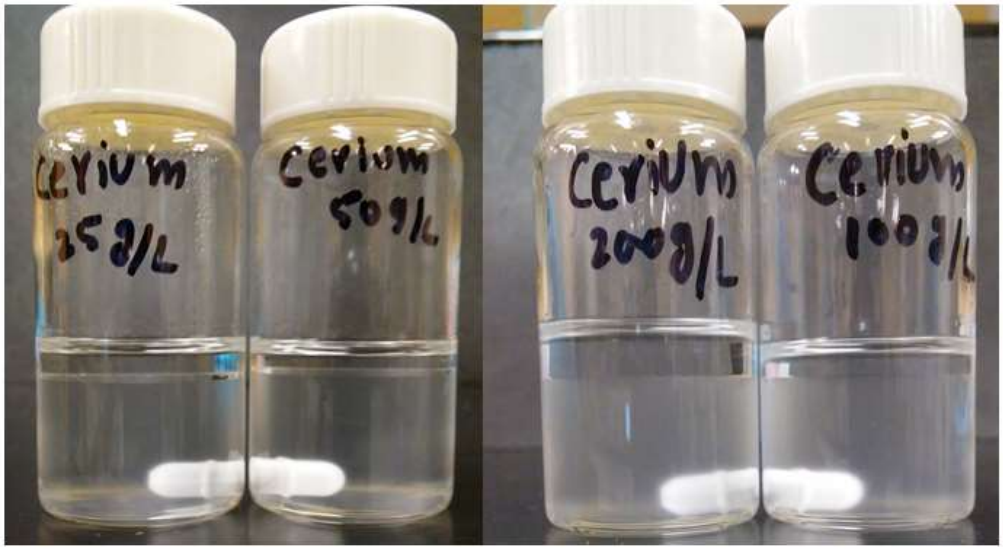

Figure 3.5: RMEs separated into two layers.

As per the recommendation of Schulman et al. [245], extra co-surfactant was added dropwise while stirring. It was observed that all the RME's instantly turns transparent with a single homogenous layer after adding 1, 0.5, 0.5, and 3.5ml of co-surfactant, as shown in Fig. 3.6.

Figure 3.6: Clear RMEs after the addition of an extra co-surfactant.

RME's having 25 and 200 g/L cerium nitrate aqueous phase requires extra co-surfactant in large amounts compared to the RME's having 50 and 100g/L cerium nitrate aqueous phase. From these experimental observations, the cerium nitrate aqueous phase of strength 100 g/L and the ratio of the aqueous phase, surfactant, co-surfactant, and oil phase were selected to be 1:1:4.5:3.5, respectively, for the rest of the experiments.

Moving forward with 100 g/L cerium nitrate solution, the solution molarity was found to be 0.306 M. Further targeting 1g RME-ceria synthesis, the volume of the aqueous solution was calculated using the simple equation from basic chemistry (eq. 9), and it comes to 18.9 ml. To make the solution preparation easier for further studies, the volume was rounded off to 20ml, which eventually led to finalize the cerium nitrate aqueous solution strength and molarity of 94.6 g/L and 0.29 M, respectively.

$$g_{(solute)} = Mol.Mass \times Molarity \times Volume \qquad (9)$$

3.5 Catalyst Synthesis

To explore the potential of nano-ceria with exposed (111) crystallographic planes for the RWGS application, five different types of bulk and supported ceria catalysts were prepared:

1. The baseline catalyst was prepared using the direct precipitation method and denoted as DP-ceria.
2. Nano-ceria was prepared via the RME method and denoted as RME-ceria.
3. Three supported $CeO_2/\gamma\text{-}Al_2O_3$ catalysts (20, 30, and 40%wt. ceria) were prepared via the RME method and denoted as 20% Ce/Al, 30% Ce/Al, and 40% Ce/Al throughout the text.

Considering the main focus of the catalyst synthesis i.e. to achieve high surface area ceria, a calcination temperature of 275°C was selected because it has been reported that ceria loses its surface almost 50% as the calcination temperature increased from 300°C to 600°C [26]. Similarly, an initial higher surface area is necessary to create enough oxygen vacancies over ceria to facilitate the RWGS reaction, as oxygen vacancies play the leading role in ceria catalysis. Another fact is that the surfactant Trinton X-100 has a boiling point of 270°C. Therefore, calcination temperature was initially set to 275°C to make sure the removal of surfactant and to keep the crystalline size as small as possible. Detailed investigation on the effect of calcination temperature is given in chapter 6.

A detailed synthesis procedure for each catalyst is presented in the upcoming respective chapters (4, 5, and 6). In the following section, simple schematic diagrams are presented for a quick understanding of the synthesis sequence.

3.5.1 Chemicals and gases

Cerium nitrate hexahydrate (99.5%, Alfa Aser) and ammonium hydroxide (28-30% NH_3 basis, Sigma-Aldrich) were used as the precursor for the preparation of RME- and DP-ceria. Aluminum nitrate nonahydrate (99+%, Acro organics) was used for the preparation of all $CeO_2/\gamma\text{-}Al_2O_3$ catalysts. Triton X-100 (Acro organics), 2-Propanaol (99.9%, Sigma-Aldrich), and cyclohexane (>99%, Sigma-Aldrich) were used as surfactant, co-surfactant, and oil phase, respectively, for the RME making. High purity H_2 (99.999%) and CO_2 (99.9%) gases were purchased from Praxair Technology, Inc.

3.5.2 DP-ceria Synthesis Schematic

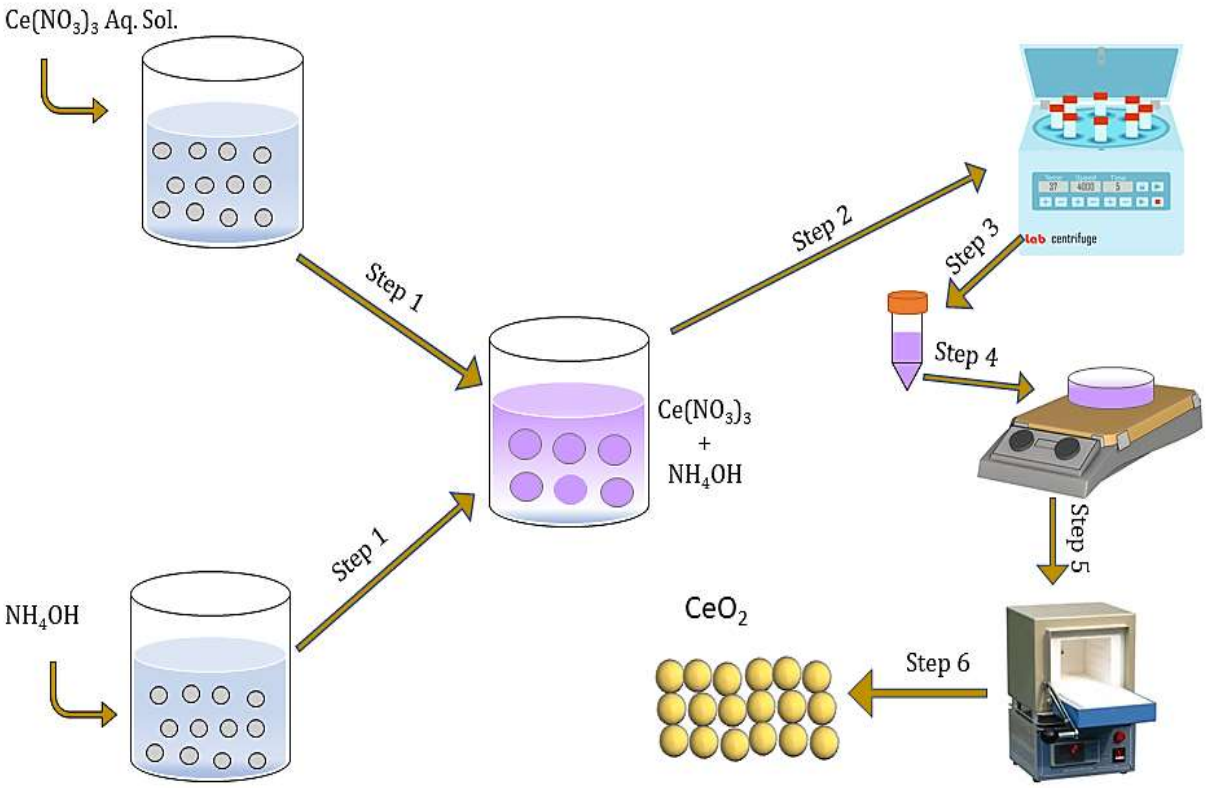

Figure 3.7: DP-ceria synthesis schematic: step1 mixing of aqueous phases, step2 centrifugation, step3 collection of wet ppt, step4 drying at 150°C, step5 calcination, step6 catalyst collection.

3.5.3 RME-ceria Synthesis Schematic

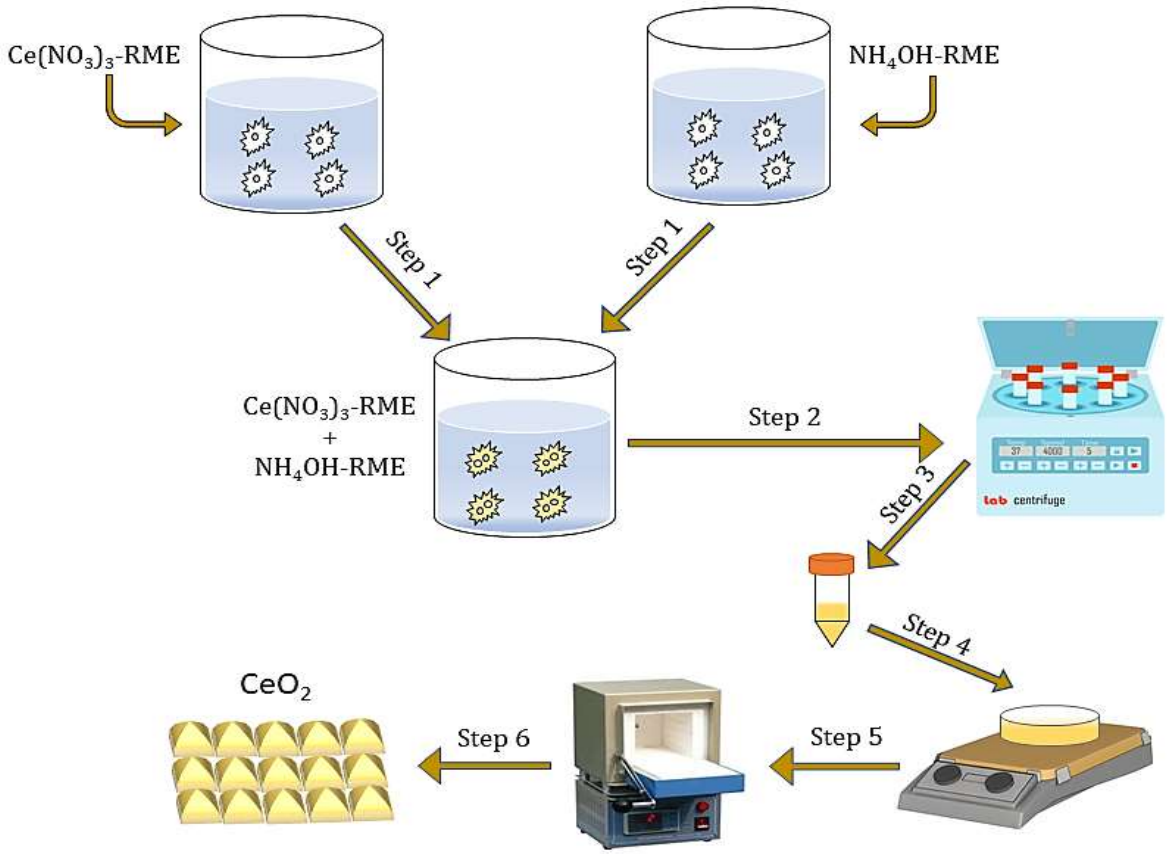

Figure 3.8: RME-ceria synthesis schematic: step1 adding $Ce(NO_3)_3$-RME to NH_4OH-RME, step2 centrifugation to separate ppt, step3 collection of wet ppt, step4 drying at 150°C, step5 calcination, step6 catalyst collection.

3.5.4 RME-ceria supported γ-Alumina Schematic

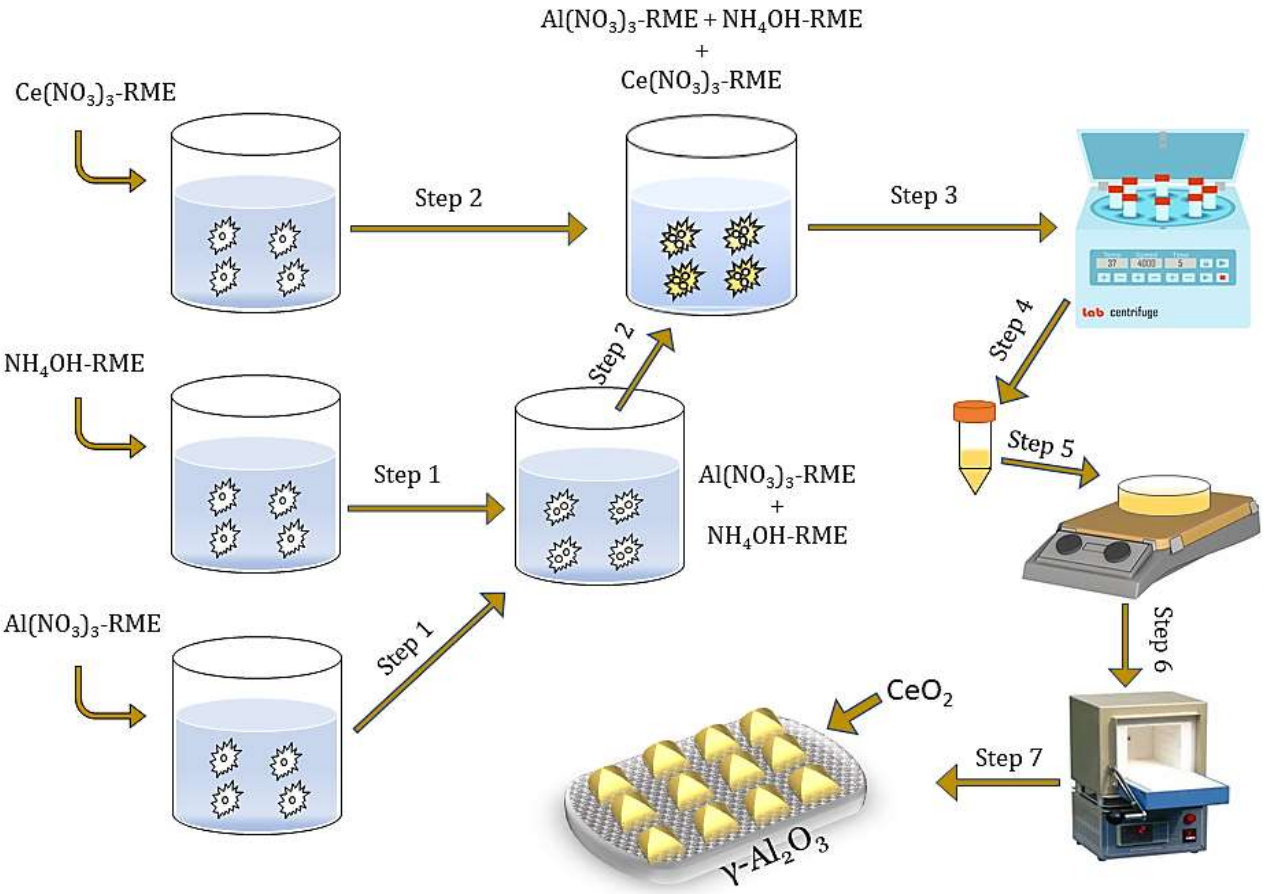

Figure 3.9: RME-CeO_2/γ-Al_2O_3 synthesis schematic: step1 adding $Al(NO_3)_3$-RME to NH_4OH-RME, step2 adding $Ce(NO_3)_3$-RME, step3 centrifugation at 3500 RPM to separate ppt, step4 collection of wet ppt, step5 drying at 150°C, step6 calcination, step7 catalyst collection.

3.6 Experimental Techniques

3.6.1 Flow System Configuration

(a)

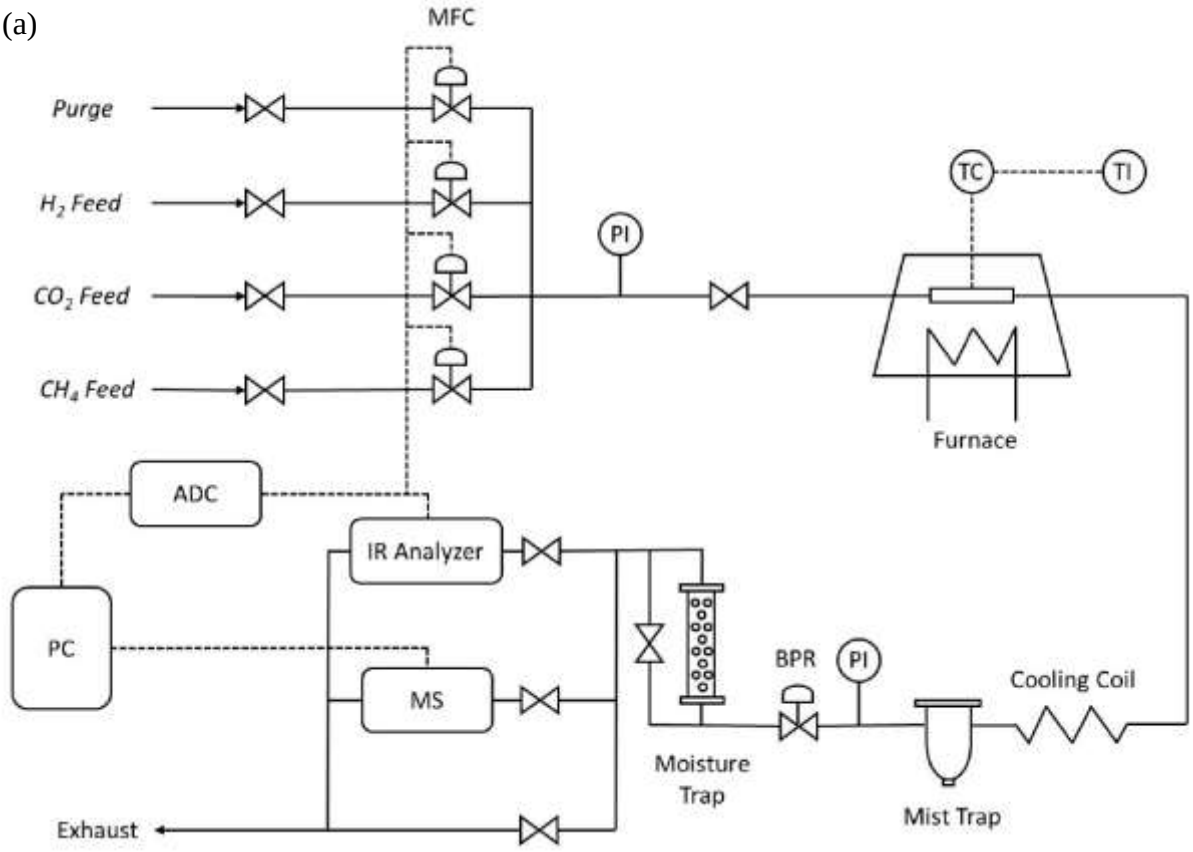

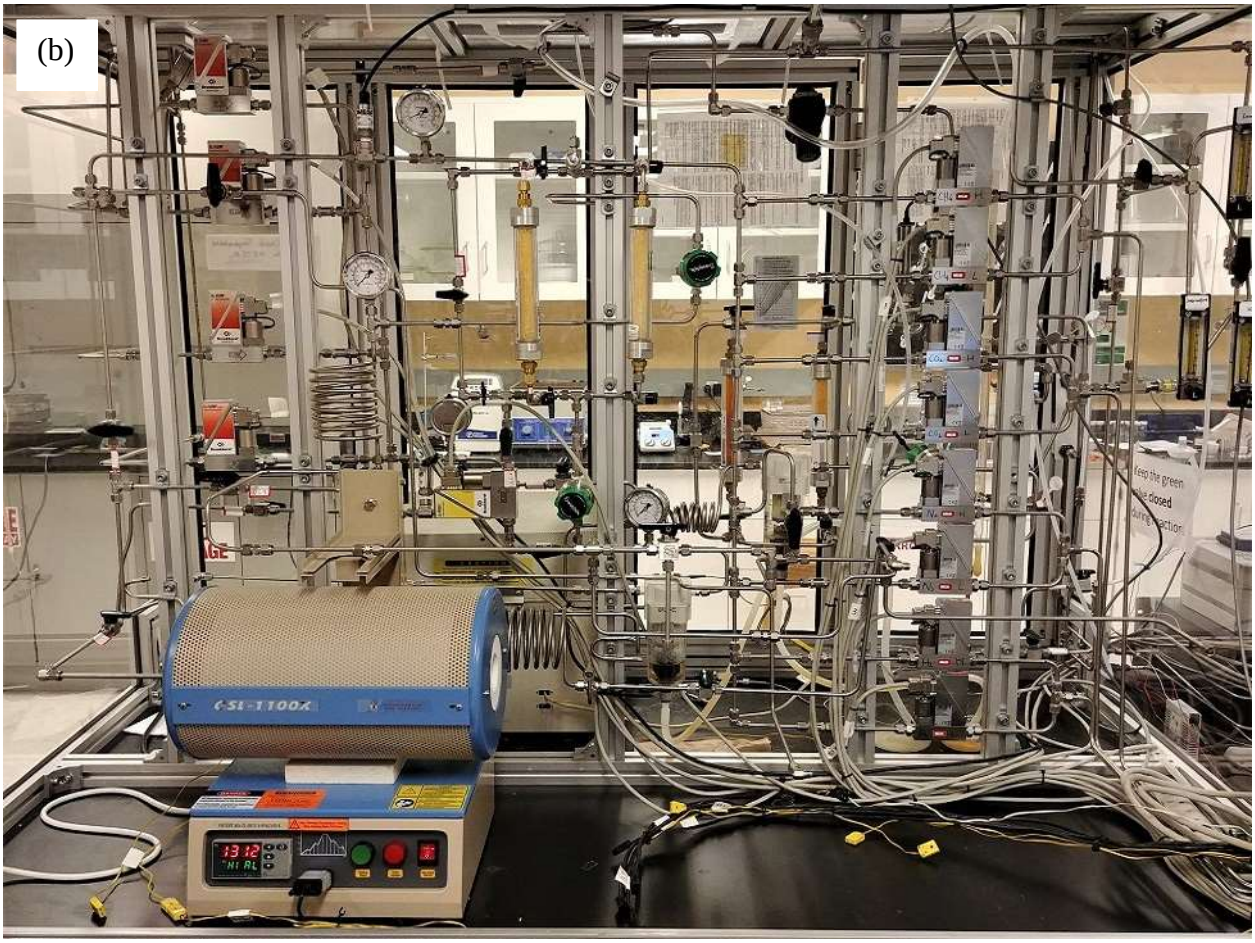

Figure 3.10: Flow system configuration for catalyst performance determination (a) schematic (b) original setup. Abbreviations: ADC (analog-to-digital converter), BPR (back pressure regulator), IR (infrared), MFC (mass flow controller), PI (pressure indicator), PC (personal computer), RH (relative humidity), TC (thermocouple), TI (temperature indicator).

Fig. 3.10(a) shows the flow sheet diagram of the original setup (Fig. 3.10(b)) for the catalyst performance evaluation. The flow rate of H_2 and CO_2 were controlled using digital mass flow controllers. The reactor was made by joining a 1/2″ stainless steel tube (Swagelok) with 1/4″ stainless steel tube (Swagelok) with the help of adapters (Swagelok). 1/2″ tube was used for the easy loading and unloading of the catalyst. Both tubes' joining point was clogged with quartz wool to hold catalyst without any escape from the system. K type thermocouple (1/8″, Omega Engineering, Inc.) was placed inside the reactor, directly touching the quartz wool near the catalyst bed to ensure the correct

temperature measurement. The catalyst was loaded from the open side of the 1/2″ tube. A quartz wool ball was inserted after catalyst loading to make a catalyst sandwich between two quartz wool pieces to get a packed bed. Next, the reactor was placed inside the furnace while ensuring the catalyst bed should remain in the tube system's center. Fig. 3.11 shows the schematic and original pictures of the kinetic reactor.

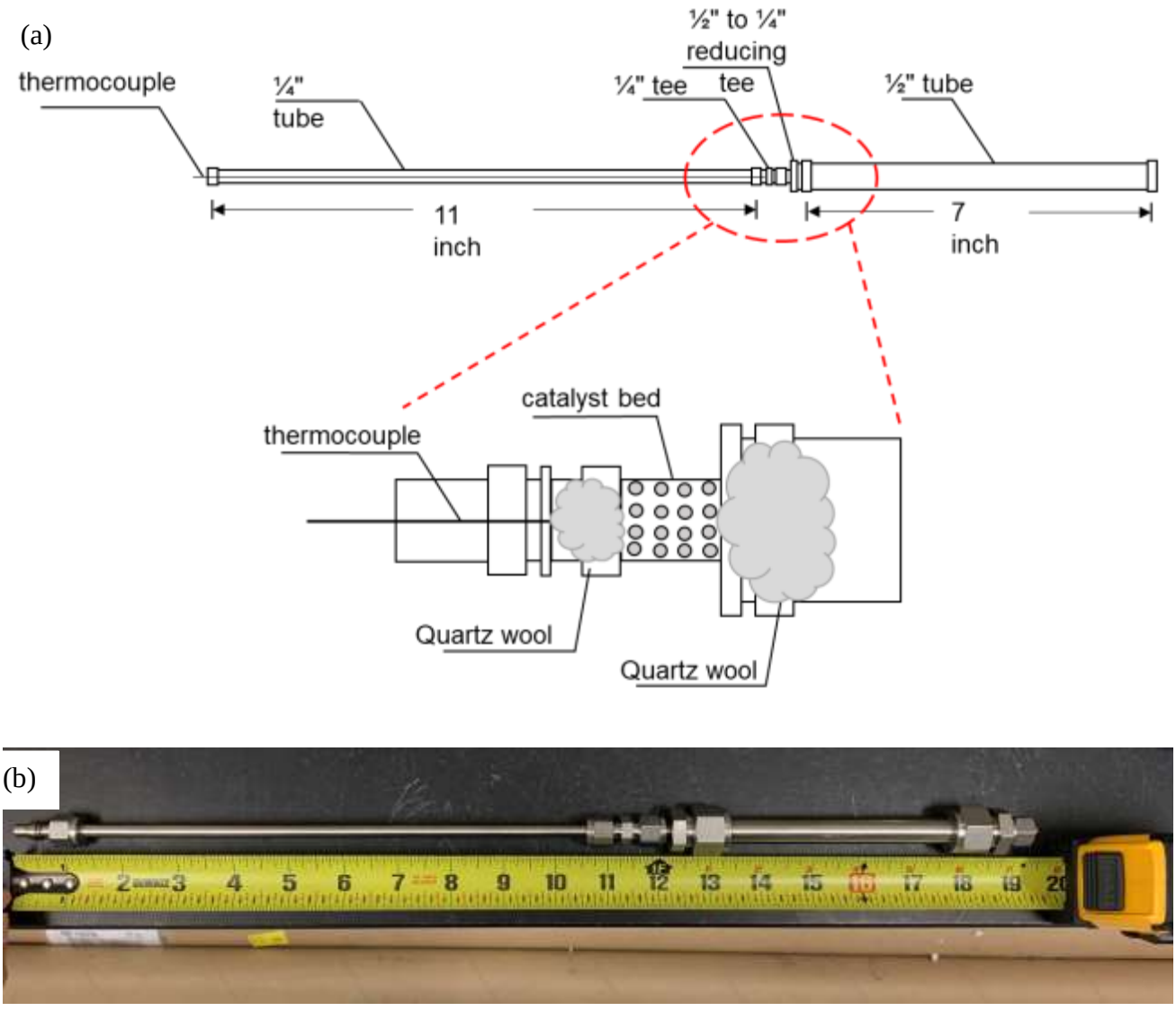

Figure 3.11: Kinetic reactor (a) schematic (b) original.

The furnace was programmed for a temperature range of 300-600°C using a built-in automatic temperature controller. An automatic back pressure regulator was used to control the pressure in the system at 3 bar (absolute), a mist trap (SMC Corporation, AFM40-N02-Z-A) was installed before the pressure regulator to remove the water produced during the reaction, and after the pressure regulator, silica gel column (orange silica gel, Fisher Scientific) was installed to remove the remaining moisture from the outlet gases before going to IR analyzer for measurement. After complete water removal, gases were allowed to enter into IR-gas analyzer (R-208, Infrared Industries, Inc., USA) to measure the composition of CO_2, CO, and CH_4 in the outlet gases, on a dry basis, continuously monitored using an analog-to-digital converter (USB 6008, National Instruments) and LabVIEW (National Instruments). Fig. 3.12 shows the complete setup used to run the long-term (~100 h) stability tests using a 1/4″ U-shaped quartz tube in the same flow system with a small furnace (KSL-1100X, MTI corporation).

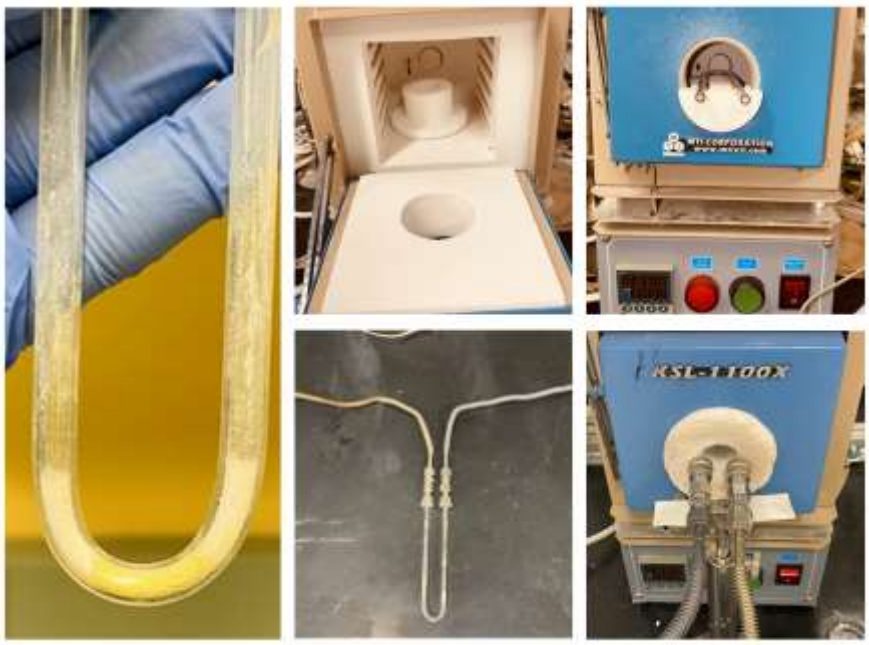

Figure 3.12: Experimental setup configuration for long term stability tests

3.6.2 Catalyst Performance and Activity Test

Before each experiment, a fresh catalyst was first reduced under a pure hydrogen environment for 2 hours. A flow of 100 ml min^{-1} of H_2 was provided at a temperature of 400°C for the reduction. The catalyst performance was measured using total CO_2 conversion and CO selectivity for the temperature range of 300-600°C at 3 bar absolute (in all experiments using stainless steel reactors) and a space velocity of 60,000 ml g_{cat}^{-1} h^{-1}.

GHSV (gas hourly space velocity) was calculated using the following formula:

$$GHSV = \frac{Q}{W_c} \qquad (10)$$

Where Q is the volumetric total gas flow rate, and Wc is the catalyst weight. CO_2 conversion (X_{CO_2}),CO selectivity (S_{CO}), and CH_4 selectivity (S_{CH_4}) was measure using the following formulas:

$$X_{CO_2} = \frac{y_{CO}+y_{CH_4}}{y_{CO_2}+y_{CO}+y_{CH_4}} \qquad (11)$$

$$S_{CO} = \frac{y_{CO}}{y_{CO}+y_{CH_4}} \qquad (12)$$

$$S_{CH_4} = \frac{y_{CH_4}}{y_{CO}+y_{CH_4}} \qquad (13)$$

Where y_{CO}, y_{CO}, and y_{CH_4} corresponds to mole fractions of the respective gases measured by the IR analyzer on a dry basis. Initially, a calibration curve was generated (while coupling the IR-cell with an in-line FTIR gas analyzer) for the continuous measurement of outlet gases. Calibration curves are presented in appendix A.

Carbon balance is defined as the total rate of carbon fed to the reactor over the total rate of carbon exiting the reactor, and it can be calculated by the following eq. 14.

$$CB = (y_{CO_2} + y_{CO} + y_{CH_4})(1 + \alpha - f_1 - 4f_2) \qquad (14)$$

Where α is the H_2 to CO_2 ratio, f_1 and f_2 are the conversions to CO and CH_4, respectively.

$$\alpha = \frac{F_{H_{2,f}}}{F_{CO_{2,f}}} \quad (15a)$$

$$f_1 = \frac{y_{CO}}{y_{CO_2} + y_{CO} + y_{CH_4}} = \frac{F_{CO,out}}{F_{CO_{2,f}}} \quad (15b)$$

$$f_2 = \frac{y_{CH_4}}{y_{CO_2} + y_{CO} + y_{CH_4}} = \frac{F_{CH_4,out}}{F_{CO_{2,f}}} \quad (15c)$$

Eq. (14) is obtained from the carbon balance definition, eq. (15d), using eq. (15a-c) and eq. (15e) to define the total outlet molar flow rate ($F_{CO,out}$ and $F_{CH_4,out}$ in Eq. (15e) correspond to H_2 consumption in RWGS and methanation, according to reaction stoichiometry):

$$CB = \frac{(y_{CO_2} + y_{CO} + y_{CH_4})F_{t,out}}{F_{CO_2,f}} \quad (15d)$$

$$F_{t,out} = F_{CO_2,f} + F_{H_2,f} - F_{CO,out} - 4F_{CH_4,out} \quad (15e)$$

Carbon balance (CB) was continuously monitored and recorded in all experiments (using LabVIEW). Deviations did not exceed 5% in all experiments, i.e., the carbon balance was in the *CB = 0.95-1.05* range.

3.6.2.1 Mass and Heat Transfer Criteria

The absence of interphase, Eq. (16,17), and intraparticle, Eq. (18,19), mass and heat transfer limitations was confirmed by calculating corresponding criteria (all symbols are listed below):

$$\frac{R'_{obs}\,\rho_b\,r_p}{k_c\,C_{CO_2,b}} \ll 0.15 \quad (\textit{Mears criterion for interphase mass transfer}) \quad (16)$$

$$\frac{|\Delta H_{RWGS}|R'_{obs}\,\rho_b\,r_p}{hT} \ll \frac{0.15TR_g}{E_a} \quad (\textit{Mears criterion for interphase heat transfer}) \quad (17)$$

$$\frac{R'_{obs}\rho_c r_p^2}{D_m C_{CO_2,s}} \ll 1 \quad (\textit{Weisz-Prater criterion for internal diffusion}) \quad (18)$$

$$\frac{|\Delta H_{RWGS}|R'_{obs}\,\rho_b\,r_p^2}{\lambda_s\,T_s} \ll \frac{0.75\,T_s\,R_g}{E_a} \quad (\textit{isothermal pellet criterion}) \quad (19)$$

where R'_{obs} is the observed reaction rate (mol kg^{-1} s^{-1}), ρ_b is the catalyst density (ml g^{-1}), r_p is the catalyst particle radius (m), $k_c$is the mass transfer coefficient, $C_{CO_2,b}$is the gas phase bulk CO_2 concentration (mol m^{-3}), ΔH_{RWGS} is the enthalpy change (kJ mol^{-1}), T is the temperature, R_g is the ideal gas constant (kJ mol^{-1} K^{-1}), h is the heat transfer coefficient (kJ m^2 s^{-1} K^{-1}), E_a is the activation energy (kJ mol^{-1}), $D_m$is the diffusion coefficient (m^2 s^{-1}), $C_{CO_2,s}$ is the surface CO_2 concentration (mol m^{-3}), λ_s solid thermal conductivity (kJ m^{-1} s^{-1} K^{-1}), and T_s surface temperature.

Interphase mass and heat transfer coefficients (k_c and h) were calculated using the following correlations:

$$\mathrm{Sh} = \frac{k_c d_p}{D_m} = 2 + 0.6\, Re^{\frac{1}{2}}\, \mathrm{Sc}^{\frac{1}{3}} \qquad (20)$$

$$\mathrm{Nu} = \frac{h d_p}{\lambda_g} = 2 + 0.6\, Re^{\frac{1}{2}}\, Pr^{\frac{1}{3}} \qquad (21)$$

where Sh is the Sherwood number, Re is the particle Reynolds number, Sc is the Schimdit number, Nu is the Nusselt number, $d_p$is the particle size (m), Pr is Prandtl number, and $\lambda_g$is the gas thermal conductivity, kJ m^{-1} s^{-1} K^{-1})

Calculations were conducted for low and high conversions in the 300-600 °C range and for the wide range of activation energies (E_a = 20-200 kJ/mol). In all cases, all transport limitations were completely negligible, as expected for the small size of catalyst pellets (350-425 μm) used in the experiments.

3.6.3 Inductively Coupled Plasma Optical Emission Spectroscopy (ICP-OES)

Catalyst composition was identified using ICP-OES (Inductively Coupled Plasma Optical Emission Spectroscopy). ICP-OES identifies and quantifies the elements present in the given sample based on their emission spectra. First, ICP produces a partially ionized gas (typically Ar, about 1% is ionized into plasma) using a 1-2.5 kW radio frequency power supply in a quartz torch, and then the

sample is introduced as aerosols into the plasma center. Sample atoms are excited by collisional activity that appeared due to high temperature. These exciting sample atoms or ions emit electromagnetic radiations of specific wavelengths while falling back to a lower energy state. The radiation emitted from ions is then focused onto the entrance slit of a monochromator or polychromator to identify and quantify the emission from different ions. The spectral lines' intensity is directly related to the quantity of the element present in the sample. Spectral lines are intense for the element, which is majorly present in the precursor. The following simple schematic diagram (Fig. 3.13) shows the complete working of the ICP-OES analysis procedure.

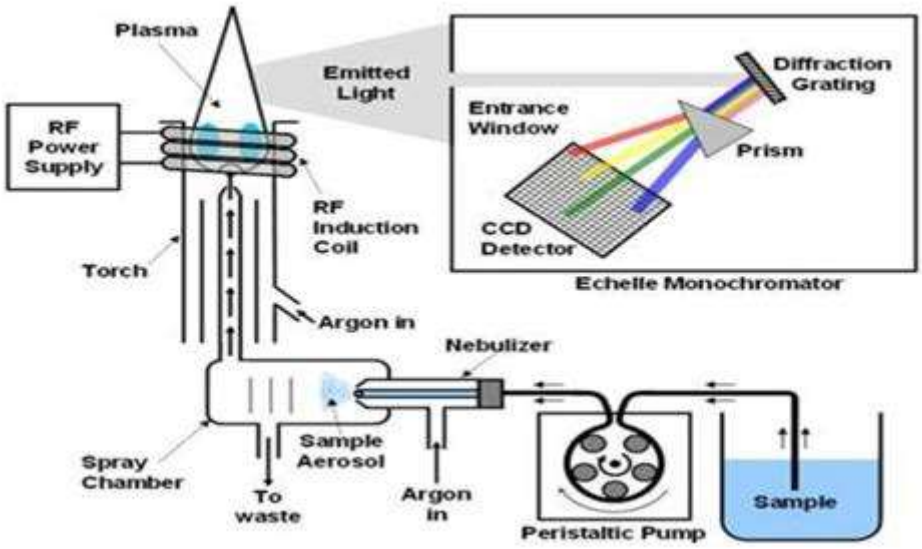

Figure 3.13: ICP-OES system schematic diagram [249].

3.6.4 X-Ray Diffraction (XRD)

X-ray diffraction (XRD) technique (D8 discover diffractometer, Bruker) was utilized to identify the crystallite size, crystallite structure, and the catalyst's theoretical density. XRD is based on the constructive interference of crystalline material with monochromic X-rays. A cathode tube generates

X-rays, which pass through a metallic slit to generate monochromic rays. The monochromic rays interact with the material under constructive interface and diffract to an angle following the Bragg's law ($n\lambda=2dSin\theta$) where n is a positive integer, d is the interplanar distance, λ is the wavelength of the incident ray, and θ is the scattering angle shown in Fig. 3.14.

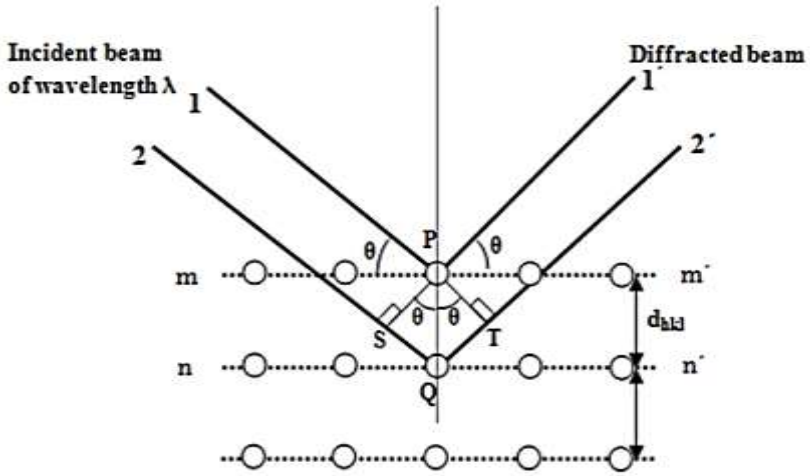

Figure 3.14: Schematic explanation of Bragg's law

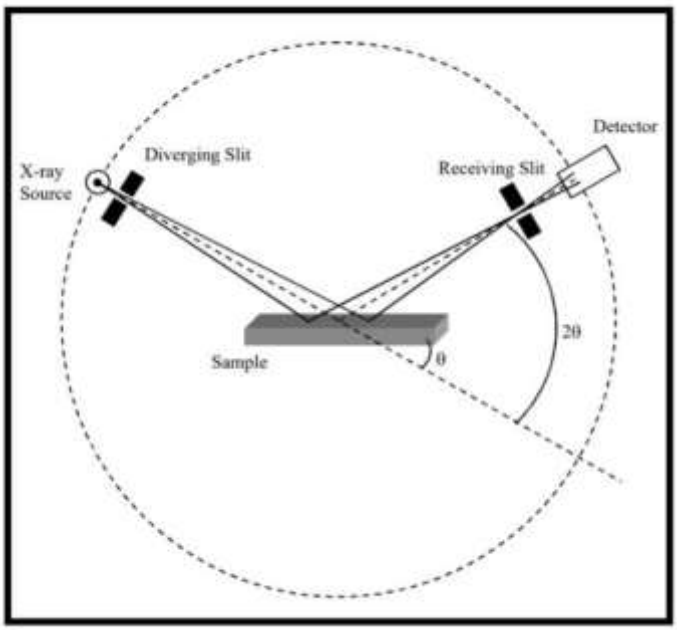

Figure 3.15: Schematic of the X-ray diffractometer [250].

XRD patterns were obtained at a scanning speed of 3 (time per step) with an increment of 0.1, and 2 ranged from 10-90. Fig. 3.15 shows the simple schematic of the X-ray diffractometer.

3.6.5 Brunauer Emmett Teller (BET) Specific Surface Area (SSA)

Specific surface area (SSA) was measured using Gemini VII 2390 BET surface area analyzer (Micromeritics Instrument Corporation). BET is the most used technique to measure the specific surface area based on inert gas's adsorption over the solid surface. The concentration of the gas absorbed over the solid surface depends upon the thermodynamic conditions, and this effect can be utilized to measure the surface area of solids.

In a typical BET surface area analyzer, the material is first heated at a temperature of 300°C under vacuum or by blowing an inert purge gas to remove any volatile contaminants. After removing the contaminants, the sample is placed under a high vacuum and a very low temperature, usually near the boiling point of nitrogen (-191.6°C). After achieving isothermal conditions, at this low temperature, an inert gas (like N_2, Ar, Kr) is introduced in a controlled manner to get adsorbed over the solid surface. During this stage, the sample is subjected to variable pressure to get an adsorption isotherm because the amount of gas adsorbed is directly related to the pressure. The resulting isotherm follows the BET model (eq. 22) as follow

$$\frac{1}{\nu\left(\frac{p_o}{p}\right)-1} = \frac{c-1}{\nu_m c}\left(\frac{p_o}{p}\right) + \frac{1}{\nu_m c} \qquad (22)$$

Where "p_o" and "p" are adsorption and saturation pressure of adsorbate at adsorption temperature, ν is the adsorbed gas quantity and ν_m the quantity of monolayer adsorbed gas, and c is the BET constant. One adsorbed nitrogen molecule occupies the cross-sectional area (ACS) of 16.2Å. Therefore, BET surface (A) can be calculated using eq. 23.

$$A = \frac{ACS * \nu_m * N_A}{M_{N_2}} \qquad (23)$$

Where N_A is the Avogadro's number, and M_{N2} is the molar mass of nitrogen (28 g/mol). The specific surface can be calculated by dividing A by sample weight.

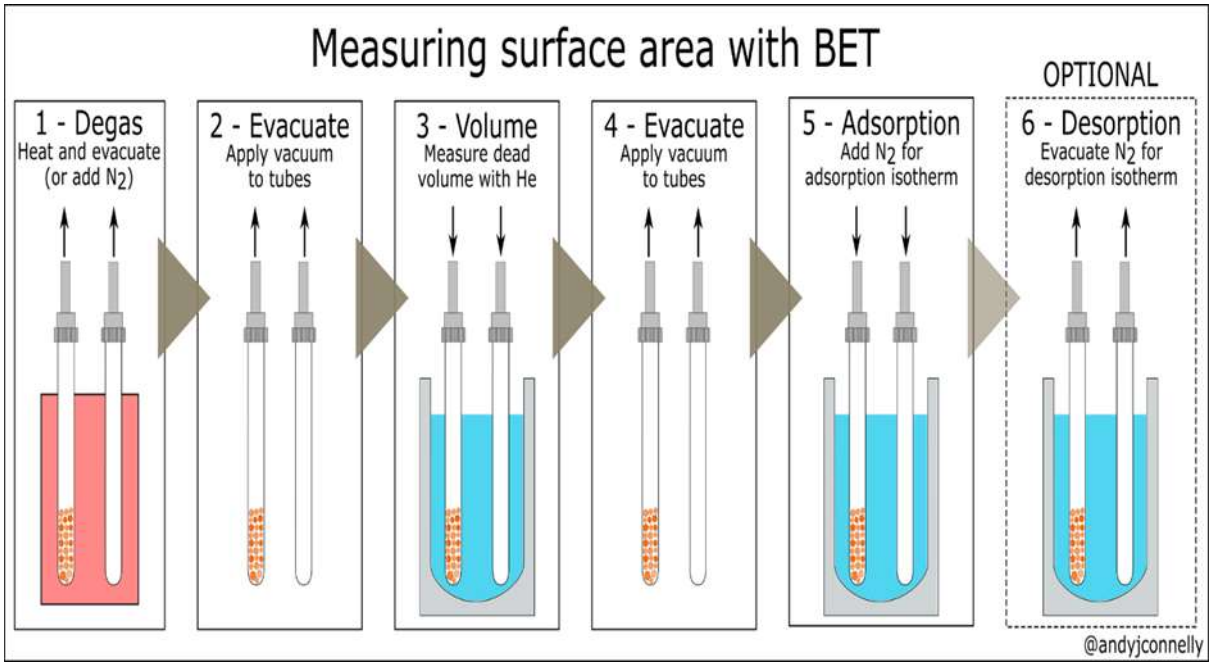

Figure 3.16: BET surface area measurement schematic [251].

3.6.6 SEM-EDS (Scanning Electron Microscopy-Energy Dispersive Spectroscopy)

SEM-EDS was utilized to determine the surface morphology and elemental mapping of the fresh and spent RME and DP-ceria using a Zeiss microscope (20kV).

SEM is a method to take high-resolution images of surfaces with the help of electron beams. The electron beam is generated just above the sample chamber in a column. The energy of incident electron rage between 100eV-30 keV. The incident electrons are concentrated into a small beam using series of electromagnetic lenses. After that, the small beam is focused onto the surface with the help of scanning coils near the column's end. Three phenomena occurred when the electron beam interacts

with the sample surface. The electrons are absorbed, reflected, or cause excitation. To create an image, SEM scanned the electron beam in a raster pattern over the surface. Typical SEM operates under a high vacuum (5-10 mbar). Fig. 3.17 shows a typical SME schematic.

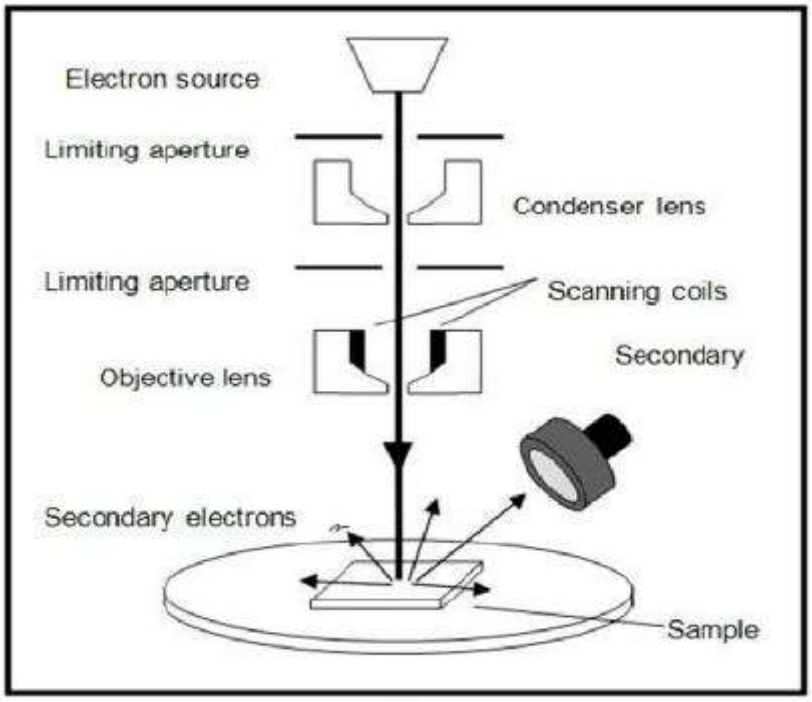

Figure 3.17: Scanning electron microscope schematic [252].

EDS (coupled with SEM) utilizes for the qualitative and quantitative chemical composition of the sample. When the sample surface is bombarded with the SEM electrons, the electrons are ejected from the surface's atoms and leaves a vacancy. These vacancies are filled by the higher energy shell electrons while emitting a characteristic X-ray of the respective element. The EDS detector measures the intensity of characteristic X-ray versus their energy. The spectrum of X-ray energy versus counts is evaluated to determine the elemental composition of the sampled volume. Fig. 3.18 shows a simple schematic of EDS.

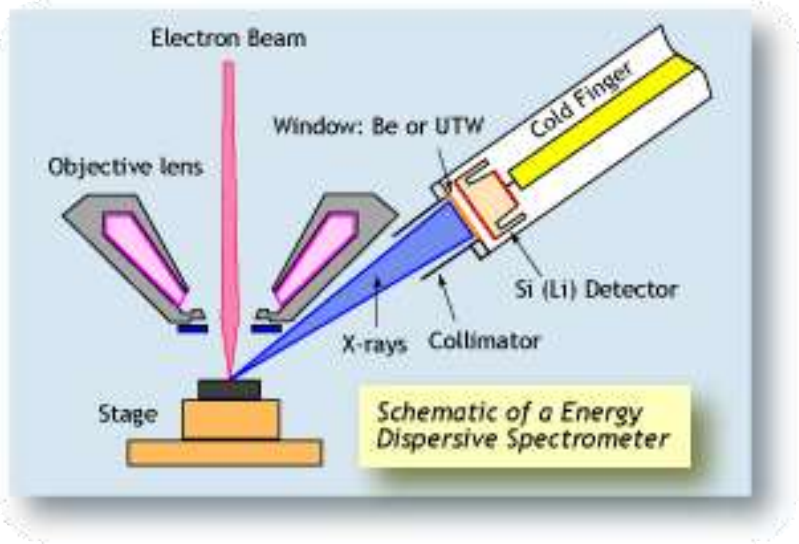

Figure 3.18: Schematic of energy-dispersive spectroscopy [253].

3.6.7 TEM (Transition Electron Microscope)

TEM utilizes high energy transmitted electron to deliver crystallographic and morphologic information of the sample. Therefore, TEM helps to give information about the sample's inner structure, while SEM is limited to the surface information of the sample. SEM and TEM's significant difference is the magnifying resolution; SEM is limited to ~1 nm while TEM can go up to 0.1 nm. Also, the TEM beam voltage (100-400keV) is much higher than SEM (up to 30keV). TEM is also operated at a high vacuum (5-10 mmHg). Fig. 3.19 shows a schematic of a typical TEM.

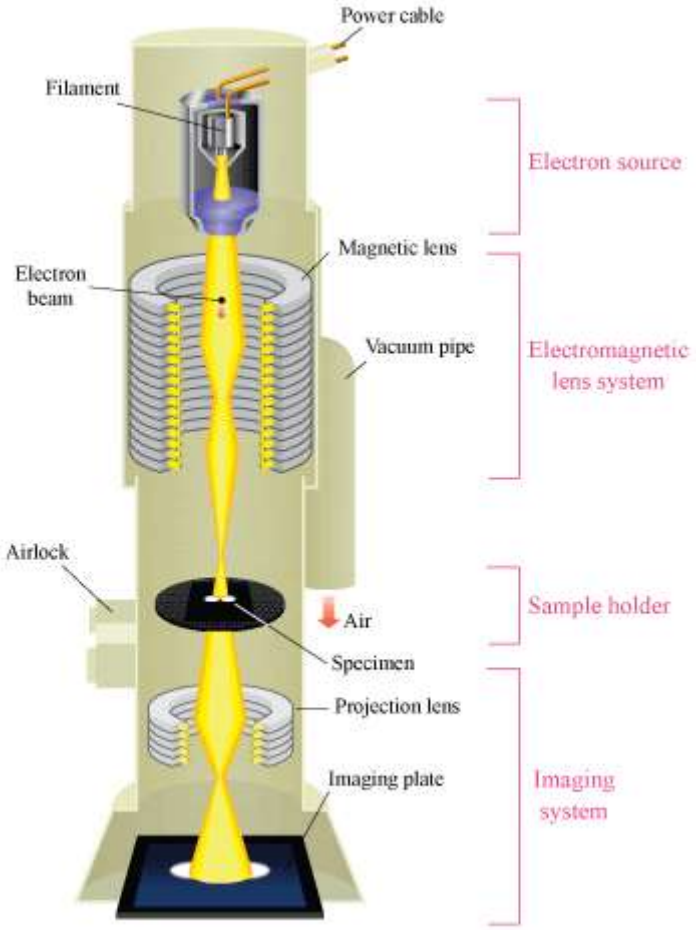

Figure 3.19: TEM Schematic [254].

3.6.8 Thermogravimetric Analysis (TGA)

TGA utilizes to investigate a material's thermal stability and find out the fraction of volatile present by monitoring the rate of change in weight as a function of temperature or time in a controlled specified condition. TGA provides multiple information about the sample, like its melting point, boiling point, combustion temperature, and composition of its constituents.

A typical TGA instrument is equipped with a thermocouple programmable auto furnace, autosampler, and a precise weight balance. Fig. 3.20 shows a schematic of a standard TGA instrument. To measure the remaining carbon, nitrogen, and water content after calcination in fresh catalysts,

thermo-gravimetric analysis (TGA), TA Instruments TGA 55, coupled with FTIR, MultiGas 2030 continuous gas analyzer (MKS Instruments) was performed. First, the TGA instrument was equilibrated at 25°C, and then the condition was left to remain isothermal for the next 10 min. After that, the sample was heated from 25-150°C at a ramping rate of 10°C/min, and then the temperature was allowed to increase from 150-800°C at a ramping rate of 2°C and at an airflow rate of 40 ml/min. The outlet gases of the TGA could pass through the FTIR gas analyzer to detect the CO_2 and CO produced during the combustion process.

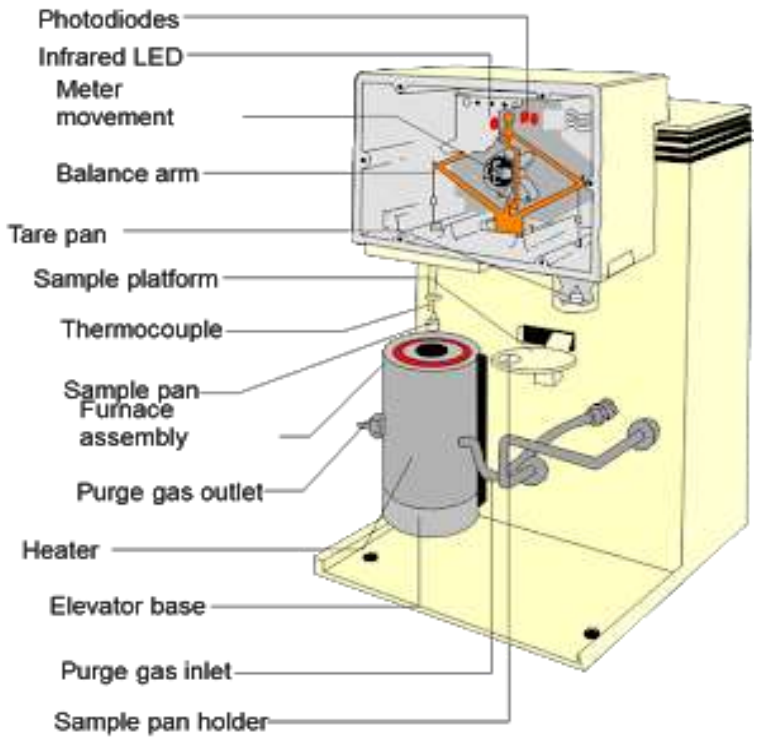

Figure 3.20: Schematic of a typical TGA instrument [255].

3.6.9 TPR (Temperature Programmed Reduction)

TPR is a useful technique applied to characterize metal oxides, mixed metal oxides, and supported metal oxides. TPR gives quantitative information about the reducibility (of oxide surface) and the reduced surface's heterogeneity. In TPR, a reducing gas mixture usually 3-17% H_2 diluted with Ar or N_2 flows over the oxide surface at variable temperatures. A TCD (Thermal conductivity detector) is equipped at the outlet, which measures the outlet gases' thermal conductivity and generates a graph between TCD signal vs. time or temperature. The TCD signal is then converted to the concentration of active gas using a level calibration. Integrating the area under the concentration vs. time (or temperature) yields total gas consumed. In this study, TPR was performed using an AMI-300lite catalyst characterization system (Altamira Instruments) to measure the extent of reduction of the prepared catalysts for a temperature range of 300-800°C. Fig. 3.21 shows a simple schematic of the process.

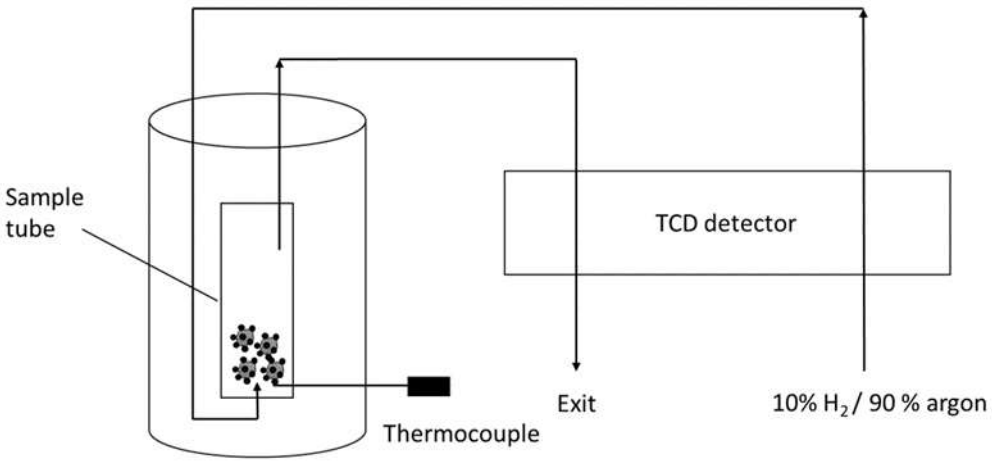

Figure 3.21: TPR Schematic.

3.6.10 CO_2-TPD (Temperature Program Desorption)

Temperature-programmed desorption (TPD) is an experimental technique commonly used to classify catalysts and adsorbent's adsorption properties, such as their acidity and basicity. The peak maximum temperature is used to calculate the adsorption site's strength, as obtained from TPD thermograms. Peaks location helps to identify the chemical form of the functional group formed on the surface of the catalyst. However, the peak location depends on various factors, including diffusion resistance, re-adsorption, catalyst weight, and carrier flow rate.

Considering the RWGS reaction, the interaction of CO_2 with bulk and supported ceria were investigated via TPD studies using AMI-300Lite, Altamira instruments, catalyst characterization instrument. The catalyst was initially pre-treated under the inert gas (Ar) at 400°C for 30 minutes to clean the surface, and then 5%CO_2/He was allowed to pass on at 25°C or 150°C for adsorption for 60 minutes. The concentration of the desorbed gases was recorded in a similar way as done in TPR. Fig. 3. 22 shows the simple schematic of the CO_2-TPD apparatus.

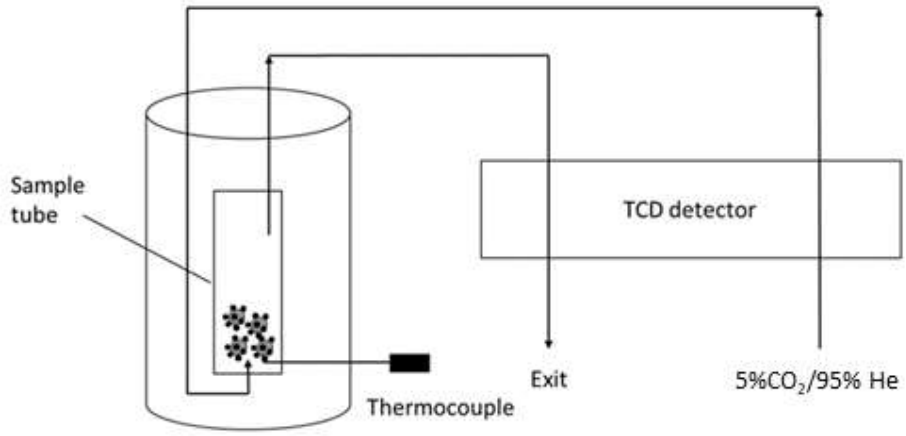

Figure 3.22: CO_2-TPD Schematic.

3.6.11 In-line FTIR and *in-situ* FTIR Reaction Mechanistic Studies

Infrared spectroscopy is a tool that analyses the infrared spectrum after the sample's absorption or emission. There are several frequencies in the beam produced from the source, and it will shine to the sample simultaneously and be replicated many times in a short duration. The adsorbed infrared wavelengths and intensity depends on the chemical bond, group, and atomic weight of the atoms bound at both ends. Infrared spectroscopy takes advantage of the fact that molecules absorb specific frequencies that are unique to their structure. These absorptions have resonant frequencies, which means that the frequency of the absorbed radiation is the same as the frequency of the vibrating bond or group. The shapes of the molecular potential energy surfaces, the masses of the atoms, and the resulting vibronic coupling define the energies. Therefore, Infrared spectroscopy helps to identify the compound with the help of chemical compound bond detection.

Two types of FTIR studies were performed during this study. First, to find the extent of coking and thermal stability of the catalyst, the outlet gases from TGA were allowed to pass through a gas FTIR analyzer (Multigas^{TM} 2030, MKS instruments). Reference gases were set up in advance, and a single beam infrared passes by specially built narrow band-pass optical filters, and the intensity of the inferred is reduced to achieve the specified signal. To calculate stream concentration, the strength of adsorption was compared with the standard comparator.

Second, to study the reaction mechanism while detecting the reaction intermediates over the catalyst surface, an *in-situ* FTIR analysis was performed using AMI-300Lite, Altamira instruments, catalyst characterization instruments equipped with a transition type FTIR unit. The sample pellet, consisting of KBr supported catalyst, transmits the inferred signal produced from the source and then reaches the detector. By analyzing the catalyst's surface, one may classify the adsorbed species and the gas phase in the reactor. Spectra are collected at specified temperatures and at different reaction times to learn more about the reaction mechanism. Background spectra were obtained at the same

temperature as the reaction conditions in a pure atmosphere in an inert gas to prevent environmental disturbance. Fig. 3.23 shows the simple schematic and original picture *in-situ* FTIR unit.

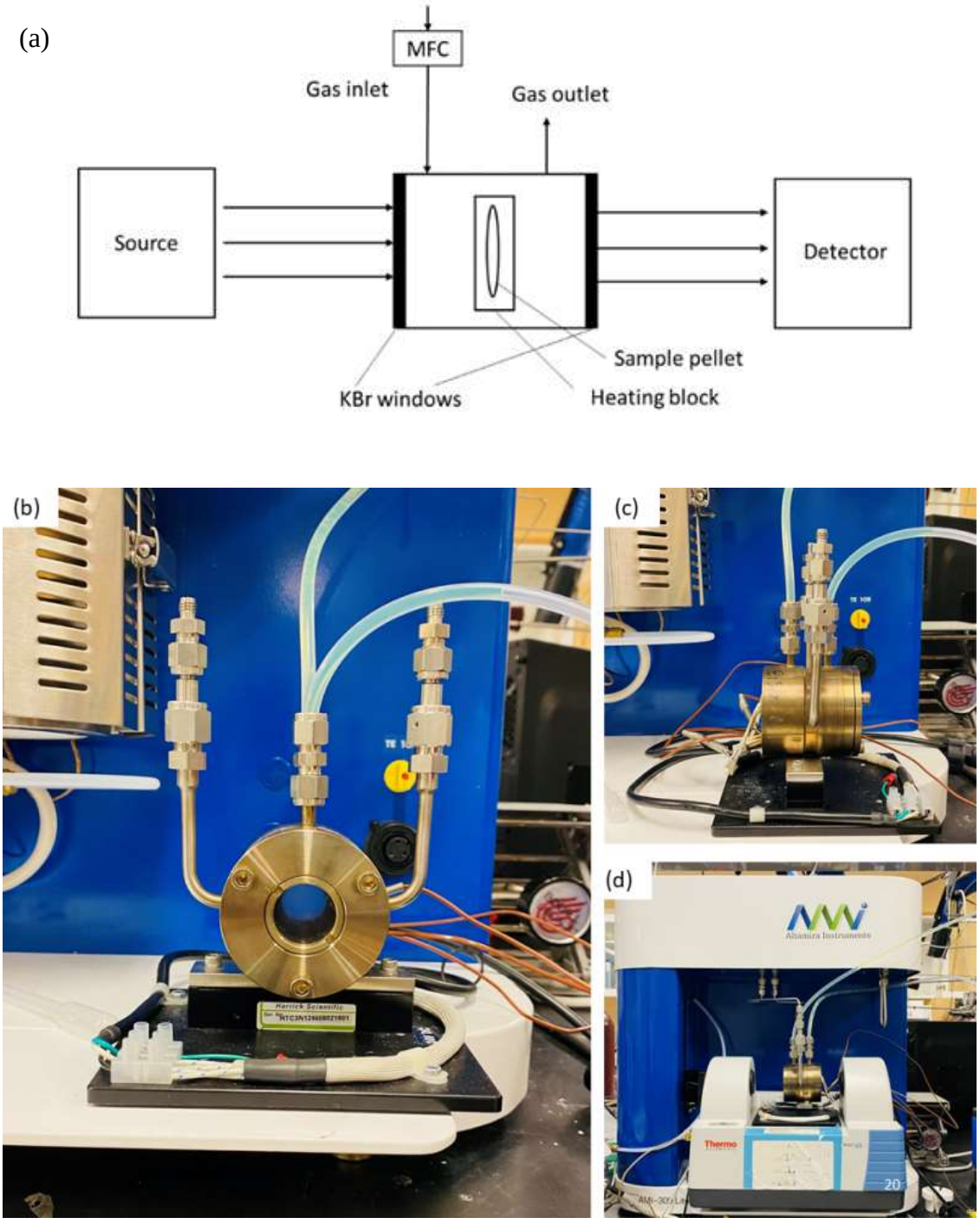

Figure 3.23: *in-situ* FTIR unit (a) schematic (b) IR-cell front view (c) IR-cell side view (d) complete original setup

Chapter 4

Highly selective CO synthesis via RWGS reaction over cerium oxide catalyst prepared via RME process

4.1 Introduction

Mitigating atmospheric CO_2 emissions is a major challenge today. According to IPCC (Intergovernmental Panel on Climate Change), to limit the upsurge of world average temperature to 2°C by 2050, there is a strong need to reduce CO_2 emissions to at least half of its present value [3]. However, instead of considering CO_2 as a pollutant, it can be taken as a renewable source of carbonnon-toxic, and cheaply available in abundant amounts for low cost [33]. Reverse water gas shift reaction has received considerable attention in the recent decade because of its versatility in catalytic CO_2 reduction technology. Thermodynamically direct conversion of CO_2 to methanol is more favorable. However, the CAMERE process revealed a 20% higher yield of methanol obtained when CO_2 is first reduced to CO (via the RWGS) and then CO to methanol, rather than hydrogenating CO_2 directly to methanol [14].

RWGS is considered as the key reaction for the catalytic hydrogenation of CO_2 because the produced CO can either produce methanol or higher hydrocarbons. It is an endothermic process with a free-energy change and enthalpy change of $\Delta G_{298\,K} = 28.6\ kJ/mol$ and $\Delta H_{298\,K} = 41.2\ kJ/mol$ (STP):

$$CO_2 + H_2 \rightleftharpoons CO + H_2O \quad (2)$$

Therefore, the RWGS reaction needs to perform at higher temperatures (around 800°C) to achieve higher CO selectivity and CO_2 conversion [112, 134, 138]. Though, higher temperatures cause sintering and deactivation of catalysts [256]. Moreover, the higher energy demand makes it uneconomical for

industrial applications. Consequently, the development of a highly active, selective, durable, and cost-effective catalyst that can help run this reaction at lower temperatures (<800°C) is necessary for the large-scale application of the RWGS. Recently, several precious metals, non-precious metals, and mixed oxide catalysts have been deployed for RWGS application.

Chen et al. [74] studied the performance of Pt/TiO_2 catalyst towards RWGS reaction. They found that the Pt particle size and reaction conditions highly affect the catalyst's selectivity towards CO or CH_4. Kattle et al. [75] also showed that the bonding energy of CO at the interface site of Pt/TiO_2 catalyst facilitates the further hydrogenation of CO to form CH_4. Porosoff et al. [76] studied the effect of secondary metal (Ni, Co, etc.) along with Pt over CeO_2 and γ-Al_2O_3 supports and identified a significant amount of CH_4 over $Pt\text{-}Ni/CeO_2$ and $Pt\text{-}Ni/\gamma\text{-}Al_2O_3$ while $Pt\text{-}Co/CeO_2$ and $Pt\text{-}Co/\gamma\text{-}Al_2O_3$ were highly selective towards CO with a CO/CH_4 ratio of 259.4 and 245.8 respectively.

Apart from noble metals, Cu and Ni-based catalysts also shows promising activity towards the RWGS. Stone et al. [93] presented a comparative study of Cu-ZnO and $Cu\text{-}ZnO/Al_2O_3$ catalyst for the RWGS reaction. They prepared different catalysts by varying concentrations of Cu and Zn from Cu rich to Zn rich. Cu rich catalyst shows the highest activity because of higher Cu dispersion in the final catalyst. Chen et al. [94-96] show that alumina-supported Cu nanoparticles enhanced the adsorption of formates. They also found out that for Cu nanoparticles and SiO_2 supported Cu; the RWGS reaction undergoes formate formation. Even the forward and reverse mechanism is independent of CO_2 and CO adsorption sites. Nickel has excellent hydrogenation catalytic activities, which leads its catalyst to be more selective for methane production rather than CO. However, oxide-supported Ni nanoparticles with high oxygen capacities are still considered for the RWGS [73]. Porosoff et al. [104] studied the CO_2 conversion to CO over six different TMCs (TiC, ZrC, NbC, TaC, Mo_2C, WC). They showed that the activity of carbides for CO_2 hydrogenation could be easily predicted by OBE (oxygen binding energy) because the formation of the oxy-carbide and the subsequent removal of O is the main crucial steps in CO_2 conversion catalytic cycle. Liu et al. [105] also show that polycrystalline α-Mo_2C is a

highly efficient catalyst towards the RWGS. It gives about 16% CO_2 conversion at 400°C and CO selectivity of >99%. Therefore, there is still a lot more to be done in developing a highly selective and durable catalyst for RWGS.

Recently, apart from the highly active noble metals (Pt, Pd, Rh etc.) and transition metals (like Cu and Ni) the rare earth metal Ce received significant attention due to its highly active behavior. CeO_2 (Ceria) based catalysts show promising results in RWGS because of their high oxygen capacity. CeO_2 can lose O^{2-} atom at high temperature and reduce cerium from Ce^{4+} to $Ce^{3+,}$ creating an oxygen vacancy in the crystal lattice while keeping the crystalline structure. This oxygen vacancy acts as the leading active site for catalytic reactions [23, 115]. Ceria exists in different morphologies (cube, road, and particle) and various crystalline planes (100,111,110). It has been reported that ceria cubes with 100 crystalline planes have two times higher activity per surface area as compare to rods and particles [22]. Wang et al. [114] showed that incorporation of CeO_2 with In_2O_3 increases the surface area of the catalyst. CeO_2 helps to adsorb dissociative H_2 and intermediate carbonates while creating more oxygen vacancies. The interaction of In_2O_3-CeO_2 catalyst creates a synergistic effect, which leads to outstanding activity for the RWGS. However, only a few studies have been reported solely targeting RWGS reaction over bare ceria.

Dai et al. [20] reported the RWGS studies over unsupported (bulk) ceria prepared using three different synthesis methods, including hard templet (Ce-HT), complex (Ce-CA), and precipitation method (CE-PC). 50mg of each catalyst was tested for a temperature range of 300°C-580°C in a quartz tube reactor at atmospheric pressure. Feed gas comprising of CO_2 (10.0% vol), H_2 (40% vol), and Ar (50% vol) was flown over the packed bed at the GHSV of 60,000 ml h^{-1} g_{cat}^{-1}. All three catalysts at all temperatures showed 100% CO selectivity and maximum CO_2 conversion of 15.9%, 9.3%, and 12.7% for Ce-HT, Ce-CA, and Ce-PC, respectively, at 580°C. Kovacevic et al. [22] reported the RWGS reaction activity over three different morphological shapes (cubes, roads, and particles) of bulk ceria. Activity tests were performed in a quartz tube reactor at the atmospheric pressure and at a constant

temperature of 580°C using a feed gas (30 ml min^{-1}) mixture of 3% H_2, 37% CO_2, and 60% N_2. In each run, the amount of catalyst was adjusted to maintain the CO_2 conversion less than 5% to ensure no discrepancy in the experiments. Nanocubes shows the maximum rate of approximately 78 µmol g_{cat}^{-1} min^{-1} CO produced. A minor deactivation was also observed in all the experiments. Similarly, Liu et al. [21] also studied the RWGS phenomena over bulk ceria (cubes, rods, and octahedra) and Ni supported ceria (nano-cubes) prepared via hydrothermal and wet impregnation method, respectively. Catalysts were tested at atmospheric pressure for the temperature range of 400°C-800°C. A reaction gas mixture of H_2:CO (1:1) was flown over the fixed bed at the rate of 100 ml min^{-1}. All bulk ceria catalysts showed 100% CO selectivity above 500°C, while the ceria nanocubes showed the highest CO_2 conversion at all temperatures. Maximum, Less than 50% CO_2 conversion was observed for ceria nanocubes at 800°C. On the other hand, Ni-supported nanoceria showed better CO_2 conversion and CO selectivity at all temperatures. Maximum approximately 50% CO_2 conversion was recorded at 800°C. These studies show minor deactivation, low surface area, or low CO_2 conversion rates even at a temperature as high as 800°C. Therefore, considering the potential of ceria for RWGS, there is a strong need to investigate the RWGS over ceria prepared via a method other than already been taken, like reverse microemulsion (RME). To the best of the author's knowledge, this study has not been reported in the catalysis field before.

This study aims to synthesize high surface area ceria, utilizing the reverse microemulsion (RME) technology, which leads to getting high activity and selectivity towards CO via the RWGS reaction in the temperature range 300°C-600°C. Characterization studies (Temperature test, XRD, ICP-OES , TPR, SEM, HRTEM, etc.) show that the ceria produced via RME process has activity and surface area doubled the ceria produced through direct precipitation.

4.2 Experimental

4.2.1 Catalyst Preparation

The baseline ceria catalyst (denoted as DP-ceria) was synthesized using the direct precipitation method. For 1 g DP-ceria, 2.52 g of cerium nitrate hexa-hydrated (99.5% $Ce(NO_3)_3 \cdot 6H_2O$, Alfa Aesar) was dissolved in distilled water (0.29 M, 20 ml solution). The cerium solution was added slowly to 20 ml of NH_4OH solution (28-30% NH_3 basis) under vigorous stirring at room temperature. Immediate after mixing solution appeared opaque, turned light purple after 30 min, and finally turned dark purple after 1 h. The final solution was centrifuged at 3500 RPM for 10 min to separate the sediments. The wet precipitates were collected in a petri dish and dried for 6 h under air at 150°C. The dried precipitates were calcined at 275°C for 4 h under the continuous airflow, pelletized (50 MPa), crushed, and sieved to 250-425 µm particles. The complete catalyst synthesis schematic is presented in section 3.5.

The ceria nano-catalyst (denoted as RME-ceria) was synthesized using the reverse microemulsion (RME) method. Cerium nitrate hexa-hydrated (99.5% $Ce(NO_3)_3 \cdot 6H_2O$, Alfa Aesar) was used as the cerium precursor, cyclohexane as oil phase, Triton X-100 as the surfactant, and propanol-2 as the co-surfactant. To prepare 1 g RME-ceria, first two blank RME's were prepared while mixing Triton X-100, propanol-2, and cyclohexane in the volume ratio 1:4.5:3.5, respectively. $Ce(NO_3)_3$-RME was prepared while adding 20 ml of 0.29 M cerium nitrate solution to one of the blank RME under vigorous stirring while keeping the final RME ratio 1:1:4.5:3.5. Similarly, $NH_4(OH)$-RME was prepared while adding NH_4OH (28-30% NH_3) under vigorous stirring as described above ($Ce(NO_3)_3$-RME). $Ce(NO_3)_3$-RME was added to $NH_4(OH)$-RME slowly under vigorous stirring at room temperature. After mixing, the immediate solution turned orange, became yellowish-orange after 30 min, and finally yellow after 1 h. Precipitates were centrifuged at 3500 RPM for 10 min to separate organic phase followed by three times water wash and centrifugation at 3500 RPM for 10 min each to ensure

maximum removal of surfactant. The wet precipitates collected in a petri dish and dried for 6 h under air at 150°C. The dried precipitates were calcined at 275°C for 4 h under the continuous airflow, pelletized (50MPa), crushed, and sieved to 250-425 µm particles. Fig. 4.1 shows the un-calcined and calcined DP-ceria (a & b) and RME-ceria (e & f), respectively.

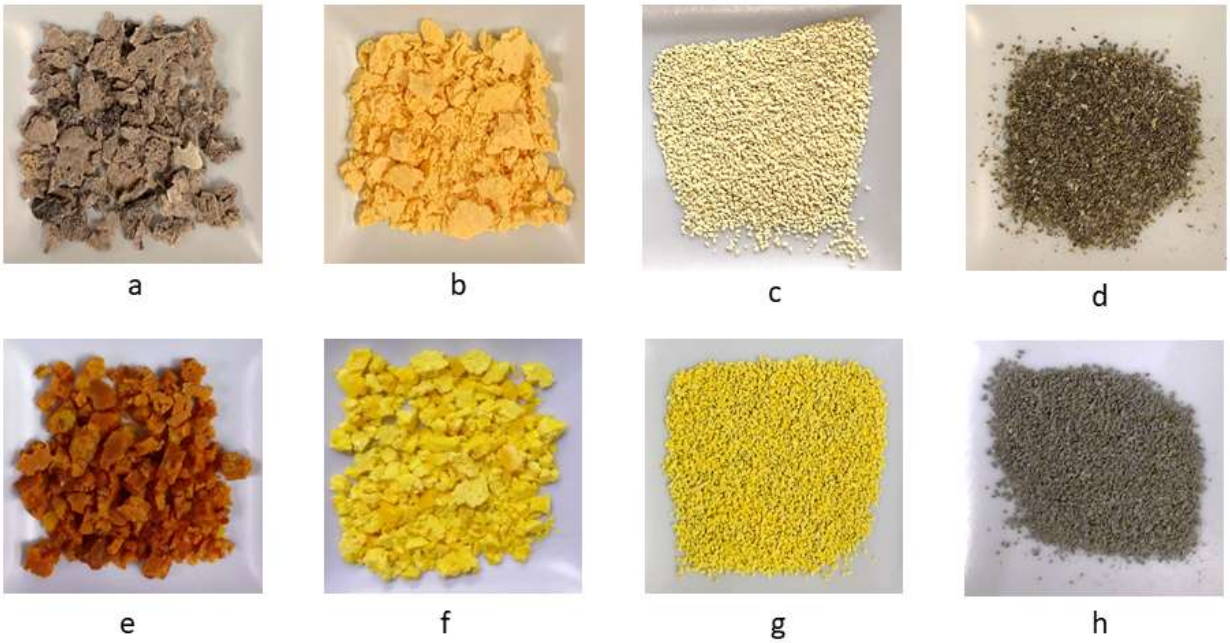

Figure 4.1: un-calcined, calcined, pelletized, and spent DP-ceria (a, b, c, d), RME-ceria (e, f, g, h), respectively.

4.2.2 Catalyst Performance and Activity

The RWGS reaction was considered as the imitate reaction to evaluate the catalytic performance of RME-ceria and DP-ceria. The RWGS catalytic activity tests were performed at 3 bar (absolute pressure) in a continuous fixed bed reactor. The reactor system was made by joining the 1/2" stainless steel tube (316L, Swagelok) with 1/4" stainless steel tube (316L, Swagelok) via a reducing adapter (served as the reactor) and straight union, as shown in schematic Fig. 4.2. Please refer to section 3.6.1 for the complete description and experimental setup of the flow system.

The total CO_2 conversion, CO Selectivity, and CH_4 selectivity were calculated according to the following equations.

$$X_{CO_2} = \frac{y_{CO}+y_{CH_4}}{y_{CO_2}+y_{CO}+y_{CH_4}} \quad (11)$$

$$S_{CO} = \frac{y_{CO}}{y_{CO}+y_{CH_4}} \quad (12)$$

$$S_{CH_4} = \frac{y_{CH_4}}{y_{CO}+y_{CH_4}} \quad (13)$$

Where, y_{CO}, y_{CO_2}, y_{CH_4}correspond to mole fractions of the respective gases measured by the IR analyzer on dry basis. S is the selectivity of CO and CH_4.

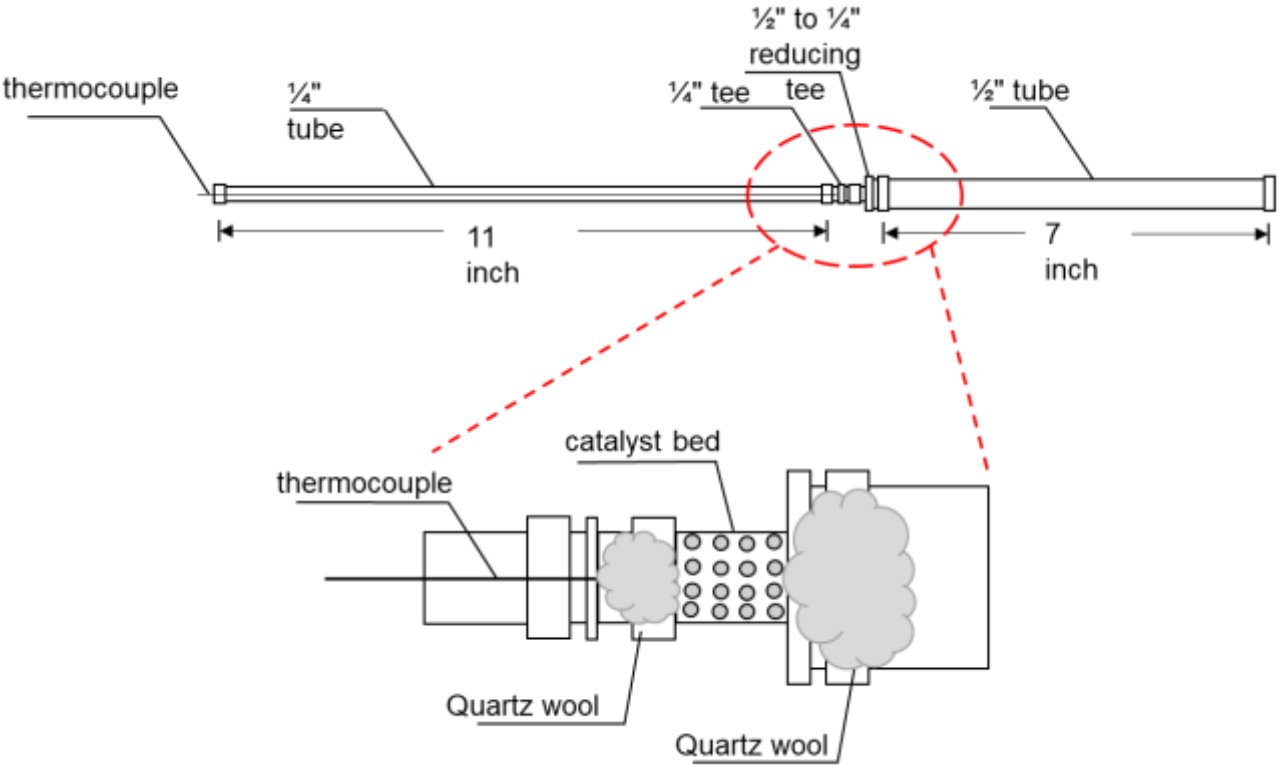

Figure 4.2: Kinetic reactor schematic

4.2.3 Catalyst Characterization

D8 discover diffractometer, Bruker was utilized to obtain the XRD patterns using Cu-Ka radiation source (λ = 1.54 Å) at 40 kV tube voltage and 40 mA of a tube current. Diffraction patterns were collected for the 2θ ranged 10° to 90° at a scan sped of 3 (time per step) with an increment of 0.1. Specific surface area (SSA) was measured using Gemini VII 2390 BET surface area analyser (Micromeritics Instrument Corporation). Ar was used as the purge gas, while N_2 was used as the main adsorbing gas to find the specific surface area using the Brunauer-Emmett-Teller (BET) method. Inductively coupled plasma optical spectroscopy was used to verify the bulk chemical composition of RME-ceria (Prodigy SPEC, Leeman Labs Inc.).

Elemental mapping and surface composition of fresh and spent catalysts were obtained using SEM-EDX (electron microscopy coupled with energy-dispersive X-ray spectroscopy) a Zeiss microscope (20 kV). The HRTEM (high resolution transition electron microscopy) micrographs were also acquired using a Zeiss microscope (100 kV). TPR (Temperature programmed reduction) analysis was performed using AMI-300Lite, Altamira instruments, catalyst characterization instruments to investigate the extent of reduction for all fresh and spent catalysts. 10% H_2/Ar mixture was blown over the catalyst, and the change in H_2 composition was observed using a TCD (thermal conductivity detector) at the outlet over the temperature range of 300°C-800°C. Thermo-gravimetric analysis (TGA, Q500, TA Instruments), coupled with an in-line gas FTIR analyzer (Multigas^{TM} 2030, MKS instruments), was performed for both fresh and spent catalysts to evaluate their thermal stability and extent of coking (after reaction). The temperature ramp was set to 10°C min^{-1} for T $\leq$ 150°C and maintained under isothermal conditions for 1 h at 150°C. After 1 h, the temperature ramp was set to 2°Cmin^{-1} for 150°C < T < 800 °C and the airflow was set to 40 ml min^{-1}.

Reaction mechanistic studies were performed for all fresh and spent catalysts using AMI-300Lite, Altamira Instruments, catalyst characterization instrument (*In-situ* FTIR reaction analysis). The *in-situ* FTIR spectra were collected in a reactor cell with KBr windows connected with inlet and outlet flows. The cell was placed in a FTIR spectrometer (Thermo Scientific™ Nicolet™ iS™5), and the temperature was controlled with a controller connected thermocouple (inside the reactor). The catalyst (~5 mg) was pressed to a potassium bromide pellet support. Each spectrum was collected at 4 cm^{-1} resolution and 32 scans from 4000 to 800 cm^{-1} in absorbance mode. The sample pellets were reduced in 10% H_2/argon at 400 °C for 1 h and then flushed with argon to remove the hydrogen. The background spectrum was collected under argon at the same temperature as the reaction condition. After the background was subtracted, reaction gas (30 ml min^{-1}, 2% CO_2/8% H_2/90% argon) was introduced to the IR cell at the same temperature.

4.3 Results and Discussion

4.3.1 Catalytic Activity Performance and Stability Studies

Two types of tests were performed to evaluate the activity and stability of the catalysts.

4.3.1.1 Activity Test

The activity of fresh RME- and DP-ceria were tested for RWGS reaction over the range of 300°C-600°C (from low to high) at a fixed GHSV of 60,000 ml g_{cat}^{-1} h^{-1}. Fig. 4.3 (right plot) shows the total CO_2 conversion and selectivity as a function of increasing temperature. It can easily be seen that conversion increases with temperature. Studies showed that for ceria, the oxygen vacancy acts as the leading active site for catalytic reactions [23, 115]. This confirms that increasing temperature helps the mobility of O^{2-} ion in the ceria lattice resulting in more oxygen vacancies. A similar effect of temperature on oxygen vacancies has been reported in the literature [20-22]. Three batches of each catalyst were tested under the same conditions to confirm the repeatability of the results. Error bars show the standard deviation between three measurements for three different catalyst batches. At all

temperatures, both catalysts show 100% CO selectivity. More than two folds conversion was recorded at a temperature higher than 500°C for the RME-ceria compared to the DP-ceria. At 600°C, approx. 42% CO_2 conversion was recorded for RME-ceria, while for the DP-ceria only 22% conversion was observed; the corresponding equilibrium conversion is about 65%. In this study, the maximum CO_2 conversion achieved (43% at 600°C) over RME-ceria is almost 3 to 4 times the maximum CO_2 conversion reported in the literature over bulk ceria i.e., 16% at 580°C [20] and 8% at 600°C [21] respectively.

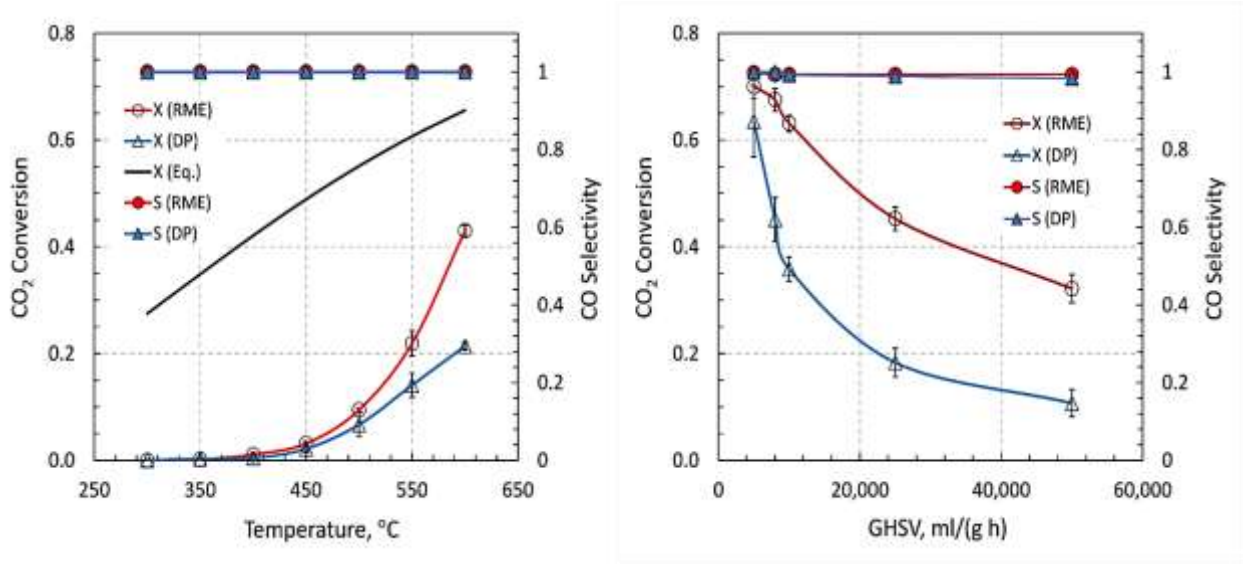

Figure 4.3: Performance comparison of three different RME- and DP-ceria batches as a function of Temperature (300°C-600°C) and GHSV (5000-50,000 ml g_{cat}^{-1} h^{-1}) at 3 bar.

After the temperature activity tests, both fresh catalysts were tested for the different GHSV's of the reaction gases (moving from low to high) at 600°C and 3 bar pressure using new reactors and fresh catalysts, Fig. 4.3 (left plot). Error bars show the results of the two different batches of each catalyst. Between 10,000-50,000 ml g_{cat}^{-1} $h^{-1,}$ both catalysts show 100% CO selectivity with significantly higher conversion as expected. It can be easily seen that with increasing GHSV, CO_2 conversion decreases,

which is evident because of the high flow rates and less contact time. Sun et al. [248] observed a similar decline in CO_2 conversion for the RWGS reaction over Mo_2C catalyst when GHSV increased from 10,000 to 50,000 ml g_{cat}^{-1} h^{-1}. However, for the entire GHSV's tested range, RME-ceria showed superior activity (almost 2 times) compared to DP-ceria.

CO generation rates and activation energies calculated from the data presented in Fig. 4.3 (right plot) are shown in Fig. 4.4 as the function of reaction temperature using eq.24 and eq.25 (a linear form of Arrhenius law). By definition, eq. 24 represents the CO_2 disappearance rate. However, in the present work, both catalysts showed 100% CO selectivity. Therefore, CO_2 disappearance rate is equal to CO generation rate.

$$R = \frac{F_{CO_2,f} \times X_{CO_2}}{W_c} \qquad (24)$$

$$In(R) = InA - \frac{E_a}{RT} \qquad (25)$$

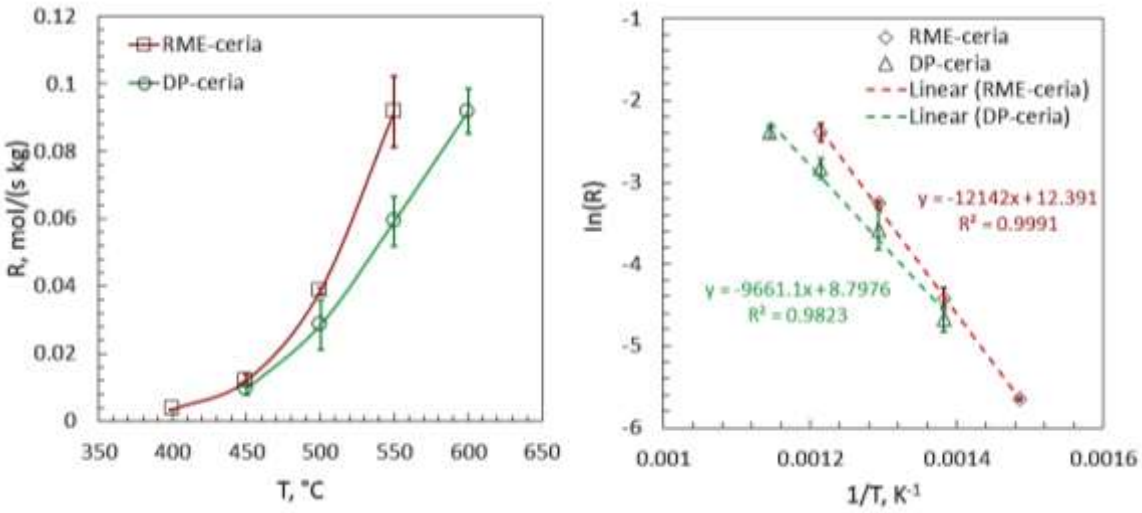

Figure 4.4: CO generation rate mol kg_{cat}^{-1} s^{-1} (left plot), Arrhenius plot In(R) Vs T-1 (right plot): activation energy for RME- DP-ceria are 77 kJ mol^{-1} and 100 kJ mol^{-1}, respectively.

Fig. 4.4 shows that the CO generation rate for RME-ceria at 550°C is the same as calculated for DP-ceria at 600°C. Also, at all temperatures > 450°C, the rate is almost double for RME-ceria than DP-ceria catalyst. At 550°C, the calculated rate (0.091 mol kg_{cat}^{-1} s^{-1}) is nearly 77 times higher than reported in the literature for bulk ceria 71 µmol g_{cat}^{-1} min^{-1}. at 560°C [22]. The activation energies for both catalysts were estimated using the Arrhenius plot (In(R) Vs. I/T). Only points obtained under differential conditions (when the conversion ~20%) were taken due to the limitation of the linear form of the Arrhenius equation. For RME-ceria the average activation energy appeared around 100 kJ $mol^{-1,}$ while for DP-ceria it's 80 kJ mol^{-1}. The lesser value of calculated activation energy over DP-ceria (80 kJ mol^{-1}) was obtained because the data was evaluated up to 600°C, a higher temperature than RME-ceria. This fact is in direct agreement with the findings of Bustamante et al. [60]. They reported that the activation energy for the RWGS reaction decreased at high temperatures and pressures. Similarly, Mordekovitz et al. [18] reported the estimated activation energy of 66 kJ mol^{-1}, calculated for the temperature range of 450°C-700°C, for the RWGS over bilk ceria. Despite the lower activation energy they achieved at the higher temperatures, the CO_2 conversion was only ~21% at 700°C, which almost half of what we attained in this study over RME-ceria at 600°C (~42%).

Another type of simple activity test was performed for each catalyst based on 3 heating-cooling cycles at the same conditions, i.e., a temperature range of 300°C-600°C (moving from low to high), 3bar absolute pressure, and GHSV of 60,000 ml g_{cat}^{-1} h^{-1}. After cycle1 (300°C-600°C), the system was allowed to cool down to 300°C and then exposed to the similar conditions performed before. Fig. 4.5(a) represents the cyclic activity for RME-ceria using a brand new stainless steel reactor. Results show stable catalyst activity up to cycle3 (almost 42 h on stream). No CH_4 or carbon formation was detected, which supports the fact that RME-ceria is stable and resistant to cooking. This excellent coking resistance of RME-ceria was later confirmed with TGA-FTIR of the spent catalyst used during the stability test (almost 70 h on stream).

Similarly, DP-ceria was subjected to similar heating-cooling cycles using a new steel reactor. Unlike RME-ceria, DP-ceria showed (Fig. 4.5(b)) a decline in the activity after the first cycle and retained the same activity for the third cycle. This activity decline for DP-ceria was later confirmed with XRD, BET and TEM due to a significant increase in crystallite size, a large decrease in surface area, and particle agglomeration during all three cycles, all catalysts showed 100% CO selectivity.

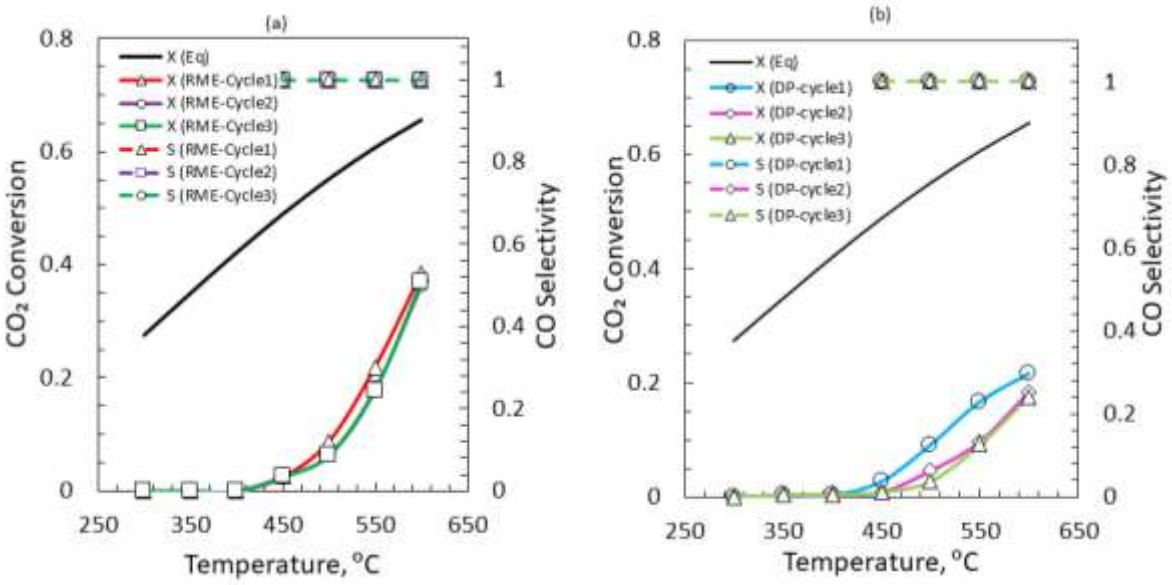

Figure 4.5: Heating-Cooling cycles for RME-ceria (a) and DP-ceria r (b) at 300°C-600°C, 3 bar and 60,000 ml g_{cat}^{-1} h^{-1v}GHSV

4.3.1.2 Catalyst Stability Tests

Owing to a range of causes such as poisoning, sintering, and coking, catalysts may be deactivated. In laboratory tests, like those on CO_2 conversion, the catalyst's stability is sometimes ignored. Since CO_2 is a very stable chemical, its activation entails high temperatures, which may potentially result in sintering and coking.

The long-term stability tests were performed in a U-shaped quartz tube reactor (1/4" diameter) for a minimum of 70 h on the stream at atmospheric pressure, 600°C, and GHSV of 60,000 ml g_{cat}^{-1} h^{-1} and 10,000 ml g_{cat}^{-1} h^{-1}, shown in Fig. 4.6. For DP-ceria (Fig. 4.6(a)) initially, the CO_2 conversion appeared around 21% at GHSV of 60,000 ml g_{cat}^{-1} h^{-1} (like the one observed during the activity test in stainless steel reactor at 3 bar, 600°C, and 60,000 ml g_{cat}^{-1} h^{-1}). It starts declining immediately, continued to decrease and stabilize after 55 h on stream at around 7%. For GHSV of 10,000 ml g_{cat}^{-1} h^{-1}, similar declining behavior was observed. Initially, the CO_2 conversion appeared very high ~53% preceded by continuous declining and stabilize after 60 h on stream at ~24%. This continuous decline happened due to the crystal growth (leading to reduced surface area), sintering, and particle agglomeration confirmed in line with XRD, BET-SSA, SEM and TEM. During both experiments, DP-ceria showed 100%CO selectivity (No CH_4). Additionally, no clogging or coking was observed during the process, which TGA-FTIR later confirmed.

Correspondingly, the stability tests for the RME-ceria (Fig. 4.6(b)) were performed in a similar way as described for DP-ceria. At GHSV of 60,000 ml g_{cat}^{-1} h^{-1}, RME-ceria showed a small decrease in conversion initially, but it stabilized after 20 h and remained stable at ~24%. However, at 10,000 ml g_{cat}^{-1} h^{-1} RME-ceria initially showed significantly high conversion ~62% near equilibrium conversion (~65%). At lower GHSV's, a slight decline in CO_2 conversion was observed, but it stabilized after 60 h on stream at ~52%. Overall, RME-ceria shows significantly stable behaviour despite its high-temperature exposure for 100 h on stream. This supports the fact that the reverse microemulsion synthesis method dramatically enhances the bulk ceria's activity and stability towards the RWGS reaction. At different GHSV's, RME-ceria showed 100% CO selectivity (No CH4). Additionally, No clogging or coking was observed during the process, which TGA-FTIR later confirmed. At ca. 20 h on stream it was observed that the incoming gases were able to make a channel (as the catalyst bed gets flat) because of not enough amount of quartz wool on both sides of the catalyst bed. Therefore, without stopping the flow, the gases were bypassed and the catalyst bed was once again tightened to

make a pack bed. As a result, a small increase in CO_2 conversion can easily be seen in Fig 4.6b at ca. 20 h.

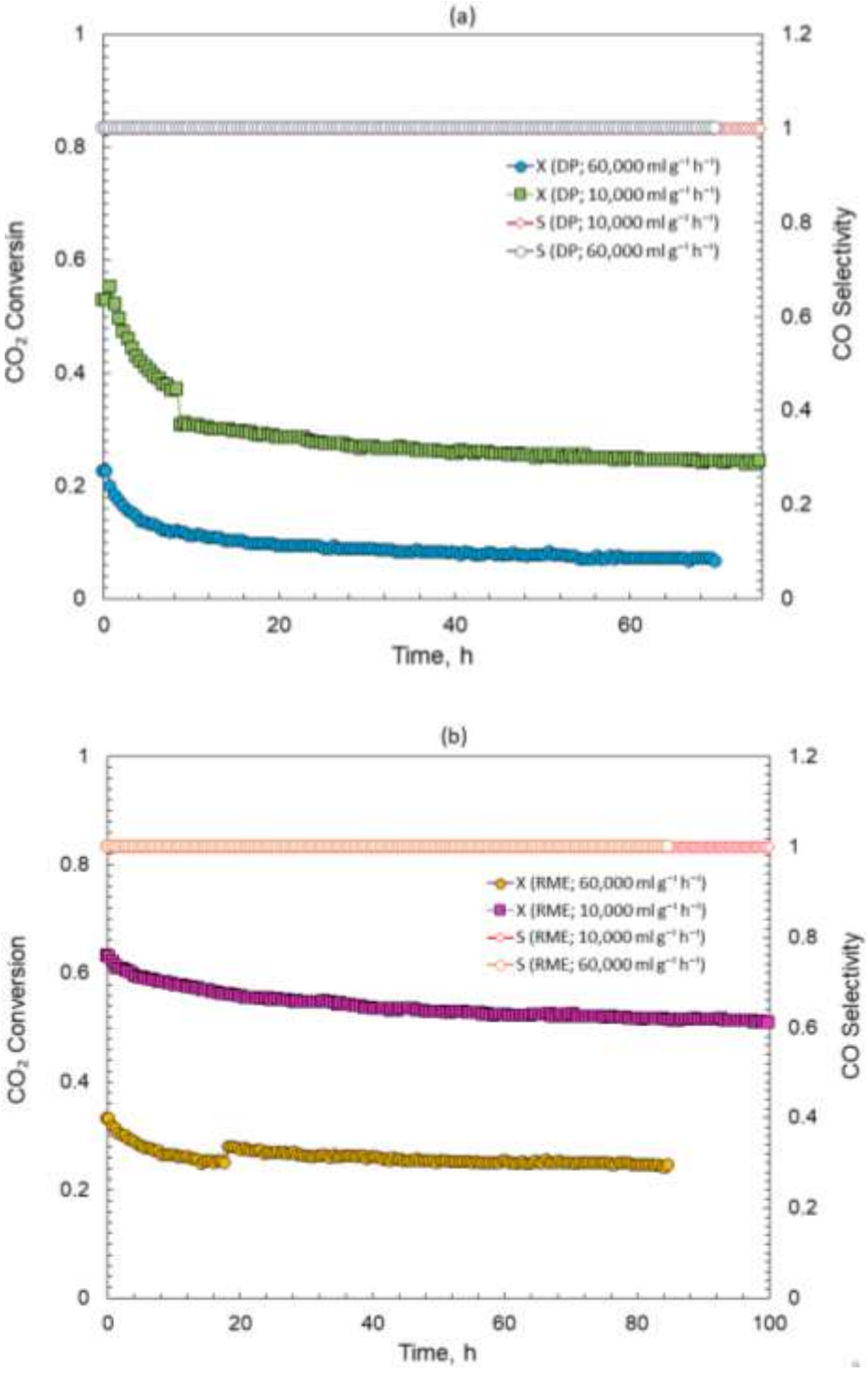

Figure 4.6: Stability test for at least 70 h at atmospheric pressure, 600°C and GHSV of 60,000 or 10,000 ml g_{cat}^{-1} h^{-1} for DP-ceria (a) and RME-ceria (b), respectively.

4.3.2 X-ray Diffraction and BET Studies

Fig. 4.7 represents the XRD spectrum for un-calcined, calcined at 275°C fresh and spent (for standard activity tests) RME-ceria and DP-ceria samples. The XRD peaks along the (111), (200), (220), (311), (222), (400), (331), and (420) planes confirm that both RME-ceria and DP-ceria have cubic fluorite structure (JCPDS 34-0394). For un-calcined RME-ceria, XRD spectrum seems to be of some amorphous solid because no sharp peaks were observed. This pattern's possible reason is the presence of the well-mixed residual surfactant (long-chain polymeric compound). Therefore, XRD pattern shows that RME process incorporates surfactant in a well-mixed fashion with RME-ceria crystals during the crystallization process, which was unable to remove even after three times water washing. On the other hand, un-calcined DP-ceria shows clear sharp peaks corresponds to cubic fluorite crystals of pure ceria (JCPDS 34-0394). After calcined at 275°C, RME-ceria shows some clear peaks, but they seem flattered compared to the DP-ceria peaks. Flatter peaks are the clear indication of smaller crystallite size. Crystallite size for all ceria samples was calculated using the Scherrer equation (26) with the XRD EVA software's built-in tool.

$$D_{(hkl)} = \frac{K\lambda}{\beta Cos\theta} \qquad (26)$$

Where λ is the XRD wavelength, β is the full width at half-maximum (in radian), θ is the diffraction angle, k is a constant, and $D_{(hkl)}$ represents the size. For each ceria sample, the average size was calculated based on the (111), (220), and (311) planes. Crystallite size, specific surface area (based on the ceria's theoretical and bulk density), and BET-surface area are tabulated in Table 4.1. For DP-ceria, the lattice parameter ranged between 5.411-5.415 Å, which is closed enough to the bulk cubic CeO_2 (5.41Å) filed in the JCPDS 34-0394. On the other hand, for RME-ceria the lattice parameter ranged from 5.411-11.1108 Å. The higher lattice parameter indicates the presence of more reduced form of CeO_2, i.e., CeO_{2-x} [225, 257]. Using the search and match tool in XRD EVA software, the RME-ceria contains a significant portion of the highly reduced form, i.e., $CeO_{1.67}$.

The BET-Specific surface area was determined for (both RME-ceria and DP-ceria) un-calcined and calcined (at 275°C) samples. For DP-ceria, the surface area for the calcined sample is less than the un-calcined sample. Before calcination, the area appeared to be 103.25 $m^2 g_{cat}^{-1}$, while after calcination, it reduces to 101.70 $m^2 g_{cat}^{-1}$. This decrease is in a perfect match with XRD data, as for DP-ceria the crystallite size changed from 6.63 nm to 7.6 nm for un-calcined and calcined ceria samples, respectively. The agglomeration of the particles, due to calcination, reduces the exposed surface area of the DP-ceria samples.

Table 4.1: XRD and BET analysis

Sample	**Average Crystalline Size**	**Theoretical Density(D_x)**	**Pure Ceria Bulk Density (D_b)**	**SSA Theoretical Density (D_x) based**	**SSA Bulk density (D_b) based**	**BET-SSA**
	nm	g_{cat}/cm^3	g/cm^3	m^2/g_{cat}	m^2/g_{cat}	m^2/g_{cat}
D-Ceria-UC	6.63	14.34	7.22	63.11	125.34	103.25
D-Ceria--Fresh	7.6			55.05	109.35	101.70
D-Ceria--Spent	21.08			19.85	39.42	7.21
RME-Ceria-UC	3.02			138.55	275.17	111.21
RME-Ceria-Fresh	4.02			104.08	206.72	146.84
RME-Ceria-spent	11.55			36.23	71.95	38.69

*Theoretical Density was Calculated using the following formula $D_x = 8*M/(N*a^3)$
Where M is the Molar mass of Ceria (172.115g/mol), N is Avogadro's number, "a" is the lattice constant and for Pure CeO_2 FCC crystal $N*a^3=96$.
* Surface area was calculated using the following formula, i.e., $SSA=6000/(D_x*Dp)$ or $SSA=6000/(D_b*D_p)$

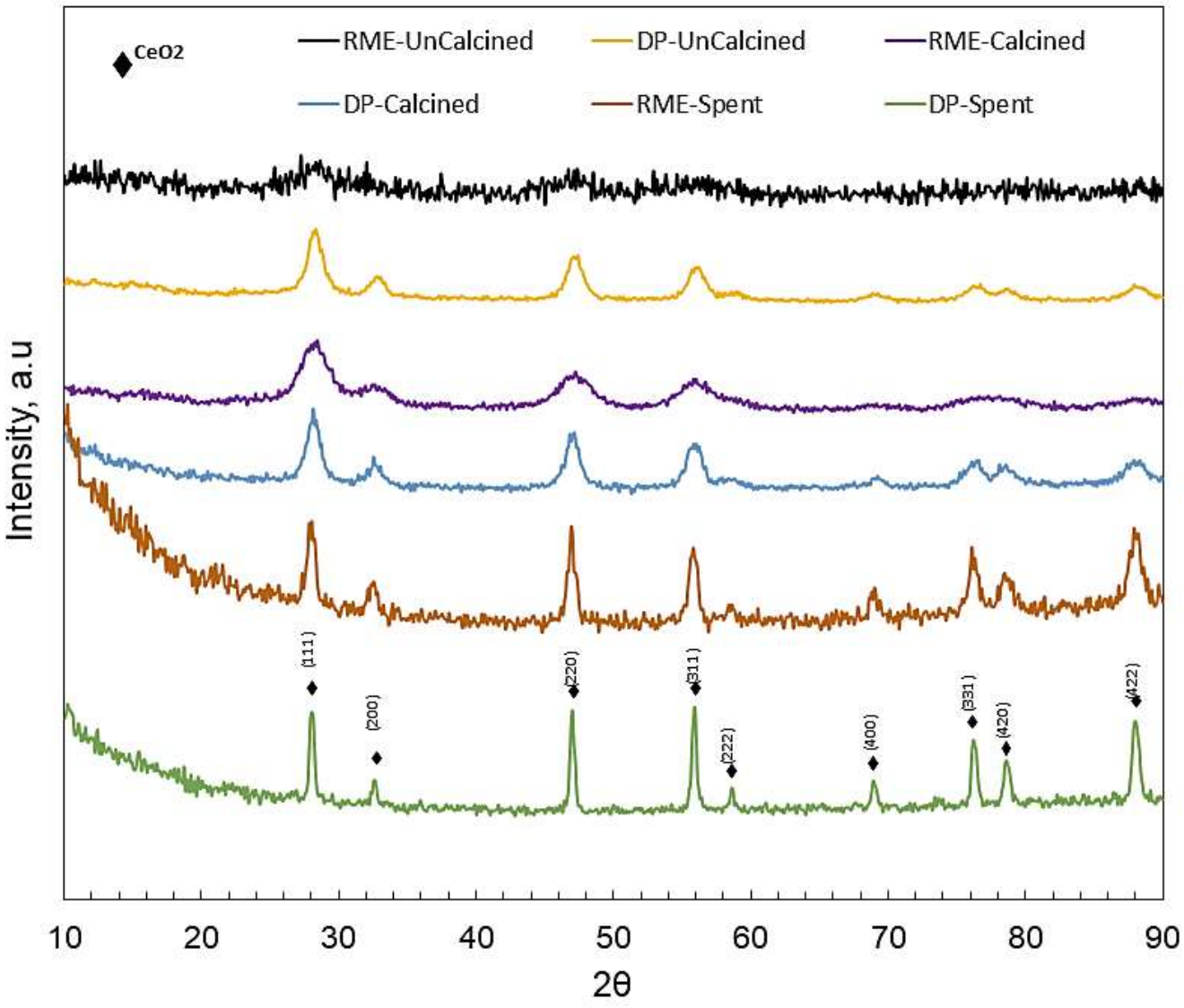

Figure 4.7: X-Ray Diffraction Spectroscopy.

On the other hand, for RME-ceria, the BET-surface area changed from 111.21 m^2 g^{-1} to 146.84 m^2/g for un-calcined and calcined, respectively. Implies for RME-ceria: The surface area increased (about 35 m^2 g^{-1}) after calcination compared to DP-ceria. This increase appeared because of the removal of the polymeric surfactant remains. The possible explanation for this increase is; the surfactant molecules are thoroughly mixed with ceria samples even after washing. This mixing helps to create pores in ceria samples after calcination [242].

4.3.3 H_2-TPR Studies

In catalytic reduction reactions, the redox properties of a catalyst play a vital role. To understand the reduction behavior of given samples H_2 temperature-programmed reduction was performed for both fresh and spent RME-Ceria and DP-Ceria. The TPR results well matched with the XRD data. TPR results show that the total H_2 consumed was 1055 µmol/g and 1232.9 µmol/g for RME-ceria and DP-ceria, respectively. Similarly, the %-H_2 reduction calculated was 9.07% and 10.61% for RME-ceria and DP-ceria, respectively. The smaller amount of H_2 consumed and low %-H_2 reduction for RME-ceria clearly shows that RME-ceria is already present in a highly reduced form compared to DP-ceria. RME-ceria already has more oxygen vacancies at room temperature than DP-ceria. Implies RME-ceria has a greater capacity to lose more oxygen than DP-Ceria without losing its fluorite structure. Apart from fresh samples, TPR data of spent catalysts also shows consistency with the XRD and BET data. The same amount of %-H_2 reduction was observed for both of the spent RME- and DP-ceria catalysts, i.e., 7.64 and 7.66, respectively. It can be seen in Table 4.1 that the BET-SSA for the spent RME-ceria is 38.69 $m^2\ g^{-1}$, while for DP-spent, it is 7.21 $m^2\ g^{-1}$, which is almost 5 times less than the SSA of RME-spent. Mean similar amount of oxygen was removed from DP-ceria even though the exposed area was 5 times less than RME-spent. The corresponding TPR profiles are presented in Fig. 4.8.

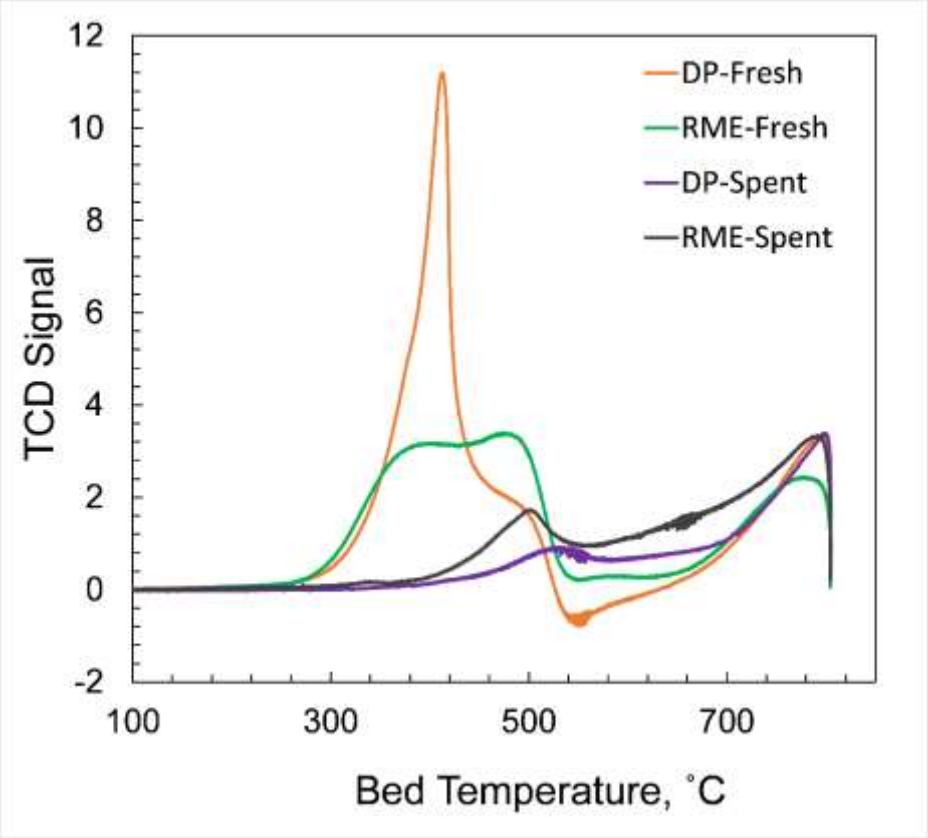

Figure 4.8: TPR profiles for fresh and spent RME- and DP-ceria.

4.3.4 SEM-EDX and ICP-OES

Fig. 9(a) shows the SEM micrographs (zoomed 500nm) for fresh and spent catalysts. Micrographs for both RME and DP-ceria look similar in direct agreement with XRD data because the crystallite size for fresh RME and DP-ceria is 4.02 and 7.06nm, respectively. It can easily be seen from Fig.4.9(a) that the particles are well connected, resulting in aggregates. Micrographs for the spent samples clearly show the agglomeration and sintering of particles as the catalyst was exposed to a higher temperature (up to 600°C during the T-test). XRD and BET-SSA confirm this fact as the exposed surface area for both catalyst RME and DP-ceria decreased significantly. Tabrizi et al. [258] and pournajaf et al. [26] observed the similar surface diffusion and agglomeration of CeO_2 particles with increasing

temperature. Higher temperatures facilitate surface diffusion that leads to neck formation and agglomeration. SEM micrographs show the cluster formation of nanoparticles. To analyze the surface dispersion of Ce and O for the given samples, SME-EDX was performed. It can easily be seen in Fig. 4.9(b) that Ce and oxygen are well dispersed over the surface for both RME and DP-ceria. A closer look also reveals that apparent oxygen concentration over the surface for RME-ceria is less than the DP-ceria, which directly agrees with the H_2-TPR results. Therefore, RME-ceria has more oxygen vacancies at room temperature than DP-ceria. The bulk composition of Ce content in the fresh RME-ceria was determined using the ICP-OES. ICP-OES results show that the bulk Ce contents were around 75%, close enough to the surface Ce content found for fresh RME-ceria through SEM-EDX, i.e., 73%.

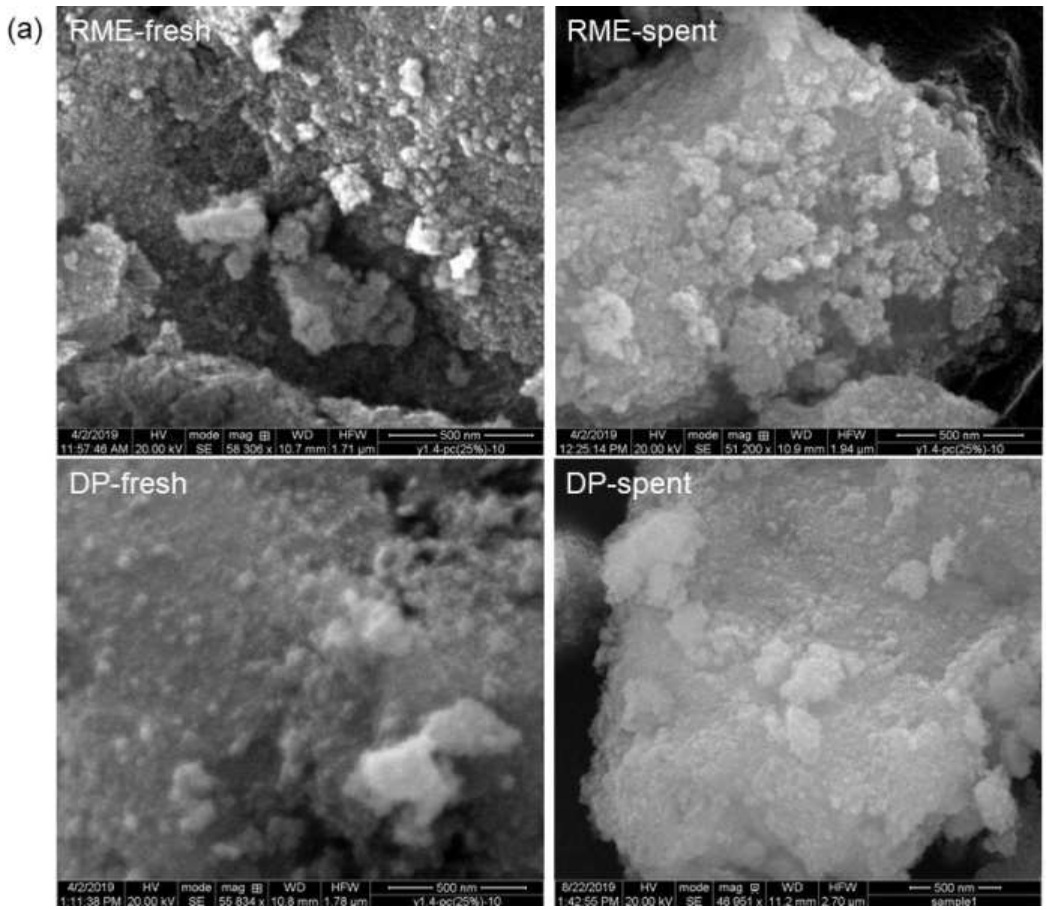

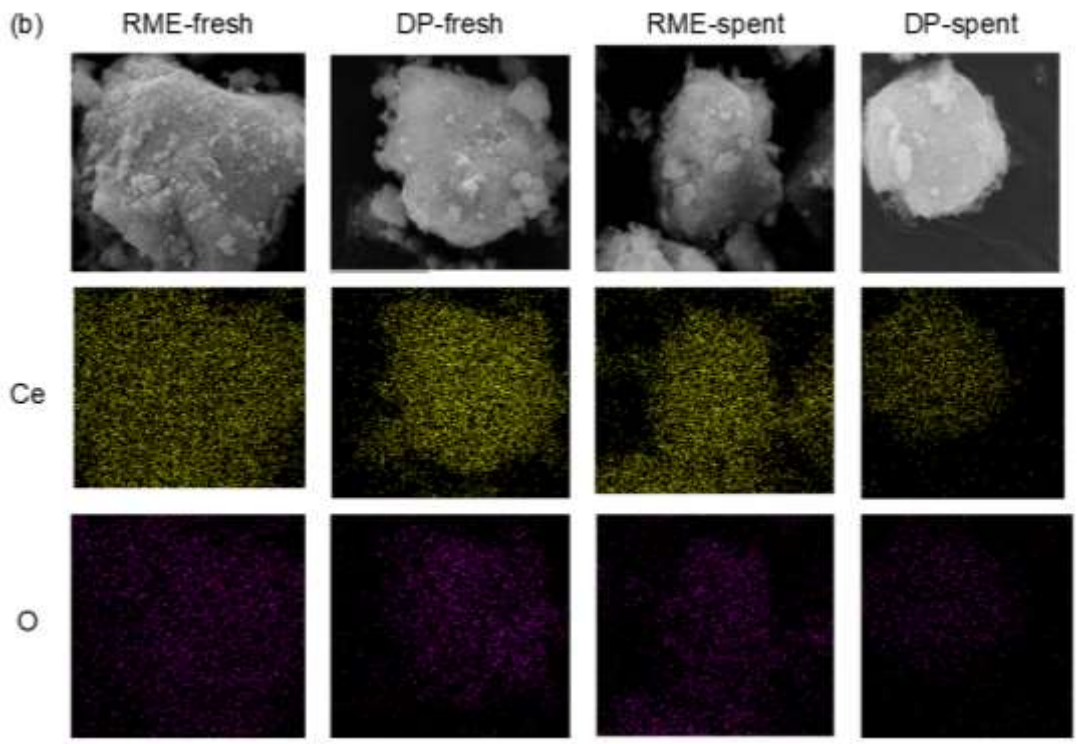

Figure 4.9: (a) SEM micrographs at 500 nm and (b) elemental mapping.

4.3.5 HRTEM Micrographs

To investigate more about the morphology and the shape of the ceria nano-crystals HRTEM micrographs were taken at 50nm and 10nm. Micrographs (Fig. 4.10) show that the particles are of nano-sized and uniform shape. RME-fresh seems to have small-sized nanoparticles with less agglomeration and high porosity than D-fresh. This fact is in direct agreement with the XRD results tabulated above. Fig. 4.10 shows that the particles significant agglomeration occurs after the reaction, leading to increased size for both RME- and the DP-ceria catalyst. This fact is also confirmed by the XRD data as the average crystallite sized risen from 4.02 to 11.55 nm and 7.6 to 21.08 nm for RME-ceria and DP-ceria, respectively. Compared to DP-ceria, the smaller increase in particle size for RME-ceria may be attributed to surfactant molecules remains [242].

Fig. 4.11 giving a more close-up look on a scale of 10 nm. Micrographs obtained at this resolution show the dominance of particle fringes with a d-spacing of 3.2Å, which is approximately equal to 3.12Å filed for the crystal facet (111) of fcc cubic ceria (JCPDS 34-0394). A large amount of HRTEM images were taken from unselected areas, fringes, and particle orientation was identified. For RME-fresh, spent, and DP-fresh surfaces were dominated to be (111) crystal facets, while for DP-spent some (200) crystal facets were also observed. These facets are observed when particles are oriented along the (110) facets. Wang and Feng [224] investigated the thorough particle shape analysis for ceria nanoparticles and revealed two crystalline structures for two different nanoparticle size range. 1) They found that for particles ranged 3-10nm, the particle is enclosed by (111) and (100) (equal to (200)) facets are dominated by truncated octahedral. 2) The larger-sized particles are dominated by octahedral enclosed with (111) facets. Their findings are well matched with the present studies. Fig. 4.11 reveals the same results for the fresh and spent catalysts.

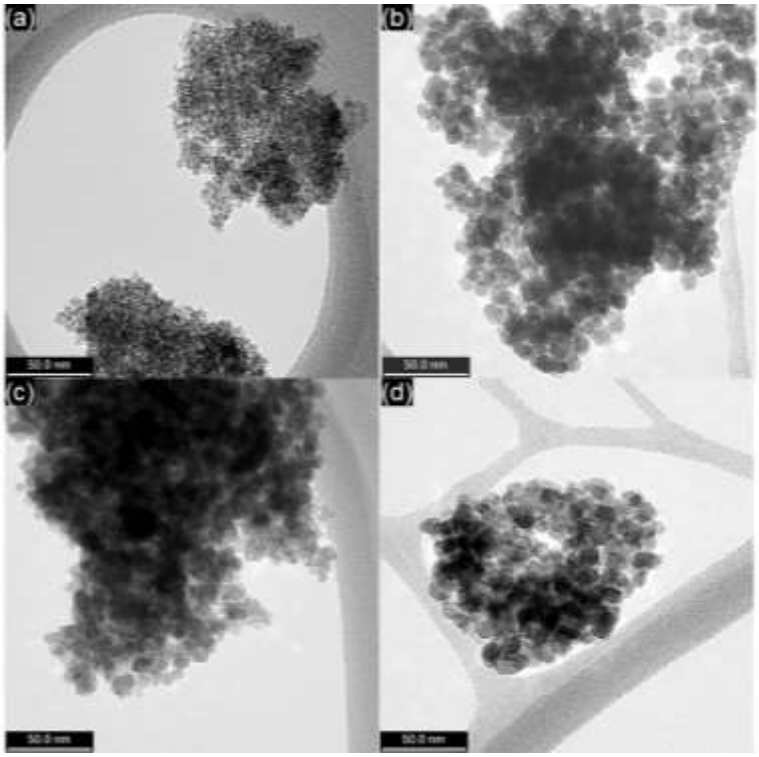

Figure 4.10: TEM micrographs at 50 nm for (a) RME-fresh, (b) DP-fresh, (c) RME-spent, and (d) DP-spent

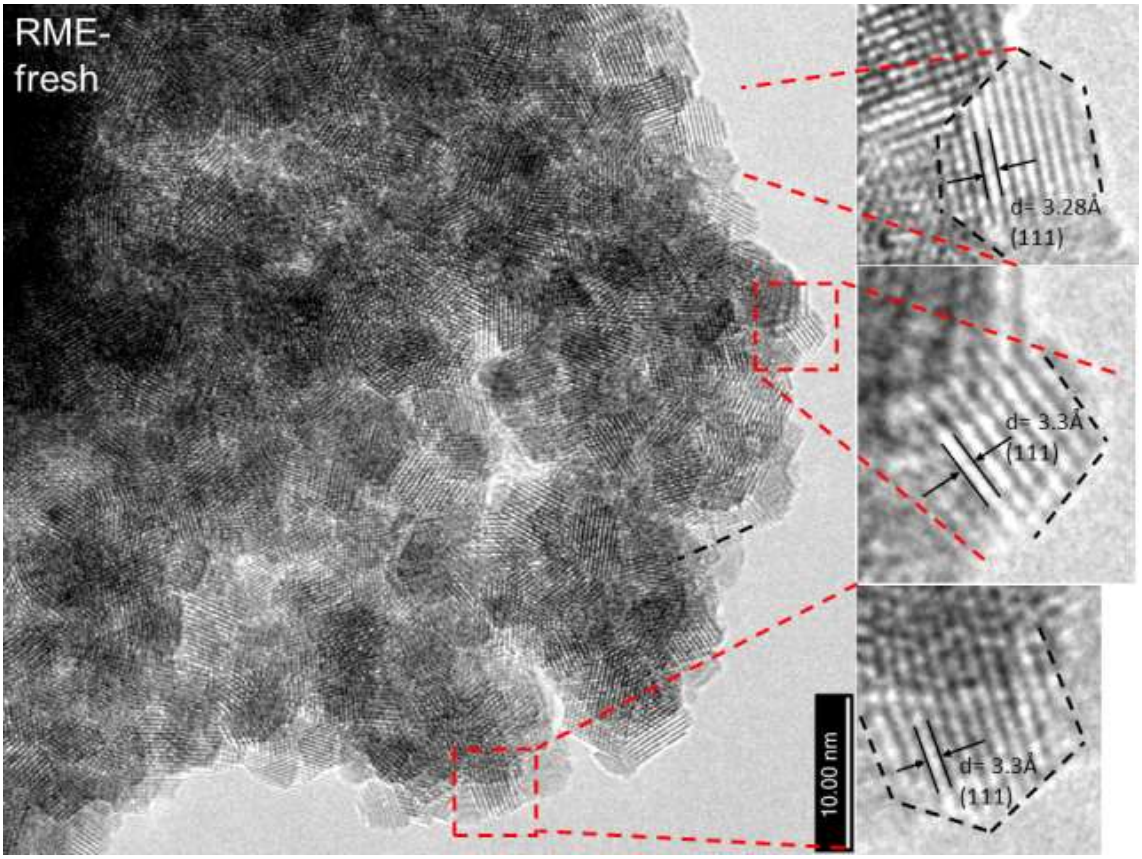
RME-
fresh
d= 3.28Å
(111)
d= 3.3Å
(111)
d= 3.3Å
(111)
10.00 nm

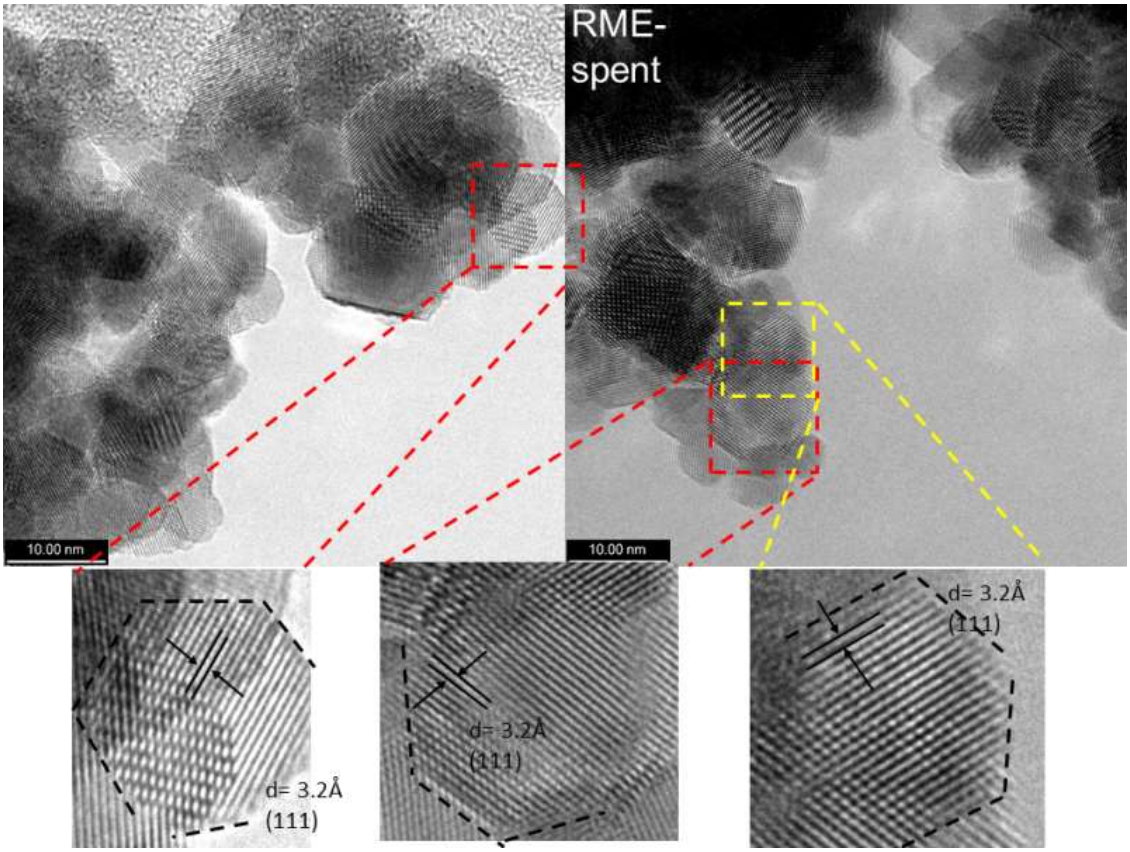
RME-
spent
10.00 nm
10.00 nm
d= 3.2Å
(111)
d= 3.2Å
(111)
d= 3.2Å
(111)

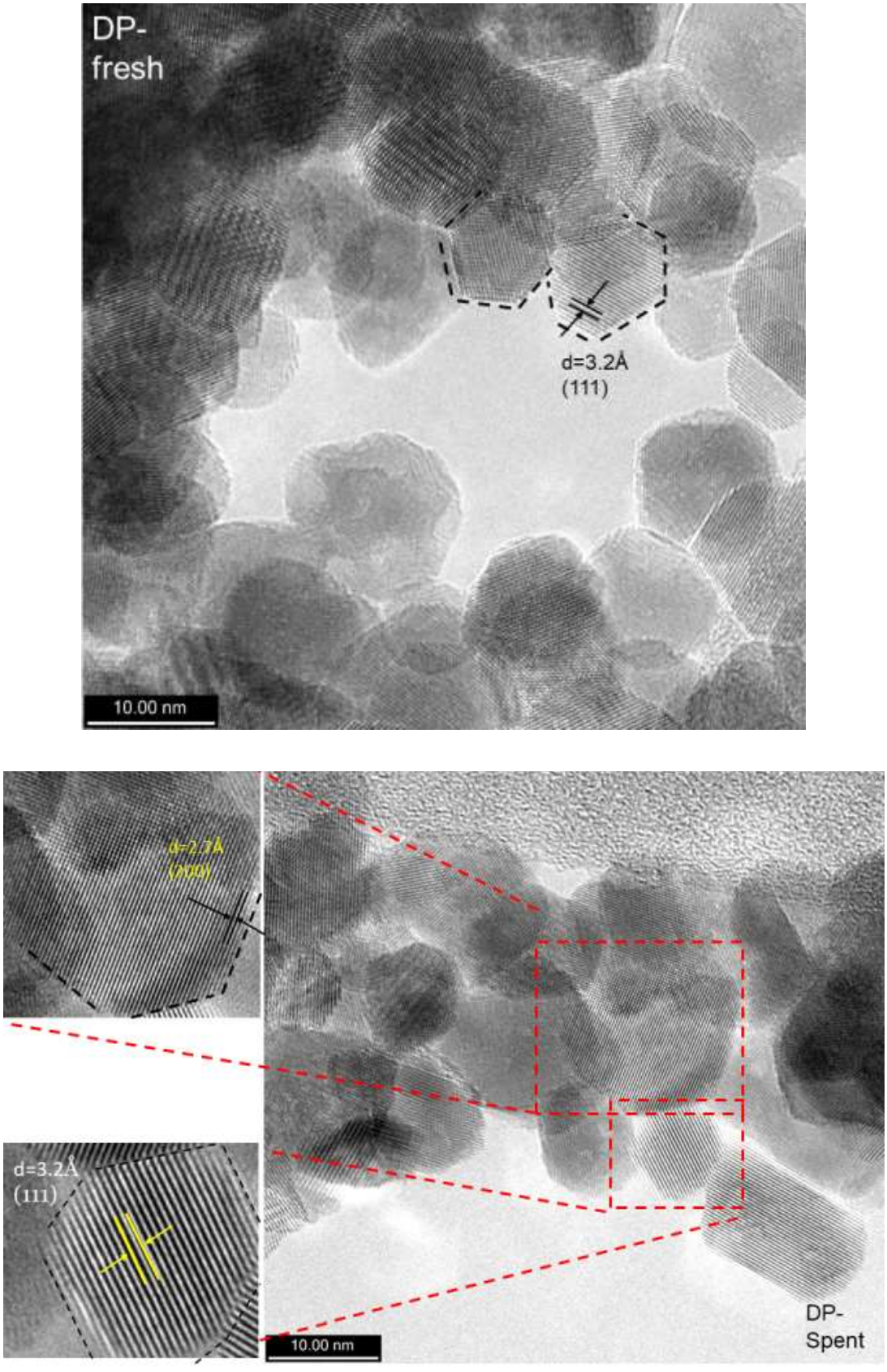

Figure 4.11: HRTEM micrographs at 10 nm for RME- and DP-ceria (fresh and spent) catalyst.

4.3.6 In-situ TGA-FTIR Studies

The thermal behavior of the fresh and spent RME- and DP-ceria was investigated by coupling the TGA with an in line FTIR gas analyzer. All the samples were pre-treated under the airflow at 150°C for 1 h. After pre-treatment, the TGA outlet was allowed to pass through the FTIR analyzer for the gases' qualitative analysis. Fig. 4.12 shows that for RME-fresh, 1.8% weight loss was observed < 450°C, attributed to the burning of the some organics in terms of carbon oxides [259, 260]. FTIR detects significant amounts of the CO_2 and CO, confirming the fact. From 450°C-800°C further weight loss of 0.3% was observed, which is attributed to the loss of oxygen and the formation of the different reduced from $CeO_{2-\delta}$, as indicated by the Ce-O phase diagrams [261-264]. TGA-FTIR results of DP-Ceria show other behavior than RME-fresh. There was no significant weight loss observed till 200°C. From 200°C-450°C, a weight loss of 2% was observed. This weight loss is related to the precursor's decomposition (-NO_3) and the crystallization of the ceria nano-crystallites [265, 266]. FTIR analysis confirms the precursor's decomposition as a significant amount of NO_2 and NO detected, as shown in Fig. 4.12.

Correspondingly, the TGA-FTIR analysis of both spent RME and DP-ceria (collected after standard temperature test) was conducted as well. Only 0.63% and 0.75% weight loss was observed for RME and DP-ceria, respectively. This loss is well related to the loss of any left over CO_2 on the catalyst and some restricting at high temperature (600°C-800°C). Like wise, to confirm the excellent coking resistance behavior of the as-prepared catalyst the TGA-FTIR for the spent RME- and DP-ceria (collected after 70 h on stream at 600°C) catalyst was performed. Results showed that no significant CO_2 or CO was detected other than already present in the air. The experiment confirms that even after a long time under high temperature, the ceria did not show high deactivation due to sintering or coking.

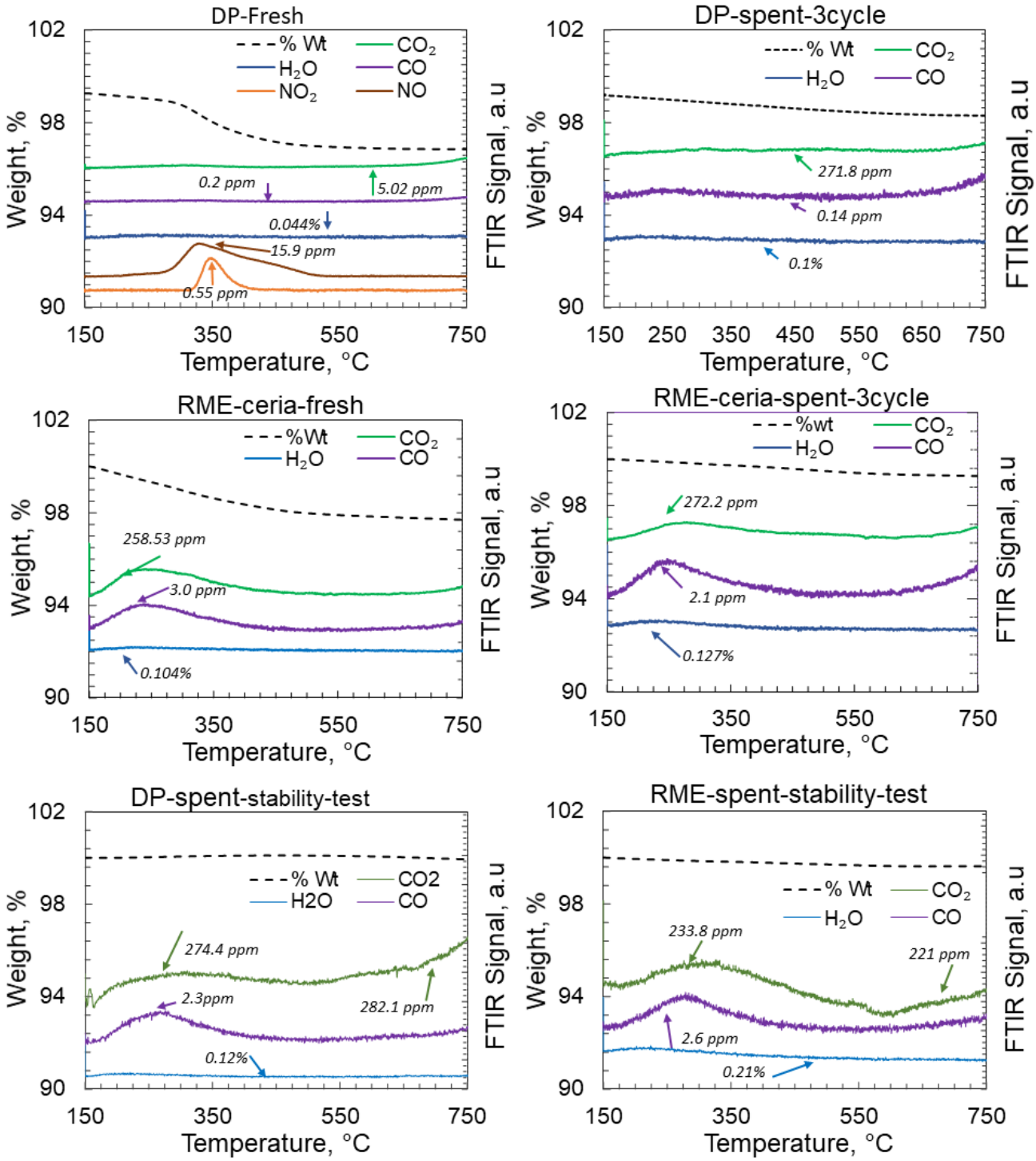

Figure 4.12: TGA-FTIR analysis for fresh and spent RME- and DP-ceria.

4.3.7 Reaction mechanistic Studies (In-situ FTIR surface reaction analysis)

Mechanistic studies are critical to understanding the surface reactions happening over the catalyst. The final reaction product produced during a catalytic reaction depends on the intermediates formed over the catalyst surface due to the adsorption and interaction of the reactant gases with the catalyst. A mixed gas feed (30 ml min^{-1}, 2% CO_2 / 8%H_2 / 90% argon) introduced into the system at 400°C and reaction spectra were collected. Fig. 4.13 represents the reaction spectra observed after 15 minutes of entering the reaction gases during the *in-situ* FTIR analysis of fresh and spent RME- and DP-ceria samples. Several peaks were detected for all samples at a similar location. Peak located at 850cm^{-1} for RME-fresh, DP-fresh, DP-spent, and peak located at 858 cm^{-1} for RME-spent represents the uni- or bidentate carbonate. Peak located at 1030 cm^{-1} for RME-spent, DP-fresh, DP-spent and peak located at 1042 cm^{-1} for RME-fresh represents unidentate carbonate. Similarly, peak located between 1100-1436 cm^{-1} again represents the uni- and bidentate carbonate formed due to CO_2 adsorption. Peak located in between 1501-1579 cm^{-1} represents the formation of inorganic carboxylate [119, 267-270]. The carbonate and carboxylate presence shows that the RWGS reaction follows the redox mechanism over the prepared unsupported RME- and DP-ceria samples as shown below (* denotes the vacancy site) [119]. Fig. 4.14 shows the Schematic of the reaction mechanism.

$$CO_2 + 2^* \rightarrow CO^* + O^* \qquad \text{(i)}$$

$$CO^* \rightarrow CO_{(g)} + * \qquad \text{(ii)}$$

$$H_{2(g)} + 2^* \rightarrow 2H^* \qquad \text{(iii)}$$

$$2H^* + O \rightarrow H_2O^* \qquad \text{(iv)}$$

$$H_2O \rightarrow H2O_{(g)} + * \qquad \text{(v)}$$

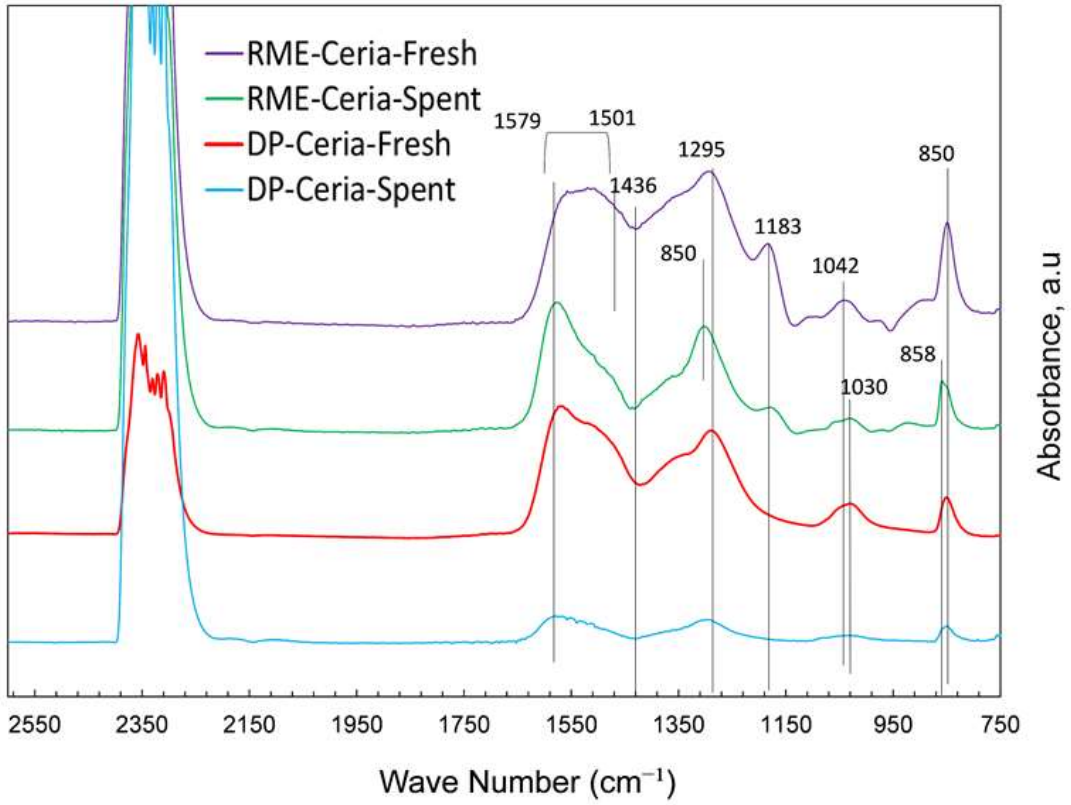

Figure 4.13: In-situ FTIR spectra over Fresh and spent RME- and DP-ceria after 15 min of reaction under 2% CO_2 / 8% H_2 / Ar.

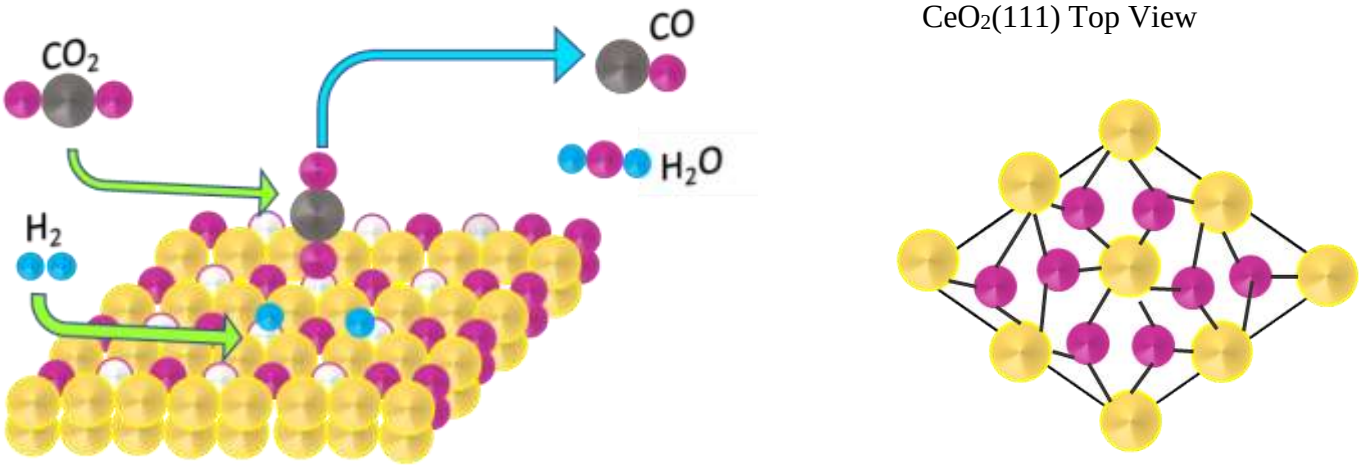

Figure 4.14: Schematic representation of RWGS reaction mechanism over unsupported ceria: Gray, blue, yellow, pink, and white circles represent carbon, hydrogen, cerium, oxygen atoms, and oxygen vacancies, respectively.

4.4 Conclusions

In this study, we presented the synthesis of pure unsupported nanoceria (RME-ceria) via the reverse microemulsion method for the application of the RWGS reaction. Using a unique microemulsion ratio, we achieved highly porous nanoparticles with the specific surface area of 142 m^2 g^{-1}. The as prepared bulk nanoceria showed excellent CO_2 conversion ~42% at 600°C relatively high GHSV of 60,000 ml g_{cat}^{-1} h^{-1}. For comparison, a baseline catalyst was also prepared via direct precipitation method (DP-ceria), which shows poor conversion rates and poor stability.

RME-ceria showed well stable activity towards RWGS without deactivation. At lower, GHSV of 10,000 ml g_{cat}^{-1} h^{-1}, nearly equilibrium CO_2 conversion (~62%) was observed initially, which stabilizes after 60hr to around 52%. However, for DP-ceria the deactivation was quite significant even at lower GHSV (10,000 ml g_{cat}^{-1} h^{-1}). It declines from 53% to 24% in 70 h. TPR studies revealed that RME-ceria is present in a highly reduced form even at room temperature and having more oxygen vacancies than DP-ceria. Oxygen vacancy is reported as the leading active site for converting CO_2 to CO over the bulk ceria [20-22]. Also, XRD studies confirmed that even after exposing the RME-ceria at 600°C for several hours, the crystallite size increases from 4 nm to 11 nm, while for DP-ceria, the increase in crystallite size was quite significant, i.e., from 7 nm to 21 nm.

This study's most important finding is that the RME-ceria showed 100% CO selectivity for 100 h on stream without any coke formation over the catalyst surface. This finding confirms the fact that RME-ceria with exposed (111) crystalline planes is highly stable, active, and resistant to coking and deactivation.

Chapter 5

Selective catalytic reduction of CO_2 over nanostructured ceria supported on γ-alumina prepared via RME process

5.1 Introduction

In past decades, several noble and non-noble catalysts have been utilized for the thermocatalytic reduction of CO_2. Bando et al. [80] studied the promoting effect of Li on the catalytic activity of RhY catalysts. They found out that the catalyst's selectivity towards the final product changes from CH_4 to CO by increasing the Li amount. To investigate the promotion of Li, they utilize *in-situ* FTIR and TPR characterization techniques. Heyl et al. [82] also studied CO_2 hydrogenation over K and Ni modified Rh/Al_2O_3 catalyst by *in-situ* and operando DRIFT spectroscopy. Studies showed that K-promotion significantly enhances the selectivity of the process towards CO. Rh- K-Ni/Al_2O_3 showed the highest CO formation, while unprompted catalysts showed preference towards CH_4. It was found that CO_2 adsorbed on the support as hydrogen carbonate rather than on the metal surface dissociative. K also enhances CO desorption and resists further CO hydrogenation to CH_4. Highly dispersed supported Au nanoparticles have received significant attention in catalytic hydrogenation of CO_2 to valuable chemicals [83-85]. Zhuang et al. [167] investigated RWGS over Ru promoted $Cu/ZnO/Al_2O_3$ catalyst. Ru significantly increases the stability and CO_2 conversion compared to the baseline catalyst. They showed that CO_2 conversion doubled over Ru promoted catalyst as compared to the baseline catalyst. Upadhye et al. [86] studied the activity of various oxide-supported (TiO_2, CeO_2, Al_2O_3) Au catalysts towards RWGS reaction in the absence and presence of visible light. They showed that the Au supported catalyst activity for RWGS is 30-1300 times higher than dark conditions under visible light. TiO_2 and CeO_2 supported Au catalysts showed the maximum CO_2 conversion rate (in visible light) of

2663 and 1417 μmol g_{cat}^{-1} $min^{-1,}$ respectively. A significant decrease in the apparent activation energy, from 47 kJ/mol in the dark to 35 kJ/mol in light, was observed due to the LSRP (localized surface plasmon resonance). Kwak et al. [102] synthesized atomically dispersed alumina and MWCNT (multiwall carbon nanotubes) supported Pd catalyst. Alumina-supported Pd shows efficient conversion of CO_2 to CO, while MWCNT supported Pd catalyst shows poor selectivity. However, the addition of La_2O_3 made Pd/MWCNT active for RWGS.

Despite the high activities of noble metal catalysts towards RWGS reaction, their large-scale application is still questioned due to high cost and rareness [10]. Cu received significant attention as an alternative due to its corrosion resistance. There are various commercial Cu based catalyst are available for WGS [87-89] and methanol synthesis [90, 91]. Jurković et al. [92] investigated different oxide-supported (Al_2O_3, CeO_2, SiO_2, TiO_2 and ZrO_2) Cu catalysts and demonstrated the effect of support on the activity of RWGS and reaction pathway. TPR studies identified alumina and ceria as the most promising supports. However, zirconia shows the worst activity and had the worst Cu dispersion as well. On the other hand, iron-based catalyst offers significant activities towards RWGS due to their stability. Kim et al. [97] investigated Fe-oxide nanoparticles catalytic activities for RWGS reaction at 600°C. Characterization studies revealed that atomic C and O formed during the reaction over the Fe-oxide surface, which then penetrates the bulk of iron oxide and forms iron carbide. Consequently, the surface Fe structure remains unchanged, which leads to the long-term stability of the catalyst. Loiland et al. [98] studied RWGS reaction over alumina supported Fe and K promoted alumina supported Fe catalysts at 723 K and 753 K and atmospheric pressure. Both catalysts show high CO selectivity (>99%). It was found out that the addition of K increases the reaction rate 3 times.

Apart from nobel and transition metals, the rare earth metal cerium (Ce) also received the researcher's significant attention for its high oxygen storage capacity. Cerium oxide-based catalysts are well known and used commercially as three way catalyst (TWC) in automotive catalytic converters, in refineries for fluid–cracking, and as dehydrogenation catalyst during styrene production [271]. In

the early 70's, noble metal promoted ceria supported alumina catalyst were used as the TWC in the automobile for CO oxidation and NO_x reduction [272]. Nowadays, CeO_2-ZrO_2 solid solutions are used as TWCs [273]. Ceria supported alumina catalyst also shows some promising results towards different chemical reactions. Mahamulkar et al. [274] investigated the oxidation of *in-situ* generated coke during ethylene pyrolysis. Ceria-supported catalyst shows resistance to coking compared to unsupported alumina and could oxidize coke at a much lower temperature than ceria alone. Aysu et al. [275] studied Pavlova microalgae pyrolysis to bio-oils over three different ceria supported alumina catalysts for the first time. Results showed that all catalysts increased the bio-oil yield with respect to the non-catalytic runs and reduced the O/C ratio from 0.69 (Pavlova sp.) to 0.1–0.15, which is close to that of crude oil. Wen et al. [276] studied the removal of Hg over alumina-supported ceria. The experimental results show that CeO_2 could catalyze the HgO removal reaction and the HgO removal efficiency of CeO_2/γ-Al_2O_3 increases with the increase of the CeO_2 loading value.

Apart from oxidation, ceria based catalysts have shown significant activity towards CO_2 reduction to CO. Zhou et al. [144] investigated various CeCu composite catalysts for the RWGS application and found that $Ce_{1.1}Cu_1$ show the highest stability and highest conversion rate of 1.38 mmol g_{cat}^{-1} min^{-1} at 400°C with CO selectivity >0.99. Similarly, Dai et al. [20] investigated CO_2 reduction over ceria prepared using three different methods: hard templet, complex, and precipitation method. They showed that all three catalyst shows 100% selectivity towards CO, while ceria prepared by hard templet method showed the highest CO_2 conversion of 16% at 580°C. To the best of the author's knowledge, no investigation was ever reported for RWGS application over CeO_2/γ-Al_2O_3.

In this study, we attempt for the first time the potential of ceria-supported γ-alumina for the application of the RWGS reaction for the temperature ranger of 300°C-600°C. Three catalysts were prepared (via the RME method) at three different loadings of ceria (20 wt%, 30 wt% and 40 wt%). All the catalysts showed complete 100% CO selectivity, while the 40 wt% ceria offers the maximum CO_2 conversion.

5.2 Experimental

5.2.1 Chemicals

Cerium nitrate hexahydrate (99.5% $Ce(NO_3)_3 \cdot 6H_2O$) was purchased from Alfa Aesar, Thermo Fisher Scientific Inc. Aluminum nitrate nona-hydrate (99+% $Al(NO_3)_3$) and Triton X-100 surfactant were purchased from Acros Organics, Fisher Scientific Inc. 2-Propanol (99.9%), Cyclohexane (>99%), and NH_4OH (28-30% NH_3 basis) were purchased from Sigma-Aldrich Inc. All the chemicals were used as is without any further purification. All the aqueous solutions were prepared using deionized water.

5.2.2 Catalyst Preparation

20%, 30%, and 40% (by weight) $CeO_2/\gamma\text{-}Al_2O_3$ catalysts (denoted as 20%Ce/Al, 30%Ce/Al, and 40%Ce/Al throughout the text) prepared in three different batches each (denoted B1, B2, and B3) using reverse microemulsion (RME) method as described in chapter 3 and 4. In a typical synthesis, three blank RME's were initially prepared while mixing Trinton X-100, 2-propanol, and cyclohexane in a specified ratio of 1:4.5:3.5, respectively. After, calculated amounts of $Ce(NO_3)_3$ and $Al(NO_3)_3$ were dissolved in deionized water to form 0.29 M and 1 M aqueous solutions, respectively (denoted as Ce_{aq} and Al_{aq}). Finally, Ce_{aq}, $Al_{aq,}$ and NH_4OH were poured into the respective blank RME's to prepare the corresponding RME solutions denoted as Ce-RME, Al-RME, and NH_4-RME. Firstly, Al-RME was added slowly to NH_4-RME under vigorous stirring and left for 1 hour. After 1 hour, Ce-RME was added to the above mixture. The opaque solution immediately turned to light yellowish-brown, and after another hour, it turned bright yellow. The final mixture was left for several hours for gravity settling. After removing the clear upper solution, the settled wet precipitates were centrifuged at 3500 RPM for 10 min followed by washing (three times) with deionized water and centrifugation at 3500 RPM for10 min each to remove the maximum possible amount of surfactant. The wet precipitates were

collected in a glass petri dish and were air-dried at 150°C for 6 h. Fig. 5.1 shows each step described above. The full schematic of the synthesis process is presented in Chapter 3, section 3.5.4.

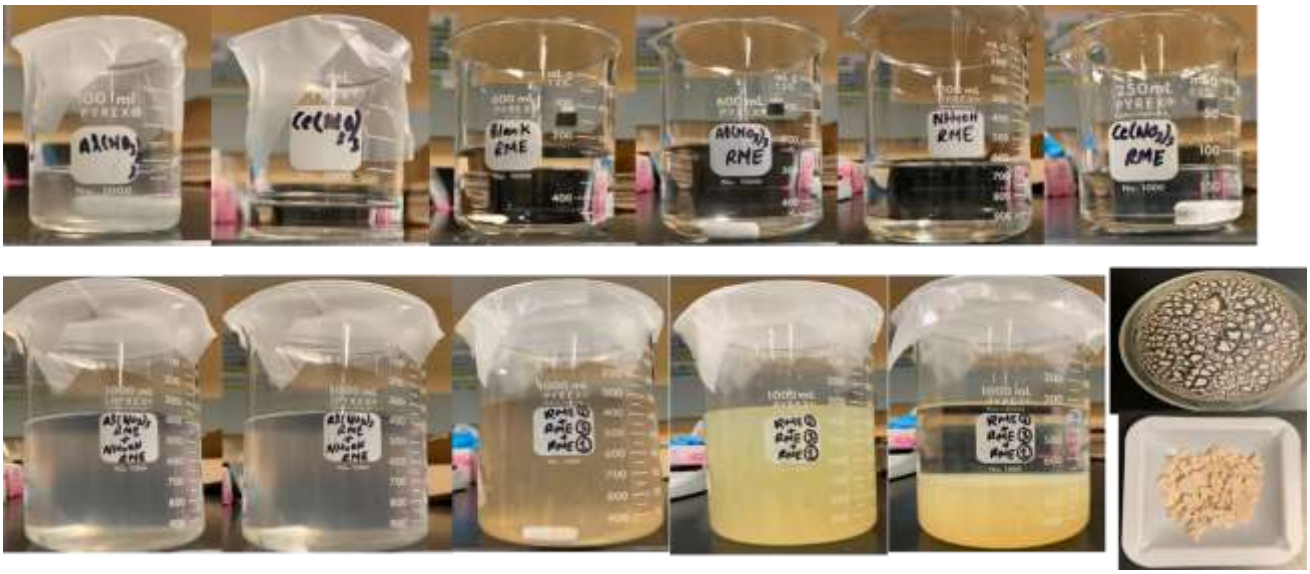

Figure 5.1: $CeO_2/\gamma\text{-}Al_2O_3$ catalyst preparation sequence.

After drying, each catalyst was calcined at 275°C under continuous airflow in a muffle furnace for 4 h, pelletized (50 MPa), crushed, and sieved to 250-425 µm particles. Fig. 5.2 shows calcined pelletized fresh (before activity test) and spent (after activity test) catalysts.

Figure 5.2: Calcined pelletized fresh and spent catalysts.

5.2.3 Catalytic activity test

The RWGS catalytic activities over 20%Ce/Al, 30%Ce/Al, and 40%Ce/Al were evaluated in a continuous flow fixed bed reactor at 3 bar absolute pressure and temperature ranged 300°C-600°C. The reactor system was made by joining the 1/2" stainless steel tube (316L, Swagelok) with 1/4" stainless steel tube (316L, Swagelok) via a reducing adapter (served as the reactor) and straight union, as shown in the schematic. Please refer to Fig. 3.11 for the kinetic reactor schematic and section 3.6.1 for the complete description and experimental setup of the flow system.

The total CO_2 conversion, CO Selectivity, and CH_4 selectivity were calculated according to the following equations.

$$X_{CO_2} = \frac{y_{CO}+y_{CH_4}}{y_{CO_2}+y_{CO}+y_{CH_4}} \qquad (11)$$

$$S_{CO} = \frac{y_{CO}}{y_{CO}+y_{CH_4}} \qquad (12)$$

$$S_{CH_4} = \frac{y_{CH_4}}{y_{CO}+y_{CH_4}} \qquad (13)$$

5.2.4 Catalyst Characterization

The crystallite size and structure (of all $CeO_2/\gamma\text{-}Al_2O_3$ catalysts) was measured using D8 discover diffractometer, Bruker with a Cu-Ka radiation source ($\lambda = 1.54$ Å) 40 kV tube voltage and 40 mA of a tube current. XRD patterns were recorded for a scan speed of 3, and a step size of 0.1° with 2θ ranged 10° - 90°. Specific surface area (SSA) was determined for all the fresh and spent catalysts using AMI-300lite (Altamira Instruments, USA) catalyst characterization unit. Helium was used as the purge gas, while 10% N_2/He was used as the absorbing gas to calculate the surface area using single point BET-equation. ICP-OES (Inductively coupled plasma optical emission spectroscopy, Prodigy SPEC, Leeman Labs Inc) was used to measure the bulk concentration and exact loading of ceria over γ-alumina.

Porous structure, elemental mapping, and surface composition of fresh and spent catalysts were obtained using HRSEM-EDX (high resolution electron microscopy coupled with energy-dispersive X-ray spectroscopy) a Zeiss Ultra microscope (20 kV). TPR (Temperature programmed reduction) analysis was performed using AMI-300Lite, Altamira instruments, catalyst characterization instruments to investigate the extent of reduction for all fresh and spent catalysts. 10% H_2/Ar mixture was blown over the catalyst, and the change in H_2 composition was observed using a TCD (thermal conductivity detector) at the outlet over the temperature range of 300°C-800°C. Thermo-gravimetric analysis (TGA, Q500, TA Instruments), coupled with an in-line gas FTIR analyzer (Multigas^{TM} 2030, MKS instruments), was performed for both fresh and spent catalysts to evaluate their thermal stability and extent of coking (after reaction). The temperature ramp was set to 10°C min^{-1} for $T \leq 150$°C and maintained under isothermal conditions for 1 h at 150°C. After 1 h, the temperature ramp was set to 2°C min^{-1} for 150°C < T < 800°C and the airflow was set to 40 ml min^{-1}.

5.3 Results and Discussion

5.3.1 Catalytic Activity and Stability Studies

5.3.1.1 Catalytic Activity and Selectivity

The catalytic activity for RWGS reaction over 20%, 30%, 40%Ce/Al, and RME-Ceria was evaluated as a function of increasing temperature. To assess the performance repeatability, three different batches of each catalyst were prepared separately and subjected to the same reaction condition of 300°C-600°C temperature, 3 bar absolute pressure, and GHSV of 60,0000 ml g_{cat}^{-1} h^{-1} using brand new reactors. All catalysts show 100% CO selectivity for each batch tested separately.

A monotonic increase in CO_2 conversion was observed as the reaction temperature increased from 300°C-600°C, but no significant CO_2 conversion was observed before 400°C for all the samples. Fig. 5.3(a) represents a CO_2 conversion comparison for all the catalysts. Error bars represent the standard deviation for three measurements taken for three different catalyst batches. 20%Ce/Al shows the least CO_2 conversion at all the temperatures, while the rest shows almost similar conversion at all the temperatures except 600°C. 40%Ce/Al offers a nearly 1% higher conversion than 30%Ce/Al at 600°C and comparable activity (at all temperatures) to unsupported RME-ceria with just loading of 40% by weight over γ-alumina. This fact is precisely opposite to what Chen et al. showed for the oxidation of phenol over Ceria/γ-Alumina [277]. They showed that as ceria content increased from 20% the phenol conversion starts falling from the best value. This is proper evidence of what we observed in this study that 20%Ce/Al showed less CO_2 reduction to CO, while 30% and 40%Ce/Al showed higher CO_2 reduction. This means the higher loading of ceria over γ-alumina prepared via the RME method has a superior activity for efficiently reducing CO_2 to CO. A similar effect of the synthesis method for selective catalytic reduction of NO to NH_3 was observed by Guo et al. [278]. They showed that CeO_2/γ-Al_2O_3 catalyst prepared by the Sol-gel method has the higher NO conversion at all temperatures ranged 200°C-400°C compared to the same catalyst prepared via co-precipitation and wet impregnation.

Studies showed that in ceria-based catalysis, oxygen vacancies act as the leading active sites for catalytic reactions [23, 115]. The results for 30% and 40%Ce/Al showed almost similar activities to that of RME-ceria, which leads to the fact that both catalysts have an almost identical amount of active sites as that of bulk RME-ceria. This fact later confirmed with the BET and HRSEM-EDX studies that the specific surface area for 30%Ce/Al is more than doubled and for 40%Ce/Al is almost doubled than RME-ceria, also ceria is well dispersed over the surface of γ-Al_2O_3.

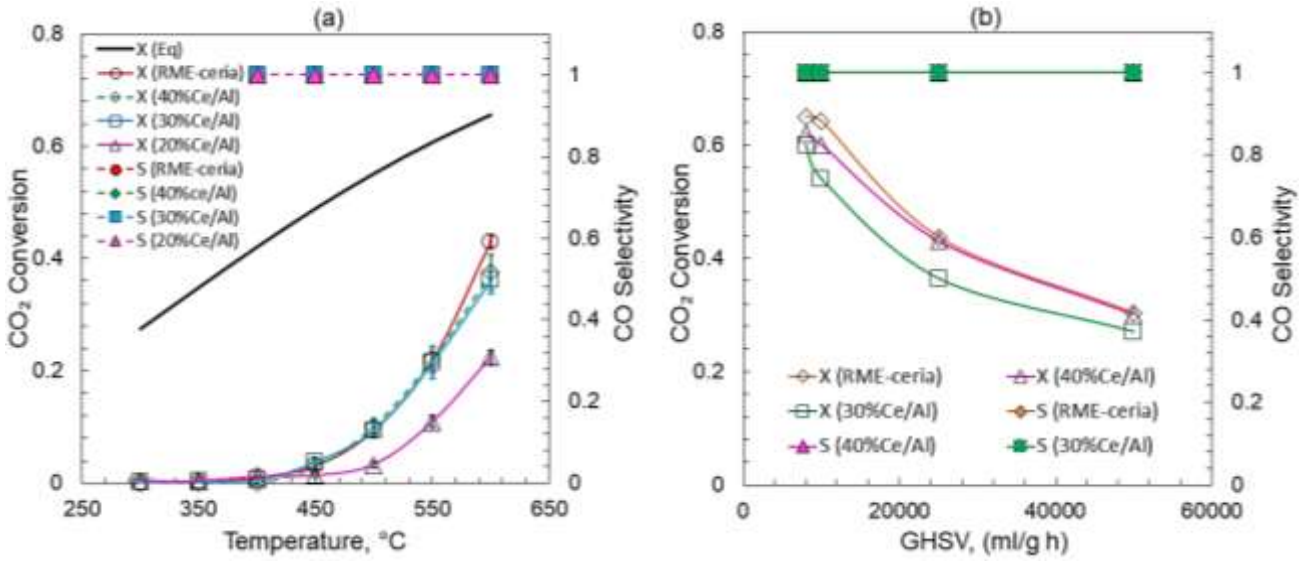

Figure 5.3: RWGS reaction activity for three different catalyst batches: 20%Ce/Al, 30%Ce/Al 40%Ce/Al and RME-ceria.

In addition to evaluating each catalyst at various temperatures, RME-ceria, 30%, and 40%Ce/Al catalysts were also assessed at different GHSVs of incoming reaction gasses at 600°C and 3 bar pressure to see the impact of space velocity on CO_2 conversion. 20%Ce/Al catalyst was not assessed under various GHSV's because of low CO_2 conversion observed at all temperatures during the activity tets compared to 30% and 40%Ce/Al. All catalysts show the same trend as expected, i.e., at low space velocities, significantly higher conversion was recorded because of higher gas-catalyst contact time. Fig. 5.3(b) shows that at very low GHSV's (< 10,000), RME-ceria showed exact equilibrium

conversion (~65% with 100% CO selectivity), whereas 40%Ce/Al showed comparable CO_2 conversion of 62% with 100% CO selectivity. A similar effect of lower GHSV's for RWGS has been reported in the literature [248]. However, for the entire GHSV's tested range, 30%Ce/Al showed lower conversion and activity relative to RME-ceria and 40%Ce/Al.

CO generation rates and activation energies (E_a) calculated from the data presented in Fig. 3(a) (right plot) are shown in Fig. 5.4 as the function of reaction temperature using eq.24 and eq.25 (a linear form of Arrhenius law).

$$R = \frac{F_{CO_2,f} \times X_{CO_2}}{W_c} \qquad (24)$$

$$In(R) = InA - \frac{E_a}{RT} \qquad (25)$$

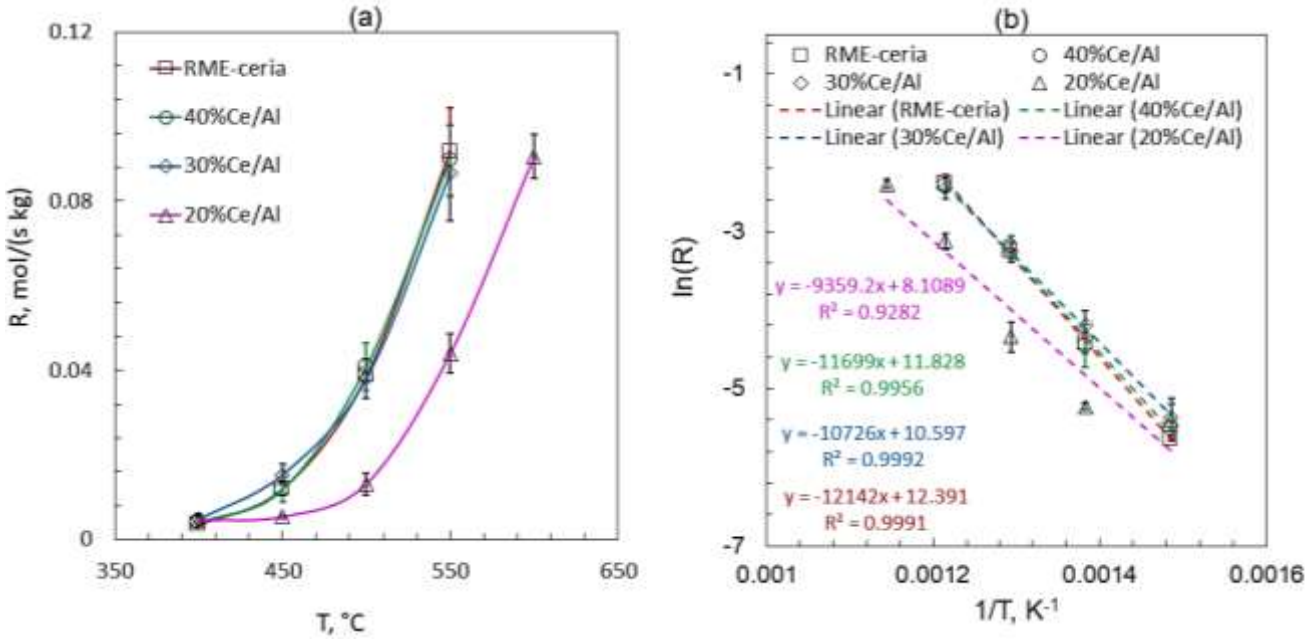

Figure 5.4: CO generation rate mol kg_{cat}^{-1} s^{-1} (left plot), Arrhenius plot In(R) vs. T^{-1} (right plot).Corresponding activation energies for 20%, 30% and 40%Ce/Al is 77.81, 89.17 and 100 kJ mol^{-1} respectively,

Fig. 5.4(a) shows that CO generation rates for RME-ceria, 30%, and 40%Ce/Al is almost the same for all the temperature tested at GHSV of 60,000 ml g_{cat}^{-1} h^{-1}. However, at all temperatures the rate for 20%Ce/Al is significantly lower than the other two catalysts. Activation energies for all the catalysts were estimates using the Arrhenius plot (In(R) Vs. I/T) Fig 5.4(b). Only points obtained under differential conditions (when the conversion ~20%) were taken due to the limitation of the linear form of the Arrhenius equation. For 40%Ce/Al the average activation energy appeared around 97.26 kJ $mol^{-1,}$ nearly equal to calculated for RME-ceria, i.e., 100 kJ mol^{-1}. However, for 20%Ce/Al and 30%Ce/Al, the calculated activation energies are 77.81 and 89.17 kJ mol^{-1}, respectively. A similar effect of lower activation energy with a lower CO generation rate was observed for the DP-ceria (80 kJ mol^{-1}) discussed in Chapter 4.

To examine the reproducibility of RWGS over the as-prepared catalysts (after exposure to higher temperatures), a basic three heating-cooling cycle experiment was conducted for all catalysts (20%, 30%, and 40%Ce/Al) at the same condition of 300°C-600°C (moving low to high), 3 bar, and 60,000 ml g_{cat}^{-1} h^{-1}. After cycle1 (300°C-600°C), the system was allowed to cool down to 300°C and then exposed to the similar conditions performed before. Fig. 5.5 shows the cyclic reaction activity for all the as-prepared catalysts using brand new reactors. Results show stable catalyst activity up to cycle-3 (almost 42 h on stream). No CH_4 or carbon formation was detected, which supports the fact all CeO_2/γ-Al_2O_3 (20%, 30%, and 40%) catalysts are stable and resistant to cooking, likewise RME-ceria. This excellent coking resistance was later confirmed with TGA-FTIR of the spent catalysts recovered after the cyclic test of 40%Ce/Al catalyst (almost 42 h on stream). Mahamulkar et al. [274] showed a similar coking resistant behavior of ceria supported alumina catalyst for the oxidation of *in-situ* generated coke during ethylene pyrolysis. They reported that ceria supported catalyst shows resistance to coking compared to unsupported alumina.

Consequently, for the performed experiments, all catalysts showed 100% CO selectivity and zero-carbon formation. However, among all the ceria supported γ-alumina catalysts, 40%Ce/Al showed

superior and comparable activity as of RME-ceria at all the tested conditions. Therefore, 40%Ce/Al being the optimum formulation of ceria supported γ-alumina was further studied for the long-term stability tests at different GHSV's to confirm the stable CO_2 conversion and superior coking resistant ability.

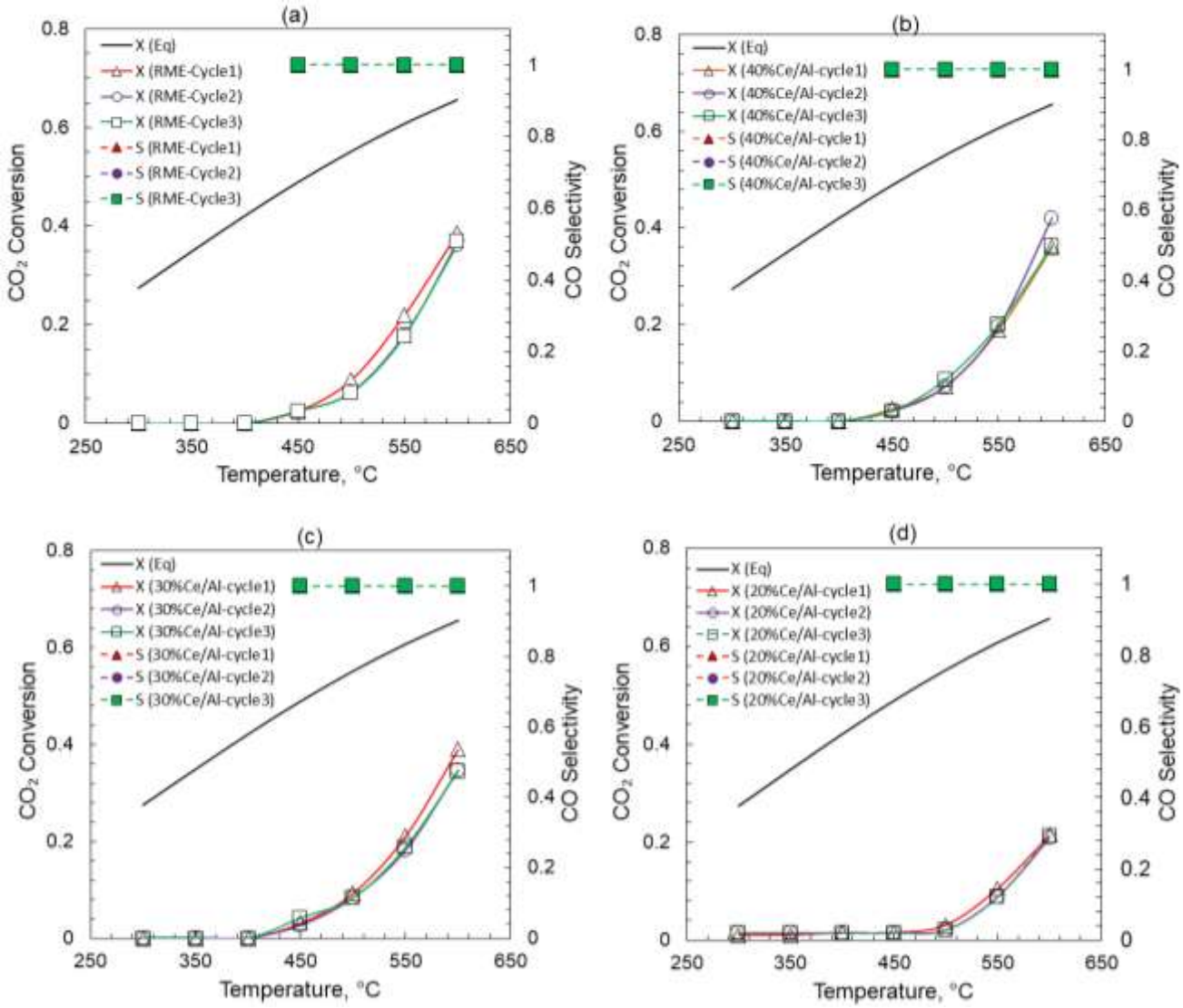

Figure 5.5:Heating-Cooling cycles for 20% (d), 30%(c), 40%Ce/Al(b) and RME-ceria(a) at 300°C-600°C, 3 bar and 60,000 ml g_{cat}^{-1} h^{-1} GHSV.

5.3.1.2 Stability Test

The catalyst stability is an important parameter, which is usually over looked or ignored. It is essential to know the catalytic stability for a preferred reaction and resistance towards sintering, coking, and deactivation because catalysts usually show excellent conversion for some hours but start losing their activity over time.

Among all the $CeO_2/\gamma\text{-}Al_2O_3$ catalysts, 40%Ce/Al appeared as the optimum catalyst for the CO_2 reduction to CO under the specified reaction conditions. Considering the fact, 40%Ce/Al catalyst was subject to undergo two stability tests using a U-shaped quartz tube reactor (1/4" dia) for a minimum of 70 h on stream at atmospheric pressure, 600°C, and GHSV of 60,000 ml g_{cat}^{-1} h^{-1} and 10,000 ml g_{cat}^{-1} h^{-1}, shown in Fig. 5.6. A complete experimental setup is presented in section 3.6.1 Fig. 3.12(c). At GHSV of 60,000 ml g_{cat}^{-1} h^{-1}, initially, a slight decrease in conversion was observed; however, it stabilized after 40 h and remained stable at ~23%, which is similar to what we observed for unsupported RME-ceria (Fig 4.6) at the same conditions, i.e., conversion stabilized at ~24% after a slight decrease. Though, at 10,000 ml g_{cat}^{-1} h^{-1}, initially, a significantly high CO_2 conversion ~60% (near-equilibrium conversion ~65%) was observed. At lower GHSV's, a slight decline in conversion was recorded, but it stabilized after 23 h (earlier than RME-ceria) on stream at ~50%. However, after 60 h on stream 40%Ce/Al regains its activity and CO_2 conversion stabilizes at 53%, precisely the same as observed for RME-ceria (Fig 4.6).

Overall, 40%Ce/Al shows significantly stable behavior despite its high-temperature exposure for 70 h on stream. This supports the fact that the reverse microemulsion synthesis method dramatically enhances the supported ceria activity and stability towards the RWGS reaction. At different GHSV's, RME prepared 40%Ce/Al catalyst showed 100% CO selectivity (No CH4). Additionally, no clogging or coking was observed during the process, which TGA-FTIR later confirmed.

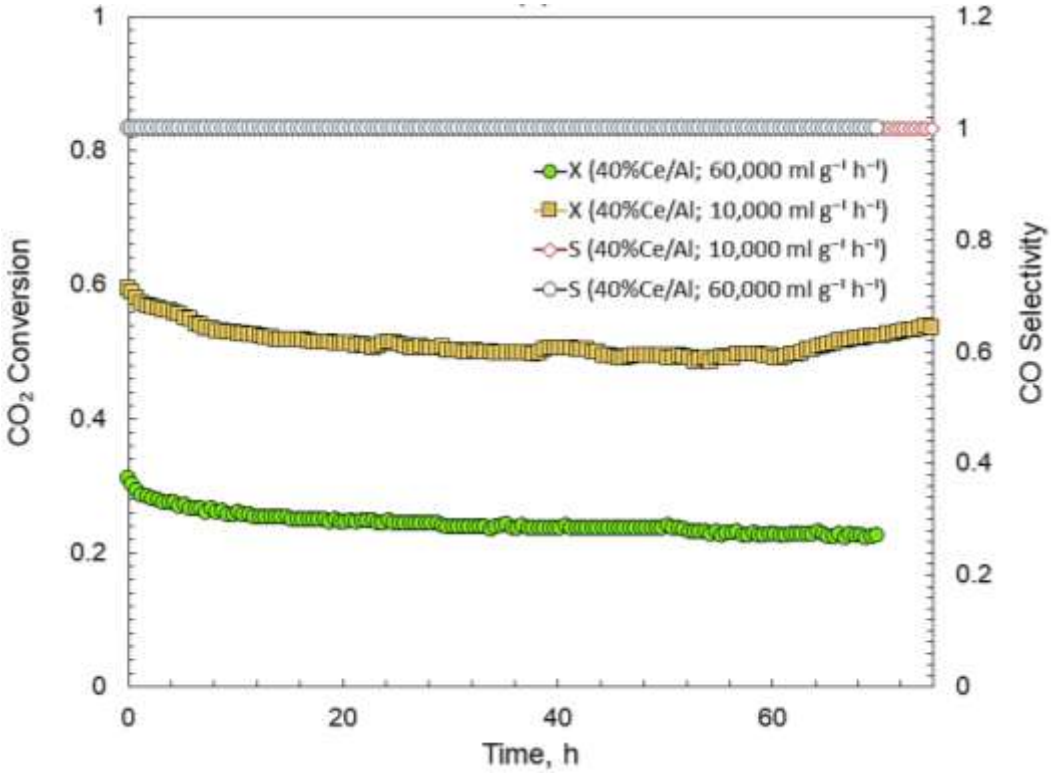

Figure 5.6: Stability test for 40%Ce/Al at atmospheric pressure, 600°C and GHSV of 60,000 ml g_{cat}^{-1} h^{-1} and 10,000 ml g_{cat}^{-1} h^{-1}.

5.3.2 X-ray diffraction, SSA-BET, and ICP-OES Studies

Ceria average crystalline size over γ-alumina, specific surface area (S_{BET}), and chemical composition for the fresh and spent catalysts are summarized in Table 1. 20%Ce/Al-fresh showed the highest surface area of 310 m^2 g_{cat}^{-1}. Though, a significant decrease in surface area was measured for the higher loading of ceria over alumina. A similar kind of decreasing S_{BET} area, for higher ceria loadings was observed by Damyanova et al. [279]. They showed that at higher ceria loadings, the surface area decreased due to the plugging of the pores of γ-alumina with ceria. The decrease in surface area and thermal stability of alumina are directly related to the ceria loading. However, all CeO_2/Al_2O_3 catalysts showed almost doubled the surface area we reported for RME-ceria. These significantly

higher surface areas are evident in the catalysts highly porous structure, which was later confirmed in line with HRSEM.

Literature showed that lower ceria loading helps alumina against high surface area loss by preventing the transformation of γ-alumina to α-alumina [280, 281]. This reason can be easily justified because after exposure to 600°C, the surface area loss was only 50% for 20%Ce/Al, while 30% and 40%Ce/Al showed 70% reduction in surface area. This indicates that the surface area does not play any significant role in the activity of CO_2 conversion over $CeO_2/\gamma\text{-}Al_2O_3$ catalysts as the higher conversion was observed over 30% and 40%Ce/Al catalyst. A similar effect has been reported in the literature by Chen et al. [277]. They said that the surface area of the catalyst does not affect the conversion of phenol. However, during the cyclic activity tests, all catalysts showed stable conversion at all temperatures for each coming cycle even after losing their surface area of about 50-70%. Considering catalysis as the surface phenomena, this behaviour of nanoceria is unusual. This unusual nanoceria activity is well explained and proved by Paidi et al. [282]. They studied the catalytic reduction of NO by CO over different morphological shapes of ceria and ceria-supported alumina catalysts. They showed that this superior activity of ceria is related to the reduction of Ce^{4+} to Ce^{3+} due to the creation of oxygen vacancies. These oxygen vacancies are highly mobile and create a oxygen vacancy transport within the ceria fluorite structure, leading to an increased density of Ce^{3+} defects in bulk. This effect leads them to identify the bulk ceria base activity. Therefore, they proved bulk Ce^{3+} (generate via oxygen vacancy transport) is the origin of the base activity of pure ceria, which is its intrinsic property. This unique property of ceria could lead to producing new materials with enhanced activities.

Actual ceria loading was measured using the ICP-OES technique, and the results showed a very small variation in loading from the target value, as shown in Table. 5.1.

Table 5.1: Chemical analysis, crystallite size and specific surface area

Sample	CeO_2 Content (ICP-OES)	CeO_2 Crystallite size	S_{BET}
	Wt%	nm	g/m^2
20%Ce/Al-fresh	20.20	2.90	310
20%Ce/Al-spent	-	6.14	158.30
30%Ce/Al-fresh	34.09	3.64	299.7
30%Ce/Al-spent	-	6.87	105.43
40%Ce/Al-fresh	47.86	5.56	292.06
40%Ce/A-spent	-	7.72	97.64
RME-Ceria-fresh	100	4.02	146.84
RME-Ceria-spent	-	11.55	38.69

XRD patterns for all the fresh catalyst (calcined at 275°C) and spent (collected after 3cycle test) are shown in Fig. 5.7. All the samples show clear diffraction peaks of CeO_2 except 20%Ce/Al, indicating a very small crystallite size of ceria particles supported over γ-alumina. This fact is well, matched with the crystallite sizes calculated using the built-in Scherrer equation tool in the Bruker XRD Eva software. It can be seen that ceria crystallite size increased as the loading increased, which is endorsing the results of S_{BET} as well. The increased ceria crystallite size showing the clogging of pores resulting in less exposed surface area and porosity of the catalyst. This fact is well matched with results of S_{BET} and HRSEM. However, this massive decrease in surface area is not related to the growth of ceria crystals only, because the ceria crystallites growth over spent CeO_2/Al_2O_3 is not significant, as shown in Table. 1. This fact is well explained by Mohammed et al. [283]. They showed that γ-alumina particles undergo large enlargement (from 56.26 nm to 93.84 nm) when catalyst calcination

temperature rise from 500°C to 650°C. This enlargement causes a decrease in pore volume and leads to significant decrease in surface area. This finding well matched with what we observed in this study.

Also, The XRD peaks along the (111), (200), (220), (311), (222), (400), (331), and (420) planes confirm the fluorite (JCPDS 34-0394) structure of the ceria particles supported over γ-alumina. No Clear peaks of the γ-alumina were observed because of the low calcination temperature and showed the γ-alumina support's amorphous nature. However, the scan and match tool available in Bruker XRD Eva software confirmed the presence of γ-alumina. Bare RME γ-alumina (prepared using the RME method) was calcined at 550°C to match the alumina peaks in ceria-supported γ-alumina samples. A slight shift of the XRD peaks in the 2θ range of 43-49 can be seen in Fig. 5.7. This shift's possible reason is (1) the interaction between ceria and alumina (2) alumina surface coverage by ceria crystallites. A similar shift of XRD pattern was observed by Damyanova et al. [279].

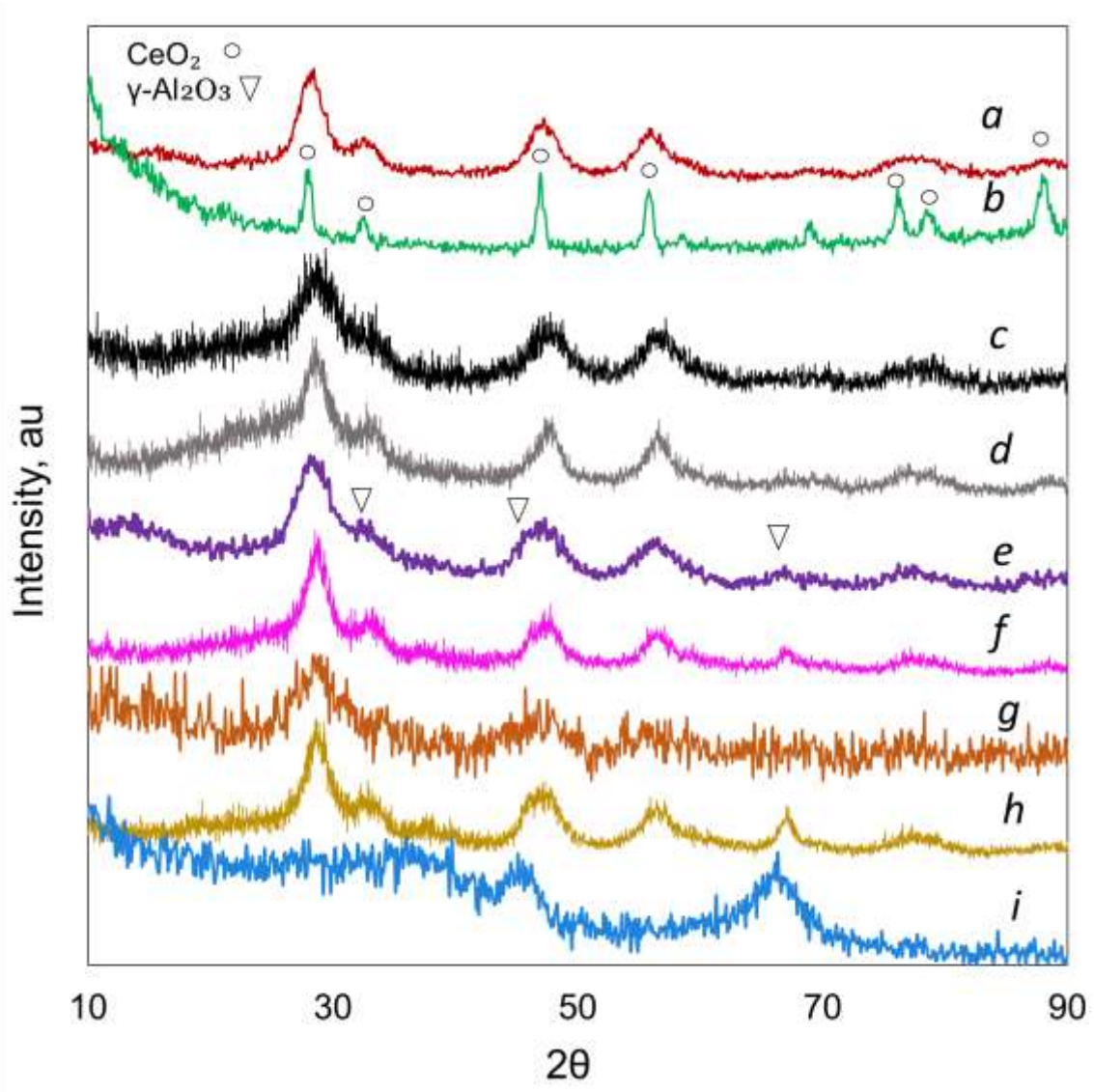

Figure 5.7: X-ray diffraction pattern for RME-ceria-fresh (a) RME-ceria-spent (b) 40%Ce/Al-fresh (c) 40%Ce/Al-spent (d) 30%Ce/Al-fresh (e) 30%Ce/Al-spent (f) 20%Ce/Al-fresh (g) 20%Ce/Al-spent (h) γ-Al_2O_3 (i)

5.3.3 H_2-TPR studies

The TPR profiles of unsupported and γ-alumina supported ceria are shown in Fig. 5.8. Fresh unsupported RME-ceria showed three clear peaks (α, β, δ): the first peak α appeared at ca. 385°C, second β at ca. 485°C and the third δ at ca. 770°C (Fig. 5.8(a)). The first peak α corresponds to the surface oxygen reduction [284]. Peak β corresponds to the non-stoichiometric ceria oxide, i.e., CeO_{2-x}

[285]. Various studies showed that CeO_{2-x} could only be obtained ≥ 500°C in air or H_2 environment without losing the original cubic fluorite structure [286, 287]. The last peak δ is attributed to the complete reduction of CeO_2 to Ce_3O_2 [286], which is completely matched with the present work as catalyst changed their color during the course of TPR from yellow to gray to golden yellow.

The TPR profiles of the supported alumina ceria catalyst are different from the unsupported RME ceria. All three 20%, 30%, and 40%Ce/Al catalyst show a slight shift in the peak α and β compared to bulk RME-ceria, while the third sharp peak δ at 770°C is missing for the all. The small shift of the peaks can be attributed to the interaction between the ceria and alumina support [279]. For all Ce/Al samples, the α peak is significant and is related to the reduction of small ceria crystallite, the second peak is related to the well-dispersed bulk ceria over alumina support [286]. A small H_2 consumption observed for all supported catalysts above 700°C is attributed to ceria interaction with γ-Al_2O_3 support under high temperature. This prolonged reduction at high temperatures reduced Ce^{4+} to Ce^{3+} and helps create new interaction with alumina support to form cerium allominate while occupying Al^{+3} sites in the first layer by the Ce^{3+} [288]. For all the samples broadening of reduction peak (α and β) and shift to H_2 consumption can be seen in the low and medium temperature range. Peak β is linked to the reduction of large crystallites in bulk ceria. Therefore, the amount of H_2 consumed for this region increased as the ceria loading increased and reached the maximum for pure ceria [289]. This fact is well-matched with the result presented in Fig. 5.8(a). Total H_2 consumed for 20%, 30% , 40%Ce/Al and RME-ceria fresh catalyst is 350.7, 358.52, 587.94, and 1055 µmol $g_{cat}^{-1,}$ respectively.

Fig. 5.8(a) shows that the major reduction of the samples happened in the temperature range of 380°C-600°C and peak β appeared nearly 550°C for all the Ce/Al samples, which plays the leading role in creating nonstoichiometric ceria. This nonstoichiometric ceria led to more oxygen vacancies, more mobility of Ce^{3+} in the bulk that would eventually result in two folds of conversion increased observed for all sample when the temperature increased from 550°C to 600°C. Therefore, the initial reduction temperature of 400°C is essential in facilitating the RWGS reaction over the Ce/Al samples.

Fig. 5.8(b) showed the TPR comparison of fresh and spent 40%Ce/Al catalyst. It can easily be seen that for spent catalyst, the peak α is missing, which well-matched with the fact that after exposure to high temperature, the crystallite size increased because peak α is related to the small crystallites reduction [284]. Furthermore, a small shift in peak was observed for the spent catalyst which again support the fact that high-temperature exposure helps in increasing the interaction of ceria and alumina. Finally, 40%Ce/Al spent showed a significant peak around 770°C, which was missing for the fresh catalysts. This again shows that after exposure to long-term high-temperature ceria and alumina interact, it leads to a solid solution to make $CeAlO_3$ [279, 288].

To investigate further, H_2-TPR for the 40%Ce/Al-spent was performed coupled with the in line FTIR to see the reduction products output (Fig. 5.9). A very minute amount of lower hydrocarbons along with a strong CO signal was observed. This finding again strongly supports the high selectivity of the ceria-based catalyst for RWGS reaction because even in a highly reducing environment, a very minute amount of CH_4 and a large amount of CO were observed. This shows that even in highly reducing environment, the as-prepared catalyst resists the reduction of already adsorbed CO_2 on the catalyst surface to hydrocarbons especially CH_4.

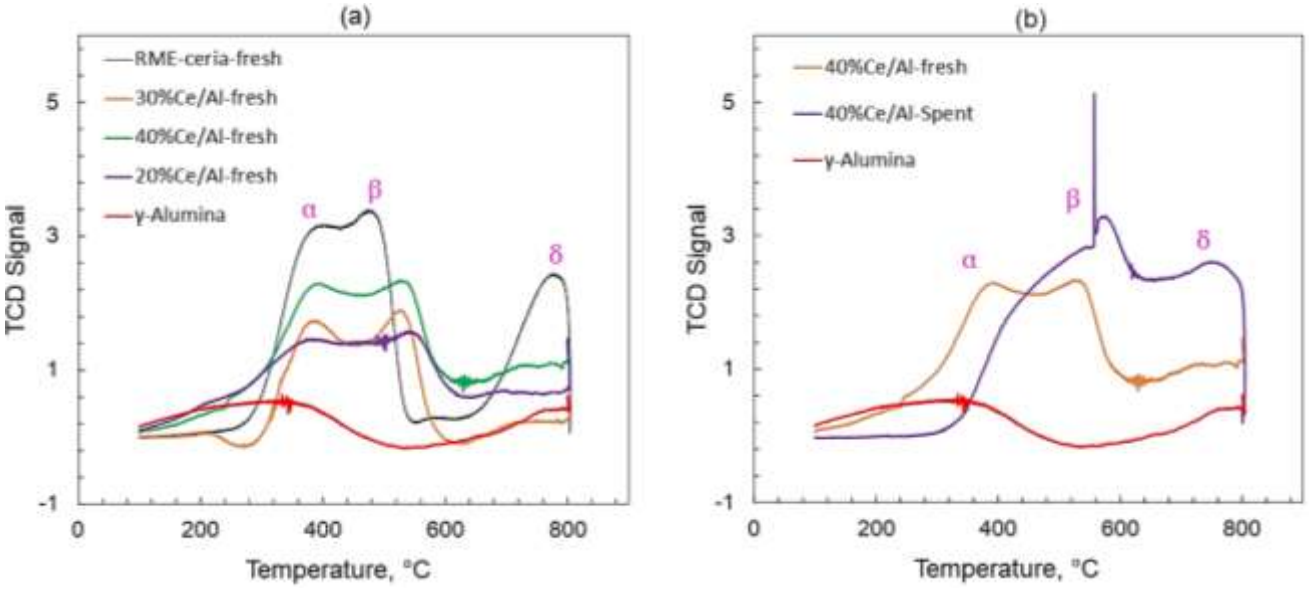

Figure 5.8: H_2-TPR-profiles (a) for all fresh catalyst (b) for 40%Ce/Al fresh vs. spent.

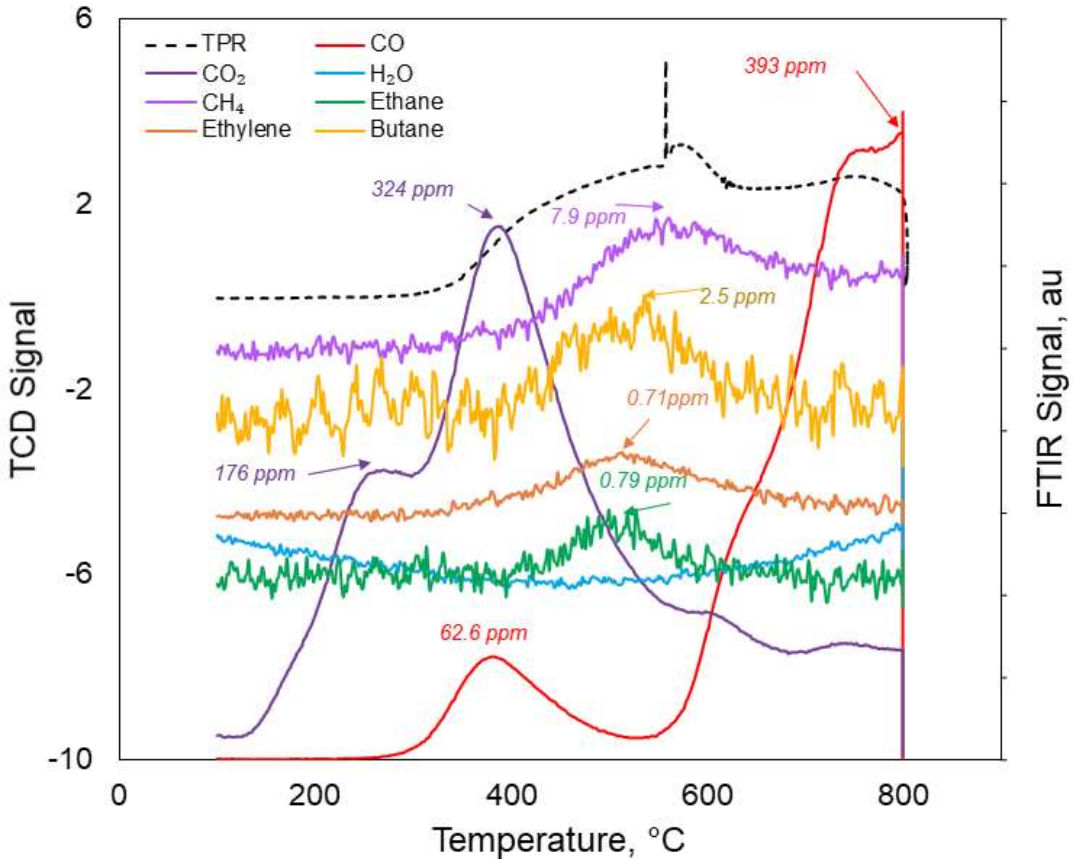

Figure 5.9: In-situ H_2-TPR-FTIR profile for 40%Ce/Al-spent recovered after 3-cycle stability test.

5.3.4 HRSEM-EDX Studies

Fig. 5.10 shows the HRSEM micrographs taken at 1 μm, 500 nm, and 300 nm (left to right) for the 40%Ce/Al fresh & spent catalyst. The highly porous structure of the fresh catalys can easily be seen in Fig. 5.10 (a,b,c). Also, in Fig. (b & c), the polyhedral growth of ceria particles over alumina can be seen as well. Fig. 5.10 (d, e, f) shows the micrographs for the spent sample. It can easily be seen that the spent sample is appeared agglomerated, and pores are clogged, which is in true agreement with the XRD and S_{BET} data. Because as the catalyst exposed to the higher temperature, the crystallite size increased, pore volume decreased, and the surface area decreased [283, 290]. Micrographs for the fresh

catalyst showed the crystal growth in a cluster like structure which is attributed to the large surface area of the catalyst (292 m^2 g_{cat}^{-1}). However, this cluster growth makes them unstable, and particles agglomerate with high temperature [290], as observed in this study.

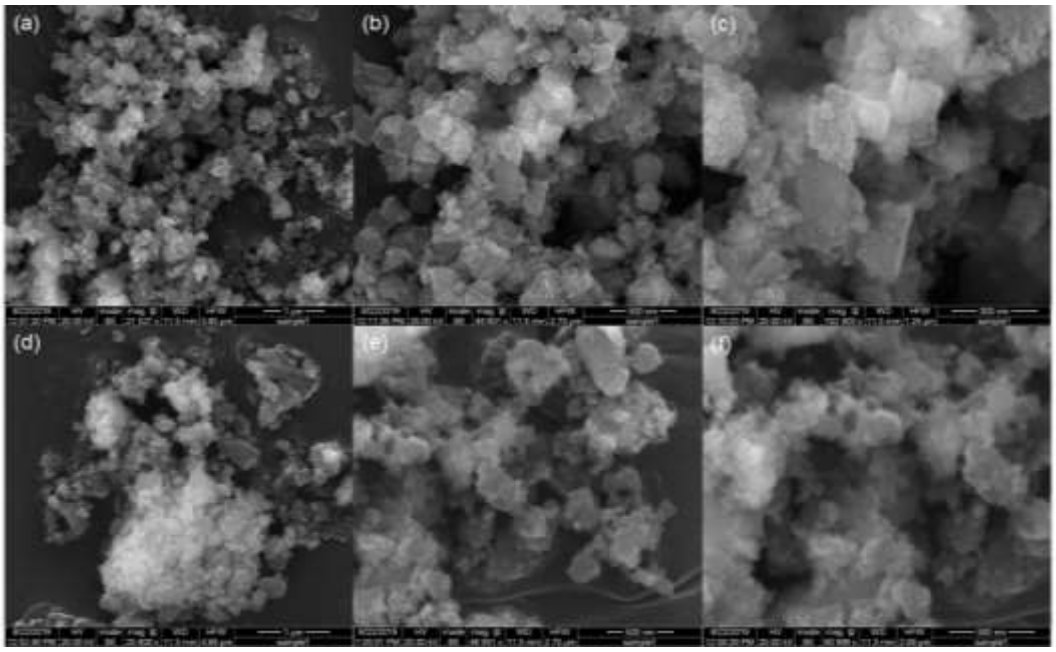

Figure 5.10: SEM-EDX micrographs for 40% Fresh (a, b, c) 40%Ce/Al-spent (d,e,f).

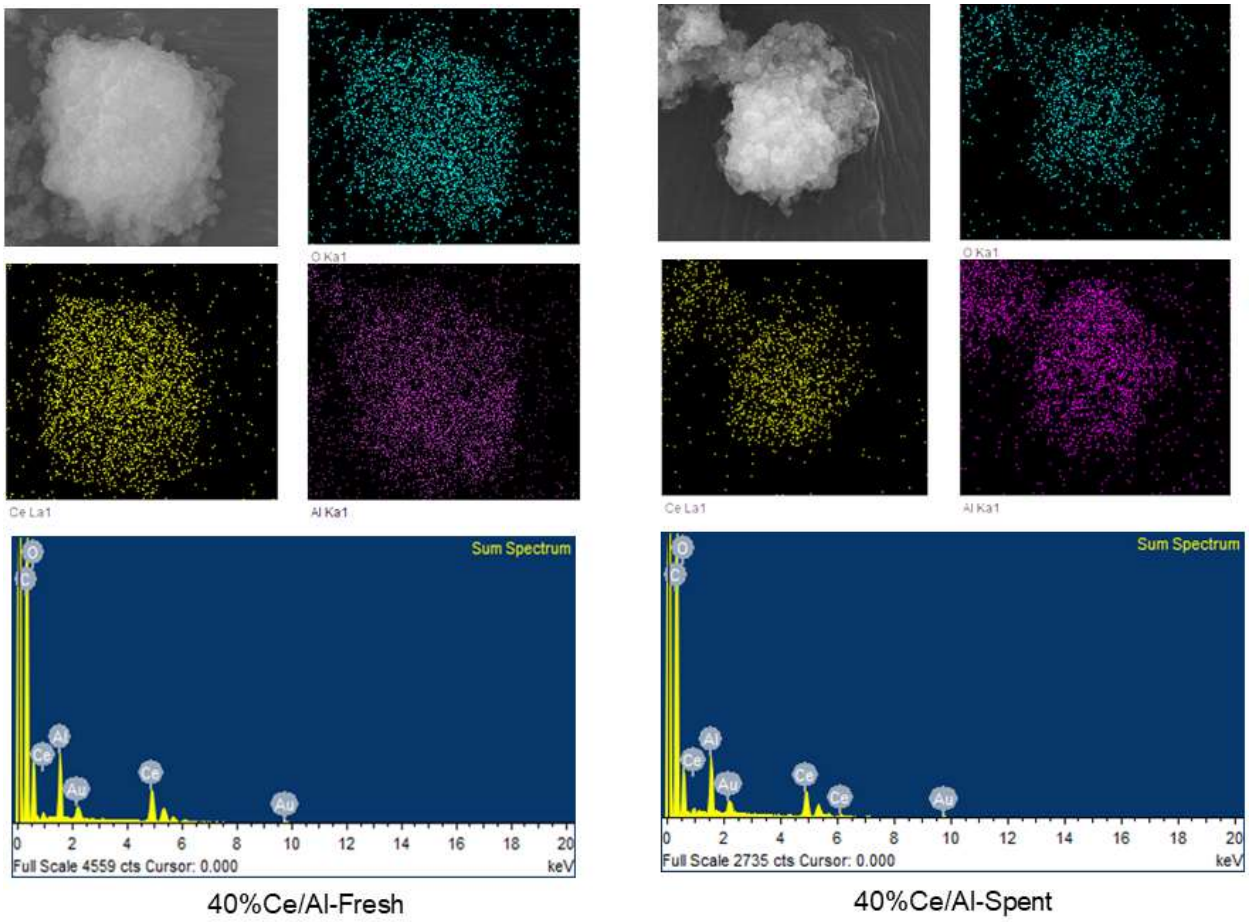

Figure 5.11: SEM-EDX elemental mapping.

To further investigate the dispersion and the surface elemental composition of ceria over alumina, EDX was performed for fresh and spent 40%Ce/Al catalyst. It can be seen that for fresh and spent 40%ce/Al, cerium atoms are very well dispersed over the alumina surface and readily available for the reduction. This highly dispersed nature of ceria over alumina is well matched with the literature [279]. It was reported that a well dispersed monolayer of cerium atoms appeared over alumina support that readily available to reduce to CeO_{2-x}. this similar fact can be seen in Fig 5.11. Elemental mapping shows detected impurities as C and Au which were appeared because of the carbon tape and Au coating.

5.3.5 In-Situ TGA-FTIR Studies

To investigate the thermo-gravimetric properties and the extent of coking, in-situ TGA-FTIR was performed for all the samples. All samples were pretreated under air flow of 60 ml min^{-1} at 150°C for 1 h and then subjected to elevated temperature as described in experimental section 5.2 . 20%, 30%, and 40%-fresh catalysts showed almost similar weight loss of almost 4% till 550°C with a continuous significant amount of evolved CO_2 (Fig. 5.12). This loss might be attributed to the burning of the residual organic in the sample [259, 260]. From 550°C-800°C a very small change in mass was detected which might be attributed to the loss of the oxygen from the sample as both alumina and ceria losses oxygen at elevated temperature [261-263]. Similarly, fresh RME-ceria showed a 2% weight loss till 450°C and a very small loss till 800°C.

To investigate the extent of coking over spent RME-ceria and 40%Ce/Al recovered after 3heating-cooling cycle test (42 h on stream) TGA-FTIR was performed under the same condition. For 40%Ce/Al less than 2% weight loss was observed, which is attributed to the loss of the oxygen which the sample gained back after air exposure. During this Ph.D. study, it was observed that the spent catalyst starts changing its color from gray to yellow after several hours of exposure to the open air at room temperature. This observation strongly supports the highly reducing nature of RME prepared sample. For the spent 40%Ce/Al no significant signal of CO_2 was observed, confirming the absence of any carbonaceous compounds over the spent catalyst, and highly supporting the fact that RME prepared 40%ceria/Al catalyst is resistant to coking.

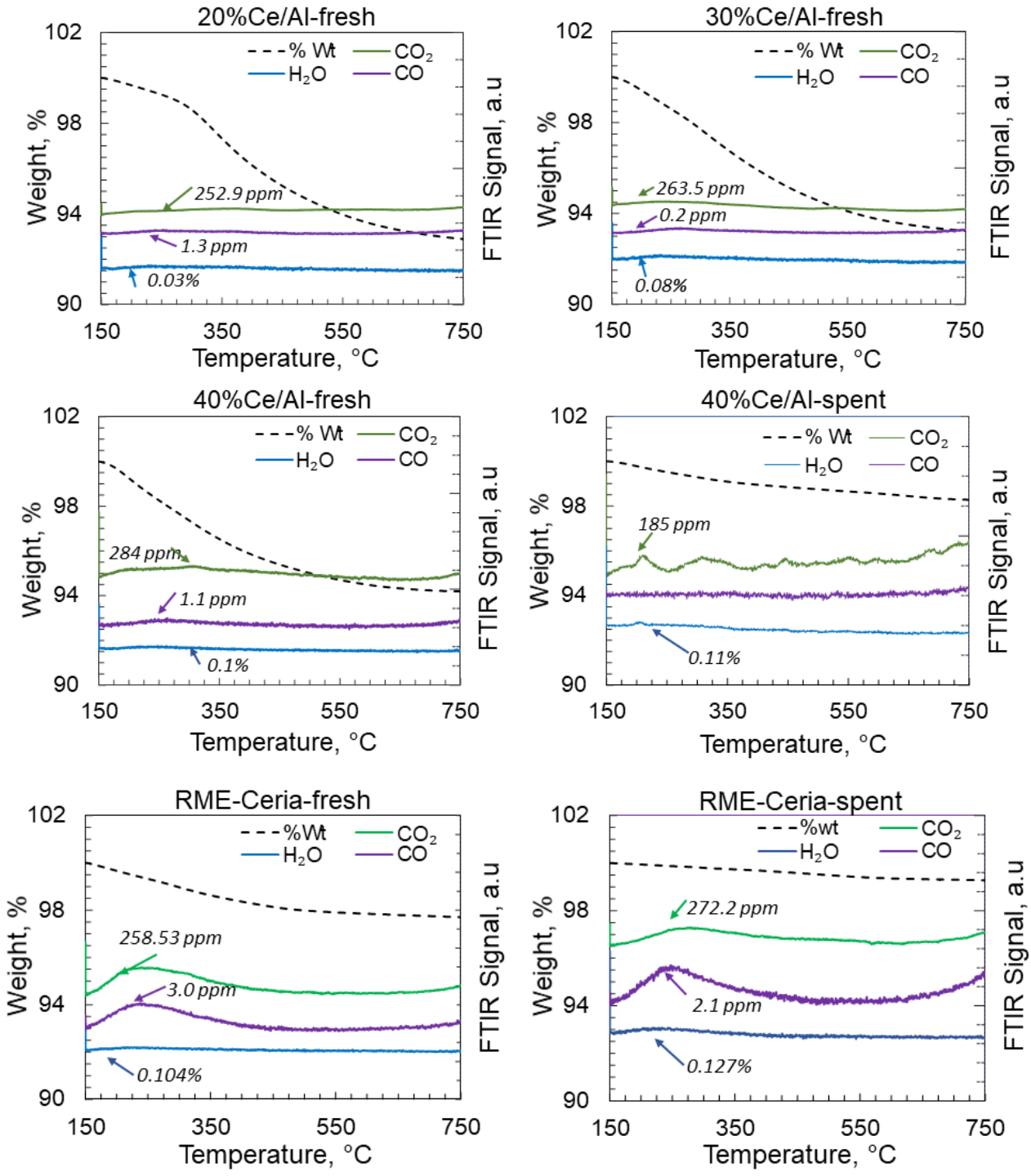

Figure 5.12: TGA-FTIR for fresh & spent catalysts.

5.4 Conclusion

A thorough investigation of RWGS reaction was carried out using different ceria supported γ-alumina catalysts. All the investigation showed that with increasing loading of ceria over γ-alumina the catalyst's reducing abilities improved. The supported ceria has much higher surface areas compared to the bare ceria but it was shown that the surface area in case of the supported catalyst does not play any significant role in the over all conversion. Superior 40%Ceria/Al catalyst was proven to be because oof the bulk based activity of Ce^{3+}.

XRD pattern showed that supported ceria particles correspond to the fluorite structure of pure ceria. It was observed that the crystallite size of ceria particle decreased from 2.9 nm to 5.56 nm as the ceria loading increased from 20% to 40% wt. However, the BET-SSA results showed as the ceria loading increased from 20% to 30% the surface areas decreased from 310 $m^2\ g_{cat}^{-1}$ to 292 $m^2\ g_{cat}^{-1}$. TPR data showed the with increasing loading of ceria /γ-alumina, the amount of consumed H_2 increased and reaches the maxim for the bulk pure RME-ceria. HRSEM studies show the cluster growth of the γ-alumina with well-dispersed ceria particles. Studies further confirm the polyhedral development of the ceria particles. TGA-FTIR studies proved the stable nature and the coking resistance of the as-prepared ceria-supported catalyst. 40%Ce/Al catalyst showed almost equilibriu conversion at lower GHSV's.

Consequently, it can be finally concluded that the 40%Ce/Al showed superior activity towards RWGS (especially at low GHSV) with 100%CO selectivity and excellent coking resistance. This study gives a sightful work for the future application of ceria-supported γ-alumina for RWGS.

Chapter 6

Effect of calcination temperature on relevant active sites, their identification and mechanistic studies over 40%RME-ceria/γ-alumina

6.1 Introduction

The conversion of CO_2 to synthetic fuels via CCU technology has dual advantages. It can mitigate CO_2 emissions directly and can help to produce synthetic fuels and other valuable chemicals. The catalytic conversion of CO_2 to useful chemicals and fuels is more viable because it mitigates CO_2 20-40 times higher than the sequestration process over a span of 20 years [8, 9]. This route seems to be more attractive because it can reduce GHGs and produce some valuable synthetic fuels, which will eventually reduce the consumption of natural fossil fuels. Reduction of CO_2 to CO using renewable H_2 is vital because the syngas ($CO+H_2$) produced can be utilized to make either methanol or higher hydrocarbons.

A higher surface area is considered a vital step in catalysis because higher surface area provides more reaction sites to the incoming reaction gases to get adsorbed and undergoes a reaction faster [72]. Therefore, the activity of a catalyst is directly proportional to the number of active sites present on the surface. A higher surface area for an active catalytic agent can be achieved by supporting it on a higher surface area porous metallic oxide support. For example, α-alumina has areas ranging from 1-10 m^2 g^{-1}, while γ-alumina provides areas ranging from 100-300 m^2 g^{-1}. The high surface area supports also help in better dispersion of the catalytic agent, reducing the chance of sintering or agglomeration [72]. Kim et al. [77] showed that Pt/TiO_2 catalyst produces more CO_2 conversion than Pt/Al_2O_3 because of the strong metal-support interaction and high reducibility of support. However, the surface properties are greatly affected by the calcination temperature as well.

Pournajaf et al. [26] reported that the ceria nanoparticles' surface area decreased to 50% as the temperature increased from 300-600°C. Also, the crystallite size increased from 5 nm to 20 nm. A similar effect of a large decrease in surface area was reported by Chen et al [23]. They showed that the surface area for ceria decreased from 125 m^2 g_{cat}^{-1} to 50 m^2 g_{cat}^{-1} as the calcination temperature increased from 200°C to 600°C. He et al [24] aslo reported that the ceria particle size increased from 60 nm to 80 nm as the calcination temperature rises from 700°C to 900°C. Furthermore, Mohammed et al. [283] showed that γ-alumina particles undergo considerable enlargement (from 56.26 nm to 93.84 nm) when catalyst calcination temperature rises from 500°C to 650°C. This enlargement causes a decrease in pore volume and leads to a significant reduction in surface area.

In the previous study, we reported the excellent activity and stability of 40%Ce/Al for the conversion of CO_2 to CO visa reverse water gas shift. Generally, catalysis is considered the surface phenomenon. However, in bulk RME-ceria and RME-Ce/Al catalyst bulk based activities have been observed. The literature strongly emphasizes the effect of calcination temperature on the catalyst properties, especially particle size and surface area, which are considered as the key point in catalysis. Therefore it is necessary to study the effect of calcination temperature on the activity and selectivity of the 40%Ce/Al. The present work will give an insight into the topic through the different characterization techniques. XRD diffraction patterns were collected to calculate the crystallite size, BET-SSA was performed to see the effect on the surface area. H_2-TPR and CO_2-TPD were performed to see the reducing abilities and the present active sits on the catalyst surface, respectively. In the end, in-situ FTIR studies were performed to determine the exact reaction mechanism over 40%Ce/Al catalyst.

6.2Experimental

6.2.1 Catalyst Preparation

The 40%Ce/Al catalyst was synthesized following the recipe described in section 5.2.2. The as-prepared dried catalyst was calcined at 275, 375, 475, and 575°C under continuous airflow in a muffle furnace for 4 h, pelletized (50 MPa), crushed, and sieved to 250-425 µm particles.

6.2.2 Catalytic Activity test

The RWGS catalytic activities over as prepared 40%Ce/Al calcined at 275, 375, 475 and 575°C were evaluated in a continuous flow fixed bed reactor at 3 bar absolute pressure and temperature ranged 300°C-600°C. The reactor system was made by joining the 1/2" stainless steel tube (316L, Swagelok) with 1/4" stainless steel tube (316L, Swagelok) via a reducing adapter (served as the reactor) and straight union, as shown in the schematic. Please refer to Fig. 3.11 for the kinetic reactor schematic and section 3.6.1 for the flow system's complete description and experimental setup.

The total CO_2 conversion, CO Selectivity, and CH_4 selectivity were calculated according to the following equations.

$$X_{CO_2} = \frac{y_{CO}+y_{CH_4}}{y_{CO_2}+y_{CO}+y_{CH_4}} \qquad (11)$$

$$S_{CO} = \frac{y_{CO}}{y_{CO}+y_{CH_4}} \qquad (12)$$

$$S_{CH_4} = \frac{y_{CH_4}}{y_{CO}+y_{CH_4}} \qquad (13)$$

6.2.3 Catalyst Characterization

D8 discover diffractometer, Bruker was utilized to obtain the XRD patterns using Cu-Ka radiation source (λ = 1.54 Å) at 40 kV tube voltage and 40 mA of a tube current. Diffraction patterns were collected for the 2θ ranged 10° to 90° at a scan sped of 3 (time per step) with an increment of 0.1. Specific surface area (SSA) was determined for all the fresh and spent catalysts using AMI-300lite (Altamira Instruments, USA) catalyst characterization unit. Helium was used as the purge gas, while 10% N_2/He was used as the absorbing gas to calculate the surface area using single point BET-equation.

TPR (Temperature programmed reduction) analysis was performed using AMI-300Lite, Altamira instruments, catalyst characterization instruments to investigate the extent of reduction for all fresh and spent catalysts. 10% H_2/Ar mixture was blown over the catalyst, and the change in H_2 composition was observed using a TCD (thermal conductivity detector) at the outlet over the temperature range of 300°C-800°C. CO_2-TPD studies were performed using AMI-300Lite, Altamira instruments, catalyst characterization instruments to investigate the relevant active sites. In one experiment, the catalyst sample was reduced under 10%H_2/Ar for 2 h at 400°C, preceded by CO_2 adsorption at 25°C for 1 h. However, for the other experiment, the catalyst was treated under He (without reduction) at 400°C for 2 h, preceded with the same CO_2 adsorption at 25°C for 1 h. After CO_2 adsorption, the temperature was allowed to increase from 25°C to 800°C at a ramping rate of 10°C/min. The amount of CO_2 desorbed was monitored with an in-line TCD and FTIR gas analyzer.

Reaction mechanistic studies were performed for all fresh and spent catalysts using AMI-300Lite, Altamira Instruments, catalyst characterization instrument (*In-situ* FTIR reaction analysis). The *in-situ* FTIR spectra were collected in a reactor cell with KBr windows connected with inlet and outlet flows. The cell was placed in a FTIR spectrometer (Thermo Scientific™ Nicolet™ iS™5), and the temperature was controlled with a controller connected thermocouple (inside the reactor). The catalyst (~5 mg) was pressed to a potassium bromide pellet support. Each spectrum was collected at 4-1 resolution and 32 scans from 4000 to 800 cm^{-1} in absorbance mode. The sample pellets were reduced

in 10% H_2/argon at 400 °C for 1 h and then flushed with argon to remove the hydrogen. The background spectrum was collected under argon at the same temperature as the reaction condition. After the background was subtracted, reaction gas (30 ml min^{-1}, 2% CO_2/8% H_2/90% argon) was introduced to the IR cell at the same temperature.

6.3 Results and Discussion

6.3.1 XRD Diffraction and BET Studies

Its been reported that the calcination temperature directly affects the particle size and exposed surface area of the catalyst. Both ceria [23, 24, 26] and γ-alumina [283] undergo particle growth when exposed to higher temperatures. Therefore, to study the effect of calcination temperature on the as-prepared 40%Ce/Al catalyst XRD patterns and BET-SSA was measured for all the catalysts calcined at 275, 375, 475, and 575℃. Temperature above 575℃ was not considered because it has been reported that ceria loses almost half of its exposed surface area as calcination temperature rises from 300℃ to 600℃ [26]. Chen et al also reported the same effect of losing 50% of the initial surface area by ceria particles when the calcination temperature increased from 200°C to 600°C [23]. A similar surface area loss for γ-alumina has been reported [283].

Fig. 6.1 shows the XRD patterns collected for all the catalysts. All the catalysts showed flatted peaks indicating the nano-scaled crystallites. Crystallite size for ceria particles supported on γ-alumina was calculated using the Scherrer equation, as shown in Table 6.1. It can bee seen that a small increase in the crystallite size has been observed as the temperature rises from 275℃ to 375℃. However, the average size does not change further as the temperature increased from 375℃ to 475℃. This shows that the ceria particles supported on the γ-alumina are resisting against the size increase in this temperature range. A similar effect has been reported in the literature that the ceria supported on γ-alumina helps enhance the catalyst's thermal stability [279]. Further, as the temperature rose from 475℃ to 575℃ a large increase in the crystallite from 7nm to 16.8 nm was observed. This large

increase well matched with the BET-SSA results that the surface area decreased to a significant amount, as shown in Table.6.1. this large decrease in surface area is well-matched with studies reported by Pournajaf et al. [26] for ceria and Mohammed et at. [283] all for γ-alumina. However, BET-SSA results showed that the surface area increased when the calcination temperature increased from 275°C to 375℃. This could be explained by the fact that the surfactant used in the synthesis process has a boiling point of 270℃. Therefore, there are quite significant chances of surfactant remains present in the cluster of porous γ-alumina at the calcination temperature near to boiling point. However, as the calcination temperature increased and the leftover organic burnt out, it increased surface area and porosity because the crystallite does not change at 375℃ [242].

All the XRD patterns show clear peaks for the ceria correspond to the fluorite (JCPDS 34-0394) structure of the ceria particles supported over γ-alumina.

Table 6.1: XRD and BET analysis

Sample	**Calcination Temperature**	**CeO_2 Crystallite size**	**S_{BET}**
	℃	nm	g/m^2
40%Ce/Al-fresh	275	5.56	292.06
40%Ce/Al-fresh	375	7	357.35
40%Ce/Al-fresh	475	6.79	313.70
40%Ce/Al-fresh	575	16.8	239.75

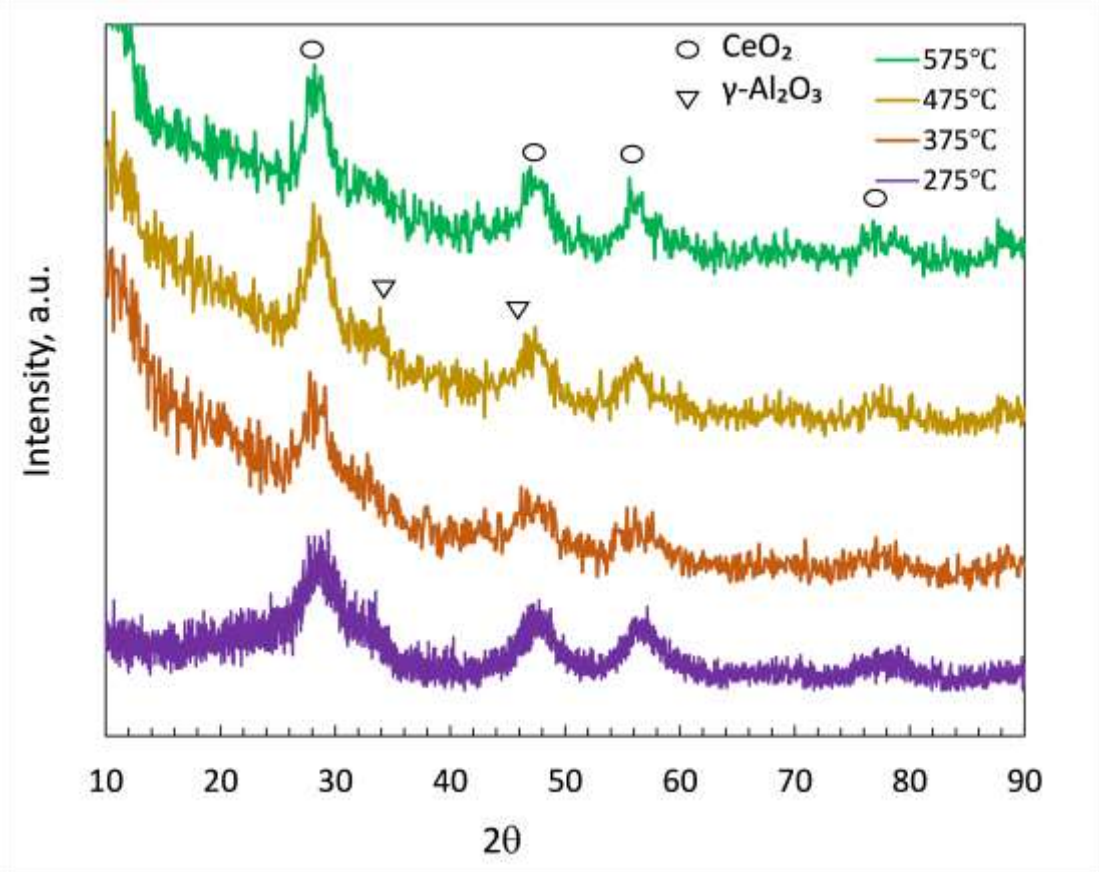

Figure 6.1: XRD diffraction patterns for 40%Ce/Al fresh samples calcined at 275, 375,474, and 575°C.

6.3.2 H_2-TPR Studies

XRD and BET studies showed a significant effect of calcination temperature on the particle size and surface area for the as-prepared catalyst. Considering the highly reducing abilities for [202-204] ceria, it was of high interest to see the effect of calcination temperature on the surface reduction of the ceria support γ-alumina catalyst.

Fig. 6.2 shows the TPR profiles for 40%Ce/Al catalyst calcined at different temperatures. It can easily be seen that the samples calcined at 275°C and 375°C showed similar TPR profiles with clear all three typical TPR peaks (α, β, and δ). The first peak α corresponds to the surface oxygen reduction

[284]. Peak β corresponds to the non-stoichiometric ceria oxide, i.e., CeO_{2-x} [285]. However, in ceria supported on γ-alumina, the peak δ is related to the higher interaction of ceria and alumina, leading to a solid solution to form $CeAlO_3$ [279, 288]. Various studies showed that CeO_{2-x} could only be obtained $\geq$ 500°C in air or H_2 environment without losing the original cubic fluorite structure [286, 287]. The last peak δ is attributed to the complete reduction of CeO_2 to Ce_3O_2 [286], which is completely matched with the present work as catalyst changed their color during TPR from yellow to gray to golden yellow.

The above results are in direct agreement with XRD and BET-SSA. XRD results showed that as the calcination temperature increased from 275°C to 475°C, the crystallite size does not change much. From the TPR profiles, we can easily see that the sample calcined at 275°C 375°C, and 475°C showed a clear peak α related to the small ceria particles present on the alumina surface [284]. However, for the sample calcined at 575°C, the peak α is completely missing. The absence of peak α shows that the crystals are grown up due to high temperature. These results are in direct agreement with the XRD data. XRD data showed that as the temperature increased from 275°C to 575°C, the crystallite size increased from 5.56 nm to 16.8 nm. Similarly, the sample calcined at 375°C showed a larger area under the curve compared to the sample calcined at 275°C. This fact is well-matched with the BET-SSA and the H_2 consumption results. Results showed H_2 consumption of 810 µmol g^{-1} and 587. 94 µmol g^{-1} for sample calcined at 375°C and 275°C, respectively. The sample calcined at 575°C showed a very sharp peak β, which is again well matched with the XRD data because the crystallite size for this ample is 16.8 nm. However, the sample highest amount of consumed H_2, which is in agreement with the literature. The superior reducing ability of ceria is a well-known fact [286, 287]. It quickly loses oxygen in the H_2 environment and gets quickly oxidizes in the air. In this study, all the samples were calcined for 4 h under the air atmosphere. The highly riched oxidizing environment lead ceria to quickly oxidize and gain more oxygen in the lattice as the ceria has superior OSC (oxygen storage capacity) [291].

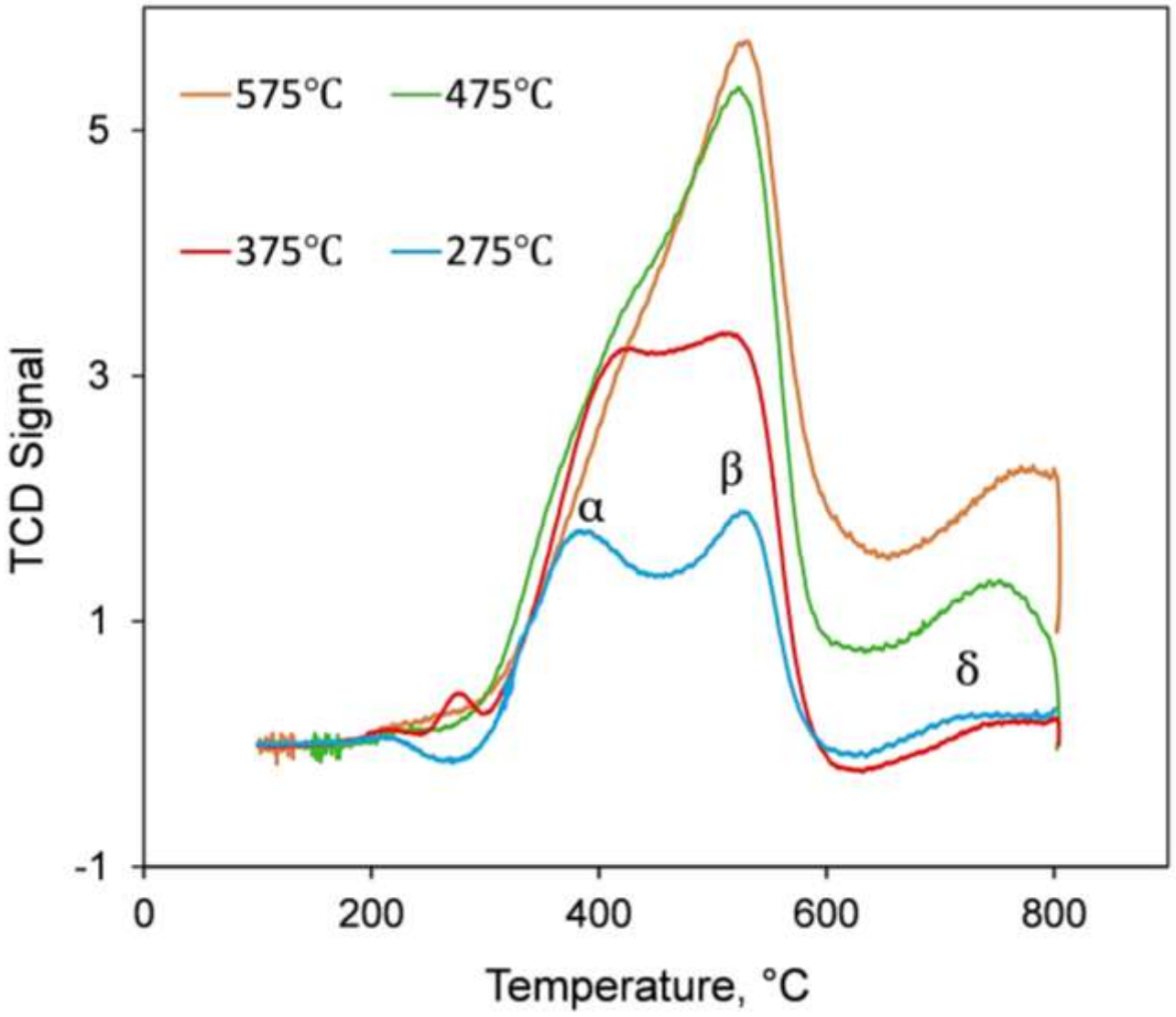

Figure 6.2:TPR profiles for 40%Ce/Al fresh samples calcined at 275, 375,474, and 575°C.

Sample calcined at 275°C and 375°C showed a weak peak δ compared to the samples calcined at 475°C and 575°C. This is again in agreement with the literature that when ceria-supported γ-alumina samples get exposed to higher temperatures, they create significant interaction, leading to solid solution formation [279, 288]. The samples calcined at 475°C and 575°C were exposed to higher temperatures, which led them to create more interactions between ceria and γ-alumina that eventually led them to make $CeAlO_3$. However, the interactions were weak for the samples calcined at 275C and

375C. Previous studies (section 5.3.3) showed similar results when TPR profiles of fresh and spent 40%Ce/Al calcined at 275°C were compared. Results showed a clear peak δ for the spent catalyst, which was missing for the fresh catalyst. This fact could be explained with the help of literature [279, 288] that after exposure to 600°C the sample could have significant interactions between ceria and alumina, leading to a clear peak during the TPR experiments.

6.3.3 Catalytic Activity Comparison

XRD, BET-SSA, and TPR studies showed a significant effect of calcination on the crystallite size, surface area, and interaction between ceria and γ-alumina support. Therefore, it was necessary to see if calcination temperature affects the catalytic activity of as-prepared 40%Ce/Al catalyst. To see the effect, all the samples were subjected to undergo standard catalytic activity temperature test .i.e., the catalysts were tested for the temperature range of 300°C-600°C (moving low to high), at an absolute pressure of 3 bar, and a GHSV of 60,000 ml g_{cat}^{-1} h^{-1}, as shown in Fig. 6.3.

Fig. 6.3(a) shows the temperature test's outcome for all the samples calcined at 275, 375, 475, and 575°C. It can be seen that all the samples showed 100%CO selectivity and almost the same CO_2 conversion at all temperatures, irrespective of initial calcination temperature. This means calcination does not play any role in enhancing or reducing as-prepared 40%Ce/Al catalyst activity, regardless of the other characterization studies results.

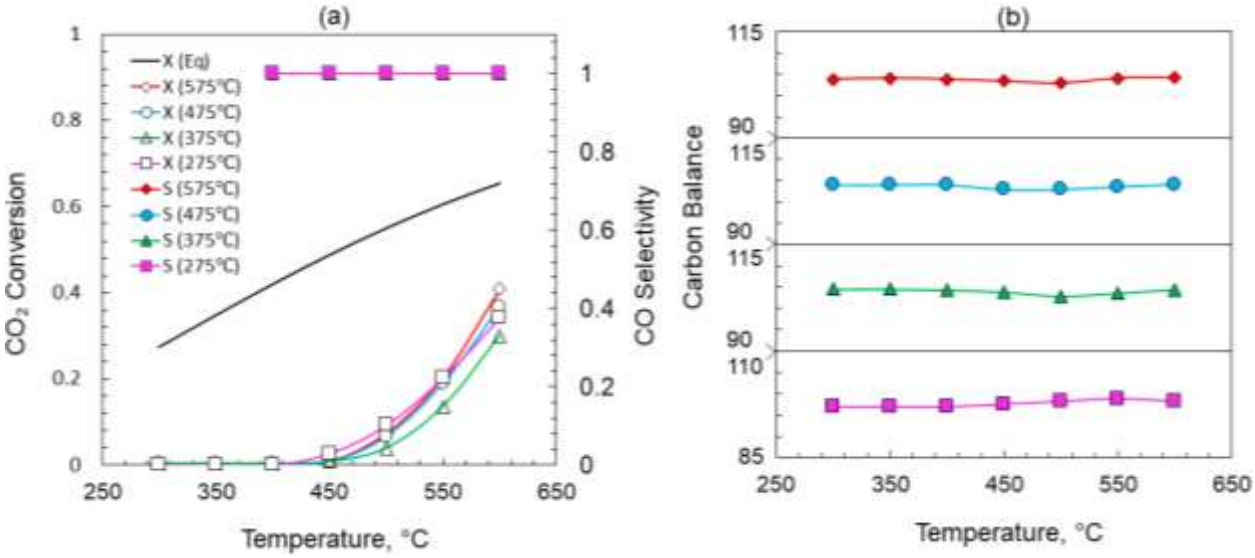

Figure 6.3: (a)Standard temperature test results at 300°C-600°C, 3bar, and GHSV 60,000 ml g_{cat}^{-1} h^{-1} (b) carbon balance .

This unusual behavior is well-matched with previous results reported in sections 4.3.1.2 and 5.3.1.2 for unsupported RME-ceria, and RME-ceria supported γ-alumina. Paidi et al. [282] showed that due to the formation of the surface oxygen vacancy under a reducing environment, an oxygen transport within the fluorite structure appeared, leading to an increased density of Ce^{3+} defects in bulk. Therefore, they proved bulk Ce^{3+} (generate via oxygen vacancy transport) is the origin of the base activity of pure ceria, which is its intrinsic property. Likewise, 40%Ce/Al calcined at 275°C, all the other samples calcined at 375, 475, and 575°C showed zero CH4 and coke formation. Again proving the highly coking resistant nature of RME prepared 40%Ce/Al. For all the experiments, the carbon balance (measured using eq. 14) remained stable, as shown in Fig. 6.3(b).

6.3.4 Active Catalytic Sites and Mechanistic studies

6.3.4.1 CO_2-TPD-FTIR Studies

CO_2-TPD analysis may provide information on the nature of CO_2 adsorption active sites on the catalyst surface. The catalytic activity of a catalyst towards CO_2 reduction is directly proportional to the catalyst's adsorption ability for the gas phase CO_2. Its been reported that the initial desorption temperature and a desorption peak temperature of the adsorbed gas species on the catalyst can be used to determine the catalyst's adsorption potential for gas species [139].

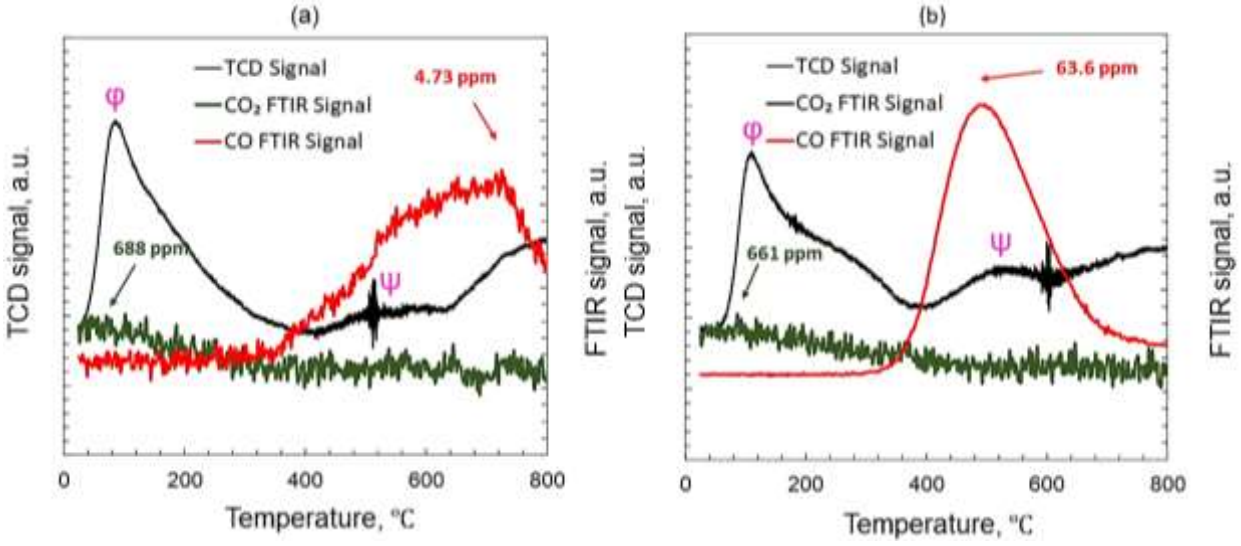

Figure 6.4: CO_2-TPD-FTIR curves for 40%Ce/Al calcined at 275°C without pre-reduction (a) with reduction (b).

To investigate the present active sites on 40%Ce/Al calcined at 275°C, two types of CO_2-TPD experiments were performed using an in-line FTIR gas analyzer. Fig. 6.4(b) showed the results when the catalyst was reduced at 400°C under 10%H_2/Ar for 2 h before the CO_2 adsorption, while Fig. 6.4

(a) shows the results for the catalyst without pre-reduction. However, the catalyst was treated under He for 2 h to remove any pre-absorbed species on the surface before CO_2 adsorption step occurs.

Both samples showed two clear peaks (φ and ψ). Peak φ started at around 35°C and went till 400°C with attaining its maxima at about 94°C. Peak ψ lies in the range of 400°C-800°C. Both peaks represent two types of adaptive sites. First leads to linear adsorption (O=C=O—M), while the second leads to bridge-bonded adsorption (M—O—C—O—M) [292]. Peak φ appeared in the low-temperature range and showed easier desorption, while peak lies in the high-temperature range showed difficult desorption. Fig. 6.4(a) showed a weak signal for the peak ψ, and also the corresponding FTIR signals showed a minute amount of CO appeared in that temperature range. This led to the presence of less active sites for the unreduced sample. However, the sample with pre-reduction at 400°C showed a strong peak ψ along with a powerful signal of CO (detected with in-line FTIR) that appeared in the corresponding temperature range. This clearly shows that reduction significantly enhances more active sites on the surface of the as-prepared catalyst. These results well matched with the activity test results. In all activity tests, no significant conversion was observed for any sample. However, all samples showed almost two folds of conversion for each coming temperature up till 600°C. These results well matched with the TPR data because all the samples undergo a high level of reduction in the temperature range of 400C-600C, leading to more oxygen vacancies that act as the leading active sites in ceria catalysis. However, it is a proven fact that the formed oxygen vacancies create Ce^{3+} in bulk, and these Ce^{3+} atoms are mainly responsible for the bulk-based ceria activity [282]. This fact is well proved here because the sample with pre-reduction showed a higher CO signal in parallel to higher peak ψ.

Some other studies showed that the functional group's chemical form influences the type of gas desorbed (whether it is CO_2, CO, or H_2O) and the peak temperatures in a TPD pattern [293]. It has been reported that the gases that evolved (during TPD-experiments) from the catalyst surface in the temperature range of 100°C-400°C are mostly due to the carboxylic functional group's presence [294].

Furthermore, the gases that appeared in the temperature range of 400°C-600°C showed the presence of acid anhydride functional group [295-297].

6.3.4.2 Reaction Mechanistic Studies (*In-situ* FTIR Surface Reaction Analysis)

In order to explain the surface reactions of the catalyst, mechanistic experiments are important. The final product generated during a catalytic reaction depends heavily on the intermedia created by adsorption and interaction between reactant gases and catalysis on the catalyst surface. A mixed gas feed (30 ml min^{-1}, 2% CO_2 / 8%H_2 / 90% argon) introduced into the system at 400°C, and reaction FTIR spectra were collected. Fig. 6.6 represents the reaction spectra observed at 0 min (after immediate entering), 1 min, 2 min, and 15 min after entering the reaction gases during the in-situ FTIR analysis 40%Ce/Al calcined at 275°C. 10%H_2/Ar was allowed to pass over the catalyst during the heating ramp rate to get a reduced surface before encountering the catalyst with reaction gases.

After 60 seconds, clear peaks appeared, showing the surface reaction and the intermediate over the surface. Peaks located between 1100-1436 cm^{-1} represent the uni- and bidentate carbonate formed due to CO_2 adsorption [119, 267-270]. Similarly, the peaks that appeared at 1456-1489 cm^{-1} show the surface carbonate [298]. Furthermore, the peaks located between 1507-1558cm^{-1} show the formation of bicarbonates [298, 299]. However, unlike RME-ceria, some surface formate species also appeared at 1652-1638 cm^{-1} [300, 301], which clear appeared due to the presence of γ-Al_2O_3. Additionally, Some carbonyl species were also detected at 1693-1733 cm^{-1} [300] along with some chemisorbed CO 1843 cm^{-1} [301]. Signal between 2200-2400 cm^{-1} showing the gas phase CO_2 [302]. The presence of the carbonate and formates shows that the RWGS reaction follows the associative mechanism over the as-prepared supported 40%Ce/Al catalyst (* denotes the vacancy site) [74, 142]. Fig. 6.5 shows the Schematic of the reaction mechanism.

$$H_{2(g)} + 2* \rightarrow H* + H* \quad \text{(i)}$$

$$CO_{2(g)} + * \rightarrow CO_2* \quad \text{(ii)}$$

$$CO_2* + H* \rightarrow HCOO* + * \quad \text{(iii)}$$

$$HCOO* (COOH*) + * \rightarrow HCO* (COH*) + 2O* \quad \text{(iv)}$$

$$HCO* (COH*) + * \rightarrow 2CO* + 2H* \quad \text{(v)}$$

$$H* + O* \rightarrow OH* + * \quad \text{(vi)}$$

$$H* + OH* \rightarrow H_2O* \quad \text{(vii)}$$

$$H_2O* \rightarrow H_2O_{(g)} + * \quad \text{(viii)}$$

$$CO* \rightarrow CO_{(g)} + * . \quad \text{(ix)}$$

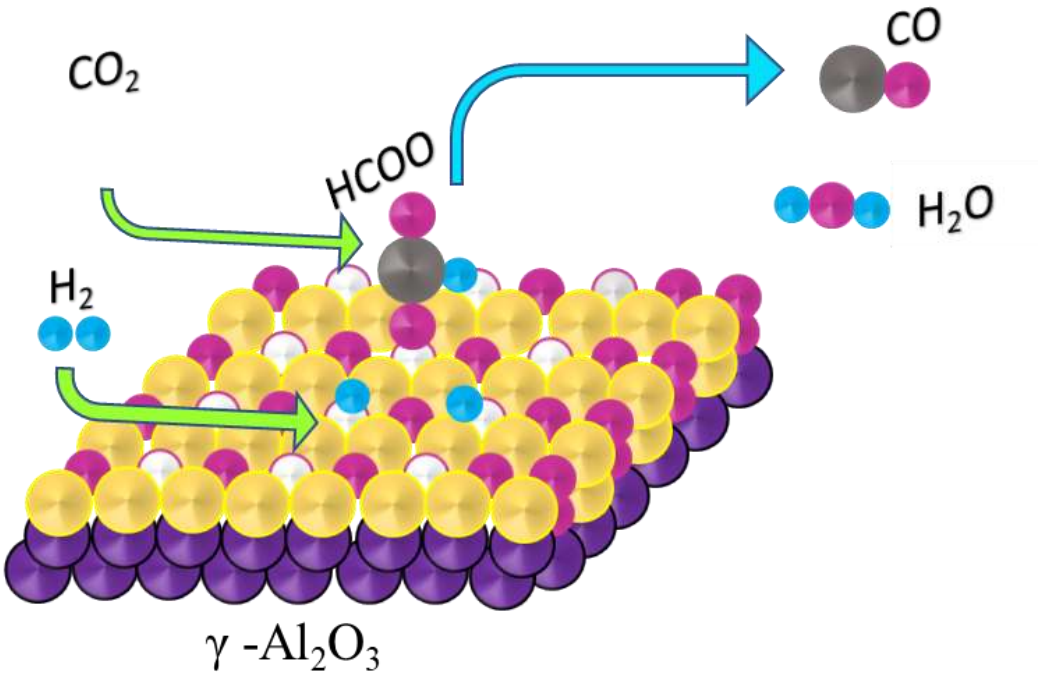

Figure 6.5: Schematic representation of RWGS reaction mechanism over unsupported ceria: Gray, blue, yellow, pink, purple, and white circles represent carbon, hydrogen, cerium, aluminum, oxygen atoms, and oxygen vacancies, respectively.

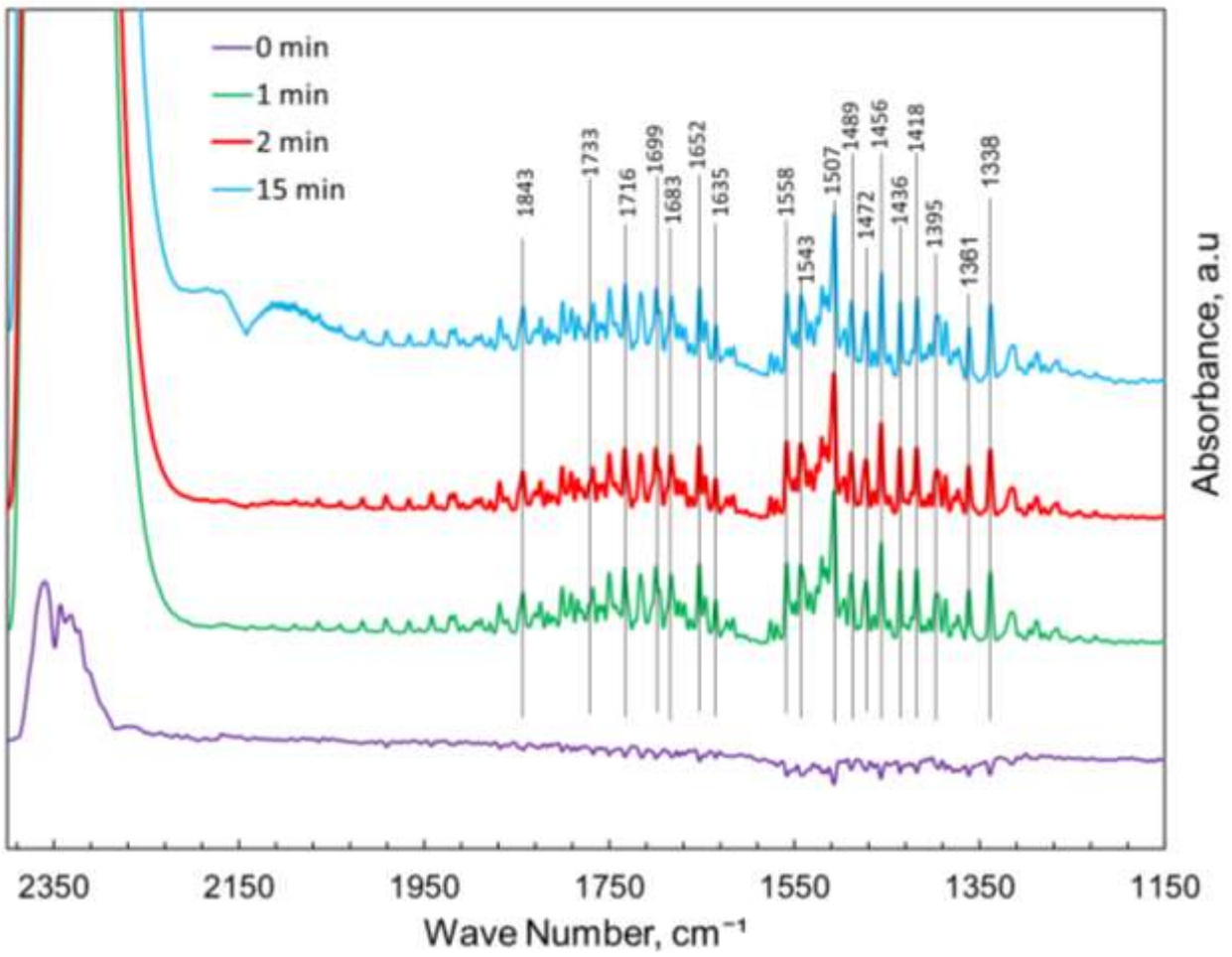

Figure 6.6: In-situ FTIR spectra over Fresh 40%Ce/Al calcined at 275°C after 0, 1, 2 and 15 min of reaction under 2% CO_2 /8% H_2/Ar at 400°C.

6.4 Conclusion

In this study, the effect of calcination temperature on the catalytic activity and the surface properties of as-prepared 40%Ce/Al catalyst was thoroughly investigated. The as-prepared catalyst was calcined at four different temperatures of 275, 375,475, and 575°C. Using various characterization techniques, we confirmed the bulk based activity for 40%Ce/Al and the reaction mechanism for RWGS reaction.

XRD results showed an appreciable increase in the crystallite size of ceria supported on γ-alumina i.e., it rose from 5.56 nm to 16.8 nm as the temperature increases from 275°C to 575°C. BET-SSA

results show similar decreasing behavior except the catalyst calcined at 375°C. The reason for this exception was well explained with literature that the increase in the surface area happened because of the burning of the leftover organic in the porous cluster of γ-alumina. H_2-TPR results showed a rise in H_2 consumption for the samples calcined at higher temperatures. This direct relation of H_2 consumption is well-matched with the highly reducing abilities of the ceria crystal present on the surface of the γ-alumina.

Furthermore, to identify the surface active site and reaction mechanism followed over supported Ce/Al catalysts, CO_2-TPD in-line with FTIR gas analyzer and *in-situ*-FTIR reaction mechanistic experiments were performed. CO_2-TPD results showed an excellent agreement with the TPR and the catalyst activity test results. It was found that the catalyst must go under reduction to have essential active sites on the surface of the catalyst for the dynamic adsorption of reaction gases. Finally, *in-situ* FTIR reaction mechanistic studies were performed, and it was concluded that unlike RME-ceria, 40%Ce/Al showed a formate mechanism for converting CO_2 CO via RWGS reaction.

Chapter 7

Investigation of coke formation in stainless steel reactor and metal dusting at elevated temperature under RWGS reaction

7.1 Introduction

Metal dusting is a severe form of corrosive degradation that Fe, Co, and Ni-base high-temperature alloys undergo when subjected to carbon supersaturated environments ($a_c > 1$) [17, 303]. It's a catastrophic carburization phenomenon that makes powdery coke and metal particles due to metal disintegration [304]. The anomaly is thought to predominantly occur in a temperature range of 400-700°C [17, 303]. The phenomenon becomes more dominant when carbonaceous gases (CO-H_2-H_2O) pass over the catalytic metallic surfaces at elevated temperatures. It's an annoying phenomenon, especially in industrial heat exchangers, because coking hinders gas flow, requires high pressure and temperature gradient [17]. Hochman [305, 306] was the first who did the early study on metal dusting. However, Grabke et al. [307-313] and Chun et al. [314, 315] investigated more details. These studies reported that CO is the most potent metal dust molecule and the involvement of H_2 helps to intensify the degradation of the metal surface. When contemplating metal dust corrosion in CO or C_xH_y (hydrocarbons) containing conditions, the following reactions can lead to the transfer of carbon to the metal surface [17, 303, 304, 307].

$$CO + H_2 \rightleftharpoons C + H_2O \qquad (27)$$

$$2CO \rightleftharpoons C + CO_2 \qquad (28)$$

$$C_xH_y \rightleftharpoons y/2\ H_2 + xC \qquad (29)$$

Eq. (28) is known as the Boudouard reaction. However, it does not play any significant role due to its slower kinetics. Grabke et al. [316] and Shatynski et al. [317] showed that among all the mentioned reactions, Eq.(27) shows the fastest kinetics that is resulting in extreme metal dusting at elevated temperatures in a CO-H_2 environment. In iron and steel alloys, carbon formation also occurs due to the solid-state reaction involving metal carbide dissolution. For iron and steel alloys following mechanism is proposed for the potential metal dusting[17, 306]:

(i) Oversaturation of metal due to inward carbon diffusion formed by surface reaction (eq. (1))

(ii) Cementite formation M_3C (M = Fe, Ni) that resists further carbon penetration.

(iii) As a result, a high carbon activity is developed at the surface, graphite nucleates locally, and the carbon activity is reduced to $a_c > 1$, making cementite unstable.

(iv) Cementite decomposes as $M_3C \rightarrow 3M + C$ (30)

The formed carbon atoms connected to the outer graphitic layer and the metal atoms diffuse and agglomerate to form small nano particles on the surface.

(v) These metal nanoparticles act as a catalyst and facilitate the reaction (eq. 27) for additional carbon deposition. In most cases, filamentous carbon growth can be seen behind these metal particles.

The following sequence can explain the formation of carbon filament on the metal particles free surface:

$$CO\ (g) \rightleftharpoons O\ (ad) + C\ (dissolved) \quad (31a)$$

$$O\ (ad) + H_2 \rightleftharpoons H_2O \quad (31b)$$

$$C\ (dissolved) \rightleftharpoons C\ (graphite) \quad (31c)$$

The carbon diffuses to a plane where graphite can easily nucleate and attaches to the carbon filament that grows from this location. Chun et al. [303] presented a simple schematic (Fig. 7.1) to

understand the above-mentioned mechanism included his experimental findings on the right side of the picture.

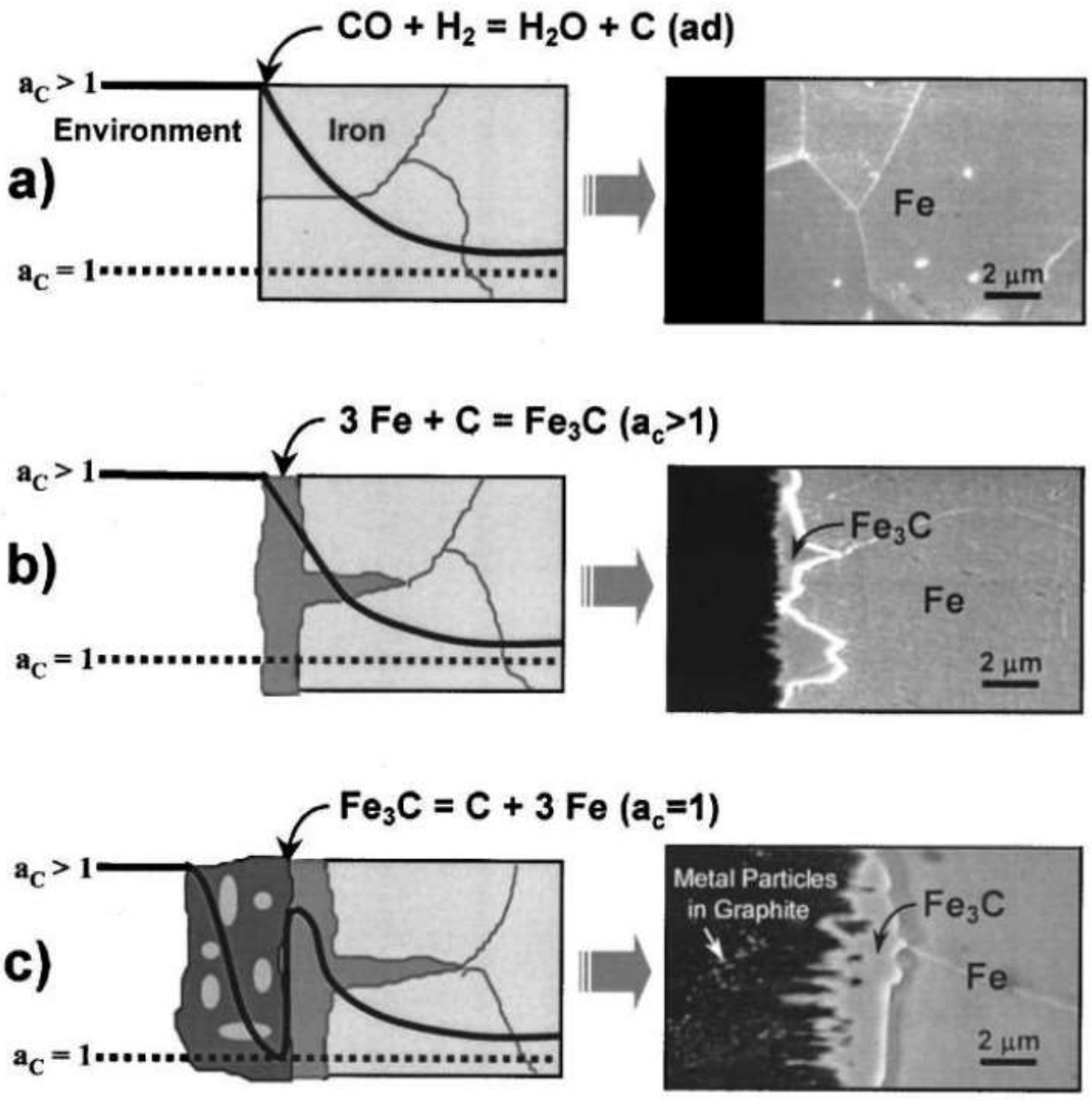

Figure 7.1: Schematic of the proposed mechanism in metal dusting of iron and steel [303].

Fig. 7.1(a) show the initial C deposition on the metal surface due to the reaction of CO and H_2. Fig. 7.1(b) show the formation of metastable Fe_3C on the surface. Fig. 7.1(c) shows that the further carbon deposition reduces the carbon activity to 1 at the Fe_3C/graphite interface, which prompted Fe_3C dissociation. The resulted carbon atoms formed attached to graphite [303]. However, the metal particles generated move away from the Fe_3C/graphite interface and appeared on the edges of the filaments [318].

For this Ph.D. study, CeO_2 was selected as a potential catalytic agent because of its excellent reducing abilities [202-204], 100% CO selectivity (via RWGS reaction) [20-22], and coking resistance [274]. However, during different experimentation, we observe a significant amount of coke deposits on the downstream side of the reactor (after the catalyst bed) when old reactor systems (almost 42 h on stream) were used for the evaluation of as-prepared catalysts for RWGS applications. A comprehensive investigation was performed to find the root cause of this coking, and results prove that the coke formation on the downstream side has resulted from the metal dusting of stainless steel tubes at elevated temperatures under a highly active carbonaceous gas mixture of CO-H_2-H_2O. Finally, a safe time frame was proposed for the use of stainless steel tubing for RWGS applications at elevated temperatures. The given study could be used as a reference in the future to apply stainless steel alloy in RWGS applications.

7.2 Experimental

7.2.1 Materials

1/2" and 1/4" inch stainless steel tubes (316L alloy, ASTM A479) and reducing adapters were purchased from Swagelok incorporation to make kinetic reactors for the catalytic activity test. As-prepared RME-ceria (section 4.2.1) and 40%Ce/Al (section 5.2.2) catalysts were deployed to investigate coking and metal dusting.

7.2.2 Performance and Activity

To investigate the coke formation and metal dusting in the stainless steel kinetic reactors, under highly active carbonaceous environment (CO-H_2-H_2O), RME-ceria and DP-ceria were deployed for the production of syngas. The reactor system was made by joining the 1/2" stainless steel tube (316L, Swagelok) with 1/4" stainless steel tube (316L, Swagelok) via a reducing adapter (served as the reactor) and straight union. Please refer to Fig. 3.11 for the kinetic reactor schematic and section 3.6.1 for the complete description and experimental setup of the flow system. Kinetic reactors (with and without catalyst bed) were evaluated for the temperature range of 300°C-600°C at 3 bar absolute pressure and GHSV of 60,000 ml g_{cat}^{-1} h^{-1}. In an empty reactor test, inert quartz wool was used in place of the catalyst.

The total CO_2 conversion, CO selectivity, and CH_4 selectivity were calculated according to the following equations.

$$X_{CO_2} = \frac{y_{CO}+y_{CH_4}}{y_{CO_2}+y_{CO}+y_{CH_4}} \qquad (11)$$

$$S_{CO} = \frac{y_{CO}}{y_{CO}+y_{CH_4}} \qquad (12)$$

$$S_{CH_4} = \frac{y_{CH_4}}{y_{CO}+y_{CH_4}} \qquad (13)$$

7.2.3 Characterization Studies

D8 discover diffractometer, Bruker was utilized to obtain the XRD patterns using Cu-Ka radiation source (λ = 1.54 Å) at 40 kV tube voltage and 40 mA of a tube current. Diffraction patterns were collected for the 2θ ranged 10° to 90° at a scan sped of 3 (time per step) with an increment of 0.1. Elemental mapping, and surface composition of coke was obtained using HRSEM-EDX (high resolution electron microscopy coupled with energy-dispersive X-ray spectroscopy) a Zeiss Ultra microscope (20 kV). Thermo-gravimetric analysis (TGA, Q500, TA Instruments), coupled with an in-

line gas FTIR analyzer (Multigas^{TM} 2030, MKS instruments), was performed to determine the type of coke. The temperature ramp was set to 10°C min^{-1} for T ≤ 150°C and maintained under isothermal conditions for 1 h at 150°C. After 1 h, the temperature ramp was set to 2°C min^{-1} for 150°C < T < 800°C and the airflow was set to 40 ml min^{-1}.

7.3 Results and Discussion

7. 3.1 Activity, Steel Dusting, and Coke Formation

These investigations were taken into account when we found an unexpected rise in CO2 conversion during the 3 Heating-cooling cyclic test of RME-ceria, conducted using the old kinetic reactor (already 28 h on stream) shown in Fig. 7.2. (a).

In this experiment, the system was allowed to undergo a temperature change of 300°C-600°C (moving low to high) at 3bar pressure and a GHSV of 60,000 ml g_{cat}^{-1} h^{-1} for the cycle1. After cycle1 (300°C-600°C), the system was allowed to cool down to 300°C and then exposed to the similar conditions performed before. Fig. 7.2 shows that a similar stable CO_2 conversion (as of the standard catalytic activity test of RME-ceria) was recorded during cycle1 when the old stainless steel (already 28 h on stream) reactor was used. However, for each coming cycle, the activity increased to almost two folds as recorded for each corresponding temperature during the standard catalytic activity test of RME-ceria. Generally, catalysis is considered as the surface phenomenon, though for ceria, bulk-based activities have been proved [282]. However, this unusual increase in ceria catalytic activity was not possible even considering bulk-based activities for ceria. Consequently, This increase was regarded as an indication that the stainless steel reactor starts facilitating the RWGS reaction after prolonged exposure to elevated temperatures (up to 600°C), which was later confirmed with experimental results in line with the literature [15-17, 303]. During this experiment, the CO selectivity remained 100% (no CH_4), and the carbon balance was around 0.97. However, during the unloading of the kinetic

reactor (from the flow system), a very minute amount of coke flakes was observed on the downstream side.

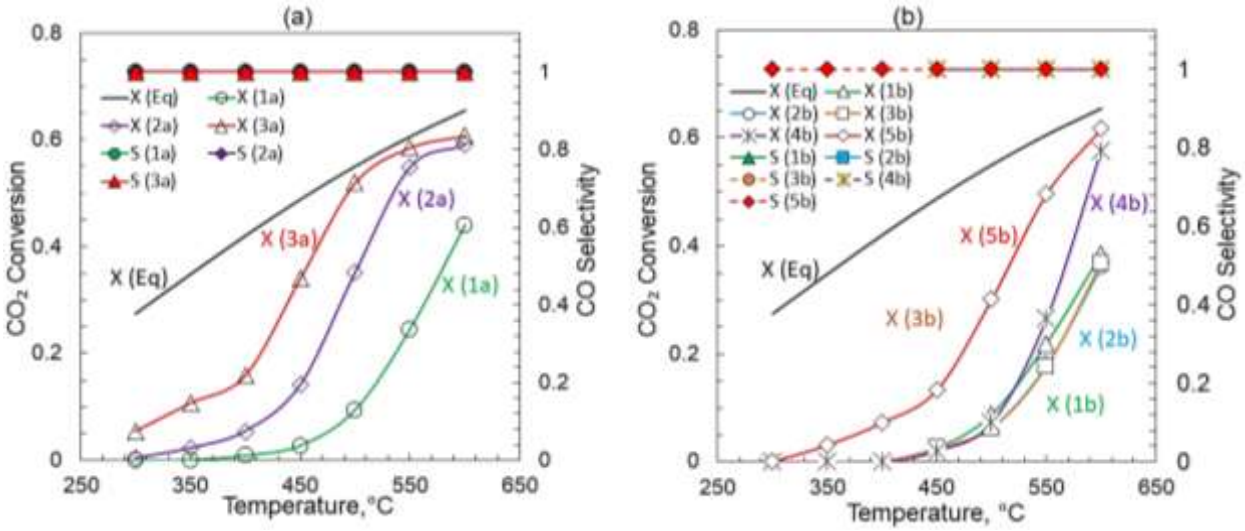

Figure 7.2: Kinetic reactor activity in (a) 3Heating -cooling cycle test (when the old reactor was used) (b) 5Heating-Cooling cycle test (when the new reactor was used) at 300°C-600°C, 3bar, and GHSV of 60,000 ml g_{cat}^{-1} h^{-1}. Where "X" shows conversion, the numeric letter shows the corresponding cycle, and the alphabets "a & b" offers the figure caption.

To confirm this fact, another test based on 5heating-cooling cycles was performed using RME-ceria (as the catalytic agent) at the same condition (described above for 3cycle test) using a brand new stainless steel reactor (Fig. 3.11), shown in Fig. 7.2(b). It can easily be seen that till cycle3 (almost 42 h on stream), catalytic activity remained stable (similar to the standard activity tests described in section 4.2.2) at all the temperatures tested. However, for cycle4, a significant increase in CO_2 conversion was observed as the temperature reached 550°C. Similarly, for cycle5, a similar increasing activity trend was recorded as followed in the 3-heating-cooling cycle test. Again, a minute amount of Coke was observed during the unloading of the kinetic reactor. This observation is well-matched with the findings of Müller et al. [17] and Chun et al. [303]. They reported that under a highly active

carbonaceous environment of CO-H_2-H_2O, the iron and steel alloys undergo a degradation process known as metal dusting, leading to the disintegration of cementite into metal particles and carbon. These metal particles act as the new catalytic sites for the coke formation (eq. 31a-c). The continuous exposure to a temperature above 540°C creates pits in the metal, and activation energy for coke formation decreased from 51kJ mol^{-1} to 11kJ mol^{-1} for Austenitic steel (contains Cr > 16%) closer to the 316L stainless steel used in the present studies.

To investigate the long-term stability of 316L stainless steel alloy at 600°C in high carbonaceous environment of CO-H_2-H_2O, standard stability tests (almost 100 h on stream) were performed using both RME-ceria and 40%Ce/Al (as the catalytic agent) using brand new stainless steel reactors at 600°C, 3bar and GHSV of 60,000 ml g_{cat}^{-1} h^{-1}. Along with CO_2 conversion, CO/CH_4 selectivity, and carbon balance, the pressure was continuously monitored to observe the kinetic reactor's clogging due to coke formation. Fig. 7.3(a) shows the total CO_2 conversion and CO selectivity for RME-ceria, while Fig. 7.3(b) shows the corresponding carbon balance (CB) and pressure. Initially, 44% conversion was recorded (similar to what we observe during standard activity tests), but it starts decreasing and reached 39% after 12 h. However, right after this point, the conversion increased and went to ~60% after 32 h on stream. CO selectivity started declining and continued to decrease till 100 h. Corresponding, pressure and carbon balance(CB) showed that at 38 h the pressure begins to increase while the carbon balance starts to fall. This increasing pressure and decreasing CB indicated that the system is building up with heavy coke. The pressure rises to 8 bar, and the flow through the system almost stopped. However, high pressure pushed the coke and made some channels for the gases to pass, and the pressure suddenly dropped back to the initial value of 3bar. Later, the pressure started rising again and reached a maximum value of 12 bar after 100 h on stream. A similar trend was observed when 40%Ce/Al was used as the catalytic agent to produce syngas in a brand new kinetic reactor. However, in this experiment, an increase in CO_2 conversion was observed after 6 h on stream, which is still in line with the results obtained during 3 cyclic test because each catalyst's performance was tested at a

single temperature for 110 min. Therefore, it can be accepted that 316L stainless steel could be utilized for the evaluation of RWGS studies for up to 6 h on stream at a single elevated temperature. However, for temperatures less than 500℃ it can be used for long-term activities. At the end of RME-ceria stability test, the reactor assembly was thoroughly investigated physically to find the exact collaging point in the system. Furthermore, the coke samples collected were further characterized through XRD, HRSEM, and TGA-FTIR to confirm the type of coke, its morphology, and metallic nanoparticles presence due steel dusting.

The results obtained from stability tests are again well-matched with the literature. Chun et al. [303, 314] studied the mechanism of Fe dusting at 550℃ under CO and H_2 environment. They found that at H_2:CO of 50:50 the rate appeared to be fastest, while at higher H_2 content, the carbon formation rate was still higher than low H_2 content. On the other hand, Müller et al. [17] studied the metal dusting of various alloys at different temperatures with varying CO: H_2 mixtures. They reported that cementite decomposition becomes faster above 540℃ than any other process with lower activation energy. Above this temperature, the decomposition process directly depends on CO and H_2 partial pressures and independent of H_2O partial pressure. The coking formation corresponds very clearly to the reaction given in eq. 31(a-c), i.e., the carbon transfer from the dusting process to the metal particles by CO decomposition. In this high-temperature range, the reaction is only proportional to pCO. These findings are well-matched with the results presented above.

.

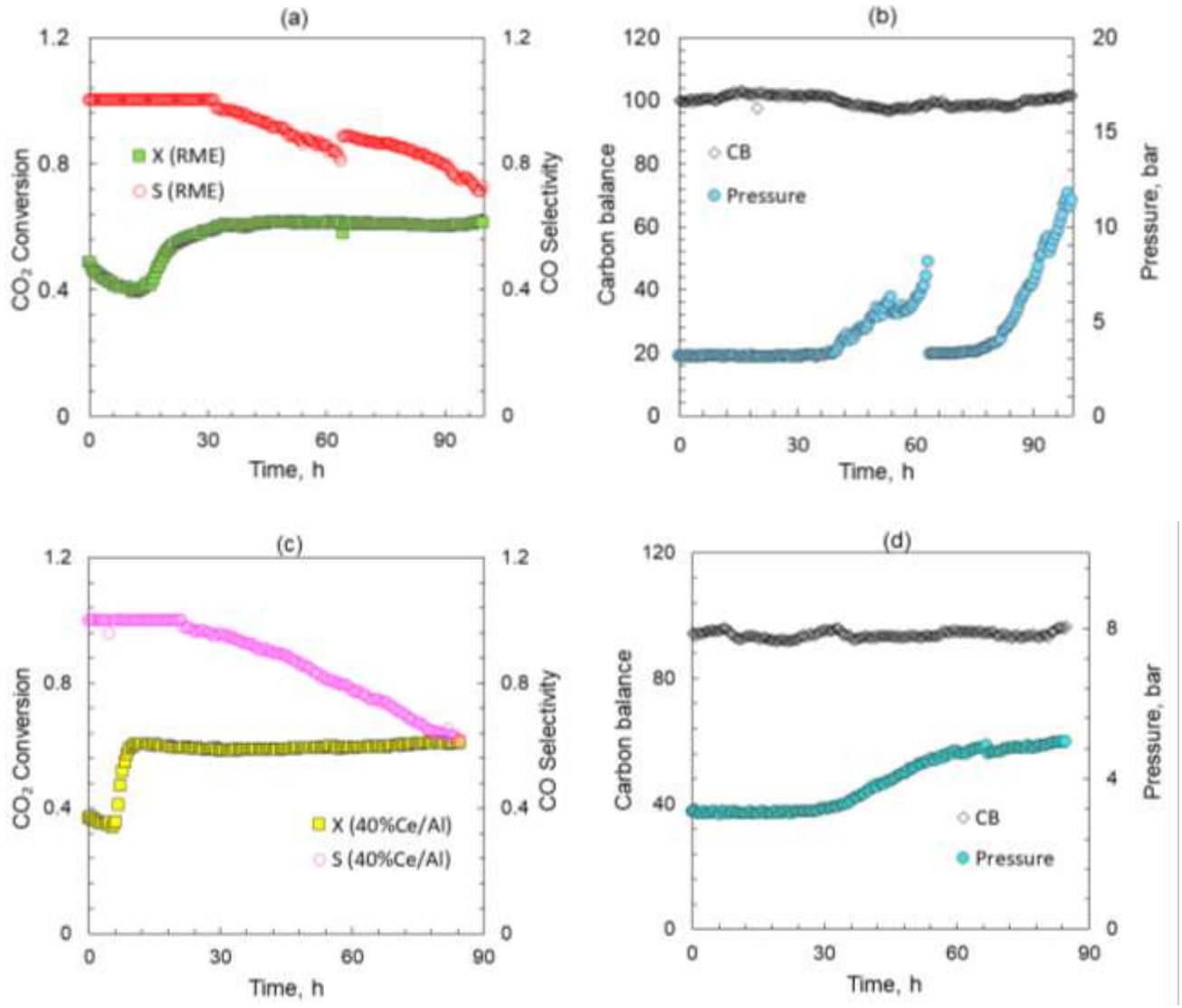

Figure 7.3: Long-term stability test of kinetic reactor under CO-H_2 environment using RME-ceria as the catalytic agent (a&b) using 40%Ce/Al as the catalytic agent (c&d).

To further support the dependence of stainless steel disintegration into metallic particles and coke at elevated temperatures on the carbonaceous gases present in the system, an empty reactor (having inert quartz wool in place of catalyst) was subjected to the similar condition of standard stability test (600°C, 3bar, and GHSV of 60,0000 ml g_{act}^{-1} h^{-1}). GHSV was calculated using the inert quartz wool weight placed inside the reactor. Fig. 7.4(a) shows the standard activity test performance for the empty

stainless-steel reactor, which was performed at the start of this Ph.D. study to check the stainless-steel reactivity towards the incoming gases. The experimental conditions were 300℃-600℃ (going low to high) 3bar absolute pressure and GHSV of 60,000 ml $g_{cat}^{-1}h^{-1}$. The initial experiments showed stainless steel noncatalytic behavior towards the gas mixture of H_2:CO_2 4:1 up to 550℃. No CO_2 conversion was observed even for 2 h on stream at each temperature up to 550℃. Despite, a very minute (~2%) CO was detected at 600℃ after 2 h on stream. Results were significantly satisfied to carry on the work using stainless reactors as now appreciable conversion was seen even at 600℃. However, later during the cyclic test, the appeared unusual activity of RME-ceria pushed to further investigate the issue. Therefore, a long-term stability test was performed using an empty reactor having inert quartz wool in place of catalyst. The kinetic reactor was subjected to a similar condition of standard stability test of 600℃, 3bar, and GHSV of 60,0000 ml g_{act}^{-1} h^{-1}. Fig. 4(b) shows the even up to 12 h on stream at 600℃, the detected CO was not above 2%, and the amount does not increase from 4% even 80 h on stream. These findings again support the fact that stainless steel itself is noncatalytic up to 550℃, but it starts showing higher catalytic activity when its subjected to high temperature especially in a higher concentration of CO and H_2. At a low concentration of CO, even at 600℃, there was no metal dusting or coke formation was observed.

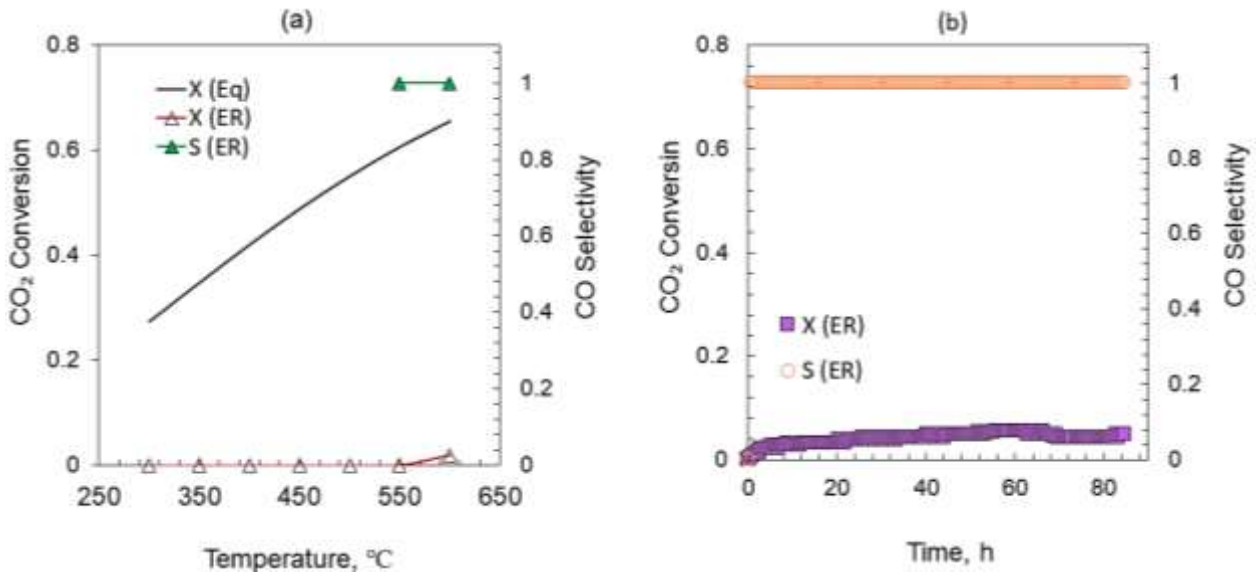

Figure 7.4: Empty reactor test for the RWGS activity of kinetic reactor without catalyst, (a) standard temperature test at 300°C-600°C, 3bar, GHSV 60,000 ml g_{cat}^{-1} h^{-1} (b) long term stability test at 600°C, 3bar, GHSV 60,000 ml g_{cat}^{-1} h^{-1}.

7.3.2 Kinetic Reactor Physical Investigation

After RME-ceria long-term stability test (Fig. 3(a)), the recovered kinetic reactor was thoroughly investigated to locate the actual clogging point (due to coke growth) to recover catalyst and coke sample for further characterization. Fig. 5 shows the real images taken after opening and cutting different parts of the kinetic reactor assembly.

Fig. 7.5(b) showed that when the thermocouple was taken out of the outlet of 1/4" inch tube, it was covered all over with black coke. A 12" inch long thermocouple was installed in a way that its tip touches the quartz wool, which is in touch with the catalyst bed on the other side. The first step in the investigation was to recover the catalyst safely. The catalyst bed was recovered after opening the 1/2" inch tube, as shown in Fig. 7.5(b). A few small chunks of carbon were observed in the spent catalyst,

which probably grew due to the synthesis gas backflow when the system pressure rises. No coke or metal degradation was observed on the inlet and outlet side of the catalyst bed.

(a)

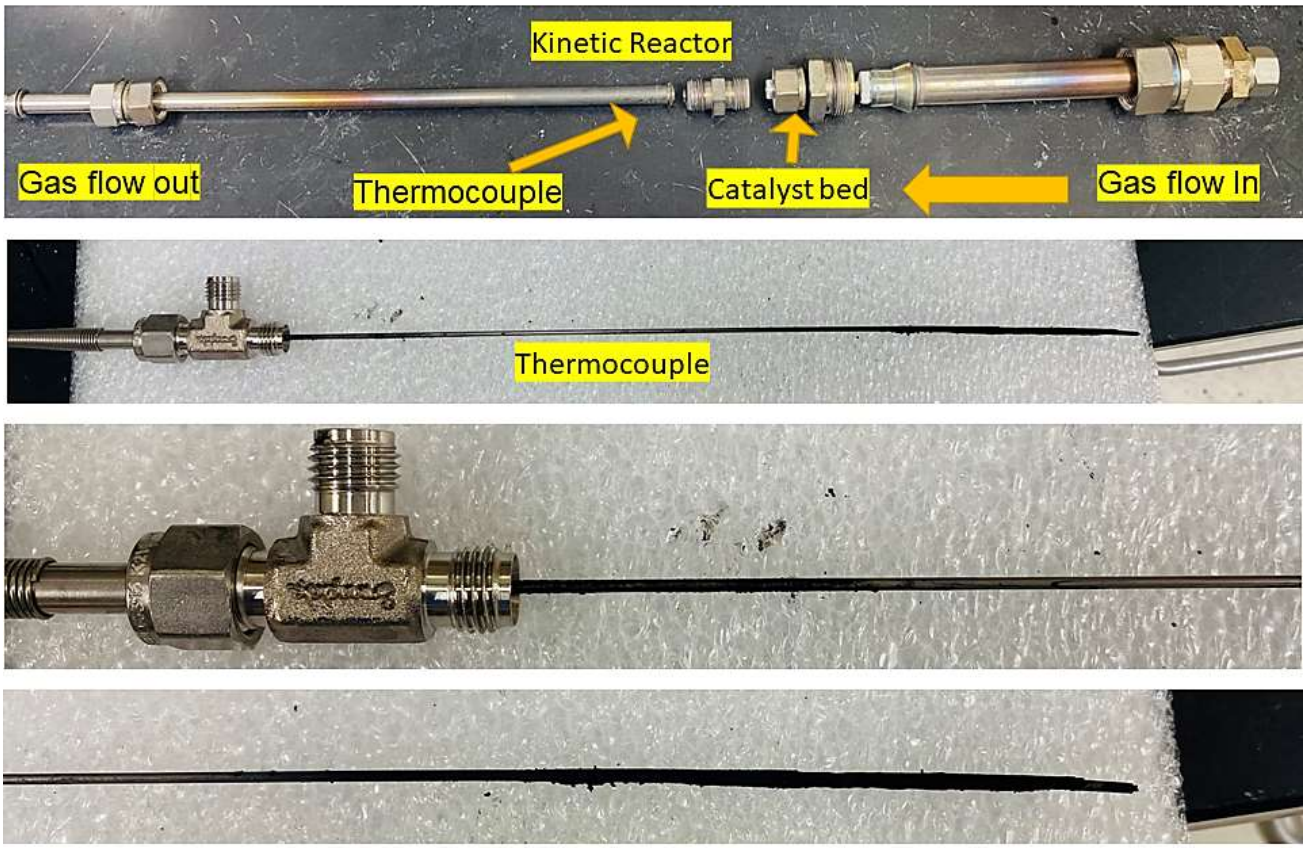

(b)

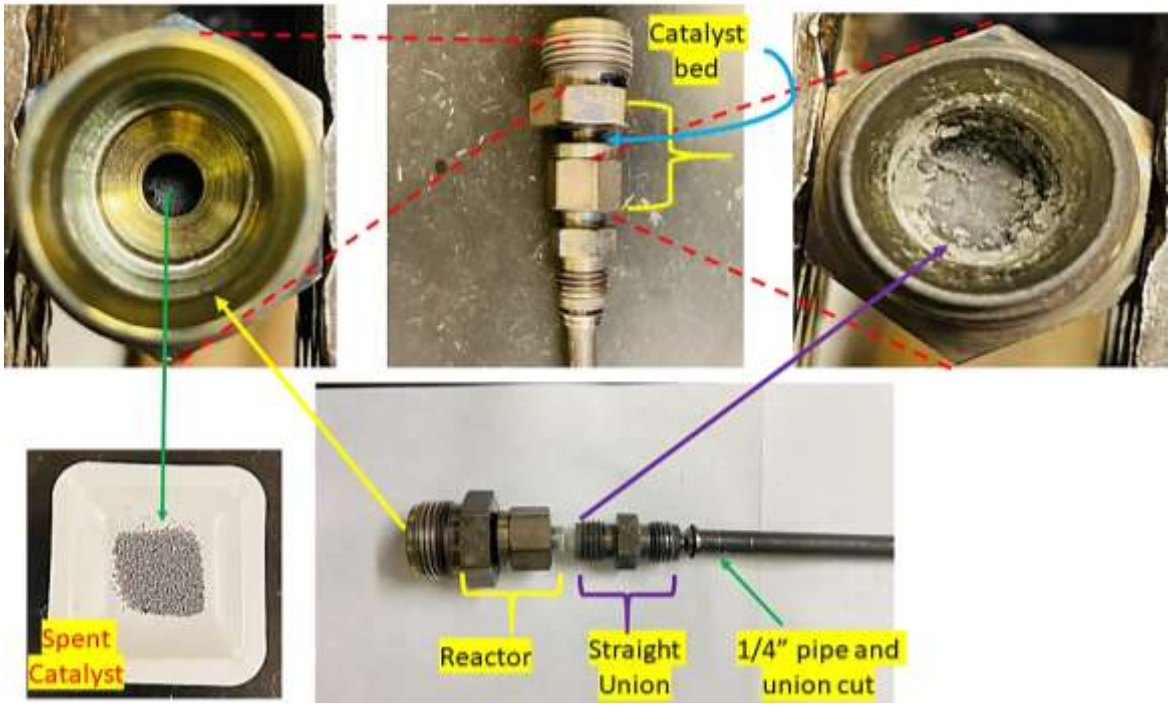

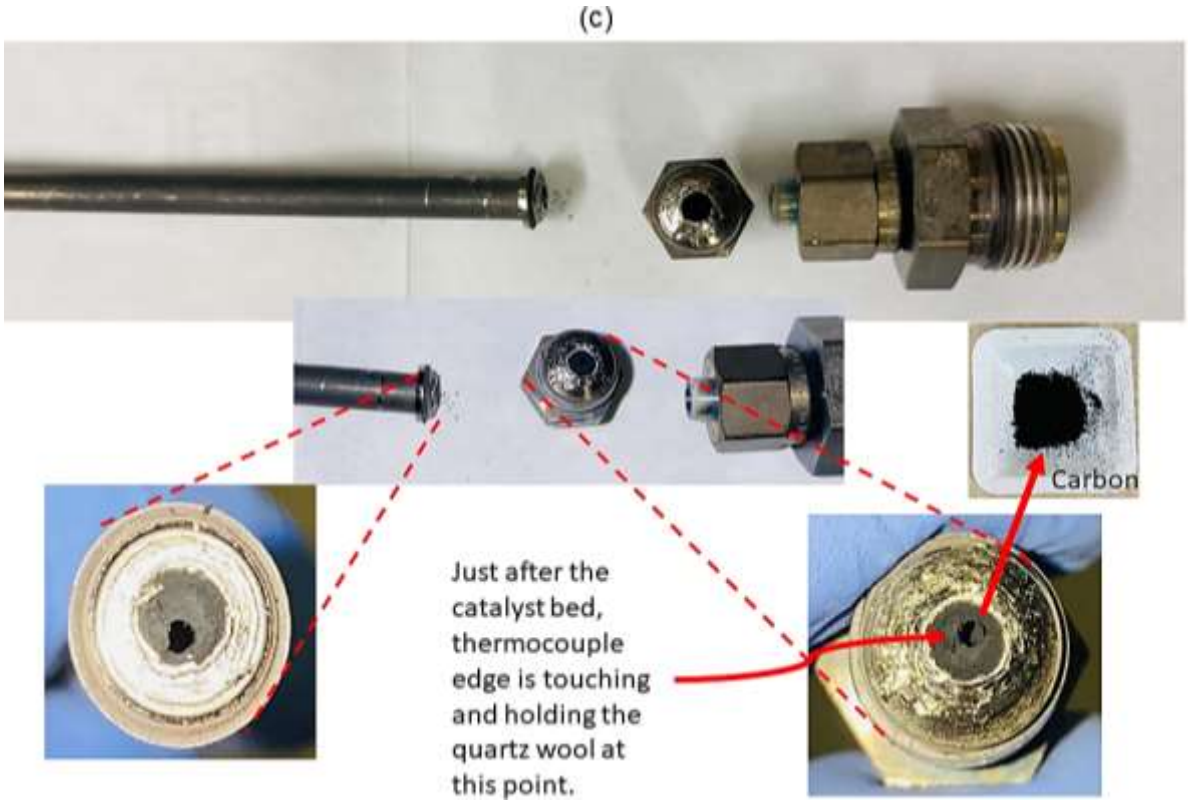

Figure 7.5: Kinetic reactor physical investigation, (a) complete kinetic reactor with thermocouple (b) open upstream side of the kinetic reactor and catalyst recovery (c) downstream side of the kinetic reactor (the point where thermocouple touches the wool holding catalyst)

Fig. 7.5(b) shows that the point where the catalytic bed touches the quartz wool was still white, indicating no coke formation in the assembly's upstream section. However, when the joining area of straight union and 1/4" tube was cut (the point at which thermocouple touches the other side of the quartz wool holding the catalyst bed), the end appeared completely clogged with coke grew all over the cross-section. The small holes in the bottom part of Fig. 7.5(c) (right and left bottom corners) showed the thermocouple's location in the assembly. The coke was recovered and subjected to XRD, HRSEM, and TGA-FTIR for in-depth analysis. This physical investigation again supports the fact that the metal dusting and coke formation appear in stainless steel in highly active carbonaceous zones at elevated temperatures.

7.3.3 SEM-EDX Spectroscopy

Fig. 6 shows the SEM micrographs obtained at 1 µm and 500nm for the coke deposits collected after RME-ceria (Fig. 7.6(a&b)) and 40%Ce/Al (Fig. 6(c&d)) 100 h stability tests, respectively. Fig. 7.6 shows an exact filamentous growth of the deposited coke. This filamentous structure of the coke is well-matched with the literature [17, 303-305, 318]. According to muller et al. , Coke grows evenly on the samples after metal dusting of iron and low alloy steels (as seen in Fig. 6(a)). Metal dusting and coke development begin locally on high alloy steels in most cases, in locations where the oxide scale has defects. The coke then spreads in these spots in the shape of strings, tubes, and the metal waste induces pit formation. They further reported that coke grows in the form of filaments over high alloy steels and carried metal nanoparticles on the edges. In Fig. 7.6 (b&d) small metal nano particles can be seen clearly at the edges of the filaments. Similarly, Chun et al. [303] and Pippel et al. [318] showed that the metal particles generated (as a result of cementite decomposition) moved away from the Fe_3C/graphite interface and appeared on the edges of the filaments.

To further investigate the presence of metal nanoparticles on the edges of the filaments, EDX for the collected coke was performed, as shown in Fig.7.7 Both the coke samples (collected after RME-ceria and 40%Ce/Al stability tests) clearly showed fine nanometa particles on edges and well dispersed all over the filamentous network. EDX majorly detects Fe and Cr on the surface because 316L steel contains Cr (16-18%), the highest percent metal present.

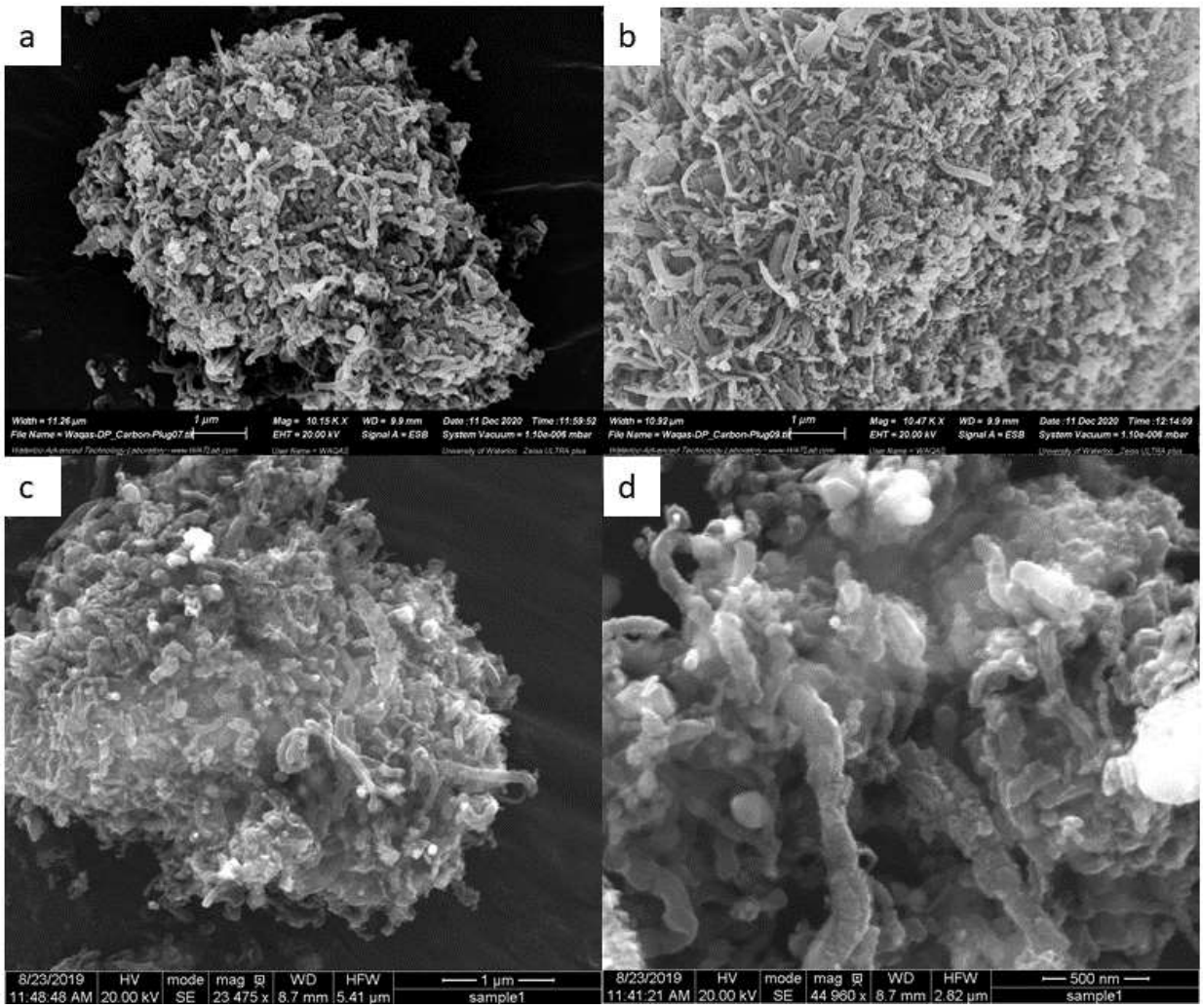

Figure 7.6: SEM micrographs taken at 1µm and 500 nm for coke sample collected after stability test of RME-ceria (a & b) and 40%Ce/Al (c&d)

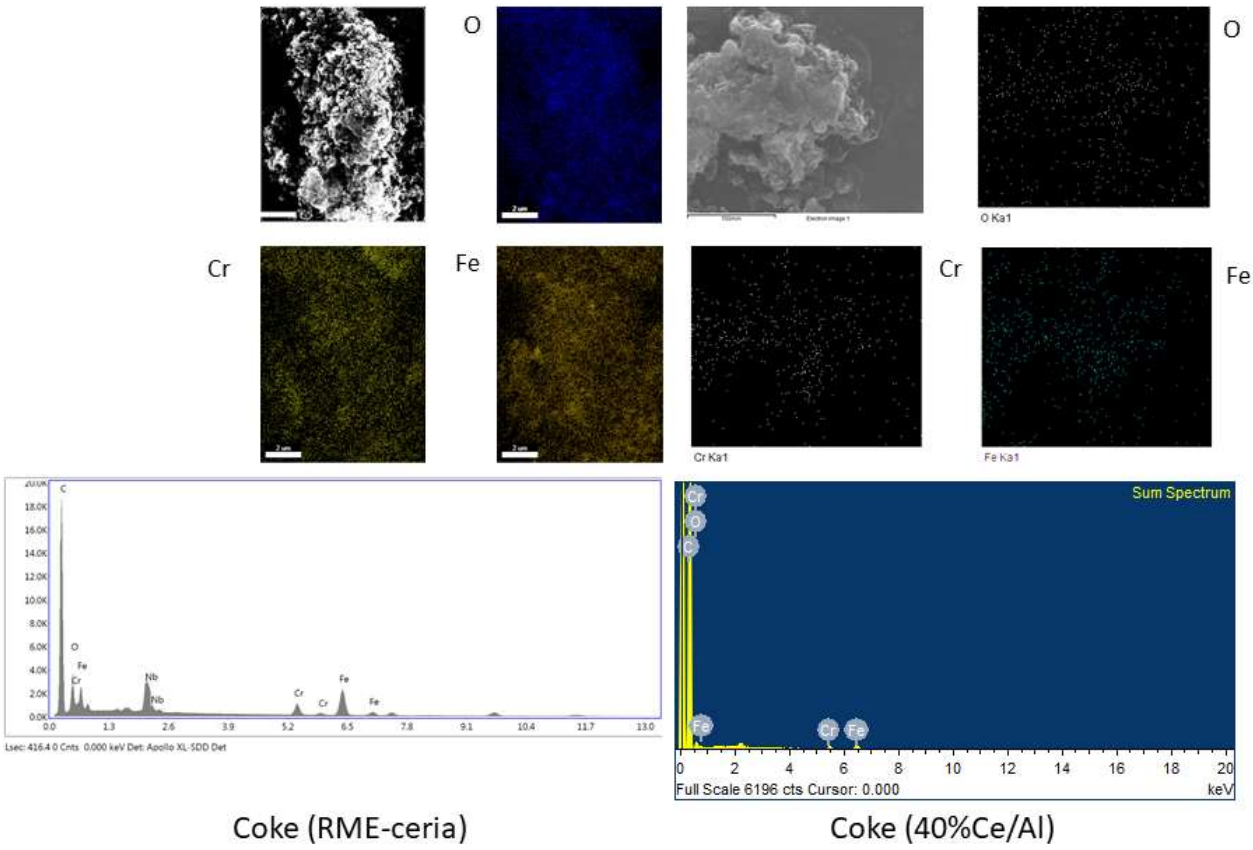

Figure 7.7: Elemental mapping and of coke sample collected after stability test of (a) RME-ceria (b) 40%Ce/Al.

7.3.3 TGA-FTIR

SEM-EDX images confirm the coke's filamentous growth and the presence of metal particles on the surface. However, to further confirm the coke's nature and the metallic particles' presence in the samples, thermogravimetric analysis with in-line FTIR were performed. The combustion gases fro the TGA outlet were allowed to pass through the FTIR, and the recoded data was synchronized later with weight loss and temperature to recognize the coke type.

Fig. 8 shows the TGA-FTIR plots for the coke samples collected after RME-ceria and 40%Ce/Al stability test. Fig. 7.8(a) shows that as the temperature reached 350°C, the weight of the sample starts increasing. This mass gain is attributed to the oxidation of the metallic particles present in the coke

sample. These metallic particles must come from the steel dusting because the spent catalyst was safely recovered after the stability test from the separate compartment, and there was no chance for the catalyst to escape and get mixed with coke growing on the downstream side of the kinetic reactor. Similarly, A very slight weight increase was observed for the coke sample recovered after the 40%Ce/Al stability test, shown in Fig. 7.8(b). These results well-matched with SEM-EDX as EXD detects a very minute amount of Fe and Cr for the coke collected from the kinetic reactor of 40%Ce/Al compared to the coke collected for RME-ceria used kinetic reactor. Furthermore, both sample shows similar clear sharp peaks for CO_2 and CO at around 625°C. It has been reported in the literature the coke burns in the temperature range of 500-650°C is filamentous coke [319-321]. The presence of filamentous coke and metal particles in the coke sample confirms that the coke appears as a result of the metal dusting of steel under a highly active carbonaceous environment at elevated temperature.

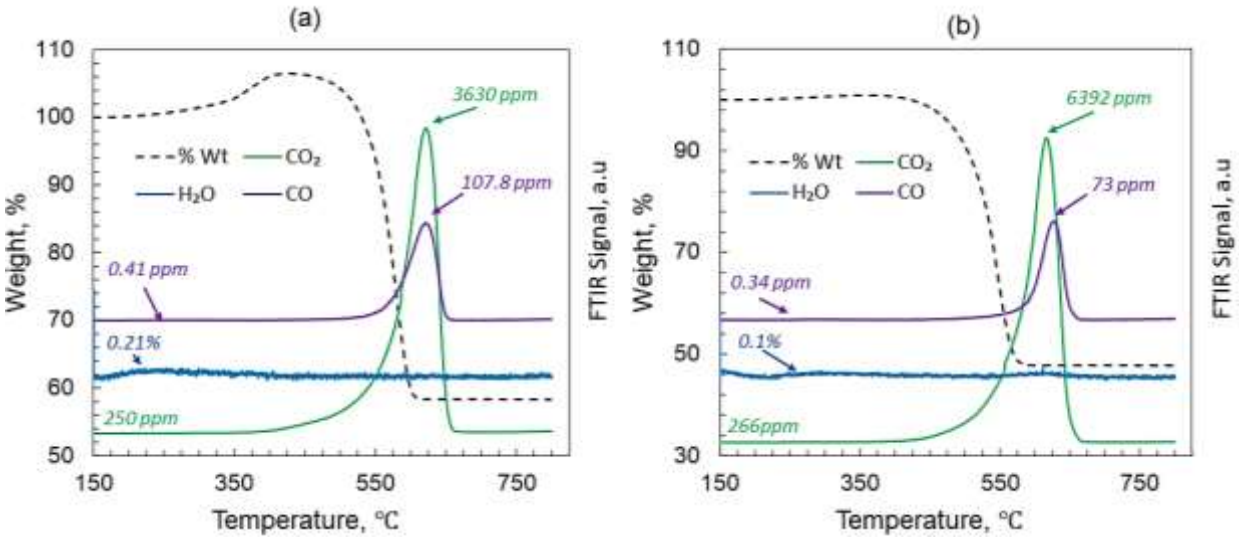

Figure 7.8: TGA-FTIR plots for the coke samples collected after stability test of (a) RME-ceria (b) 40%Ce/Al.

7.3.5 XRD study

Fig. 7.9 shows the XRD diffraction pattern obtained for the sample collected after the TGA-FTIR of the coke. The diffraction pattern indicates the presence of all three (Fe, Cr, Ni) major components of the 316L steel in the final mixture in different oxides form. Iron is present in the form of magnetite and showed two clear peaks at 35.1° and 62.4°. However, Ni was detected as Nickle chromate, and chromium was detected as chromium carbide. This simple XRD scan for the recovered oxidized coke sample after TGA-FTIR further confirms the presence of metal particles in the coke.

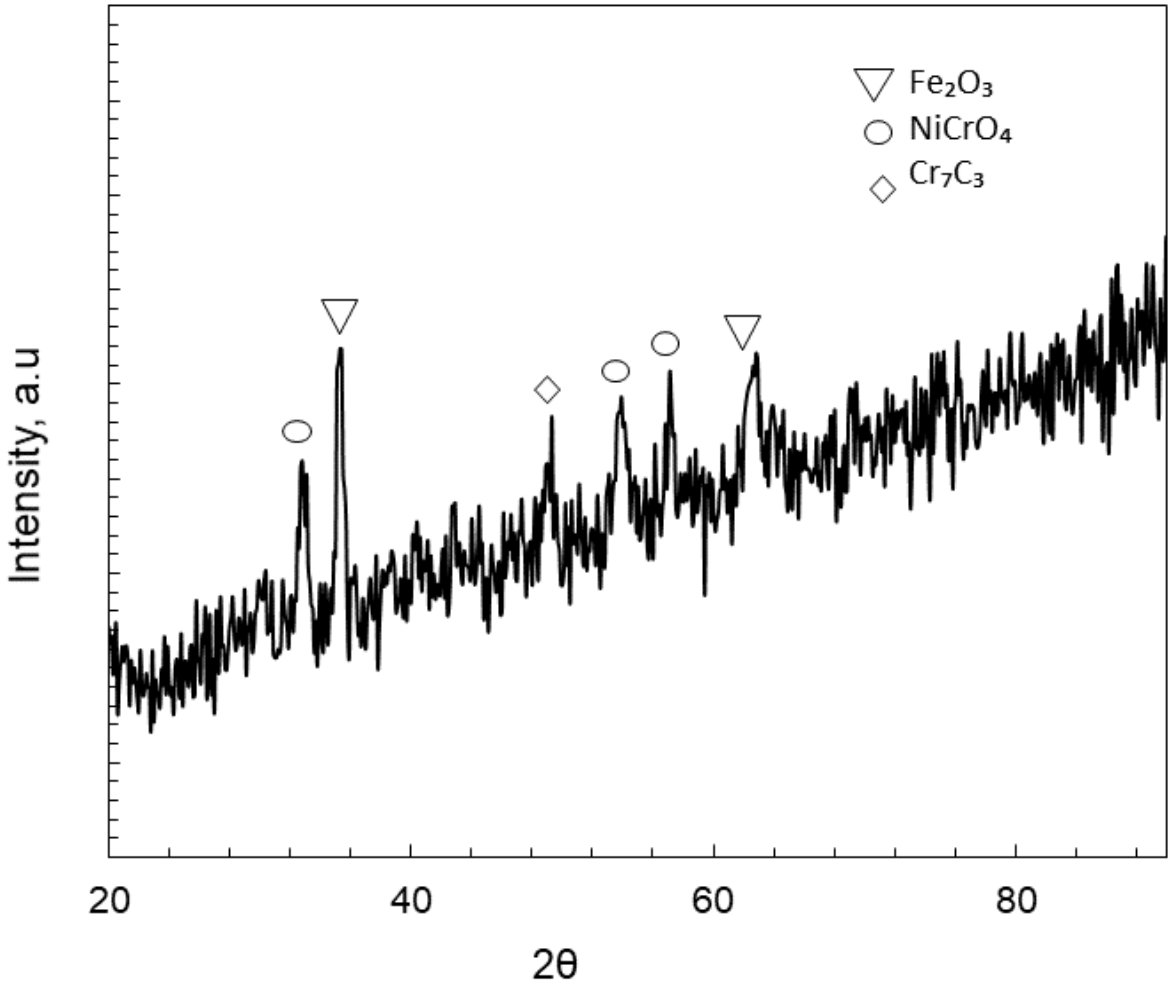

Figure 7.9: XRD pattern for the oxidized coke sample recovered after TGA-FTIR.

7.4 Conclusion

In this study, metal dusting of 316L stainless steel alloy under highly active carbonaceous gas mixture and the resulted coke formation was thoroughly investigated. Different activity tests were performed using RME-ceria and 40%Ce/Al as the catalytic agents for the generation of syngas. Using different characterization techniques, we finally proposed a time frame for the application of 316L steel for the study of RWGS reaction at elevated temperatures.

Activity test showed that 316L stainless steel does not show any reactivity towards RWGS reaction below 550°C. Furthermore, a very minute amount of CO (~2%) was detected during the empty reactor test at 600°C. The long-term stability test using an empty kinetic reactor showed that the CO does not go above 4% even after 80 h on stream at 600°C. However, under highly active carbonaceous mixtures, the activity test showed that 316L steel starts facilitating RWGS reaction due to internal carburization and metal dusting after 6 h on stream. Therefore, on the basis of this investigation, it was proposed that 316L steel is useful to study RWGS reaction below 550 for several hours, while at 600°C, a time limit of 6 h should be imposed.

Studies further confirmed that the coke that appeared on the downstream side of the kinetic reactor is formed as a result of the metal dusting. Metal dusting facilitates the decomposition of cementite that leads to producing nanometal particles. These nano metal particles acts as the catalyst for the conversion of CO to coke via Boudouard reaction. The coke grows behind the nanoparticles in a filament-like structure, leading metal particles to appear on the filaments' edges.

SEM and TGA-FTIR studies confirmed the filamentous nature of the coke formed. However, the XRD patterns confirm the presence of metal particles in the final sample obtained after the complete oxidation of the coke sample.

Chapter 8

General Conclusions, contributions, and recommendations

8.1 General Conclusions

This chapter summarizes all the key findings of this research study. First, portion of this work focuses on the application of bulk ceria prepared via RME and direct precipitation method. Results showed the excellent activity of RME-ceria for RWGS application. The second portion deals with the application of ceria-supported γ-alumina catalyst. It gives a deep insight into ceria and alumina's synergetic effect towards the reverse water gas shift reaction. The third part is the continuation of the second part. It gives a comprehensive overview for effect of calcination temperature on the different properties of the as-prepared 40%Ce/Al catalyst. Finally, the last part deals with applications of stainless steel tubes in a high carbonaceous environment. With the help of different characterization techniques, this study recommended a timeline for the long-term use of stainless steel pipes for RWG applications.

8.1.1 Highly selective CO synthesis via RWGS reaction over cerium oxide catalyst prepared via RME-Process

The first part of this Ph.D. study work is related to the application of RME prepared CeO_2 exposing (111) for conversion of CO_2 to CO via RWGS reaction. To compare the results and activity of as-prepared RME-ceria, another ceria sample was prepared using the direct precipitation method and named as DP-ceria. Catalyst were evaluated using various characterization techniques resulted in the excellent activity of RME-ceria for RWGS. The main conclusion drawn are:

1. RME process successfully developed highly porous, high surface area ceria (142 $m^2 g_{cat}^{-1}$) with exposed (111) facets with polyhedral geometry.

2. The as-prepared bulk nanoceria showed excellent CO_2 conversion ~42% at 600°C a relatively high GHSV of 60,000 ml g_{cat}^{-1} h^{-1}.
3. At a lower GHSV of 10,000 ml g_{cat}^{-1} h^{-1}, nearly equilibrium CO_2 conversion (~62%) was observed initially, which stabilizes after 60hr to around 52%.
4. XRD studies confirmed that even after exposing the RME-ceria at 600°C for several hours, the crystallite size increases from 4 nm to 11 nm, while for DP-ceria, the increase in crystallite size was quite significant i.e., from 7 nm to 21 nm. XRD studies also confirm the presence of highly reduced for of ceria, i.e., $CeO_{1.67}$.
5. SEM-EDX results showed the well-dispersed ceria and oxygen atoms all over the surface.
6. TPR studies showed that RME-ceria has more oxygen vacancies at room temperature than the DP-ceria, which confirms the high reducing abilities of the RMe-ceria.
7. TGA-FTIR studies for the spent catalyst (collected after long-term stability test) confirm zero coke in the sample. And proved the excellent coking resistance of RME-ceria.
8. Finally, the mechanistic studies confirm that RWGS follows a redox mechanism over bulk RME-ceria.

Overall, RME-ceria appeared 100%CO selectivity, with excellent coking resistance, highly stable conversion (especially at low GHSV), and resistance to deactivation

8.1.2 Selective catalytic reduction of CO_2 over nanostructured ceria supported on γ-alumina prepared via RME

This part of the study involved the application of RME prepared supported ceria over γ-alumina. To find out the optimum ceria loading, three catalysts were prepared using 20wt%, 30wt%, and 40wt% ceria over γ-alumina. The main conclusion drawn are:

1. 40%Ce/Al showed excellent activity for all the conditions tests.

2. BET-SSA showed a very high specific area achieved for all the catalysts. Especially 40%Ce/Al with an initial surface area of 292.03 m^2 g_{cat}^{-1} showed comparable activity at all the temperature and GHSV test as of RME-ceria.
3. HRSEM studies revealed the catalyst's highly porous nature and showed the cluster-like growth of alumina with ceria particles well dispersed all over the γ-alumina surface.
4. Activity tests showed that showed stable 55% conversion at low GHSV of 10,000 ml g_{cat}^{-1} h^{-1} for 100 h on stream without any coke formation or significant deactivation.
5. TGA-FTIR studies of the spent catalyst conform to the excellent coking resistance of 40%Ce/Al likewise RME-ceria.
6. The most important fact discovered during this study is the bulk-based activity of ceria. It was confirmed that even after losing 70% of surface area, 40%ce/Al catalyst showed stable conversion test for all the temperatures. This excellent conversion is an intrinsic property of ceria, and it happened due to oxygen transport in the crystal leads to form Ce^{3+} in bulk.

Finally, the 40%Ce/Al catalyst appears as the optimum formulation for RWGS applications.

8.1.3 Effect of calcination temperature on relevant active sites, their identification, and mechanistic studies over 40% RME-ceria/γ-alumina

After finding the optimum formulation for the RME-supported ceria over the γ-alumina catalyst, it was necessary to study the effect of calcination temperature on the activity and other 40%Ce/Al catalyst properties. Further, CO_2 mechanism was also determined using CO_2-TPD and *in-situ* FTIR analysis.

The main conclusions drawn are:

1. Calcination temperature directly affected the crystallite size and the BET-SSA of the as-prepared 40%Ce/Al.
2. The result showed that crystallite size increased from 5.56 nm to 16.8 nm as the calcination temperature rises from 275°C to 575°C.

3. Similarly, surface area decreased from 292.06 m^2 g_{cat}^{-1} to 239.75 m^2 g_{cat}^{-1} as the calcination temperature increased from 375°C to 575°C
4. CO_2-TPD studies showed the pre-reduction plays a vital role in enhancing the activity of the catalyst with a significant increase in active sites. A pre-reduction temperature of 400°C is necessary to start the reaction over the surface. Studies further confirm Ce/Al catalyst's bulk-based activity because of the bridge-bonded adsorption of CO_2 on the metal ions.
5. In-situ FTIR studies confirm that 40%ce/Al showed CO_2 to CO via the formate mechanism because of the presence of the γ-alumina.

Finally, it was concluded that 40%Ce/Al catalyst follows the bulk based activity process as even after losing 70% surface, the activity remained stable and prone to coking.

8.1.4 Investigation of coke formation in stainless steel reactor and metal dusting at elevated temperatures under RWGS

The final part of this Ph.D. studies focuses on the application of stainless steel in RWGS application. These investigations were taken into account when we detect a suspicious increase in the catalytic activity of as-prepared RME-ceria. The main conclusion drawn are:

1. Under highly active carbonaceous gas mixture of CO-H_2-H_2O stainless steel undergoes severe carrion knows as metal dusting. This disintegration leads to form nano metal particles that facilitate the filamentous coke formation on the steel wall.
2. SEM-EXD, XRD, and TGA-FTIR studies confirm the presence of metal particles in coke samples collected.
3. Various activity tests were performed. It was recommended that 316L stainless steel start to undergo metal dusting after exposure to 6 h on stream at a temperature above 550°C under the carbonaceous environment of H_2-CO. Below 550°C, it could be used for long-term RWGS applications.

Finally, this study could be used as a guideline for the application of stainless steel alloy used at elevated temperatures in a highly active carbonaceous environment.

8.2 Recommendations for Future Work

Based on the comprehensive study for the application of RME- based ceria for RWGS applications following recommendation could be followed to explore further

1. RME prepared supported ceria γ-alumina showed excellent activity and stability for the RWGS reaction, and this is the first study on its application for the RWGS ever studies. Therefore, it's a strong need to explore the further properties of the 40%Ce/Al catalyst using XPS, TEM, and Raman spectroscopy. This will lead to enhance its activity even at higher GHSV's.
2. In catalysis, promoters sometimes play a vital role in tunning activity and selectivity. Despite 100% selectivity, it is recommended that the Cu, CO, and Fe should be utilized to see the effect on the conversion at higher GSHV's.
3. During the course of this Ph.D. the catalyst was always synthesized in batches. However, for pilot scale and for further commercial-scale applications, the process needs to be modified to automatic or semi-automatic for quick catalyst making.
4. Considering the highly active nature of bulk RME-ceria and 40%Ce/Al catalyst a comprehensive economic analysis could be considered as a separate Ph.D. or M.Sc. project to explore its commercial applications.
5. Considering space explorations, the effect of the incoming gas mixture could be taken into account.

References

[1] B. Li, Y. Duan, D. Luebke, B. Morreale, Advances in CO_2 capture technology: A patent review, Applied Energy 102 (2013) 1439-1447

[2] C. Song, Global challenges and strategies for control, conversion and utilization of CO_2 for sustainable development involving energy, catalysis, adsorption and chemical processing, Catalysis Today 115 (2006) 2-32

[3] D.Z. Victor D. G., E. H. M. Ahmed, P. K. Dadhich, J. G. J. Olivier, H. H. Rogner, K. Sheikho, and M. Yamaguchi, Introductory Chapter. In: Climate change 2014: Mitigation of climate change. Contribution of working group III to the fifth assessment report of the intergovernmental panel on climate change [Edenhofer, O., R. Pichs-Madruga, Y. Sokona, E. Farahani, S. Kadner, K. Seyboth, A. Adler, I. Baum, S. Brunner, P. Eickemeier, B. Kriemann, J. Savolainen, S. Schlömer, C. von Stechow, T. Zwickel and J.C. Minx (eds.)] Cambridge University Press, Cambridge, United Kingdom and New York, NY, USA., 2014.

[4] M. Mikkelsen, M. Jørgensen, F.C. Krebs, The teraton challenge. A review of fixation and transformation of carbon dioxide, Energy Environ. Sci. 3 (2010) 43-81

[5] X. Xiaoding, J.A. Moulijn, Mitigation of CO_2 by Chemical Conversion: Plausible Chemical Reactions and Promising Products, Energy & Fuels 10 (1996) 305-325

[6] H. Yang, Z. Xu, M. Fan, R. Gupta, R.B. Slimane, A.E. Bland, I. Wright, Progress in carbon dioxide separation and capture: A review, Journal of Environmental Sciences 20 (2008) 14-27

[7] D. Simakov, Renewable Synthetic Fuels and Chemicals from Carbon Dioxide: Fundamentals, Catalysis, Design Considerations and Technological Challenges, 2017.

[8] G. Centi, S. Perathoner, Opportunities and prospects in the chemical recycling of carbon dioxide to fuels, Catalysis Today 148 (2009) 191-205

[9] W. Wang, S. Wang, X. Ma, J. Gong, Recent advances in catalytic hydrogenation of carbon dioxide, Chem Soc Rev 40 (2011) 3703-3727

[10] M.D. Porosoff, B. Yan, J.G. Chen, Catalytic reduction of CO_2 by H_2 for synthesis of CO, methanol and hydrocarbons: challenges and opportunities, Energy & Environmental Science 9 (2016) 62-73

[11] G. Centi, E.A. Quadrelli, S. Perathoner, Catalysis for CO_2 conversion: a key technology for rapid introduction of renewable energy in the value chain of chemical industries, Energy & Environmental Science 6 (2013)

[12] H. Yang, C. Zhang, P. Gao, H. Wang, X. Li, L. Zhong, W. Wei, Y. Sun, A review of the catalytic hydrogenation of carbon dioxide into value-added hydrocarbons, Catalysis Science & Technology 7 (2017) 4580-4598

[13] Y. Nigara, B. Cales, Production of Carbon Monoxide by Direct Thermal Splitting of Carbon Dioxide at High Temperature, Bulletin of the Chemical Society of Japan 59 (1986) 1997-2002

[14] O.-S. Joo, K.-D. Jung, I. Moon, A.Y. Rozovskii, G.I. Lin, S.-H. Han, S.-J. Uhm, Carbon Dioxide Hydrogenation To Form Methanol via a Reverse-Water-Gas-Shift Reaction (the CAMERE Process), Industrial & Engineering Chemistry Research 38 (1999) 1808-1812

[15] A. Wolf, A. Jess, C. Kern, Syngas Production via Reverse Water-Gas Shift Reaction over a Ni-Al_2O_3 Catalyst: Catalyst Stability, Reaction Kinetics, and Modeling, Chem Eng Technol 39 (2016) 1040-1048

[16] F. Bustamante, R.M. Enick, A.V. Cugini, R.P. Killmeyer, B.H. Howard, K.S. Rothenberger, M.V. Ciocco, B.D. Morreale, S. Chattopadhyay, S. Shi, High-temperature kinetics of the homogeneous reverse water-gas shift reaction, AIChE Journal 50 (2004) 1028-1041

[17] E.M. Müller-Lorenz, H.J. Grabke, Coking by metal dusting of steels, Materials and Corrosion 50 (1999) 614-621

[18] Y. Mordekovitz, L. Shelly, B.A. Rosen, S. Hayun, Surface properties of Ca, Ti-doped CeO_2 and their influence on the reverse water-gas shift reaction, Journal of the American Ceramic Society (2021)

[19] M. Konsolakis, M. Lykaki, S. Stefa, S.A.C. Carabineiro, G. Varvoutis, E. Papista, G.E. Marnellos, CO_2 Hydrogenation over Nanoceria-Supported Transition Metal Catalysts: Role of Ceria Morphology (Nanorods versus Nanocubes) and Active Phase Nature (Co versus Cu), Nanomaterials (Basel) 9 (2019)

[20] B. Dai, S. Cao, H. Xie, G. Zhou, S. Chen, Reduction of CO_2 to CO via reverse water-gas shift reaction over CeO_2 catalyst, Korean Journal of Chemical Engineering 35 (2017) 421-427

[21] Y. Liu, Z. Li, H. Xu, Y. Han, Reverse water–gas shift reaction over ceria nanocube synthesized by hydrothermal method, Catalysis Communications 76 (2016) 1-6

[22] M. Kovacevic, B.L. Mojet, J.G. van Ommen, L. Lefferts, Effects of Morphology of Cerium Oxide Catalysts for Reverse Water Gas Shift Reaction, Catalysis Letters 146 (2016) 770-777

[23] L. Chen, P. Fleming, V. Morris, J.D. Holmes, M.A. Morris, Size-Related Lattice Parameter Changes and Surface Defects in Ceria Nanocrystals, The Journal of Physical Chemistry C 114 (2010) 12909-12919

[24] Y. He, B. Yang, G. Cheng, Controlled synthesis of CeO_2 nanoparticles from the coupling route of homogenous precipitation with microemulsion, Materials Letters 57 (2003) 1880-1884

[25] T. Masui, K. Fujiwara, K.-i. Machida, G.-y. Adachi, T. Sakata, H. Mori, Characterization of Cerium(IV) Oxide Ultrafine Particles Prepared Using Reversed Micelles, Chemistry of Materials 9 (1997) 2197-2204

[26] R. Pournajaf, S.A. Hassanzadeh-Tabrizi, M. Jafari, Reverse microemulsion synthesis of CeO_2 nanopowder using polyoxyethylene(23)lauryl ether as a surfactant, Ceramics International 40 (2014) 8687-8692

[27] T.A. Boden, R.J. Andres, G. Marland, Global, Regional, and National Fossil-Fuel CO_2 Emissions (1751 - 2014) (V. 2017), (2017). Retrieved from **https://www.osti.gov/servlets/purl/1389331**

[28] Global CO_2 emission from fossil fuel combustion and some industrial process (2014). Retrieved from **https://www.epa.gov/ghgemissions/global-greenhouse-gas-emissions-data**

[29] Facility greenhouse gas reporting: overview of 2019 reported emissions. Retrieved from **https://www.canada.ca/en/environment-climate-change/services/climate-change/greenhouse-gas-emissions/facility-reporting/overview-2019.html**

[30] BP statistical review of world energy, (2020). Retrieved from **https://www.bp.com/content/dam/bp/business-sites/en/global/corporate/pdfs/energy-economics/statistical-review/bp-stats-review-2020-full-report.pdf**

[31] D.J. P. Styring, H. de Coninck, H. Reith, K. Armstrong, Carbon Capture and Utilisation in the green economy, (2011). Retrieved from **http://co2chem.co.uk/wp-content/uploads/2012/06/CCU%20in%20the%20green%20economy%20report.pdf**

[32] H.H. Khoo, J. Bu, R.L. Wong, S.Y. Kuan, P.N. Sharratt, Carbon capture and utilization: Preliminary life cycle CO_2, energy, and cost results of potential mineral carbonation, Energy Procedia 4 (2011) 2494-2501

[33] K.M. Yu, I. Curcic, J. Gabriel, S.C. Tsang, Recent advances in CO_2 capture and utilization, ChemSusChem 1 (2008) 893-899

[34] V. Havran, M.P. Duduković, C.S. Lo, Conversion of Methane and Carbon Dioxide to Higher Value Products, Industrial & Engineering Chemistry Research 50 (2011) 7089-7100

[35] R.S. Norhasyima, T.M.I. Mahlia, Advances in CO_2 utilization technology: A patent landscape review, Journal of CO_2 Utilization 26 (2018) 323-335

[36] H.H. Khoo, R.B.H. Tan, Environmental Impact Evaluation of Conventional Fossil Fuel Production (Oil and Natural Gas) and Enhanced Resource Recovery with Potential CO_2 Sequestration, Energy & Fuels 20 (2006) 1914-1924

[37] K. Damen, A. Faaij, W. Turkenburg, Health, Safety and Environmental Risks of Underground CO_2 Storage – Overview of Mechanisms and Current Knowledge, Climatic Change 74 (2006) 289-318

[38] F.D. Meylan, V. Moreau, S. Erkman, CO_2 utilization in the perspective of industrial ecology, an overview, Journal of CO_2 Utilization 12 (2015) 101-108

[39] S.-M. Lu, A global review of enhanced geothermal system (EGS), Renewable and Sustainable Energy Reviews 81 (2018) 2902-2921

[40] J.C.M. Pires, COP21: The algae opportunity?, Renewable and Sustainable Energy Reviews 79 (2017) 867-877

[41] J. Gressel, C.J.B. van der Vlugt, H.E.N. Bergmans, Environmental risks of large scale cultivation of microalgae: Mitigation of spills, Algal Research 2 (2013) 286-298

[42] P.K. Usher, A.B. Ross, M.A. Camargo-Valero, A.S. Tomlin, W.F. Gale, An overview of the potential environmental impacts of large-scale microalgae cultivation, Biofuels 5 (2014) 331-349

[43] S. Giannoulakis, K. Volkart, C. Bauer, Life cycle and cost assessment of mineral carbonation for carbon capture and storage in European power generation, International Journal of Greenhouse Gas Control 21 (2014) 140-157

[44] A.A. Olajire, A review of mineral carbonation technology in sequestration of CO_2, Journal of Petroleum Science and Engineering 109 (2013) 364-392

[45] Y. Demirel, M. Matzen, C. Winters, X. Gao, Capturing and using CO_2 as feedstock with chemical looping and hydrothermal technologies, International Journal of Energy Research 39 (2015) 1011-1047

[46] J. Wei, Q. Ge, R. Yao, Z. Wen, C. Fang, L. Guo, H. Xu, J. Sun, Directly converting CO_2 into a gasoline fuel, Nat Commun 8 (2017) 15174

[47] T. Sakakura, J.C. Choi, H. Yasuda, Transformation of carbon dioxide, Chem Rev 107 (2007) 2365-2387

[48] E.E. Benson, C.P. Kubiak, A.J. Sathrum, J.M. Smieja, Electrocatalytic and homogeneous approaches to conversion of CO_2 to liquid fuels, Chem Soc Rev 38 (2009) 89-99

[49] J. Louie, Transition Metal Catalyzed Reactions of Carbon Dioxide and Other Heterocumulenes, Current Organic Chemistry 9 (2005) 605-623

[50] M. Aresta, A. Dibenedetto, Utilisation of CO_2 as a chemical feedstock: opportunities and challenges, Dalton Trans (2007) 2975-2992

[51] Y. Sun, Chemicals from CO_2 via heterogeneous catalysis at moderate conditions, Studies in Surface Science and Catalysis - STUD SURF SCI CATAL 153 (2004) 9-16

[52] A.J. Martín, G.O. Larrazábal, J. Pérez-Ramírez, Towards sustainable fuels and chemicals through the electrochemical reduction of CO_2: lessons from water electrolysis, Green Chemistry 17 (2015) 5114-5130

[53] M. Aresta, A. Dibenedetto, A. Angelini, Catalysis for the valorization of exhaust carbon: from CO_2 to chemicals, materials, and fuels. technological use of CO_2, Chem Rev 114 (2014) 1709-1742

[54] A.A. Olajire, Recent progress on the nanoparticles-assisted greenhouse carbon dioxide conversion processes, Journal of CO_2 Utilization 24 (2018) 522-547

[55] P. Kaiser, R.B. Unde, C. Kern, A. Jess, Production of Liquid Hydrocarbons with CO_2 as Carbon Source based on Reverse Water-Gas Shift and Fischer-Tropsch Synthesis, Chemie Ingenieur Technik 85 (2013) 489-499

[56] Y.A. Daza, J.N. Kuhn, CO_2 conversion by reverse water gas shift catalysis: comparison of catalysts, mechanisms and their consequences for CO_2 conversion to liquid fuels, RSC Advances 6 (2016) 49675-49691

[57] M.P. Rohde, D. Unruh, G. Schaub, Membrane Application in Fischer−Tropsch Synthesis to Enhance CO_2 Hydrogenation, Industrial & Engineering Chemistry Research 44 (2005) 9653-9658

[58] M.P. Rohde, D. Unruh, G. Schaub, Membrane application in Fischer–Tropsch synthesis reactors—Overview of concepts, Catalysis Today 106 (2005) 143-148

[59] K. Oshima, T. Shinagawa, Y. Nogami, R. Manabe, S. Ogo, Y. Sekine, Low temperature catalytic reverse water gas shift reaction assisted by an electric field, Catalysis Today 232 (2014) 27-32

[60] F. Bustamante, R. Enick, K. Rothenberger, B. Howard, A. Cugini, M. Ciocco, Kinetic study of the reverse water gas shift reaction in high-temperature, high-pressure homogeneous systems, ACS Fuel Chem Div Prepr 47 (2002) 663-664

[61] M. Saito, K. Murata, Development of high performance Cu/ZnO-based catalysts for methanol synthesis and the water-gas shift reaction, Catalysis Surveys from Asia 8 (2004) 285-294

[62] M. Saito, M. Takeuchi, T. Fujitani, J. Toyir, S. Luo, J. Wu, H. Mabuse, K. Ushikoshi, K. Mori, T. Watanabe, Advances in joint research between NIRE and RITE for developing a novel technology for methanol synthesis from CO_2 and H_2, Applied Organometallic Chemistry 14 (2000) 763-772

[63] D. Mignard, C. Pritchard, Processes for the Synthesis of Liquid Fuels from CO_2 and Marine Energy, Chemical Engineering Research and Design 84 (2006) 828-836

[64] C.S. Chen, W.H. Cheng, S.S. Lin, Enhanced activity and stability of a Cu/SiO_2 catalyst for the reverse water gas shift reaction by an iron promoter, Chem Commun (Camb) (2001) 1770-1771

[65] J.E. Whitlow, C.F. Parrish, Operation, Modeling and Analysis of the Reverse Water Gas Shift Process, AIP Conference Proceedings 654 (2003) 1116-1123. Retrieved from **https://aip.scitation.org/doi/abs/10.1063/1.1541409**

[66] D. VanderWiel, J. Zilka, Y. Wang, A. Tonkovich, R. Wegeng, Carbon Dioxide Conversions in Microreactors, (2000)

[67] C. Bosch, W. Wild, Hydrogen Production, Journal of Industrial & Engineering Chemistry 7 (1915) 83-83

[68] D.S. Mallapragada, N.R. Singh, V. Curteanu, R. Agrawal, Sun-to-Fuel Assessment of Routes for Fixing CO_2 as Liquid Fuel, Industrial & Engineering Chemistry Research 52 (2013) 5136-5144

[69] F.T. Zangeneh, S. Sahebdelfar, M.T. Ravanchi, Conversion of carbon dioxide to valuable petrochemicals: An approach to clean development mechanism, Journal of Natural Gas Chemistry 20 (2011) 219-231

[70] M. Stanbury, J.-D. Compain, M. Trejo, P. Smith, E. Gouré, S. Chardon-Noblat, Mn-carbonyl molecular catalysts containing a redox-active phenanthroline-5,6-dione for selective electro- and photoreduction of CO_2 to CO or HCOOH, Electrochimica Acta 240 (2017) 288-299

[71] F. Cao, Liu, D., Hou, Q., Fang, D., Thermodynamic Analysis of CO_2 Direct Hydrogenation Reactions, (2001) J. Nat. Gas Chem., 10 (1), pp. 24-33 (2001)

[72] J.J. Carberry, Chemical and catalytic reaction engineering, McGraw-Hill, New York, 1976.

[73] X. Su, X. Yang, B. Zhao, Y. Huang, Designing of highly selective and high-temperature endurable RWGS heterogeneous catalysts: recent advances and the future directions, Journal of Energy Chemistry 26 (2017) 854-867

[74] X. Chen, X. Su, H. Duan, B. Liang, Y. Huang, T. Zhang, Catalytic performance of the Pt/TiO_2 catalysts in reverse water gas shift reaction: Controlled product selectivity and a mechanism study, Catalysis Today 281 (2017) 312-318

[75] S. Kattel, B. Yan, J.G. Chen, P. Liu, CO_2 hydrogenation on Pt, Pt/SiO_2 and Pt/TiO_2: Importance of synergy between Pt and oxide support, Journal of Catalysis 343 (2016) 115-126

[76] M.D. Porosoff, J.G. Chen, Trends in the catalytic reduction of CO_2 by hydrogen over supported monometallic and bimetallic catalysts, Journal of Catalysis 301 (2013) 30-37

[77] S.S. Kim, H.H. Lee, S.C. Hong, A study on the effect of support's reducibility on the reverse water-gas shift reaction over Pt catalysts, Applied Catalysis A: General 423-424 (2012) 100-107

[78] P. Zhang, M. Chi, S. Sharma, E. McFarland, Silica encapsulated heterostructure catalyst of Pt nanoclusters on hematite nanocubes: synthesis and reactivity, Journal of Materials Chemistry 20 (2010)

[79] I. Ro, C. Sener, T.M. Stadelman, M.R. Ball, J.M. Venegas, S.P. Burt, I. Hermans, J.A. Dumesic, G.W. Huber, Measurement of intrinsic catalytic activity of Pt monometallic and $Pt\text{-}MoO_x$ interfacial sites over visible light enhanced $PtMoO_x/SiO_2$ catalyst in reverse water gas shift reaction, Journal of Catalysis 344 (2016) 784-794

[80] X. Yang, X. Su, X. Chen, H. Duan, B. Liang, Q. Liu, X. Liu, Y. Ren, Y. Huang, T. Zhang, Promotion effects of potassium on the activity and selectivity of Pt/zeolite catalysts for reverse water gas shift reaction, Applied Catalysis B: Environmental 216 (2017) 95-105

[81] K. Kitamura Bando, K. Soga, K. Kunimori, H. Arakawa, Effect of Li additive on CO_2 hydrogenation reactivity of zeolite supported Rh catalysts, Applied Catalysis A: General 175 (1998) 67-81

[82] D. Heyl, U. Rodemerck, U. Bentrup, Mechanistic Study of Low-Temperature CO_2 Hydrogenation over Modified Rh/Al_2O_3 Catalysts, 6 (2016) 6275-6284

[83] R. Carrasquillo-Flores, I. Ro, M.D. Kumbhalkar, S. Burt, C.A. Carrero, A.C. Alba-Rubio, J.T. Miller, I. Hermans, G.W. Huber, J.A. Dumesic, Reverse Water-Gas Shift on Interfacial Sites Formed by Deposition of Oxidized Molybdenum Moieties onto Gold Nanoparticles, J Am Chem Soc 137 (2015) 10317-10325

[84] J.A. Rodriguez, J. Evans, L. Feria, A.B. Vidal, P. Liu, K. Nakamura, F. Illas, CO_2 hydrogenation on Au/TiC, Cu/TiC, and Ni/TiC catalysts: Production of CO, methanol, and methane, Journal of Catalysis 307 (2013) 162-169

[85] R.A. Koeppel, A. Baiker, C. Schild, A. Wokaun, Carbon dioxide hydrogenation over Au/ZrO_2 catalysts from amorphous precursors: catalytic reaction mechanism, Journal of the Chemical Society, Faraday Transactions 87 (1991)

[86] A.A. Upadhye, I. Ro, X. Zeng, H.J. Kim, I. Tejedor, M.A. Anderson, J.A. Dumesic, G.W. Huber, Plasmon-enhanced reverse water gas shift reaction over oxide supported Au catalysts, Catalysis Science & Technology 5 (2015) 2590-2601

[87] G. Aguila, A. Valenzuela, S. Guerrero, P. Araya, WGS activity of a novel Cu–ZrO_2 catalyst prepared by a reflux method. Comparison with a conventional impregnation method, Catalysis Communications 39 (2013) 82-85

[88] O. Jakdetchai, T. Nakajima, Mechanism of the water–gas shift reaction over Cu(110), Cu(111) and Cu(100) surfaces: an AM1-d study, Journal of Molecular Structure: THEOCHEM 619 (2002) 51-58

[89] D.-W. Jeong, H.-S. Na, J.-O. Shim, W.-J. Jang, H.-S. Roh, U.H. Jung, W.L. Yoon, Hydrogen production from low temperature WGS reaction on co-precipitated Cu–CeO_2 catalysts: An optimization of Cu loading, International Journal of Hydrogen Energy 39 (2014) 9135-9142

[90] E.L. Kunkes, F. Studt, F. Abild-Pedersen, R. Schlögl, M. Behrens, Hydrogenation of CO_2 to methanol and CO on Cu/ZnO/Al_2O_3: Is there a common intermediate or not?, Journal of Catalysis 328 (2015) 43-48

[91] S. Kattel, B. Yan, Y. Yang, J.G. Chen, P. Liu, Optimizing Binding Energies of Key Intermediates for CO_2 Hydrogenation to Methanol over Oxide-Supported Copper, J Am Chem Soc 138 (2016) 12440-12450

[92] D.L. Jurković, A. Pohar, V.D.B.C. Dasireddy, B. Likozar, Effect of Copper-based Catalyst Support on Reverse Water-Gas Shift Reaction (RWGS) Activity for CO_2

Reduction, Chem Eng Technol 40 (2017) 973-980

[93] F.S. Stone, Cu–ZnO and Cu–ZnO/Al_2O_3 Catalysts for the Reverse Water-Gas Shift Reaction. The Effect of the Cu/Zn Ratio on Precursor Characteristics and on the Activity of the Derived Catalysts, Topics in Catalysis 22 (2003) 305-318

[94] C.S. Chen, W.H. Cheng, S.S. Lin, Mechanism of CO formation in reverse water–gas shift reaction over Cu/Al_2O_3 catalyst, Catalysis Letters 68 (2000) 45-48

[95] C.-S. Chen, W.-H. Cheng, Study on the Mechanism of CO Formation in Reverse

Water Gas Shift Reaction Over Cu/SiO_2 Catalyst by Pulse Reaction, TPD and TPR, Catalysis Letters 83 (2002) 121-126

[96] C.S. Chen, J.H. Wu, T.W. Lai, Carbon Dioxide Hydrogenation on Cu Nanoparticles, The Journal of Physical Chemistry C 114 (2010) 15021-15028

[97] D.H. Kim, S.W. Han, H.S. Yoon, Y.D. Kim, Reverse water gas shift reaction catalyzed by Fe nanoparticles with high catalytic activity and stability, Journal of Industrial and Engineering Chemistry 23 (2015) 67-71

[98] J.A. Loiland, M.J. Wulfers, N.S. Marinkovic, R.F. Lobo, Fe/γ-Al_2O_3 and Fe–K/γ-Al_2O_3 as reverse water-gas shift catalysts, Catalysis Science & Technology 6 (2016) 5267-5279

[99] X.F. Yang, A. Wang, B. Qiao, J. Li, J. Liu, T. Zhang, Single-atom catalysts: a new frontier in heterogeneous catalysis, Acc Chem Res 46 (2013) 1740-1748

[100] B. Qiao, A. Wang, X. Yang, L.F. Allard, Z. Jiang, Y. Cui, J. Liu, J. Li, T. Zhang, Single-atom catalysis of CO oxidation using Pt1/FeO_x, Nat Chem 3 (2011) 634-641

[101] J.C. Matsubu, V.N. Yang, P. Christopher, Isolated metal active site concentration and stability control catalytic CO_2 reduction selectivity, J Am Chem Soc 137 (2015) 3076-3084

[102] J.H. Kwak, L. Kovarik, J. Szanyi, Heterogeneous Catalysis on Atomically Dispersed Supported Metals: CO_2 Reduction on Multifunctional Pd Catalysts, ACS Catalysis 3 (2013) 2094-2100

[103] R.B. Levy, M. Boudart, Platinum-like behavior of tungsten carbide in surface catalysis, Science 181 (1973) 547-549

[104] M.D. Porosoff, S. Kattel, W. Li, P. Liu, J.G. Chen, Identifying trends and descriptors for selective CO_2 conversion to CO over transition metal carbides, Chem Commun (Camb) 51 (2015) 6988-6991

[105] X. Liu, C. Kunkel, P. Ramírez de la Piscina, N. Homs, F. Viñes, F. Illas, Effective and Highly Selective CO Generation from CO_2 Using a Polycrystalline α-Mo_2C Catalyst, ACS Catalysis 7 (2017) 4323-4335

[106] W. Xu, P.J. Ramírez, D. Stacchiola, J.L. Brito, J.A. Rodriguez, The Carburization of Transition Metal Molybdates ($MxMoO_4$, M = Cu, Ni or Co) and the Generation of Highly Active Metal/Carbide Catalysts for CO_2 Hydrogenation, Catalysis Letters 145 (2015) 1365-1373

[107] X. Zhang, X. Zhu, L. Lin, S. Yao, M. Zhang, X. Liu, X. Wang, Y.-W. Li, C. Shi, D. Ma, Highly Dispersed Copper over β-Mo_2C as an Efficient and Stable Catalyst for the Reverse Water Gas Shift (RWGS) Reaction, ACS Catalysis 7 (2016) 912-918

[108] O.S. Joo, K.D. Jung, Stability of $ZnAl_2O_4$ catalyst for reverse-water-gas-shift reaction (RWGSR), Bulletin of the Korean Chemical Society 24 (2003) 86-90

[109] S.-W. Park, O.-S. Joo, K.-D. Jung, H. Kim, S.-H. Han, Development of ZnO/Al_2O_3 catalyst for reverse-water-gas-shift reaction of CAMERE (carbon dioxide hydrogenation to form methanol via a reverse-water-gas-shift reaction) process, Applied Catalysis A: General 211 (2001) 81-90

[110] L.d.R. Silva-Calpa, P.C. Zonetti, C.P. Rodrigues, O.C. Alves, L.G. Appel, R.R. de Avillez, The $Zn_xZr_{1-x}O_{2-y}$ solid solution on m-ZrO_2: Creating O vacancies and improving the m-ZrO_2 redox properties, Journal of Molecular Catalysis A: Chemical 425 (2016) 166-173

[111] P.C. Zonetti, S. Letichevsky, A.B. Gaspar, E.F. Sousa-Aguiar, L.G. Appel, The $NixCe_{0.75}Zr_{0.25-x}O_2$ solid solution and the RWGS, Applied Catalysis A: General 475 (2014) 48-54

[112] M. Wenzel, N.V.R. Aditya Dharanipragada, V.V. Galvita, H. Poelman, G.B. Marin, L. Rihko-Struckmann, K. Sundmacher, CO production from CO_2 via reverse water–gas shift reaction performed in a chemical looping mode: Kinetics on modified iron oxide, Journal of CO_2 Utilization 17 (2017) 60-68

[113] D.H. Kim, J.L. Park, E.J. Park, Y.D. Kim, S. Uhm, Dopant Effect of Barium Zirconate-Based Perovskite-Type Catalysts for the Intermediate-Temperature Reverse Water Gas Shift Reaction, ACS Catalysis 4 (2014) 3117-3122

[114] W. Wang, Y. Zhang, Z. Wang, J.-m. Yan, Q. Ge, C.-j. Liu, Reverse water gas shift over In_2O_3 – CeO_2 catalysts, Catalysis Today 259 (2016) 402-408

[115] B. Bulfin, A.J. Lowe, K.A. Keogh, B.E. Murphy, O. Lübben, S.A. Krasnikov, I.V. Shvets, Analytical Model of CeO_2 Oxidation and Reduction, The Journal of Physical Chemistry C 117 (2013) 24129-24137

[116] T. Inoue, T. Iizuka, K. Tanabe, Hydrogenation of carbon dioxide and carbon monoxide over supported rhodium catalysts under 10 bar pressure, Applied Catalysis 46 (1989) 1-9

[117] S. Fujita, Mechanism of the reverse water gas shift reaction over Cu/ZnO catalyst*1, Journal of Catalysis 134 (1992) 220-225

[118] D.J. Pettigrew, D.L. Trimm, N.W. Cant, The effects of rare earth oxides on the reverse water-gas shift reaction on palladium/alumina, Catalysis Letters 28 (1994) 313-319

[119] M.J.L. Ginés, A.J. Marchi, C.R. Apesteguía, Kinetic study of the reverse water-gas shift reaction over $CuO/ZnO/Al_2O_3$ catalysts, Applied Catalysis A: General 154 (1997) 155-171

[120] Y. Liu, D. Liu, Study of bimetallic $Cu–Ni/\gamma\text{-}Al_2O_3$ catalysts for carbon dioxide hydrogenation, International Journal of Hydrogen Energy 24 (1999) 351-354

[121] H. Kusama, K.K. Bando, K. Okabe, H. Arakawa, CO_2 hydrogenation reactivity and structure of Rh/SiO_2 catalysts prepared from acetate, chloride and nitrate precursors, Applied Catalysis A: General 205 (2001) 285-294

[122] C.-S. Chen, W.-H. Cheng, S.-S. Lin, Study of reverse water gas shift reaction by TPD, TPR and CO_2 hydrogenation over potassium-promoted Cu/SiO_2 catalyst, Applied Catalysis A: General 238 (2003) 55-67

[123] C. Chen, Study of iron-promoted Cu/SiO_2 catalyst on high temperature reverse water gas shift reaction, Applied Catalysis A: General 257 (2004) 97-106

[124] A. Goguet, F.C. Meunier, D. Tibiletti, J.P. Breen, R. Burch, Spectrokinetic Investigation of Reverse Water-Gas-Shift Reaction Intermediates over a Pt/CeO_2 Catalyst, The Journal of Physical Chemistry B 108 (2004) 20240-20246

[125] L. Wang, S. Zhang, Y. Liu, Reverse water gas shift reaction over Co-precipitated $Ni\text{-}CeO_2$ catalysts, Journal of Rare Earths 26 (2008) 66-70

[126] R.W. Dorner, D.R. Hardy, F.W. Williams, H.D. Willauer, Effects of ceria-doping on a CO_2 hydrogenation iron–manganese catalyst, Catalysis Communications 11 (2010) 816-819

[127] M.R. Gogate, R.J. Davis, Comparative study of CO and CO_2 hydrogenation over supported Rh–Fe catalysts, Catalysis Communications 11 (2010) 901-906

[128] S. Alayoglu, S.K. Beaumont, F. Zheng, V.V. Pushkarev, H. Zheng, V. Iablokov, Z. Liu, J. Guo, N. Kruse, G.A. Somorjai, CO_2 Hydrogenation Studies on Co and CoPt Bimetallic Nanoparticles Under Reaction Conditions Using TEM, XPS and NEXAFS, Topics in Catalysis 54 (2011) 778-785

[129] S.S. Kim, H.H. Lee, S.C. Hong, The effect of the morphological characteristics of TiO_2 supports on the reverse water–gas shift reaction over Pt/TiO_2 catalysts, Applied Catalysis B: Environmental 119-120 (2012) 100-108

[130] B. Zhao, Y.-x. Pan, C.-j. Liu, The promotion effect of CeO_2 on CO_2 adsorption and hydrogenation over Ga_2O_3, Catalysis Today 194 (2012) 60-64

[131] A.G. Kharaji, A. Shariati, M.A. Takassi, A Novel γ-Alumina Supported Fe-Mo Bimetallic Catalyst for Reverse Water Gas Shift Reaction, Chinese Journal of Chemical Engineering 21 (2013) 1007-1014

[132] B. Lu, K. Kawamoto, Preparation of monodispersed NiO particles in SBA-15, and its enhanced selectivity for reverse water gas shift reaction, Journal of Environmental Chemical Engineering 1 (2013) 300-309

[133] L. Wang, H. Liu, Y. Liu, Y. Chen, S. Yang, Effect of precipitants on Ni-CeO_2 catalysts prepared by a co-precipitation method for the reverse water-gas shift reaction, Journal of Rare Earths 31 (2013) 969-974

[134] B. Lu, K. Kawamoto, Preparation of mesoporous CeO_2 and monodispersed NiO particles in CeO_2, and enhanced selectivity of NiO/CeO_2 for reverse water gas shift reaction, Materials Research Bulletin 53 (2014) 70-78

[135] M.D. Porosoff, X. Yang, J.A. Boscoboinik, J.G. Chen, Molybdenum Carbide as Alternative Catalysts to Precious Metals for Highly Selective Reduction of CO_2 to CO, Angewandte Chemie 126 (2014) 6823-6827

[136] R. Büchel, A. Baiker, S.E. Pratsinis, Effect of Ba and K addition and controlled spatial deposition of Rh in Rh/Al_2O_3 catalysts for CO_2 hydrogenation, Applied Catalysis A: General 477 (2014) 93-101

[137] A.G. Kharaji, A. Shariati, M. Ostadi, Development of Ni-Mo/Al_2O_3 catalyst for reverse water gas shift (RWGS) reaction, J Nanosci Nanotechnol 14 (2014) 6841-6847

[138] F.-m. Sun, C.-f. Yan, Z.-d. Wang, C.-q. Guo, S.-l. Huang, Ni/Ce–Zr–O catalyst for high CO_2 conversion during reverse water gas shift reaction (RWGS), International Journal of Hydrogen Energy 40 (2015) 15985-15993

[139] B. Dai, G. Zhou, S. Ge, H. Xie, Z. Jiao, G. Zhang, K. Xiong, CO_2 reverse water-gas shift reaction on mesoporous M-CeO_2 catalysts, The Canadian Journal of Chemical Engineering 95 (2017) 634-642

[140] L. Wang, H. Liu, Y. Chen, S. Yang, Reverse water–gas shift reaction over co-precipitated Co–CeO_2 catalysts: Effect of Co content on selectivity and carbon formation, International Journal of Hydrogen Energy 42 (2017) 3682-3689

[141] L. Pastor-Pérez, F. Baibars, E. Le Sache, H. Arellano-García, S. Gu, T.R. Reina, CO_2 valorisation via Reverse Water-Gas Shift reaction using advanced Cs doped Fe-Cu/Al_2O_3 catalysts, Journal of CO_2 Utilization 21 (2017) 423-428

[142] X. Chen, X. Su, H.-Y. Su, X. Liu, S. Miao, Y. Zhao, K. Sun, Y. Huang, T. Zhang, Theoretical Insights and the Corresponding Construction of Supported Metal Catalysts for Highly Selective CO_2 to CO Conversion, ACS Catalysis 7 (2017) 4613-4620

[143] B. Liang, H. Duan, X. Su, X. Chen, Y. Huang, X. Chen, J.J. Delgado, T. Zhang, Promoting role of potassium in the reverse water gas shift reaction on Pt/mullite catalyst, Catalysis Today 281 (2017) 319-326

[144] G. Zhou, B. Dai, H. Xie, G. Zhang, K. Xiong, X. Zheng, CeCu composite catalyst for CO synthesis by reverse water–gas shift reaction: Effect of Ce/Cu mole ratio, Journal of CO_2 Utilization 21 (2017) 292-301

[145] G. Yin, X. Yuan, X. Du, W. Zhao, Q. Bi, F. Huang, Efficient Reduction of CO_2 to CO Using Cobalt-Cobalt Oxide Core-Shell Catalysts, Chemistry 24 (2018) 2157-2163

[146] K. Zhao, Q. Bkour, X. Hou, S.W. Kang, J.C. Park, M.G. Norton, J.-I. Yang, S. Ha, Reverse water gas shift reaction over $CuFe/Al_2O_3$ catalyst in solid oxide electrolysis cell, Chemical Engineering Journal 336 (2018) 20-27

[147] L. Lin, S. Yao, Z. Liu, F. Zhang, N. Li, D. Vovchok, A. Martínez-Arias, R. Castañeda, J. Lin, S.D. Senanayake, D. Su, D. Ma, J.A. Rodriguez, In Situ Characterization of Cu/CeO_2 Nanocatalysts for CO_2 Hydrogenation: Morphological Effects of Nanostructured Ceria on the Catalytic Activity, The Journal of Physical Chemistry C 122 (2018) 12934-12943

[148] L.F. Bobadilla, J.L. Santos, S. Ivanova, J.A. Odriozola, A. Urakawa, Unravelling the Role of Oxygen Vacancies in the Mechanism of the Reverse Water–Gas Shift Reaction by Operando DRIFTS and Ultraviolet–Visible Spectroscopy, ACS Catalysis 8 (2018) 7455-7467

[149] L. Yang, L. Pastor-Pérez, S. Gu, A. Sepúlveda-Escribano, T.R. Reina, Highly efficient Ni/CeO_2-Al_2O_3 catalysts for CO_2 upgrading via reverse water-gas shift: Effect of selected transition metal promoters, Applied Catalysis B: Environmental 232 (2018) 464-471

[150] C. Panaritis, M. Edake, M. Couillard, R. Einakchi, E.A. Baranova, Insight towards the role of ceria-based supports for reverse water gas shift reaction over RuFe nanoparticles, Journal of CO_2 Utilization 26 (2018) 350-358

[151] M. Ronda-Lloret, S. Rico-Francés, A. Sepúlveda-Escribano, E.V. Ramos-Fernandez, $CuOx/CeO_2$ catalyst derived from metal organic framework for reverse water-gas shift reaction, Applied Catalysis A: General 562 (2018) 28-36

[152] A. Ranjbar, A. Irankhah, S.F. Aghamiri, Reverse water gas shift reaction and CO_2 mitigation: nanocrystalline MgO as a support for nickel based catalysts, Journal of Environmental Chemical Engineering 6 (2018) 4945-4952

[153] Y. Tao, Y. Zhu, C. Liu, H. Yue, J. Ji, S. Yuan, W. Jiang, B. Liang, A highly selective Cr/ZrO_2 catalyst for the reverse water-gas shift reaction prepared from simulated Cr-containing wastewater by a photocatalytic deposition process with ZrO_2, Journal of Environmental Chemical Engineering 6 (2018) 6761-6770

[154] A. Aitbekova, L. Wu, C.J. Wrasman, A. Boubnov, A.S. Hoffman, E.D. Goodman, S.R. Bare, M. Cargnello, Low-Temperature Restructuring of CeO_2-Supported Ru Nanoparticles Determines Selectivity in CO_2 Catalytic Reduction, J Am Chem Soc 140 (2018) 13736-13745

[155] L. Wang, H. Liu, Mesoporous $Co\text{-}CeO_2$ catalyst prepared by colloidal solution combustion method for reverse water-gas shift reaction, Catalysis Today 316 (2018) 155-161

[156] L. Pastor-Pérez, M. Shah, E. le Saché, T. Ramirez Reina, Improving Fe/Al_2O_3 Catalysts for the Reverse Water-Gas Shift Reaction: On the Effect of Cs as Activity/Selectivity Promoter, Catalysts 8 (2018)

[157] S.-C. Yang, S.H. Pang, T.P. Sulmonetti, W.-N. Su, J.-F. Lee, B.-J. Hwang, C.W. Jones, Synergy between Ceria Oxygen Vacancies and Cu Nanoparticles Facilitates the Catalytic Conversion of CO_2 to CO under Mild Conditions, ACS Catalysis 8 (2018) 12056-12066

[158] K.P. Reddy, S. Dama, N.B. Mhamane, M.K. Ghosalya, T. Raja, C.V. Satyanarayana, C.S. Gopinath, Molybdenum carbide catalyst for the reduction of CO_2 to CO: surface science aspects by NAPPES and catalysis studies, Dalton Trans 48 (2019) 12199-12209

[159] L. Lin, S. Yao, N. Rui, L. Han, F. Zhang, C.A. Gerlak, Z. Liu, J. Cen, L. Song, S.D. Senanayake, H.L. Xin, J.G. Chen, J.A. Rodriguez, Conversion of CO_2 on a highly active and stable Cu/FeOx/CeO_2 catalyst: tuning catalytic performance by oxide-oxide interactions, Catalysis Science & Technology 9 (2019) 3735-3742

[160] S.M. Lee, H.K. Eom, S.S. Kim, A study on the effect of CeO_2 addition to a Pt/TiO_2 catalyst on the reverse water gas shift reaction, Environ Technol (2019) 1-27

[161] Y. Yu, R. Jin, J. Easa, W. Lu, M. Yang, X. Liu, Y. Xing, Z. Shi, Highly active and stable copper catalysts derived from copper silicate double-shell nanofibers with strong metal-support interactions for the RWGS reaction, Chem Commun (Camb) 55 (2019) 4178-4181

[162] Y. Han, H. Xu, Y. Su, Z.-l. Xu, K. Wang, W. Wang, Noble metal (Pt, Au@Pd) nanoparticles supported on metal organic framework (MOF-74) nanoshuttles as high-selectivity CO_2 conversion catalysts, Journal of Catalysis 370 (2019) 70-78

[163] S. Sengupta, A. Jha, P. Shende, R. Maskara, A.K. Das, Catalytic performance of Co and Ni doped Fe-based catalysts for the hydrogenation of CO_2 to CO via reverse water-gas shift reaction, Journal of Environmental Chemical Engineering 7 (2019)

[164] Y. Shen, Z. Cao, Z. Xiao, An Efficient Support-Free Nanoporous Co Catalyst for Reverse Water–Gas Shift Reaction, Catalysts 9 (2019)

[165] S. Zhuang, N. Han, T. Wang, X. Meng, B. Meng, Y. Li, J. Sunarso, S. Liu, Enhanced CO selectivity for reverse water-gas shift reaction using Ti_4O_7-doped $SrCe_{0.9}Y_{0.1}O_{3-\delta}$ hollow fibre membrane reactor, The Canadian Journal of Chemical Engineering 97 (2019) 1619-1626

[166] X. Lu, Y. Liu, Y. He, A.N. Kuhn, P.C. Shih, C.J. Sun, X. Wen, C. Shi, H. Yang, Cobalt-Based Nonprecious Metal Catalysts Derived from Metal-Organic Frameworks for High-Rate Hydrogenation of Carbon Dioxide, ACS Appl Mater Interfaces 11 (2019) 27717-27726

[167] Y. Zhuang, R. Currie, K.B. McAuley, D.S.A. Simakov, Highly-selective CO_2 conversion via reverse water gas shift reaction over the 0.5wt% Ru-promoted Cu/ZnO/Al_2O_3 catalyst, Applied Catalysis A: General 575 (2019) 74-86

[168] Q. Zhang, L. Pastor-Pérez, W. Jin, S. Gu, T.R. Reina, Understanding the promoter effect of Cu and Cs over highly effective β-Mo_2C catalysts for the reverse water-gas shift reaction, Applied Catalysis B: Environmental 244 (2019) 889-898

[169] Chou, Loiland, Lobo, Reverse Water-Gas Shift Iron Catalyst Derived from Magnetite, Catalysts 9 (2019)

[170] Y. He, K.R. Yang, Z. Yu, Z.S. Fishman, L.A. Achola, Z.M. Tobin, J.A. Heinlein, S. Hu, S.L. Suib, V.S. Batista, L.D. Pfefferle, Catalytic manganese oxide nanostructures for the reverse water gas shift reaction, Nanoscale 11 (2019) 16677-16688

[171] A. Ranjbar, A. Irankhah, S.F. Aghamiri, Catalytic activity of rare earth and alkali metal promoted (Ce, La, Mg, K) Ni/Al_2O_3 nanocatalysts in reverse water gas shift reaction, Research on Chemical Intermediates 45 (2019) 5125-5141

[172] Y.K. Suneetha, S. Siddiqui, Synthesis and Characterization of Nanosize Catalyst for the RWGS Process and Performance Examination using a Pilot-Scale High-Pressure Reactor, International Journal of Innovative Technology and Exploring Engineering 9 (2019) 5215-5220

[173] Y. Shen, Z. Xiao, J. Liu, Z. Wang, Facile Preparation of Inverse Nanoporous Cr_2O_3/Cu Catalysts for Reverse Water-Gas Shift Reaction, ChemCatChem 11 (2019) 5439-5443

[174] P.S. Murthy, Z. Wang, L. Wang, J. Zhao, Z. Wang, W. Liang, J. Huang, Improved CO_2 Hydrogenation on Ni–ZnO/MCM-41 Catalysts with Cooperative Ni and ZnO Sites, Energy & Fuels 34 (2020) 16320-16329

[175] C.A.H. Price, L. Pastor-Perez, T.R. Reina, J. Liu, Yolk-Shell structured NiCo@SiO_2 nanoreactor for CO_2 upgrading via reverse water-gas shift reaction, Catalysis Today (2020)

[176] Z. Sakhaei, M. Rezaei, Mechanochemical synthesis of ZnO.Al_2O_3 powders with various Zn/Al molar ratios and their applications in reverse water-gas shift reaction, Environ Sci Pollut Res Int (2020)

[177] J.R. Morse, M. Juneau, J.W. Baldwin, M.D. Porosoff, H.D. Willauer, Alkali promoted tungsten carbide as a selective catalyst for the reverse water gas shift reaction, Journal of CO_2 Utilization 35 (2020) 38-46

[178] X. Hu, X. Hu, Q. Guan, W. Li, Adjusting the active sites of Cu and ZnO by coordination effect of H_3BTC and its influence on enhanced RWGS reaction, Sustainable Energy & Fuels 4 (2020) 2937-2949

[179] E. le Saché, L. Pastor-Pérez, B.J. Haycock, J.J. Villora-Picó, A. Sepúlveda-Escribano, T.R. Reina, Switchable Catalysts for Chemical CO_2 Recycling: A Step Forward in the Methanation and Reverse Water–Gas Shift Reactions, ACS Sustainable Chemistry & Engineering 8 (2020) 4614-4622

[180] L. Yang, L. Pastor-Pérez, J.J. Villora-Pico, S. Gu, A. Sepúlveda-Escribano, T.R. Reina, CO_2 valorisation via reverse water-gas shift reaction using promoted Fe/CeO_2-Al_2O_3 catalysts: Showcasing the potential of advanced catalysts to explore new processes design, Applied Catalysis A: General 593 (2020)

[181] A. Okemoto, M.R. Harada, T. Ishizaka, N. Hiyoshi, K. Sato, Catalytic performance of MoO_3/FAU zeolite catalysts modified by Cu for reverse water gas shift reaction, Applied Catalysis A: General 592 (2020)

[182] Z. Zhen, W. Tang, W. Chu, T. Zhang, L. Lv, S. Tang, Microemulsion solventing-out co-precipitation strategy for fabricating highly active Cu–ZnO/Al_2O_3 dual site catalysts for reverse water gas shift, Catalysis Science & Technology 10 (2020) 2343-2352

[183] G. Zhou, F. Xie, L. Deng, G. Zhang, H. Xie, Supported mesoporous Cu/$CeO_{2-\delta}$ catalyst for CO_2 reverse water–gas shift reaction to syngas, International Journal of Hydrogen Energy 45 (2020) 11380-11393

[184] Y. Zhang, L. Liang, Z. Chen, J. Wen, W. Zhong, S. Zou, M. Fu, L. Chen, D. Ye, Highly efficient Cu/CeO_2-hollow nanospheres catalyst for the reverse water-gas shift reaction: Investigation on the role of oxygen vacancies through in situ UV-Raman and DRIFTS, Applied Surface Science 516 (2020)

[185] J. Wen, C. Huang, Y. Sun, L. Liang, Y. Zhang, Y. Zhang, M. Fu, J. Wu, L. Chen, D. Ye, The Study of Reverse Water Gas Shift Reaction Activity over Different Interfaces: The Design of Cu-Plate ZnO Model Catalysts, Catalysts 10 (2020)

[186] Y. Ma, Z. Guo, Q. Jiang, K.-H. Wu, H. Gong, Y. Liu, Molybdenum carbide clusters for thermal conversion of CO_2 to CO via reverse water-gas shift reaction, Journal of Energy Chemistry 50 (2020) 37-43

[187] X. Liu, A. Pajares, D.J.D. Calinao Matienzo, P. Ramírez de la Piscina, N. Homs, Preparation and characterization of bulk Mo_XC catalysts and their use in the reverse water-gas shift reaction, Catalysis Today 356 (2020) 384-389

[188] B. Lu, Z. Zhang, X. Li, C. Luo, Y. Xu, L. Zhang, High-efficiency CuCe(rod) catalysts for CO_2 hydrogenation with high Cu content, Fuel 276 (2020)

[189] A.H. Braga, N.J.S. Costa, K. Philippot, R.V. Gonçalves, J. Szanyi, L.M. Rossi, Structure and activity of supported bimetallic NiPd nanoparticles: influence of preparation method on CO_2 reduction, ChemCatChem 12 (2020) 2967-2976

[190] D. Vovchok, C. Zhang, S. Hwang, L. Jiao, F. Zhang, Z. Liu, S.D. Senanayake, J.A. Rodriguez, Deciphering Dynamic Structural and Mechanistic Complexity in Cu/CeO_2/ZSM-5 Catalysts for the Reverse Water-Gas Shift Reaction, ACS Catalysis 10 (2020) 10216-10228

[191] M. Juneau, M. Vonglis, J. Hartvigsen, L. Frost, D. Bayerl, M. Dixit, G. Mpourmpakis, J.R. Morse, J.W. Baldwin, H.D. Willauer, M.D. Porosoff, Assessing the viability of K-Mo_2C for reverse water–gas shift scale-up: molecular to laboratory to pilot scale, Energy & Environmental Science 13 (2020) 2524-2539

[192] A. Pajares, H. Prats, A. Romero, F. Viñes, P.R. de la Piscina, R. Sayós, N. Homs, F. Illas, Critical effect of carbon vacancies on the reverse water gas shift reaction over vanadium carbide catalysts, Applied Catalysis B: Environmental 267 (2020)

[193] A.M. Bahmanpour, F. Héroguel, M. Kılıç, C.J. Baranowski, P. Schouwink, U. Röthlisberger, J.S. Luterbacher, O. Kröcher, Essential role of oxygen vacancies of Cu-Al and Co-Al spinel oxides in their catalytic activity for the reverse water gas shift reaction, Applied Catalysis B: Environmental 266 (2020)

[194] C. Castillo-Blas, C. Álvarez-Galván, I. Puente-Orench, A. García-Sánchez, F.E. Oropeza, E. Gutiérrez-Puebla, Á. Monge, V.A. de la Peña-O'Shea, F. Gándara, Highly efficient multi-metal catalysts for carbon dioxide reduction prepared from atomically sequenced metal organic frameworks, Nano Research 14 (2020) 493-500

[195] L. Li, X. Pan, D. Lan, H. Xu, J. Ge, H. Zhang, Z. Zheng, J. Liu, Z. Xu, J. Liu, Etching of cubic Pd@Pt in UiO-66 to obtain nanocages for enhancing CO_2 hydrogenation, Materials Today Energy 19 (2021)

[196] G. Varvoutis, M. Lykaki, E. Papista, S.A.C. Carabineiro, A.C. Psarras, G.E. Marnellos, M. Konsolakis, Effect of alkali (Cs) doping on the surface chemistry and CO_2 hydrogenation performance of CuO/CeO_2 catalysts, Journal of CO_2 Utilization 44 (2021)

[197] S.T. Oyama, G.A. Somorjai, Homogeneous, heterogeneous, and enzymatic catalysis, Journal of Chemical Education 65 (1988)

[198] Industrial Catalysis: A Practical Approach, 2nd edition By J. Hagen. 2006. Wiley-VCH: Weinheim. Price £115. 507 + xviii pp. ISBN 3-527-31144-0, Organic Process Research & Development 10 (2006) 683-684. Retrieved from **https://doi.org/10.1021/op050247m**

[199] P.W.N.M. van Leeuwen, Homogeneous Catalysis, 2004.

[200] V. Polshettiwar, R. Luque, A. Fihri, H. Zhu, M. Bouhrara, J.M. Basset, Magnetically recoverable nanocatalysts, Chem Rev 111 (2011) 3036-3075

[201] G.A. Somorjai, Introduction to Surface Chemistry and Catalysis, Wiley1994.

[202] Z.A. Qiao, Z. Wu, S. Dai, Shape-controlled ceria-based nanostructures for catalysis applications, ChemSusChem 6 (2013) 1821-1833

[203] J. Beckers, G. Rothenberg, Sustainable selective oxidations using ceria-based materials, Green Chemistry 12 (2010)

[204] L. Vivier, D. Duprez, Ceria-based solid catalysts for organic chemistry, ChemSusChem 3 (2010) 654-678

[205] S. Agarwal, B. Mojet, L. Lefferts, A. Datye, Ceria Nanoshapes-Structural and Catalytic Properties, Catalysis by Materials with Well-Defined Structures (2015) 31-70

[206] Tana, M. Zhang, J. Li, H. Li, Y. Li, W. Shen, Morphology-dependent redox and catalytic properties of CeO_2 nanostructures: Nanowires, nanorods and nanoparticles, Catalysis Today 148 (2009) 179-183

[207] C. Sun, H. Li, L. Chen, Nanostructured ceria-based materials: synthesis, properties, and applications, Energy & Environmental Science 5 (2012)

[208] M.E. Khan, M.M. Khan, M.H. Cho, $Ce^{(3+)}$-ion, Surface Oxygen Vacancy, and Visible Light-induced Photocatalytic Dye Degradation and Photocapacitive Performance of CeO_2-Graphene Nanostructures, Sci Rep 7 (2017) 5928

[209] A.F. Diwell, R.R. Rajaram, H.A. Shaw, T.J. Truex, The Role of Ceria in Three-Way Catalysts, in: A. Crucq (Ed.) Studies in Surface Science and Catalysis, Elsevier1991, pp. 139-152.

[210] C. Xia, M. Liu, Microstructures, conductivities, and electrochemical properties of $Ce_{0.9}Gd_{0.1}O_2$ and GDC–Ni anodes for low-temperature SOFCs, Solid state ionics 152 (2002) 423-430

[211] B. Steele, Oxygen transport and exchange in oxide ceramics, Journal of Power Sources 49 (1994) 1-14

[212] Z. Wu, M. Li, S.H. Overbury, On the structure dependence of CO oxidation over CeO_2 nanocrystals with well-defined surface planes, Journal of Catalysis 285 (2012) 61-73

[213] X. Liu, K. Zhou, L. Wang, B. Wang, Y. Li, Oxygen Vacancy Clusters Promoting Reducibility and Activity of Ceria Nanorods, Journal of the American Chemical Society 131 (2009) 3140-3141

[214] K. Zhou, X. Wang, X. Sun, Q. Peng, Y. Li, Enhanced catalytic activity of ceria nanorods from well-defined reactive crystal planes, Journal of Catalysis 229 (2005) 206-212

[215] L. Liu, Y. Cao, W. Sun, Z. Yao, B. Liu, F. Gao, L. Dong, Morphology and nanosize effects of ceria from different precursors on the activity for NO reduction, Catalysis Today 175 (2011) 48-54

[216] A. Trovarelli, C. de Leitenburg, M. Boaro, G. Dolcetti, The utilization of ceria in industrial catalysis, Catalysis Today 50 (1999) 353-367

[217] S. Czernik, R. Evans, R. French, Hydrogen from biomass-production by steam reforming of biomass pyrolysis oil, Catalysis Today 129 (2007) 265-268

[218] R.J. Gorte, Ceria in catalysis: From automotive applications to the water–gas shift reaction, AIChE Journal 56 (2010) 1126-1135

[219] R. Gorte, S. Zhao, Studies of the water-gas-shift reaction with ceria-supported precious metals, Catalysis Today 104 (2005) 18-24

[220] G. Jacobs, P.M. Patterson, L. Williams, D. Sparks, B.H. Davis, Low Temperature Water–Gas Shift: Role of Pretreatment on Formation of Surface Carbonates and Formates, Catalysis Letters 96 (2004) 97-105

[221] K. Jia, H. Zhang, W. Li, Effect of Morphology of the Ceria Support on the Activity of Au/CeO_2 Catalysts for CO Oxidation, Chinese Journal of Catalysis 29 (2008) 1089-1092

[222] T. Désaunay, G. Bonura, V. Chiodo, S. Freni, J.P. Couzinié, J. Bourgon, A. Ringuedé, F. Labat, C. Adamo, M. Cassir, Surface-dependent oxidation of H_2 on CeO_2 surfaces, Journal of Catalysis 297 (2013) 193-201

[223] R. Wang, S.I. Mutinda, The dynamic shape of ceria nanoparticles, Chemical Physics Letters 517 (2011) 186-189

[224] Z.L. Wang, X. Feng, Polyhedral shapes of CeO_2 nanoparticles, The Journal of Physical Chemistry B 107 (2003) 13563-13566

[225] F. Zhang, S.-W. Chan, J.E. Spanier, E. Apak, Q. Jin, R.D. Robinson, I.P. Herman, Cerium oxide nanoparticles: Size-selective formation and structure analysis, Applied Physics Letters 80 (2002) 127-129

[226] D.R. Mullins, M.D. Robbins, J. Zhou, Adsorption and reaction of methanol on thin-film cerium oxide, Surface science 600 (2006) 1547-1558

[227] L.C. Wang, M. Tahvildar Khazaneh, D. Widmann, R.J. Behm, TAP reactor studies of the oxidizing capability of CO_2 on a Au/CeO_2 catalyst – A first step toward identifying a redox mechanism in the Reverse Water–Gas Shift reaction, Journal of Catalysis 302 (2013) 20-30

[228] J.M. Vohs, Site requirements for the adsorption and reaction of oxygenates on metal oxide surfaces, Chemical reviews 113 (2013) 4136-4163

[229] K. An, G.A. Somorjai, Size and Shape Control of Metal Nanoparticles for Reaction Selectivity in Catalysis, ChemCatChem 4 (2012) 1512-1524

[230] K.M. Bratlie, H. Lee, K. Komvopoulos, P. Yang, G.A. Somorjai, Platinum nanoparticle shape effects on benzene hydrogenation selectivity, Nano Lett 7 (2007) 3097-3101

[231] R. Schlögl, S.B. Abd Hamid, Nanocatalysis: mature science revisited or something really new?, Angewandte Chemie International Edition 43 (2004) 1628-1637

[232] M. Frank, M. Bäumer, From atoms to crystallites: adsorption on oxide-supported metal particles, Physical Chemistry Chemical Physics 2 (2000) 3723-3737

[233] M. Valden, X. Lai, D.W. Goodman, Onset of catalytic activity of gold clusters on titania with the appearance of nonmetallic properties, science 281 (1998) 1647-1650

[234] T. Hyeon, Chemical synthesis of magnetic nanoparticles, Chemical Communications (2003) 927-934

[235] G. Markovich, C.P. Collier, S.E. Henrichs, F. Remacle, R.D. Levine, J.R. Heath, Architectonic Quantum Dot Solids, Accounts of Chemical Research 32 (1999) 415-423

[236] V. Maheshwari, J. Kane, R.F. Saraf, Self-Assembly of a Micrometers-Long One-Dimensional Network of Cemented Au Nanoparticles, Advanced Materials 20 (2008) 284-287

[237] H. Weller, Quantized semiconductor particles: a novel state of matter for materials science, Advanced Materials 5 (1993) 88-95

[238] M.G. Bawendi, M.L. Steigerwald, L.E. Brus, The quantum mechanics of larger semiconductor clusters (" quantum dots"), Annual Review of Physical Chemistry 41 (1990) 477-496

[239] X.-D. Zhou, W. Huebner, Size-induced lattice relaxation in CeO_2 nanoparticles, Applied Physics Letters 79 (2001) 3512-3514

[240] I.I. Soykal, H. Sohn, D. Singh, J.T. Miller, U.S. Ozkan, Reduction Characteristics of Ceria under Ethanol Steam Reforming Conditions: Effect of the Particle Size, ACS Catalysis 4 (2014) 585-592

[241] L. Mao, Study of Ceria Nanoparticles Synthesis and the Performance of Nano-ceria Coating for High Temperature Oxidation Resistance in Combustion Atmosphere, The University of Wisconsin-Milwaukee, 2016, pp. 77.

[242] A. Bumajdad, M.I. Zaki, J. Eastoe, L. Pasupulety, Microemulsion-based synthesis of CeO_2 powders with high surface area and high-temperature stabilities, Langmuir 20 (2004) 11223-11233

[243] M.A. Malik, M.Y. Wani, M.A. Hashim, Microemulsion method: A novel route to synthesize organic and inorganic nanomaterials, Arabian Journal of Chemistry 5 (2012) 397-417

[244] C. Dhand, N. Dwivedi, X.J. Loh, A.N. Jie Ying, N.K. Verma, R.W. Beuerman, R. Lakshminarayanan, S. Ramakrishna, Methods and strategies for the synthesis of diverse nanoparticles and their applications: a comprehensive overview, RSC Advances 5 (2015) 105003-105037

[245] J.H. Schulman, W. Stoeckenius, L.M. Prince, Mechanism of Formation and Structure of Micro Emulsions by Electron Microscopy, The Journal of Physical Chemistry 63 (1959) 1677-1680

[246] M.P. Pileni, Reverse micelles as microreactors, The Journal of Physical Chemistry 97 (1993) 6961-6973. Retrieved from **https://doi.org/10.1021/j100129a008**

[247] M.P. Pileni, I. Lisiecki, Nanometer metallic copper particle synthesis in reverse micelles, Colloids and Surfaces A: Physicochemical and Engineering Aspects 80 (1993) 63-68

[248] G. Sun, S. Mottaghi-Tabar, L. Ricardez-Sandoval, D.S.A. Simakov, Highly Active, Selective and Stable Reverse Water Gas Shift Catalyst Based on High Surface Area MoC/γ-Al_2O_3 Synthesized by Reverse Microemulsion, Topics in Catalysis (2021)

[249] ICP-OES. Retrieved from **http://www.rohs-cmet.in/content/icp-oes**

[250] A. Koçak, MATERIALS SCIENCE AND ENGINEERING #Thin Film Preparation,Particle Size and Thickness Analysis Experimental Report, 2018.

[251] BET surface area. Retrieved from **https://andyjconnelly.wordpress.com/2017/03/13/bet-surface-area/**

[252] A. Mukhopadhyay, Measurement of magnetic hysteresis loops in continuous and patterned ferromagnetic nanostructures by static magneto-optical kerr effect magnetometer, 2015.

[253] Energy-dispersive spectroscopy. Retrieved from **https://www.copperpodip.com/post/what-is-edx-energy-dispersive-x-ray-spectroscopy**

[254] TEM schematic. Retrieved from **http://www.hk-phy.org/atomic_world/tem/tem02_e.html**

[255] S. Hunter, Molybdenum Nitrides: Structural and Reactivity Studies, 2012.

[256] G. Zhou, H. Liu, K. Cui, A. Jia, G. Hu, Z. Jiao, Y. Liu, X. Zhang, Role of surface Ni and Ce species of Ni/CeO_2 catalyst in CO_2 methanation, Applied Surface Science 383 (2016) 248-252

[257] N.S. Arul, D. Mangalaraj, J.I. Han, Facile hydrothermal synthesis of CeO_2 nanopebbles, Bulletin of Materials Science 38 (2015) 1135-1139

[258] S.A. Hassanzadeh-Tabrizi, M. Mazaheri, M. Aminzare, S.K. Sadrnezhaad, Reverse precipitation synthesis and characterization of CeO_2 nanopowder, Journal of Alloys and Compounds 491 (2010) 499-502

[259] J. Jasmine Ketzial, A. Nesaraj, Synthesis of CeO_2 nanoparticles by chemical precipitation and the effect of a surfactant on the distribution of particle sizes, 2011.

[260] W. Mista, T. Rayment, J. Hanuza, L. Macalik, Synthesis and Characterization of Metastable CeO_2–ZrO_2 Solid Solution Obtained by Polymerized Complex Method, 2004.

[261] G.V. Samsonov, The oxide handbook, Springer Science & Business Media2013.

[262] M. Mogensen, Physical, chemical and electrochemical properties of pure and doped ceria, Solid State Ionics 129 (2000) 63-94

[263] G.-y. Adachi, N. Imanaka, The Binary Rare Earth Oxides, Chemical Reviews 98 (1998) 1479-1514

[264] MATERIALS SCIENCE AND TECHNOLOGY, in: O.T. Sørensen (Ed.) Nonstoichiometric Oxides, Academic Press1981, pp. ii.

[265] G. Elmanfe, S. Bufarwa, Ceria catalyst promoted with Al^{3}† and Acidified with PO_4^{3-} synthesis and Surface Textural Properties, 2015.

[266] H.A. Khalaf, The negative effect of ceria on the propene selectivity for isopropanol decomposition over phosphated and phosphate-free ceria/alumina catalysts, SpringerPlus 2 (2013) 619

[267] C. Li, Y. Sakata, T. Arai, K. Domen, K.-i. Maruya, T. Onishi, Carbon monoxide and carbon dioxide adsorption on cerium oxide studied by Fourier-transform infrared spectroscopy. Part 1.—Formation of carbonate species on dehydroxylated CeO_2, at room temperature, Journal of the Chemical Society, Faraday Transactions 1: Physical Chemistry in Condensed Phases 85 (1989)

[268] T. Jin, Y. Zhou, G.J. Mains, J.M. White, Infrared and x-ray photoelectron spectroscopy study of carbon monoxide and carbon dioxide on platinum/ceria, The Journal of Physical Chemistry 91 (1987) 5931-5937

[269] L.H. Little, Infrared spectra of adsorbed species, Journal of Molecular Structure 1 (1968)

[270] K. Nakamoto, J. Fujita, R.A. Condrate, Y. Morimoto, Infrared Spectra of Metal Chelate Compounds. IX. A Normal Coordinate Analysis of Dithiocarbamato Complexes, The Journal of Chemical Physics 39 (1963) 423-427. Retrieved from **https://aip.scitation.org/doi/pdf/10.1063/1.1734264**

[271] S.L. Swartz, Catalysis by Ceria and Related Materials Edited by Alessandro Trovarelli (Università di Udine, Italy). Catalytic Science Series. Volume 2. Series Edited by Graham J. Hutchings. Imperial College Press: London. 2002. vviii + 508 pp. $78.00. ISBN: 1-86094-299-7, Journal of the American Chemical Society 124 (2002) 12923-12924

[272] G. Kim, Ceria-promoted three-way catalysts for auto exhaust emission control, Industrial & Engineering Chemistry Product Research and Development 21 (1982) 267-274

[273] J. Kašpar, P. Fornasiero, M. Graziani, Use of CeO_2-based oxides in the three-way catalysis, Catalysis Today 50 (1999) 285-298

[274] S. Mahamulkar, K. Yin, M.T. Claure, R.J. Davis, L. Li, H. Shibata, A. Malek, C.W. Jones, P.K. Agrawal, Thermally stable α-alumina supported ceria for coking resistance and oxidation of radical coke generated in-situ, Fuel 218 (2018) 357-365

[275] T. Aysu, J. Fermoso, A. Sanna, Ceria on alumina support for catalytic pyrolysis of Pavlova sp. microalgae to high-quality bio-oils, Journal of Energy Chemistry 27 (2018) 874-882

[276] X. Wen, C. Li, X. Fan, H. Gao, W. Zhang, L. Chen, G. Zeng, Y. Zhao, Experimental Study of Gaseous Elemental Mercury Removal with CeO_2/γ-Al_2O_3, Energy & Fuels 25 (2011) 2939-2944

[277] I.P. Chen, S.-S. Lin, C.-H. Wang, L. Chang, J.-S. Chang, Preparing and characterizing an optimal supported ceria catalyst for the catalytic wet air oxidation of phenol, 50 (2004) 49-58

[278] R.-t. Guo, Y. Zhou, W.-g. Pan, J.-n. Hong, W.-l. Zhen, Q. Jin, C.-g. Ding, S.-y. Guo, Effect of preparation methods on the performance of CeO_2/Al_2O_3 catalysts for selective catalytic reduction of NO with NH_3, Journal of Industrial and Engineering Chemistry 19 (2013) 2022-2025

[279] S. Damyanova, C.A. Perez, M. Schmal, J.M.C. Bueno, Characterization of ceria-coated alumina carrier, Applied Catalysis A: General 234 (2002) 271-282

[280] R. Blom, I.M. Dahl, Å. Slagtem, B. Sortland, A. Spjelkavik, E. Tangstad, Carbon dioxide reforming of methane over lanthanum-modified catalysts in a fluidized-bed reactor, Catalysis Today 21 (1994) 535-543

[281] M. Ozawa, M. Kimura, Effect of cerium addition on the thermal stability of gamma alumina support, Journal of Materials Science Letters 9 (1990) 291-293

[282] V.K. Paidi, L. Savereide, D.J. Childers, J.M. Notestein, C.A. Roberts, J. van Lierop, Predicting NOx Catalysis by Quantifying $Ce^{(3+)}$ from Surface and Lattice Oxygen, ACS Appl Mater Interfaces 9 (2017) 30670-30678

[283] A. Mohammed, H. Hussein, M. Mohammed, The Effect of Temperature on the Synthesis of Nano-Gamma Alumina Using Hydrothermal Method, Iraqi Journal of Chemical and Petroleum Engineering 18 (2017)

[284] H.C. Yao, Y.F.Y. Yao, Ceria in automotive exhaust catalysts: I. Oxygen storage, Journal of Catalysis 86 (1984) 254-265

[285] V. Perrichon, A. Laachir, G. Bergeret, R. Fréty, L. Tournayan, O. Touret, Reduction of cerias with different textures by hydrogen and their reoxidation by oxygen, Journal of the Chemical Society, Faraday Transactions 90 (1994) 773-781

[286] M.P. Rosynek, Catalytic Properties of Rare Earth Oxides, Catalysis Reviews 16 (1977) 111-154

[287] N. Kaufherr, L. Mendelovici, M. Steinberg, The preparation of cerium(III) aluminate at lower temperatures: IR, X-ray and electron spin resonance study, Journal of the Less Common Metals 107 (1985) 281-289

[288] Y.S. Kim, Crystallographic study of cerium aluminate (CeAlO3), Acta Crystallographica Section B Structural Crystallography and Crystal Chemistry 24 (1968) 295-296

[289] A. Piras, S. Colussi, A. Trovarelli, V. Sergo, J. Llorca, R. Psaro, L. Sordelli, Structural and Morphological Investigation of Ceria-Promoted Al_2O_3 under Severe Reducing/Oxidizing Conditions, The Journal of Physical Chemistry B 109 (2005) 11110-11118

[290] A. Amirsalari, S. Farjami Shayesteh, Effects of pH and calcination temperature on structural and optical properties of alumina nanoparticles, Superlattices and Microstructures 82 (2015) 507-524

[291] Z. Yang, K. Zhou, X. Liu, Q. Tian, D. Lu, S. Yang, Single-crystalline ceria nanocubes: size-controlled synthesis, characterization and redox property, Nanotechnology 18 (2007) 185606

[292] L. Zhang, Y. Zhang, S. Chen, Effect of promoter SiO2, TiO2 or SiO2-TiO2 on the performance of CuO-ZnO-Al2O3 catalyst for methanol synthesis from CO2 hydrogenation, Applied Catalysis A: General 415-416 (2012) 118-123

[293] T. Ishii, T. Kyotani, Chapter 14 - Temperature Programmed Desorption, in: M. Inagaki, F. Kang (Eds.) Materials Science and Engineering of Carbon, Butterworth-Heinemann2016, pp. 287-305.

[294] J.L. Figueiredo, M.F.R. Pereira, M.M.A. Freitas, J.J.M. Órfão, Modification of the surface chemistry of activated carbons, Carbon 37 (1999) 1379-1389

[295] A. Capelle, F. de Vooys, J.H. Veen, Activated Carbon--a Fascinating Material: Some Thoughts on Activated Carbon, Norit N.V.1983.

[296] C. Moreno-Castilla, M.A. Ferro-Garcia, J.P. Joly, I. Bautista-Toledo, F. Carrasco-Marin, J. Rivera-Utrilla, Activated Carbon Surface Modifications by Nitric Acid, Hydrogen Peroxide, and Ammonium Peroxydisulfate Treatments, Langmuir 11 (1995) 4386-4392

[297] C. Moreno-castilla, F. Carrasco-marín, F.J. Maldonado-hódar, J. Rivera-utrilla, Effects of non-oxidant and oxidant acid treatments on the surface properties of an activated carbon with very low ash content, Carbon 36 (1998) 145-151

[298] J. Baltrusaitis, J. Schuttlefield, E. Zeitler, V.H. Grassian, Carbon dioxide adsorption on oxide nanoparticle surfaces, Chemical Engineering Journal 170 (2011) 471-481

[299] G. Jacobs, A.C. Crawford, B.H. Davis, Water-gas shift: steady state isotope switching study of the water-gas shift reaction over Pt/ceria using in-situ DRIFTS, Catalysis Letters 100 (2005) 147-152

[300] R. Yang, Y. Fu, Y. Zhang, N. Tsubaki, In situ DRIFT study of low-temperature methanol synthesis mechanism on Cu/ZnO catalysts from CO2-containing syngas using ethanol promoter, Journal of Catalysis 228 (2004) 23-35

[301] X. Wang, H. Shi, J.H. Kwak, J. Szanyi, Mechanism of CO2 Hydrogenation on Pd/Al2O3 Catalysts: Kinetics and Transient DRIFTS-MS Studies, ACS Catalysis 5 (2015) 6337-6349

[302] Y. Yu, S. Mottaghi-Tabar, M.W. Iqbal, A. Yu, D.S.A. Simakov, CO2 methanation over alumina-supported cobalt oxide and carbide synthesized by reverse microemulsion method, Catalysis Today (2020)

[303] C.M. Chun, J.D. Mumford, T.A. Ramanarayanan, Mechanisms of Metal Dusting Corrosion of Iron, Journal of The Electrochemical Society 149 (2002)

[304] B.A. Baker, G.D. Smith, Metal Dusting Behavior of High-Temperature Alloys, CORROSION 99, 1999.

[305] R. Hochman, The fundamentals of metal dusting, API Division of Refining Proc. 46 (1966) 331

[306] R. Hochman, Properties of High Temperature Alloys with Emphasis on Environmental Effects ed ZA Foroulis and FS Pettit p. 715 in Editors, PV, 1977.

[307] H. Grabke, R. Krajak, E. Müller-Lorenz, Metal dusting of high temperature alloys, Materials and Corrosion 44 (1993) 89-97

[308] H. Grabke, R. Krajak, J.N. Paz, On the mechanism of catastrophic carburization:'metal dusting', Corrosion Science 35 (1993) 1141-1150

[309] J.N. Paz, H. Grabke, Metal dusting, Oxidation of metals 39 (1993) 437-456

[310] H. Grabke, Thermodynamics, mechanisms and kinetics of metal dusting, Materials and corrosion 49 (1998) 303-308

[311] H. Grabke, E. Müller-Lorenz, Protection of high alloy steels against metal dusting by oxide scales, Materials and Corrosion 49 (1998) 317-320

[312] J. Klöwer, H.-J. Grabke, E.M. Müller-Lorenz, Metal dusting of nickel-base alloys, Materials and Corrosion 49 (1998) 328-329

[313] S. Strauss, H. Grabke, Role of alloying elements in steels on metal dusting, Materials and corrosion 49 (1998) 321-327

[314] C. Chun, T.A. Ramanarayanan, J. Mumford, Relationship between coking and metal dusting, Materials and Corrosion 50 (1999) 634-639

[315] C. Chun, J. Mumford, T. Ramanarayanan, Carbon-Induced Corrosion of Nickel Anode, Journal of the Electrochemical Society 147 (2000) 3680

[316] H. Jürgen Grabke, G. Tauber, Kinetik der Entkohlung von α-und γ-Eisen in H_2O-H_2-Gemischen und der Aufkohlung in CO-H_2-Gemischen, Archiv für das Eisenhüttenwesen 46 (1975) 215-222

[317] S.R. Shatynski, H.J. Grabke, The kinetics of carburization of γ-iron in CO-He and CO-H_2 atmospheres at 920° C, Archiv für das Eisenhüttenwesen 49 (1978) 129-133

[318] E. Pippel, J. Woltersdorf, R. Schneider, Micromechanisms of metal dusting on Fe-base and Ni-base alloys, Materials and corrosion 49 (1998) 309-316

[319] J.E. Herrera, D.E. Resasco, In situ TPO/Raman to characterize single-walled carbon nanotubes, Chemical Physics Letters 376 (2003) 302-309

[320] A. Ochoa, B. Aramburu, B. Valle, D.E. Resasco, J. Bilbao, A.G. Gayubo, P. Castaño, Role of oxygenates and effect of operating conditions in the deactivation of a Ni supported catalyst during the steam reforming of bio-oil, Green Chemistry 19 (2017) 4315-4333

[321] A. Ochoa, B. Valle, D.E. Resasco, J. Bilbao, A.G. Gayubo, P. Castaño, Temperature Programmed Oxidation Coupled with In Situ Techniques Reveal the Nature and Location of Coke Deposited on a Ni/La_2O_3-αAl_2O_3 Catalyst in the Steam Reforming of Bio-oil, ChemCatChem 10 (2018) 2311-2321

[322] B.A. Baker, G.D. Smith, Metal dusting behavior of high-temperature alloys, CORROSION 99, OnePetro, 1999.

Appendix

Appendix A

Calibration curve for continuous measurement of outlet gases using IR-cell and LabView

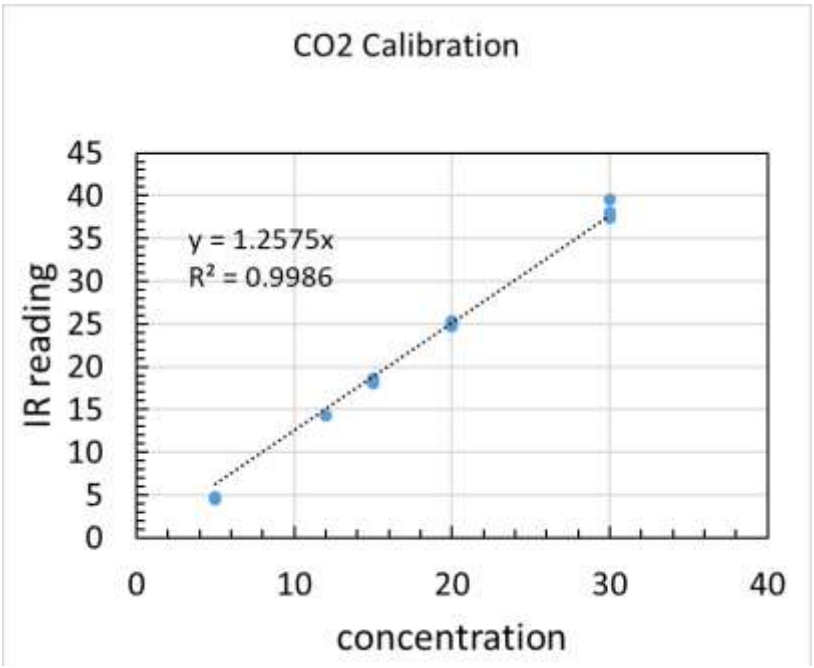

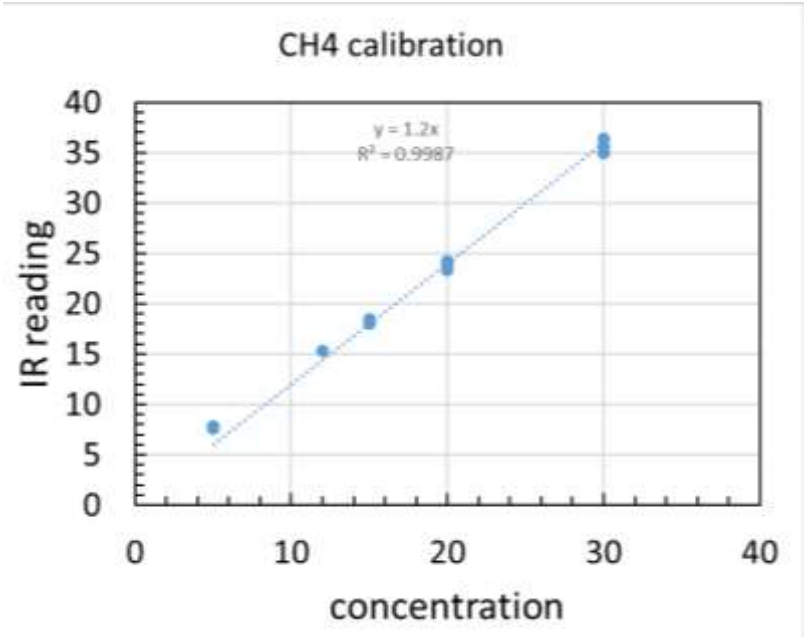

Figure S.1: Calibration curves

Appendix B

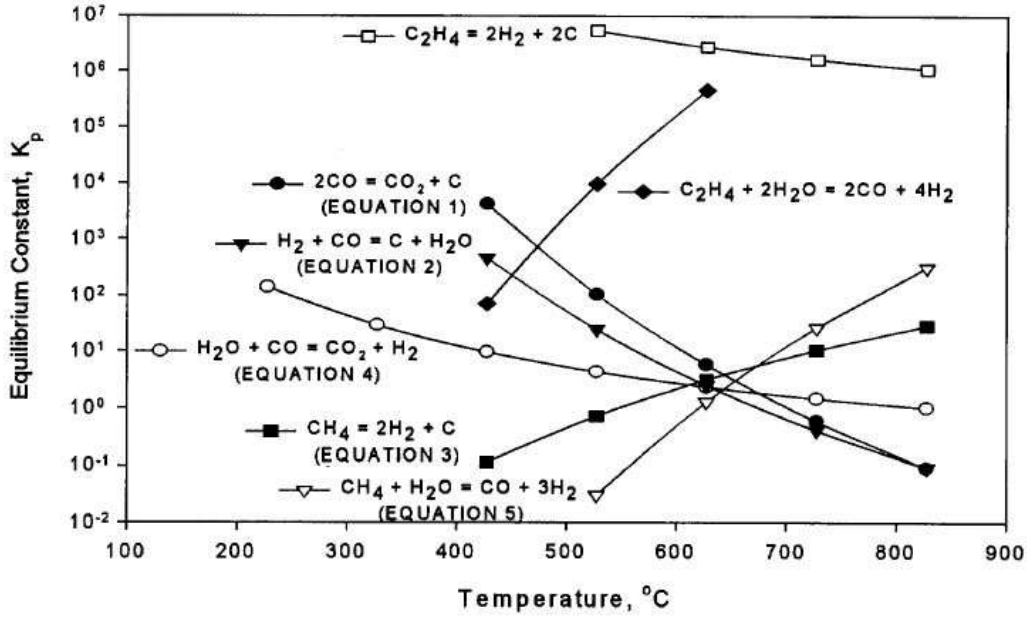

Figure S.2: Equilibrium constants for key reactions which can occur in the metal dusting environment [322].

The above figure is presented as a supplementary source of information to quickly show the favorable temperature ranges for the coke formation in the metal dusting environment.

Appendix C

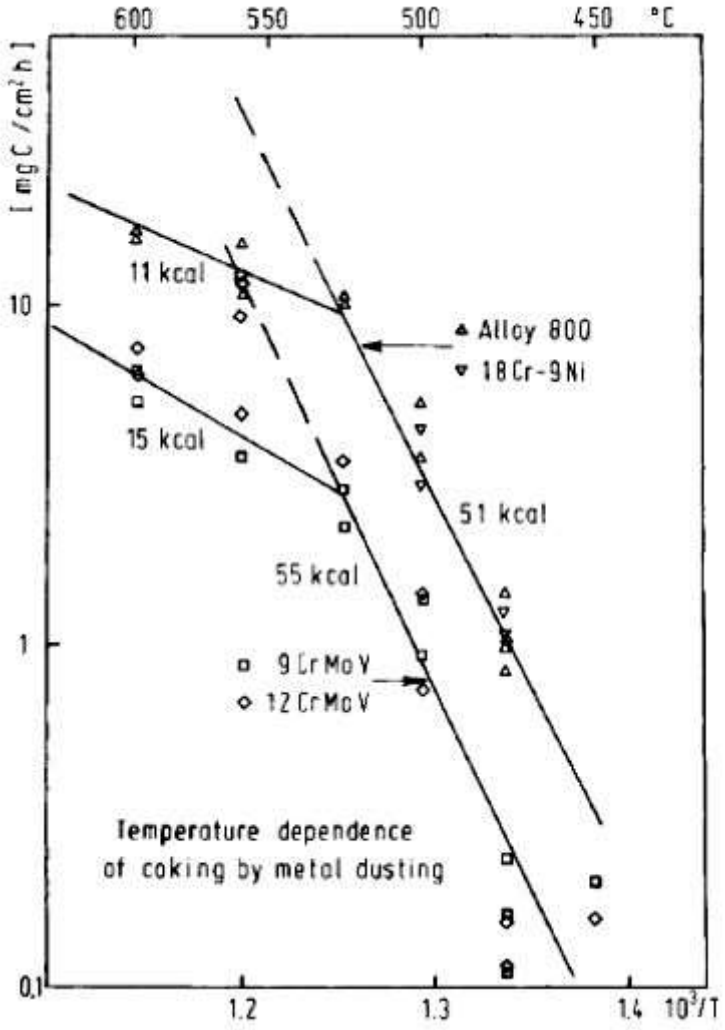

Figure S.3: Arrhenius diagram of coke rate due to the metal dusting of ferritic and austenitic steel in H_2-CO_2-H_2O [17].

The above figure is included as supplementary information to show that the activation energy is different for coke formation due to metal dusting for different temperature ranges.